MODELS FOR PROJECTILE IMPACT INTO HYBRID MULTI-LAYER ARMOR SYSTEMS WITH AXISYMMETRIC OR BIAXIAL LAYERS WITH GAPS

A Dissertation

Presented to the Faculty of the Graduate School

of Cornell University

in Partial Fulfillment of the Requirements for the Degree of

Doctor of Philosophy

by

Wei Li

May 2011

MODELS FOR PROJECTILE IMPACT INTO HYBRID MULTI-LAYER ARMOR SYSTEMS WITH AXISYMMETRIC OR BIAXIAL LAYERS WITH GAPS

Wei Li, Ph.D.

Cornell University 2011

Analytical and numerical modeling of fibrous material resistance to penetration under impact by high-velocity projectiles has been of great interest not only for personnel protection reasons but also because trial-and-error testing is costly and time-consuming. In this thesis, two PC-based models are developed for projectile impact into a multi-layer system of membrane layers with non-zero spacings between them. The projectile is a standard right circular cylinder (RCC) often used in laboratory experiments to compare material systems, and the models blend theoretical analysis and numerical simulation to characterize the interaction between the projectile and the various layers.

We first consider a system of axisymmetric layers under impact by an RCC projectile. In particular, we consider such performance measures as the critical strains in layers resulting in their failure, the strains in unfailed layers, critical layer gaps, the number of layers penetrated, and the residual velocities in cases where all layers have been penetrated. The model allows variation of mechanical properties from layer to layer as well as variations in spacings between layers, in order to study their combined effects on the ballistic performance of the system. Case studies are performed on the ballistic impact response of fibrous material systems of particular interest in body armor. These are ultra-high molecular weight polyethylene (UHMWPE) fibers such as DSM's Dyneema SK76, as well as aramid fibers such as duPont's Kevlar-29.

We also develop a semi-analytical model for a multi-layered biaxial, elastic membrane system impacted by an RCC projectile. The model builds on a single-layer membrane model, which has been under development by collaborators in the overall body armor work at Cornell University. Key assumptions and parameter values in the single layer model were guided by simulation results using a code based on the finite difference method (FDM) incorporating an algorithm frequently used in molecular dynamics simulations. The code was originally developed by researchers at DSM (makers of Dyneema) and has been modified by the author and several collaborators at Cornell University to suppress local strain concentrations and dynamic artifacts resulting from the descretization of the structure, and to better handle the current geometry.

Numerical simulations of impact into a flexible panel are performed where the main emphasis is on a comprehensive understanding of the strain and displacement fields, as well as on the velocity fields versus time. The panel is treated as a single biaxial membrane with negligible shear stiffness compared with the tensile stiffness, and is assigned the properties of Dyneema SK76 or Kevlar 29 biaxial fabrics and flexible composites having about 15 to 20 percent matrix content. Numerical results are obtained through incremental integration of differential equations using small time steps. Compared to simulations using the modified DSM code, there are several important improvements: (1) The calculation time has been accelerated by at least a factor of 1000; (2) Results under different parameter combinations can be obtained for larger geometric sizes and much longer times; and (3) Modeling multi-layer systems is now possible, and we present results for several cases.

BIOGRAPHICAL SKETCH

The author was born in Dalian, China in June, 1980. After completing his high school education in Dalian No. 24 High School in 1999, the author was admitted into Department of Mechanical Engineering in Tsinghua University, Beijing, where he received his Bachelor's degree in July, 2003 and his Master's degree in July, 2006. The author was admitted into the Sibley School of Mechanical and Aerospace Engineering, Cornell University in August, 2006, to pursue his PhD degree.

This thesis is dedicated to my father Li, Yongqing and my mother Wang, Liyan for their consistent support and encouragement on my academic pursuits during school years.

ACKNOWLEDGEMENTS

I would like to express my appreciation to my thesis advisor, Professor Stuart Leigh Phoenix, for his patient instructions and guidance during my Ph.D. study. I would also like to thank Professors Subrata Mukherjee and Gennady Samorodnitsky for serving on my special committee and for their encouragement and advice during my studies at Cornell. Dr. Abdulkadir Yavuz has also contributed much to the models developed in this thesis, for which I am eternally grateful.

TABLE OF CONTENTS

Biographical Sketch . . . iii
Dedication . . . iv
Acknowledgements . . . v
Table of Contents . . . vi
List of Tables . . . viii
List of Figures . . . ix

1 Introduction **1**

2 Single- and multi-layer models for isotropic materials **12**
2.1 Single-layer model . . . 12
2.1.1 Analysis . . . 13
2.1.2 Unit solution . . . 15
2.1.3 Cone wave behavior . . . 16
2.1.4 Velocity profiles for varying strain at the projectile edge . 22
2.1.5 Application of convolution to the unit solutions . . . 24
2.1.6 Deceleration of the projectile due to membrane reaction forces . . . 25
2.2 Multi-layer model . . . 27
2.3 Results and discussion . . . 32
2.3.1 Key parameters . . . 32
2.3.2 Single layer case . . . 34
2.3.3 Multi-layer cases . . . 36
2.4 Summary . . . 51

3 Single- and multi-layer models for biaxial materials **53**
3.1 Introduction . . . 53
3.2 Introduction to single-layer model . . . 54
3.2.1 Review of projectile impact into 1D tape . . . 55
3.2.2 Difficulties in extending results from 1D tape impact to impact into a biaxial membrane . . . 57
3.2.3 In-plane tension wave and out-of-plane cone wave profiles of deformation . . . 58
3.2.4 Vertical forces acting to decelerate the projectile . . . 64
3.2.5 Angles at the cone wave front and ratio of strains at the projectile and the cone wave front . . . 72
3.2.6 Calculating the key integral directly using an accurate expansion . . . 78
3.2.7 Strain decay along tension wave arms by wave induced drag of crossing yarns . . . 88
3.2.8 Application of Duhamel convolution to unit solutions to obtain general solutions . . . 91

3.2.9 Yarn length compatibility along the yarn axis in the cone . 92
3.2.10 Fundamental formula for strain at the cone wave-front and other key variables 94
3.2.11 Deceleration of the projectile due to membrane reaction forces 95
3.2.12 Average and peak strains around the projectile edge and at the cone wave-front nose 101
3.2.13 Out-of-plane velocity profile in the cone wave 108
3.2.14 Explicit formulas for initial strains, velocities and angles upon the impact of projectile 110
3.3 Multi-layer model for biaxial materials 112
3.4 Results and discussions 114
3.4.1 Verification and comparisons 114
3.4.2 Key parameters 117
3.4.3 Single-layer results: analysis and verification 118
3.4.4 Further exploration of the single-ply model 149
3.4.5 Three-layer system with gaps 154
3.4.6 A ten-layer system with gaps 171

4 Conclusions **186**
4.1 Summary of the thesis 186
4.2 Suggestions on future work 191

A Dimensionless framework for numerical solutions in isotropic materials **194**
A.1 Analysis and equations 194
A.2 Initial conditions 197
A.3 Summary of key equations to solve numerically 198

B Dimensionless framework for numerical solutions in bi-axial membranes **200**
B.1 Analysis and equations 200
B.2 Dimensionless initial conditions 206

Bibliography **208**

LIST OF TABLES

2.1 A list of key parameters of Kevlar and Dyneema 33
2.2 A comparison of critical layer gap $G_{n,cr}$, critical velocity $V_{n,cr}$ and relative efficiency from $n = 1$ to 10 in Kevlar and Dyneema cases 46

3.1 A list of key parameters implemented in the Kevlar and Dyneema cases (Dyneema SK76 is assumed in all the following simulations) 118
3.2 A comparison of the strain decrease from $X = 1$ to $X = 2$ and then to $X = R_c(\tau)$ at different times. 135
3.3 A comparison of the strain decrease from $X = r_p$ to $X = 2r_p$ and $X = r_c$ at different time 137
3.4 Comparison of some important quantities calculated from study of the single-layer, three-layer and ten-layer cases. 177
3.5 Comparison of some important quantities obtained from study of single-layer, three-layer and ten-layer cases. 183

LIST OF FIGURES

1.1 Schematic of a hypothetical layered fibrous structure envisioned to stop armor piercing APM2 bullets, yet half the weight of current, state-of-the art systems. 2
1.2 Schematic of blunt-nose bullet penetrating multiply layers with non-zero space - global view (courtesy DuPont) 6
1.3 Schematic of blunt-nose bullet penetrating multiply layers with non-zero space - local view (courtesy DuPont) 7
1.4 Illustration of possible differences in the impact response of a multiply system with and without layer gaps among plies 9

2.1 Geometry of the membrane impact problem and the two coordinate systems used 13
2.2 Pulley analogy analysis: the force provided by the belt on the two sides balances the centrifugal force due to its velocity, and the result is independent of the pulley radius assumed 17
2.3 $r_c(t)$ is the cone wave radius in material coordinates. In order to specify its actual length with respect to ground coordinates, we must "remove" the part that travels back, which is $u_c(t)$ 19
2.4 Schematic of two-layer problem with different materials for each layer and a gap between them of width d_m 28
2.5 Three layer system. The cone wave speed is the same when the two layers are composed of identical materials. In reality and initially there may be a very small discrepancy, it is negligible . . 31
2.6 (a) strain at projectile edge and cone wave front; (b) cone angle; (c) projectile velocity; (d) vertical displacement 35
2.7 (a) Vertical displacement (2D); (b) Vertical displacement (3D); (c) Strain (3D) 36
2.8 Three-ply no-failure case, initial velocity 500 m/s, layer gap $\frac{1}{2}G_n$: (a) Strain at projectile edge; (b) Projectile velocity; (c) Inflow velocity; (d) Cone wave radius. 37
2.9 Vertical displacement in non-penetration three-ply case:, initial velocity 500 m/s, layer gap $\frac{1}{2}G_n$ 39
2.10 Ten-layer case where no-failure occurs since the critical strain, $\varepsilon_p = 0.030$, is not reached in any layer: (a) Strain at projectile edge; (b) Projectile velocity 40
2.11 Ten layer case where all layers fail since the critical strain, $\varepsilon_p = 0.030$, is reached or exceeded in each: critical velocity 636.4 m/s . 41
2.12 Ten layer case at critical velocity 636.4 m/s where all layers fail since the critical strain, $\varepsilon_p = 0.030$, is reached or exceeded in each: (a) Projectile velocity, (b) Vertical displacement 42

2.13 "Critical velocity" vs. dimensionless layer gap G_n for different numbers of layers: a comparison of the results in this paper with those in Porwal and Phoenix(2005) [2]. (a) Kevlar, linear scale, this paper; (b) Kevlar, linear scale, in Porwal and Phoenix(2005) [2]; (c) Kevlar, log scale, this paper; (d) Kevlar, log scale, in Porwal and Phoenix(2005) [2] 44
2.14 "Critical velocity" vs. layer gap G_n for different numbers of layers of Dyneema: (a) linear scale; (b) log scale 45
2.15 Projectile velocity vs. number of layers penetrated for various cumulative gap conditions: (a) Kevlar; (b) Dyneema 48
2.16 Strain in current top layer (the next layer to be penetrated). Kevlar: (a) 450 m/s; (c) 400 m/s; (d) 350 m/s. Dyneema: (b) 700 m/s; (d) 600 m/s; (e) 500 m/s 50

3.1 Cross-sectional geometry of projectile impact into a 1D tape. . . . 55
3.2 Behavior of the inverse of the square of the strain ratio along the yarn axis inside the cone region using the DSM simulation code at approximately constant strain at the cone wave-front. 79
3.3 Behavior of a key ratio η in the analysis. 84
3.4 Comparison of peak strain $\varepsilon_{p,max}$ and strain at the centerline of x-axis ε_p with projectile mass $M_p = \infty$(red), 8.0gram(blue) and 1.1gram(green) 102
3.5 2D strain overview in $x - y$ plane (150 grid points per unit distance, r_p) at $\tau = 5$, as obtained from the Cornell modified DSM code. 103
3.6 2D strain overview in the $x - y$ plane (38 grid points per distance r_p), where $\tau = 35$, as obtained from the Cornell-modified DSM code. 105
3.7 3D strain distribution (38 grid points per r_p) for $\tau = 35$, as obtained from the Cornell-modified DSM code. 106
3.8 Comparison of semi-analytical model of the thesis with Cornell-modified DSM code results in terms of $\varepsilon_{p,Avg}$, $\varepsilon_{p,max}$ and ε_p, with three mesh sets in the DSM code: 100, 80 and 33 grid points per projectile radius r_p. 115
3.9 Evolution of velocity decay versus dimensionless time for the 9mm projectile comparing results from the Cornell semi-analytical model versus numerical simulations using the Cornell-modified DSM code with two levels of square mesh refinement. 117
3.10 Strain along the centerline of the x-axis at $\tau = 10, 20, 30, 40$ respectively (9 mm). 119
3.11 Strain distribution along projectile edge at $\tau = 0, 5, 10, 20, 40$ respectively (9 mm). 120
3.12 Curve of strain at cone wave front and projectile edge, 9 mm. . . 121

3.13 Results for some important parameters: (a) Angles at cone wave front (θ_c) and projectile edge (θ_p), effective cone wave angle (θ) and $V_{cp} = |\theta_c - \theta_p|$; (b) Projectile velocity decaying with time; (c) Inflow velocity and (d) Cone wave radius r_c. 122
3.14 Contours of vertical displacement, top view, 9mm. 124
3.15 One quarter region of the cone wave, maximum displacement around 8mm. 125
3.16 Slope distribution of yarns in the x-direction. 126
3.17 Strain distribution in the x-direction yarns, single layer, 9 mm. . . 127
3.18 Slope distribution of yarns in the x-direction. 129
3.19 The evolution of strain over time in the x-direction yarns: (a) $\tau = 10$; (b) $\tau = 20$; (c) $\tau = 30$; (d) $\tau = 40$. 131
3.20 The evolution of effective strain $\sqrt{\varepsilon_x^2 + \varepsilon_y^2}$ in x-direction yarns and y-direction yarns: (a) $\tau = 10$; (b) $\tau = 20$; (c) $\tau = 30$; (d) $\tau = 40$. . 132
3.21 Strain profile along the x-axis centerline at $\tau = 10,\ 20,\ 30,\ 40$ respectively (FSP). 134
3.22 Strain distribution around projectile edge at $\tau = 0,\ 5,\ 10,\ 20,\ 40$ respectively (FSP). 136
3.23 Profiles of strain around the cone wave front and the projectile edge, FSP projectile. 138
3.24 Results of some important parameters, FSP projectile: (a) Angles at cone wave front (θ_c) and projectile edge (θ_p), effective cone wave angle (θ and $V_{rp} = |\theta_c - \theta_p|$; (b) Projectile velocity decaying with time; (c) Inflow velocity and (d) Cone wave radius R_c. . . . 139
3.25 Vertical displacement profile within the cone wave, FSP. 140
3.26 The slope distribution within the cone wave, FSP. 141
3.27 Strain distribution in x-yarns within tensile wave front, FSP projectile. 142
3.28 The effective strain ($\sqrt{\varepsilon_x^2 + \varepsilon_y^2}$), FSP projectile. 143
3.29 The evolution of strain in x-yarns, FSP projectile: (a) $\tau = 10$; (b) $\tau = 20$; (c) $\tau = 30$; (d) $\tau = 40$. 144
3.30 The evolution of effective strain $\sqrt{\varepsilon_x^2 + \varepsilon_y^2}$, FSP projectile: (a) $\tau = 10$; (b) $\tau = 20$; (c) $\tau = 30$; (d) $\tau = 40$. 145
3.31 Comparison of slope (local cone wave obliqueness with respect to the ground) distribution, 9 mm projectile: left, DSM model; right, Cornell model. 146
3.32 Horizontal strain ε_x, 9 mm projectile: left, DSM model; right, Cornell model. 147
3.33 Effective strain $\sqrt{\varepsilon_x^2 + \varepsilon_y^2}$, 9 mm: left, DSM model; right, Cornell model. 147
3.34 The effect of initial projectile velocity on peak strain, 9 mm. . . . 150
3.35 The effect of initial projectile velocity on peak strain, FSP. 151

3.36 The effect of areal density on peak strain, 9 mm. 152
3.37 The effect of areal density on peak strain, FSP. 153
3.38 Strain distribution along the x-axis from the projectile edge to the cone wave front in a three layer system, with a layer gap of: 2 mm, vertical displacement: 8 mm, projectile type: 9 mm. 155
3.39 Various strains versus time in the three layers, layer gaps: 2 mm, vertical displacement: 8 mm, projectile type: 9 mm. 156
3.40 Results for some important model quantities for layer gap: 2 mm, final vertical displacement: 8 mm and projectile type: 9 mm: (a) Angles at the cone wave front (θ_c) the projectile edge (θ_p), the effective cone wave angle θ and the angle difference $V_{rp} = |\theta_c - \theta_p|$; (b) projectile velocity; (c) inflow velocity and (d) cone wave radius R_c. 157
3.41 Vertical displacements of the three layers, layer gap: 2 mm, vertical displacement: 8 mm, and projectile type: 9 mm. 159
3.42 The strain curves in the three layers, with layer gap: 3 mm, vertical displacement: 8 mm, and projectile type: 9 mm. 160
3.43 Behavior over time after impact of several important quantities for the case layer gap: 3 mm, and projectile type: 9 mm: (a) Angles at the cone wave front (θ_c), the projectile edge (θ_p), and the effective cone wave angle θ as well as the angle difference $V_{rp} = |\theta_c - \theta_p|$; (b) the projectile velocity; (c) inflow velocity and (d) cone wave radius R_c. 161
3.44 Strain distribution along the x-axis from the projectile edge to the cone wave front in the three layers for layer to layer gap: 2 mm, vertical displacement: 8 mm, and projectile type: FSP. 162
3.45 Various strains versus time in the three layers for a layer gap: 2 mm, maximim vertical displacement: 8 mm, and projectile type: FSP. 163
3.46 Results of some important parameters. Layer gap: 2 mm, vertical displacement: FSP: (a) Angles at cone wave front (θ_c) and projectile edge (θ_p), effective cone wave angle θ and $V_{rp} = |\theta_c - \theta_p|$; (b) projectile velocity; (c) inflow velocity and (d) cone wave radius R_c. 164
3.47 Vertical displacements in the three layers with layer gap: 2 mm, vertical displacement: 8 mm, and for projectile type: FSP. 165
3.48 Strain versus dimensionless time in three layers. Layer gap: 3 mm, maximum vertical displacement: 8 mm, projectile type: FSP 166
3.49 Plots over dimensionless time of some important quantities describing impact behavior. Layer gap: 3 mm, maximum vertical displacement: 8 mm, projectile type: FSP: (a) Angles at the cone wave front (θ_c) and the projectile edge (θ_p) as well as the effective cone wave angle θ and angle difference $V_{rp} = |\theta_c - \theta_p|$; (b) projectile velocity; (c) inflow velocity and (d) cone wave radius R_c. 167

3.50 The effect of layer gap size on strain variation and projectile deceleration with time for a 9 mm projectile: (a) strain for layer gap 2 mm; (b) strain for layer gap 3 mm; (c) projectile velocity for layer gap 2 mm; (d) projectile velocity for layer gap 3 mm. 168
3.51 The effect of layer gap size on strain variation and projectile deceleration with time for an FSP projectile: (a) strain for layer gap 2 mm; (b) strain for layer gap 3 mm; (c) projectile velocity for layer gap 2 mm; (d) projectile velocity for layer gap 3 mm. 170
3.52 Various strains vs. time for the case of ten layers. Layer gap: 0.444 mm, vertical displacement: 8 mm, projectile type: 9 mm. . 172
3.53 Behavior of various key quantities (0.444 mm layer gap): (a) Angles at the cone wave front, θ_c, and the projectile edge, θ_p, as well as the effective cone wave angle, θ, and the angle difference, $V_{rp} = |\theta_c - \theta_p|$; (b) projectile velocity; (c) inflow velocity and (d) cone wave radius R_c. 173
3.54 Various strains versus dimensionless time in a 10-layer system. Layer gap: 0.667 mm, vertical displacement: 8 mm, projectile type: 9 mm 175
3.55 Behavior of various key quantities (0.666 mm layer to layer gaps): (a) Angles at the cone wave front, θ_c, and the projectile edge, θ_p, as well as the effective cone wave angle, θ, and the angle difference, $V_{rp} = |\theta_c - \theta_p|$; (b) projectile velocity; (c) inflow velocity and (d) cone wave radius R_c. 176
3.56 The strain curves in ten layers. Layer gap: 0.444 mm, vertical displacement: 8 mm, projectile type: FSP 179
3.57 Behavior of various key quantities (0.444 mm layer to layer gaps) for the case of an FSP projectile impacting a 10-layer system: (a) Angles at the cone wave front, θ_c, and the projectile edge, θ_p, as well as the effective cone wave angle, θ, and the angle difference, $V_{rp} = |\theta_c - \theta_p|$; (b) projectile velocity; (c) inflow velocity and (d) cone wave radius R_c. 180
3.58 Strain plots versus time for a system of ten layers. Layer gap: 0.667 mm, vertical displacement: 8 mm, projectile type: FSP . . . 181
3.59 Behavior of various key quantities (0.667 mm layer to layer gaps) for the case of an FSP projectile impacting a 10-layer system: (a) Angles at the cone wave front, θ_c, and the projectile edge, θ_p, as well as the effective cone wave angle, θ, and the angle difference, $V_{rp} = |\theta_c - \theta_p|$; (b) projectile velocity; (c) inflow velocity and (d) cone wave radius R_c. 182
3.60 Various strains versus time for a ten layer system. Layer gaps: 0.444 mm and 0.667 mm, vertical displacement: 12 mm, projectile type: 9 mm 184

3.61 Strain versus lifetime curves for a system of ten ten layers impacted by an FSP. Layer gap: 0.444 mm and 0.667 mm, vertical displacement: 8 mm, projectile type: FSP 185

CHAPTER 1

INTRODUCTION

The development of lightweight fibrous materials for body armor to resist penetration by high-velocity bullets has been an important research topic since World War II and even moreso since the terrorist attack of September 11, 2001. Prior to 1972, Nylon fibers were dominant but showed considerable nonlinearity in stress-strain response, with relatively high strains to failure. Since then, new polymeric fibrous materials have been developed that exhibit greatly improved performance. Aramids (e.g. Kevlar, Twaron, Technora) and highly oriented polyethylene (e.g. Dyneema, Spectra) are commonly used and others are being developed. In tension, all these materials differ greatly from their nylon predecessors, having very high stiffness, extremely high strength to weight ratios, and very low strains to failure ($< 4\%$). They are essentially elastic in tension, both at low and high rates of loading, and stiffness differences are fairly minor. At the same time, they are similar to nylon in their transverse compressive response, undergoing large plastic deformation without a significant reduction in tensile load-carrying ability (unlike carbon or glass fibers, which can shatter). Fig. 1.1 illustrates a sequence of possible events that a lightweight material system might undergo to halt an armor-piercing bullet (e.g., APM2).

A reasonable data base exists on experimental studies of ballistic impact into multi-ply fabric and flexible composite systems. (Throughout the thesis, the words 'ply' and 'layer' will be used interchangeably to reflect membrane components of the armor system.) A commonly investigated theme is the so-called V_{50} velocity and the relationship between the striking projectile velocity and the residual velocity after penetration. Much of the accessible data reflects

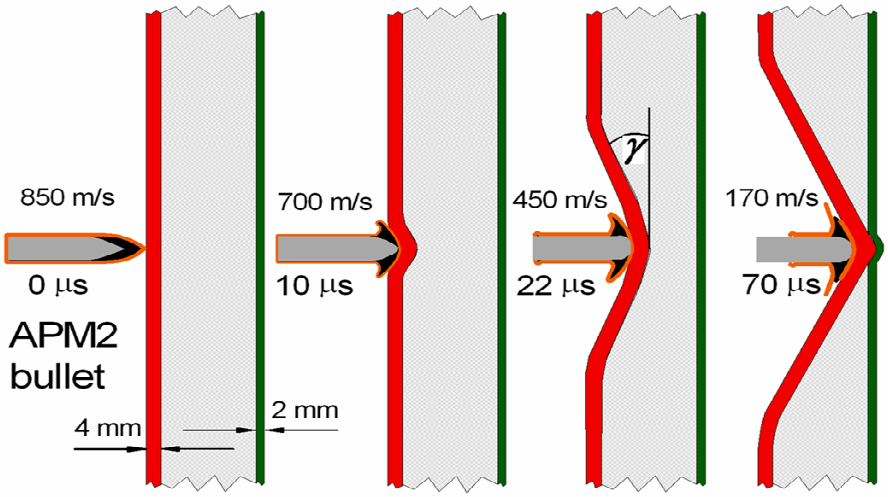

Figure 1.1: Schematic of a hypothetical layered fibrous structure envisioned to stop armor piercing APM2 bullets, yet half the weight of current, state-of-the art systems.

various uncertainties since values for key parameters are often not reported. This hampers comparison with model predictions. The trial-and-error method in experiments is costly and time-inefficient and requires a feasible model to make reasonable predictions about performance under different projectile impact conditions than used in the experiments. Unfortunately, models with high predictive accuracy have been slow to develop and have been computationally intensive. Even the fundamental problem of an un-tensioned 2D membrane impacted transversely by a blunt-nosed projectile was not adequately solved until fairly recently [1].

To understand the impact response of such systems, one must first consider the basic building blocks: single-ply fabrics, and single yarns and fibers. Unlike a drum struck with a mallet, which is under high tension initially and remains stable during wave motion, an untensioned fibrous membrane system is difficult to model because the impact velocity is large enough to drastically alter the

tension and the displacement, and deflection angles generated are large [1, 2, 3].

Nonetheless, there have been some useful analytical works published on transverse impact of 2D membranes and fabrics. The earliest work on transverse impact of a projectile into an elastic membrane appears to be that of Grigoryan [4] for point impact and neglecting circumferential stresses. Galin [5] and Dem'yanov [6] thought that neglecting circumferential stresses would lead to unreasonable results. Rakhmatulin and Dem'yanov [6] reformulated the governing partial differential equation to include circumferential stresses and Poisson's ratio effects. More approximate models of fabric impact were published after the 1970s. Vinson and Zukas [7] adopted a static conical shell theory to fabric impact by a blunt cylindrical projectile. The results were compared to his nylon fabric experiments as well as those in Roylance et al. [8, 9]. Vinson and Walker [10] used the same model to interpret the experimental results of Lee and Sun [11]. Chocron-Benlulo [12, 13] et al. extended the 1D yarn impact model by adding a strain energy based, damage variable. Scott [14] adapted a plate analysis to model the penetration of compliant composites. Walker [15, 16] developed an impact model for fabrics and flexible composites using a static deflection analysis for biaxial membranes under point loading and restrained edges. Cheeseman and Bogetti [17] have summarized recent thinking on fabric system impact.

Phoenix and Porwal [1, 2] comprehensively investigated historical and recent research on fabric system impact. They developed an efficient analytical model for investigating high velocity projectile impact onto an in-plane isotropic membrane system, and further expanded that into a multiple-layer system which allows variation of the mechanical properties from layer to layer

as well as the spacings between the layers.

Other important studies include the one by Scott et al. [18] of a single-ply aramid fabric subject to the central impact of a fragment-simulating projectile. They compared the displacement measurements directly with the simulation predictions obtained by Yen [19] and with LS-Dyna numerical simulations by Scott [20]. They also considered results from image analysis coupled with high speed digital video to measure full field surface strains and out of plane deformation of the back side of this fabric panel. Duan et al [21, 22, 23, 24] considered the friction between yarns at their crossovers and the friction between projectile and fabric. They parametrically studied the effects of the friction during the phase prior to yarn failure.

In the past ten years, a lot of work has been devoted to use of the finite element method (FEM) to simulate the impact of projectiles into fabric materials [25, 26, 27, 28, 29, 30, 31, 32, 33, 34, 35, 36, 37]. Some recent work by Grujicic etc. [38, 39] was devoted to modeling impact by projectiles of varying shapes into a single-ply, flexible-fabric armor. They attained computational efficiency improvements when calculating the mechanical response of the multi-ply, fabric-based flexible armor material to various projectiles without significantly sacrificing the key physical aspects of the fabric microstructure, architecture and behavior. Shahkarami and Vaziri [40, 41] used the finite element method to simulate projectile impact on woven fabrics and also developed a preprocessor to create a 3D mesh of the unit cell using the measured fabric cross-sectional micro-images. Parsons et al. [42] employed a continuum-level modeling technique to capture the evolution of the meso-structure of the fabric without explicitly modeling every yarn. Naik et al. [43, 44] developed an an-

alytical model designed to describe the energy absorbing mechanisms during ballistic impact.

Beyond the single ply or membrane problem, a more complicated problem is that of modeling the performance of a multi-ply system under projectile impact, particularly one with non-zero spacings or 'gaps' between layers. Such a model would provide insight on how the layers deform when decelerating the projectile, and how cone waves in individual layers develop and whether or not they interfere with each other. A more important question, however, is the extent to which spacings may degrade performance by causing uneven and sequential loading of plies, thus hindering their ability to work together in stopping the projectile. Such models may also be able to mimic the impact behavior of multi-ply composites with low transverse compressibility due to voids. It has long been known that while basic fiber properties are important, overall system effects play a key role in determining the ballistic performance of multi-layered, fabric-based armor. System variables arise in all stages of armor development and manufacturing, from individual filaments, to untwisted or twisted yarns, to the final integrated, multi-layered structure. An excellent review of the many challenges in developing body armor was recently given by Lim, Chen and Zheng [106].

Mamivand and Liaghat [45] built an analytical model to simulate ballistic impact into multi-layer fabric targets. Using their analytical formulation, the ballistic limit, surface radius of the cone formed and projectile velocity during perforation were predicted for a typical multi-layer woven fabric systems. Feli et al. [46] improved the Chocron-Galvez analytical model [12, 13] to describe the fragmented ceramic conoid. The Zaera-Sanchez-Galvez analytical model [48]

has been used for modeling the back-up woven-fabric material and deformation of yarns during perforation and also to determine the kinetic and strain energy of yarns. Barauskas and Abraitienė [49, 50, 51] developed a finite element model of a ballistic test against a particular multi-layer para-aramid textile package structure in LS-DYNA and used thin shell elements the thickness of which represented the real thickness of yarns as it can be measured in the wave. There are many other valuable papers related to multi-layer simulation and analysis that have occurred over the past decade. [52, 53, 54, 55, 56, 57, 58, 59, 60, 61, 62, 63, 64]

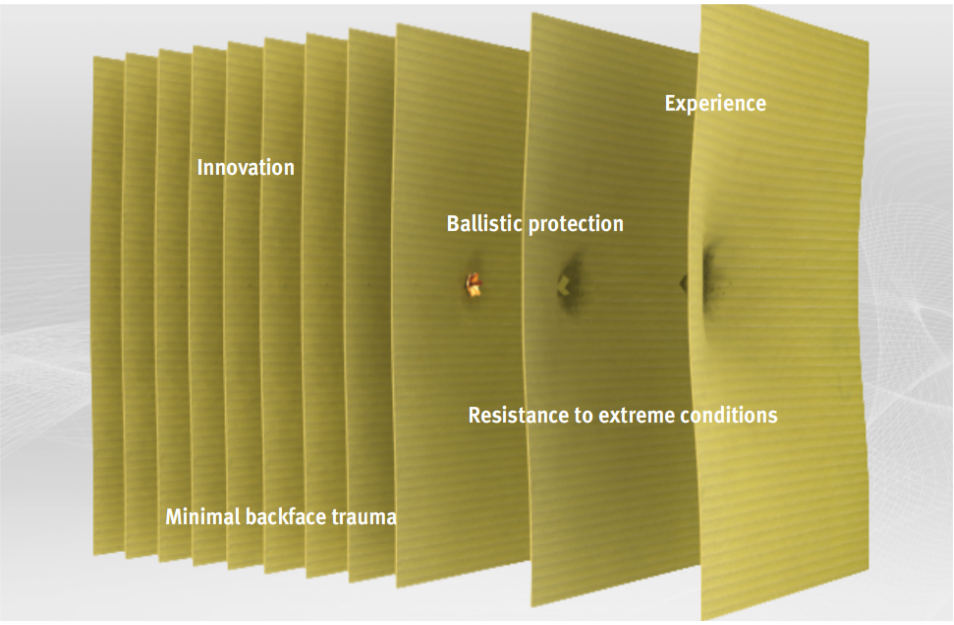

Figure 1.2: Schematic of blunt-nose bullet penetrating multiply layers with non-zero space - global view (courtesy DuPont)

To provide perspective, Fig. 1.2 and Fig. 1.3 (courtesy of DuPont), serves to illustrate the process of a high-velocity projectile penetrating a series of fibrous membrane layers. The effects of the combination of different material properties and ply spacings are of particular interest in the present thesis, though we will study the effects of much smaller spacings than the spacings illustrated in these expanded views.

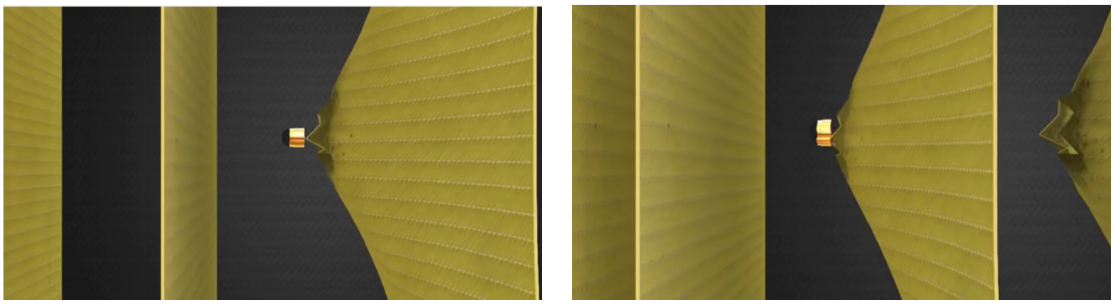

(a) (b)

Figure 1.3: Schematic of blunt-nose bullet penetrating multiply layers with non-zero space - local view (courtesy DuPont)

A large amount of experimental work has been done on impact into multi-layer fibrous systems using various standard projectiles. Among the most notable works are those of Cunniff [65, 66, 67, 68] who was able to use certain normalized variables to collapse onto one 'master curve' data on the V_{50} velocity of various material systems with varying plies and impacted by projectiles of varying diameters and masses. A simple collapse onto a master curve is less likely when individual plies differ in mechanical properties through varying the fibrous materials used. Such system effects have been studied experimentally by Cunniff [65], where significant differences were seen in V_{50} performance upon varying the ordering of the plies. He noted that at impact velocities greater than V_{50}, fabrics are perforated during the initial stress rise. In recent years, Ben-Dor et al. [69, 70, 71] used experimental data to optimize two component composite systems in body armor. A closed form solution was proposed that allowed them to determine the thicknesses of the plates in the optimal armor as functions of the specified areal density of the armor, parameters determining the material properties of the armor's components and characteristics of the impactor. Park et al. [72] performed an optimization on a multi-layered plate under ballistic impact. They changed the material from steel to aluminum

and kept the total thickness constant so that the total mass is lowered while the strength of the entire structure is improved. Ming et al. [73, 74] investigated the transverse mechanical properties of Kevlar KM2 fibers which have been widely used in body armors. Borvik et al. [75, 76, 77, 78, 79] used projectiles with three different nose shapes (blunt, hemispherical and conical) in gas gun experiments to penetrate 12 mm-thick Weldox 460 E steel plates. It was found that the nose shape of the projectile significantly affected both the energy absorption mechanism and the failure mode of the target during penetration. Gupta et al. [80, 81, 82, 83] performed experimental and numerical investigations of aluminum target plates impacted by blunt, ogive and hemispherical nosed steel projectiles. They found that, for plates with smaller thickness (0.5, 0.71, 1.0 and 1.5 mm), the most efficient penetrator is the ogive nosed projectile, and for plates with larger thickness (2.0, 2.5 and 3.0 mm), the most efficient penetrator is the blunt nosed projectile. The ballistic limit velocity of hemispherical nosed projectiles was found to be highest as compared to the other two projectiles. Many other works [84, 85, 86, 87, 88, 89, 90, 91, 92, 93, 94, 95, 96, 97, 98, 99] are also valuable contributions to understanding the relation between projectile's impact and the materials' properties and performance. Although a lot of valuable results have been obtained, the disadvantage of such experimental work by itself is its expense and the difficulty in extrapolating it to other systems.

As discussed above, although considerable work has been done on multilayered, body armor systems, few papers appear to have been done to characterize the effects of ply spacings on strain evolution and its distribution in the individual membranes, and whether air gaps between plies are detrimental or desirable. Fig. 1.4 illustrates two situations where in (a) substantial air gaps exist between plies, and in (b) the gaps are negligible. In the area of projectile

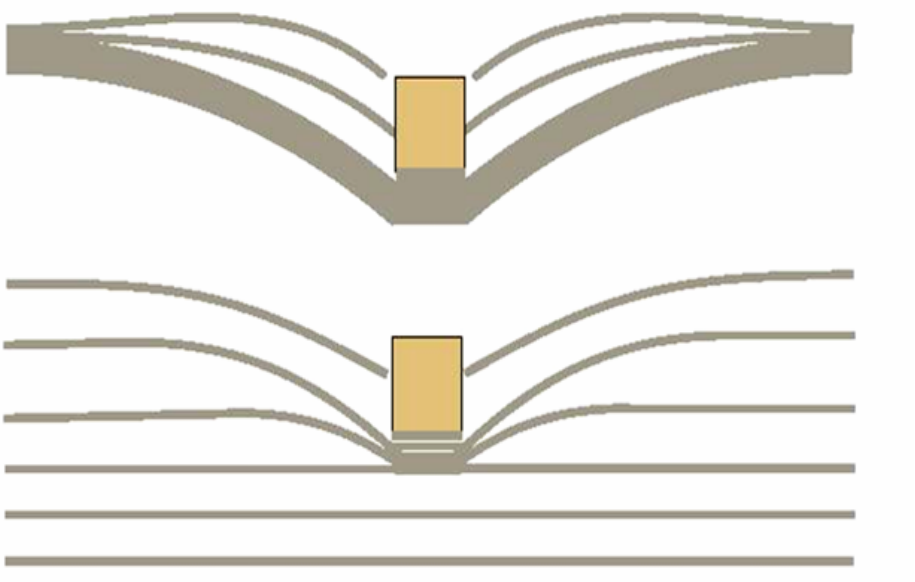

Figure 1.4: Illustration of possible differences in the impact response of a multiply system with and without layer gaps among plies

impact one might characterize the spacing between two fabric plies as the effective distance the first ply travels before it bumps firmly into the second ply. The associated time delay, depending on the projectile velocity, means that the tension and transverse waves induced in the second ply will have a time lag relative to those in the first. Typically the plies in body armor are stitched together in a quilt-like pattern, which somewhat suppresses gaps between plies. However, the actual spacing may increase with use and flexing to improve comfort, but with unknown consequences on performance.

Regarding work on the effects of ply spacings, Parga-Landa and Hernandez-Olivares [100] used equations developed for single yarns to predict the response of a multi-layered fabric, using a finite difference approach. They assumed different spacings for low and high basis weight Kevlar 29 fabrics. Chocron-Benloulo et al. [12] considered multiple layers with zero spacing and assumed that the in-plane strain is constant in all the layers. In their model, based on one-

dimensional yarn analysis, they argued that it is not enough to strain the yarn beyond its static failure strain to break it, but it is necessary that such strain persist for some time, thus motivating a fracture criterion based on a yarn damage accumulation principle. Ben-Dor et al. [101, 102, 103] studied the effect of air gaps on the ballistic performance of a ductile spaced target penetrated by rigid, sharp, conical-nosed impactors. Unlike what we shall find in the current work, they found that the ballistic limit velocity of the target increases with an increase in the widths of the air gaps and also the number of the plates in the target while the total thickness of the target material remains constant. Billon and Robinson [104] performed experiments on a multi-layered fabric system and also developed an analytical model based on energy considerations, but spacing was not considered. Novotny et al. [105] investigated the early impact behavior of single and multi-ply Kevlar fabric armor systems. They found that small reductions of strain in systems with increased areal density (due to increased denier and/or additional fabric plies) decreases the early rate of energy absorption and therefore the early ballistic efficiency. The numerical results therefore suggest that it would be beneficial to have the least amount of inter-layer gap possible to achieve the best performance in terms of early rate of energy absorption. However, none of the work above varied the spacing between layers or studied the spacing effect on projectile velocities and transverse wave movement in the membrane.

In this thesis we present two models for isotropic and biaxial materials, respectively. In the first model, we will introduce a newly improved, PC based semi-analytical model for ballistic impact into a single membrane with in-plane isotropic mechanical properties. We then generalize the single-ply model to that of a multi-ply membrane system with non-zero spacing between plies, and

where the mechanical properties can vary from layer to layer as can the individual spacings. Examples are presented of the combined ballistic impact response of various systems of interest in body armor applications.

In the second model, we present results from an analytical model and numerical simulation of the impact response of a right circular cylindrical (RCC) projectile onto a flexible biaxial panel. The simulations are carried out using a newly developed semi-analytical model with some key parameters and assumption based on an extensively modified version of a code developed at DSM. In the numerical simulations, the main emphasis is on a comprehensive understanding of the strain and displacement fields, as well as the velocity fields versus time. The panel is treated as a biaxial membrane with negligible shear stiffness compared to the tensile stiffness (as occurs in a typical open weave fabric, though the panel is a [0°/90°] panel with low resin content). The panel is square, un-tensioned and large enough that tensile wave reflections play no role. The DSM numerical code treats the panel as a square lattice of pin-jointed springs with the mass distributed uniformly at the nodes. For convenience of discussion, we refer to aligned sets of springs as yarns which are not permitted to slide over each other where they cross.

CHAPTER 2

SINGLE- AND MULTI-LAYER MODELS FOR ISOTROPIC MATERIALS

2.1 Single-layer model

The main assumptions for a single membrane layer are as follows:

1. A flat-nosed, cylindrical projectile is assumed with cylinder radius, r_p, and mass, M_p, and it has an initial velocity V_p perpendicular to the membrane.

2. The membrane is assumed to be isotropic in plane, thus giving axisymmetric behavior.

3. The projectile shape does not change during the impact and deceleration process, i.e. r_p is constant.

4. When the projectile strikes the membrane, the instantaneous velocity drop is calculated using conservation of momentum between the projectile and the the circular patch of membrane material it contacts.

5. There is no rounding at the projectile edge or cone wave front.

6. The membrane surface is large enough, such that interference from wave reflections at the boundary plays no role.

In order to describe the cone wave movement, two coordinate systems are used. One is referred to as 'material coordinates', which describe quantities in terms of the original positions of the material points in the membrane. The other one is called "ground coordinates", which describe quantities in terms of the the current positions of material points with respect to ground. As shown in

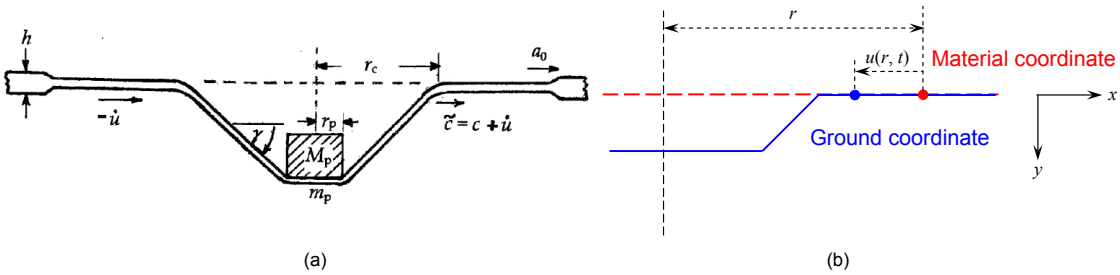

Figure 2.1: Geometry of the membrane impact problem and the two coordinate systems used

Fig. 2.1, when the projectile strikes the membrane, there is a cone wave formed. The membrane in the cone region is deformed in the transverse direction while the material outside this region moves inward. Therefore it is necessary to know both the original and current positions of certain points in the membrane.

2.1.1 Analysis

We begin by developing a revised solution for the membrane response to impact by a cylindrical projectile of mass M_p, which has initial velocity V_0 at time $t = 0^+$ right after impact, but its velocity $V(t)$, decreases over time $t \geq 0^+$, due to reaction forces from the elastic membrane. We let ρ, h and E be the membrane density, thickness and Young's modulus, respectively, and let $\varepsilon_p(t), t \geq 0^+$ be the membrane strain at the projectile edge at radius r_p. These strains induce radial tension around the projectile and act at angle $\gamma(t)$ relative to the horizontal plane of the membrane. The equation of motion for the projectile is

$$\left(M_p + \pi r_p^2 \rho h\right) \frac{dV(t)}{dt} = -\left(2\pi r_p E h\right) \varepsilon_p(t) \sin\gamma(t), t \geq 0^+ \tag{2.1}$$

Upon impact, a tensile wave front is generated in the membrane that travels

radially outward from the impact region at velocity $a_0 = \sqrt{E/\rho}$, and a tensile strain is generated in the membrane at the projectile edge that is initially approximately $\varepsilon_{p,0} \approx \left(V_0/\sqrt{2}a_0\right)^{4/3}$. The tension, $Eh\varepsilon_{p,0}$, initially draws membrane material radially inward at velocity $-\varepsilon_{p,0}V_0$, thus providing extra length to allow formation of a cone wave as the projectile deflects the membrane at the truncated cone apex.

Once the tensile wave has traveled outward a distance of one or two projectile radii $r > r_p$, the strain at the projectile edge $\varepsilon_p(t)$, quickly increases as the material further away becomes more difficult to pull inward (since the strain decreases with radius approximately as $1/r$). Eventually the strain reaches a maximum value that can be considerably more than the initial value $\varepsilon_{p,0}$, and then decays as the projectile velocity diminishes to zero. This buildup of local strain affects the time-evolution of inflow of membrane material, and one can think in terms of a sequence of infinitesimal tension waves propagating from the impact region due to the strain increments $d\varepsilon_p(t)$.

In determining the mathematical character of the tension wave, the new feature of the present analysis is to use a convolution integral of the true strain over time, based on a Duhamel integral of unit solutions $u^0(r,t)$, $\varepsilon^0(r,t)$ and $\dot{u}^0(r,t)$, representing, respectively, inflow displacement, strain and inflow velocity in response to a fixed applied strain $\varepsilon^0(r_p,t) = \varepsilon_{p,0}, t \geq 0^+$, imposed at the projectile edge. (The superscript '0' denotes unit solution quantities to distinguish them from more general quantities derived later.)

2.1.2 Unit solution

We begin by describing the unit solutions for the tension wave. We assume a flat membrane with inner boundary of radius r_p, to which we apply the radial tensile strain of $\varepsilon_{p,0}$ for $t \geq 0^+$. As time passes material is drawn towards the center and the displacement of material at original position r, and time t, is

$$u^0(r,t) = -\varepsilon_{p,0} r_p \ln\left(\frac{r_p + a_0 t}{r}\right), r_p \leq r \leq r_p + a_0 t \tag{2.2}$$

where $a_0 = \sqrt{E/\rho}$ is the tension wave speed in the membrane. (We need not concern ourselves with the physics of how such material can be absorbed at the origin because it is actually used up in the formation of the cone-wave as the projectile deflects the membrane.) The strain induced in the membrane, $\varepsilon^0(r,t)$, is the partial derivative $\partial u^0(r,t)/\partial r$, giving

$$\varepsilon^0(r,t) = \varepsilon_{p,0}\left(\frac{r_p}{r}\right), r_p \leq r \leq r_p + a_0 t \tag{2.3}$$

and the inflow velocity $\dot{u}^0(r,t)$, is the partial derivative $\partial u^0(r,t)/\partial t$, giving

$$\dot{u}^0(r,t) = -a_0 \varepsilon_{p,0} \frac{r_p}{r_p + a_0 t}, r_p \leq r \leq r_p + a_0 t \tag{2.4}$$

Outside this region all these quantities are zero.

At the inside boundary $r = r_p$, we let $u_p^0(t)$, $\varepsilon_p^0(t)$ and $\dot{u}_p^0(t)$ be $u^0(r_p,t)$, $\varepsilon^0(r_p,t)$ and $\dot{u}^0(r_p,t)$, respectively, and from Eq. (2.2), (2.3) and (2.4), we obtain

$$u_p^0(t) = -\varepsilon_{p,0} r_p \ln\left(1 + \frac{a_0 t}{r_p}\right) \tag{2.5}$$

$$\varepsilon_p^0(t) = \varepsilon_{p,0} \tag{2.6}$$

$$\dot{u}_p^0(t) = -a_0 \varepsilon_{p,0} \frac{r_p}{r_p + a_0 t} \tag{2.7}$$

Note that at the inner radius, $r = r_p$, the unit solution corresponds to constant strain.

We let $r_c(t)$ be a specific position, which later will be the position of the cone-wave front in material coordinates, and let $u_c^0(t)$, $\varepsilon_c^0(t)$ and $\dot{u}_c^0(t)$ be $u^0(r_c, t)$, $\varepsilon^0(r_c, t)$ and $\dot{u}^0(r_c, t)$, respectively. Again, from Eq. (2.2), (2.3) and (2.4), we obtain

$$u_c^0(t) = -\varepsilon_{p,0} r_p \ln\left(\frac{r_p + a_0 t}{r_c(t)}\right) \tag{2.8}$$

$$\varepsilon_c^0(t) = \varepsilon_{p,0} \frac{r_p}{r_c(t)} \tag{2.9}$$

$$\dot{u}_c^0(t) = -a_0 \varepsilon_{p,0} \frac{r_p}{r_p + a_0 t} \tag{2.10}$$

2.1.3 Cone wave behavior

Next, we consider the behavior of the cone wave assuming an arbitrary time-varying behavior of $\varepsilon_p(t)$ for $t \geq 0^+$. First we note that, as an extension of

Eq. (2.9), the strain at the projectile edge and the strain at the cone wave-front are related by

$$\varepsilon_c(t) = \varepsilon_p(t)\frac{r_p}{r_c(t)}, t \geq 0^+ \tag{2.11}$$

This is actually an approximation, but it works well because the tensile wave speed is an order of magnitude larger than the cone wave-speed thus allowing near instantaneous strain adjustments between the projectile edge and the cone-wave radius.

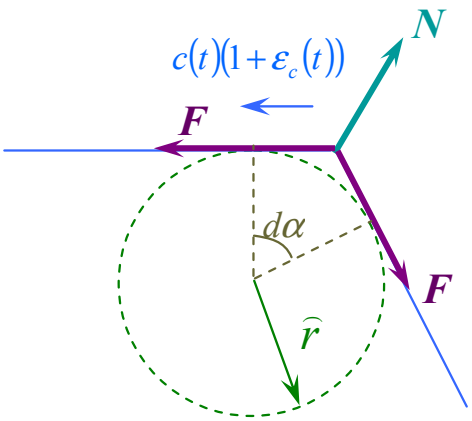

Figure 2.2: Pulley analogy analysis: the force provided by the belt on the two sides balances the centrifugal force due to its velocity, and the result is independent of the pulley radius assumed

From cone wave-front analysis we can develop an instantaneous relationship between the membrane strain $\varepsilon_c(t)$, and the cone wave-front speed $c(t)$. To do this we apply the "belt-over-pulley analogy" (Fig. 2.2) whereby the flow of membrane material past the cone wave-front can be likened to the passage of a tensioned belt over a small pulley of radius $\hat{r}$, wherein the contact pressure shrinks to zero. From a simple analysis of the centrifugal forces acting over a small wrap-around angle increment $d\alpha$, the contact force per unit length N, and

unit width is

$$N(t)\hat{r}d\alpha = 2F\frac{d\alpha}{2} - \frac{\frac{\rho h}{1+\varepsilon_c(t)}h\left(c(t)\left(1+\varepsilon_c(t)\right)\right)^2\hat{r}d\alpha}{\hat{r}} \tag{2.12}$$

where we have accounted for the slight drop in mass per unit length due to the stretching of the membrane material. Since $F(t) = hE\varepsilon_c(t)$ and $a_0^2 = E/\rho$ we have

$$N(t)\hat{r} = ha_0^2\rho\varepsilon_c(t) - \rho hc^2(t)\left(1+\varepsilon_c(t)\right) \tag{2.13}$$

and to have no contact pressure on the pulley (which doesn't exist in the actual problem) we must have $N(t)\hat{r} = 0$ so that

$$c^2(t)(1+\varepsilon_c(t)) = a_0^2\varepsilon_c(t) \tag{2.14}$$

or

$$c(t) = a_0\sqrt{\frac{\varepsilon_c(t)}{1+\varepsilon_c(t)}} \tag{2.15}$$

Note that this result does not depend on pulley radius.

To calculate strains, we must relate the wave-speed $c(t)$, to the growth of the hypotenuse of the cone wave. The length of the hypotenuse as viewed from the ground is

$$\lambda_c(t) = \sqrt{\left(r_c(t)+u_c(t)\right)^2} \tag{2.16}$$

where

$$r_c(t) = r_p + \int_0^t c(s)ds \tag{2.17}$$

is the position of the cone wave front in unstretched material coordinates, $u_c(t)$ is the displacement towards the impact region of the material point at the cone wave front due to the stretching from the tension wave, and

$$\delta(t) = \int_0^t V(s)ds \tag{2.18}$$

is the displacement of the projectile and deflection of the membrane after contacting the membrane. The rate of change of length of the hypotenuse is the time derivative of Eq. (2.16) yielding

$$\frac{d\lambda_c(t)}{dt} = \frac{\left(r_c(t) + u_c(t) - r_p\right)\tilde{c}(t) + \delta(t)V(t)}{\sqrt{\left(r_c(t) + u_c(t) - r_p\right)^2 + \delta(t)^2}} \tag{2.19}$$

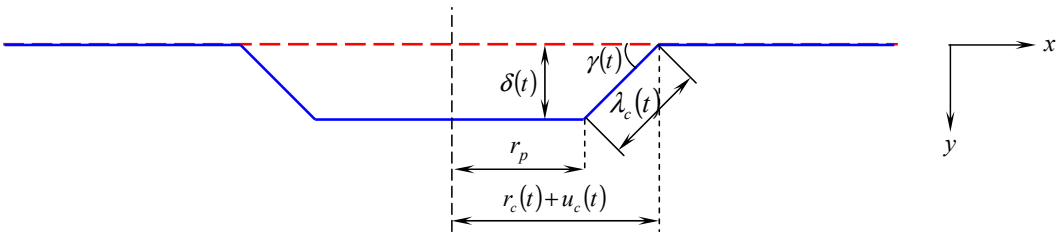

Figure 2.3: $r_c(t)$ is the cone wave radius in material coordinates. In order to specify its actual length with respect to ground coordinates, we must "remove" the part that travels back, which is $u_c(t)$

where $\tilde{c}(t)$ is the time rate of increase of the horizontal distance $r_c(t) + u_c(t) - r_p$ (Fig. 2.3) and is also the cone wave-front velocity in ground coordinates.

$$\tilde{c}(t) = c(t)(1 + \varepsilon_c(t)) + \dot{u}_c(t) \tag{2.20}$$

To understand Eq. (2.20), the factor $1 + \varepsilon_c(t)$ multiplying $c(t)$ is perhaps the least obvious and it arises because the cone wave is actually traveling in a stretched material where the particles are now farther apart, so the actual speed of travel is greater than reflected by $c(t)$ in the un-stretched material. Of course the cone wave is traveling in material, which itself is moving (relative to ground) at speed $\dot{u}_c(t)$, which is negative (i.e., the material is actually moving in the opposite direction).

The rate of length change in the hypotenuse can be decomposed into two parts: one is the change in length due to strain changes with respect to time of material already in the hypotenuse, and the other one is the inflow of material into the hypotenuse at the cone wave-front. These two terms sum to give

$$\begin{aligned}
\frac{d}{dt}\int_{r_p}^{r_c(t)} \varepsilon_p(t)\frac{r_p}{r}dr + c(t) &= \frac{d}{dt}\varepsilon_p(t) r_p \ln\left(\frac{r_c(t)}{r_p}\right) + c(t) \\
&= \dot{\varepsilon}_p(t) r_p \ln\left(\frac{r_c(t)}{r_p}\right) + \varepsilon_p(t)\frac{r_p}{r_c(t)}c(t) + c(t) \\
&= \dot{\varepsilon}_p(t) r_p \ln\left(\frac{r_c(t)}{r_p}\right) + (\varepsilon_c(t) + 1)c(t) \qquad (2.21)
\end{aligned}$$

Thus from Eq. (2.19) and (2.21) we have

$$\frac{\left(r_c(t) + u_c(t) - r_p\right)\tilde{c}(t) + \delta(t)V(t)}{\sqrt{\left(r_c(t) + u_c(t) - r_p\right)^2 + \delta(t)^2}} = (\varepsilon_c(t) + 1)\, c(t) + \dot{\varepsilon}_p(t) r_p \ln\left(\frac{r_c(t)}{r_p}\right) \qquad (2.22)$$

Note that in the case where $\dot{\varepsilon}_p(t) = 0$, the last term in Eq. (2.22) vanishes, which is the case for the unit solution with fixed strain $\varepsilon_{p,0}$, at the projectile edge. Shortly after impact, when the strain builds up to the point where $r_c(t)$ is at most a few multiples of r_p, we have

$$\dot{\varepsilon}_p(t) r_p \ln\left(\frac{r_c(t)}{r_p}\right) \leq \dot{\varepsilon}_p(t) r_p \left(\frac{r_c(t) - r_p}{r_p}\right) \approx \frac{\varepsilon_p(t) - \varepsilon_{p,0}}{t} c(t) t = \left(\varepsilon_p(t) - \varepsilon_{p,0}\right) c(t) \quad (2.23)$$

Thus the right-hand side of (2.22) becomes

$$\begin{aligned} (\varepsilon_c(t) + 1)c(t) + \dot{\varepsilon}_p(t) r_p \ln\left(\frac{r_c(t)}{r_p}\right) &\approx (\varepsilon_c(t) + 1)c(t) + \left(\varepsilon_p(t) - \varepsilon_{p,0}\right) c(t) \\ &= c(t)\left(1 + \varepsilon_c(t) + \varepsilon_p(t) - \varepsilon_{p,0}\right) \end{aligned} \quad (2.24)$$

In applications using current fibrous materials, neither $\varepsilon_p(t)$ nor $\varepsilon_c(t)$ can ever be more than 0.05, and for multi-ply systems of areal density ratio greater than 0.01, we will virtually always have $\varepsilon_p(t) < 1.5\varepsilon_{p,0}$ near the perforation threshold. Thus we can use the accurate approximation

$$c(t)\left(1 + \varepsilon_c(t)\right) = \frac{\left(r_c(t) + u_c(t) - r_p\right)\left(c(t)\left(1 + \varepsilon_c(t)\right) + \dot{u}_c(t)\right) + \delta(t)V(t)}{\sqrt{\left(r_c(t) + u_c(t) - r_p\right)^2 + \delta(t)^2}} \quad (2.25)$$

Regarding the cone angle with respect to ground we have

$$\sin\gamma(t) = \frac{\delta(t)}{\sqrt{\left(r_c(t) + u_c(t) - r_p\right)^2 + \delta(t)^2}} \quad (2.26)$$

and

$$\cos\gamma(t) = \frac{r_c(t) + u_c(t) - r_p}{\sqrt{\left(r_c(t) + u_c(t) - r_p\right)^2 + \delta(t)^2}} \quad (2.27)$$

and thus

$$c(t)\left(1 + \varepsilon_c(t)\right) = \cos\gamma(t)\left(c(t)\left(1 + \varepsilon_c(t)\right) + \dot{u}_c(t)\right) + \sin\gamma(t)V(t) \quad (2.28)$$

which also can be written as

$$c(t)\,(1+\varepsilon_c(t)) = \frac{\cos\gamma(t)\dot{u}_c(t) + \sin\gamma(t)V(t)}{1-\cos\gamma(t)} \tag{2.29}$$

2.1.4 Velocity profiles for varying strain at the projectile edge

Substitution of Eq. (2.11) into Eq. (2.14), taking the square-root, multiplying both sides by $r_c(t)/r_p$, and cancelling common factors we obtain the instantaneous equation

$$\frac{c(t)}{r_p}\sqrt{\frac{r_c(t)}{r_p}+\varepsilon_p(t)} = \frac{a_0}{r_p}\sqrt{\varepsilon_p(t)} \tag{2.30}$$

However we also have the instantaneous result

$$\frac{d}{dt}\left(\frac{r_c(t)}{r_p}+\varepsilon_p(t)\right) = \frac{d\varepsilon_p(t)}{dt} + \frac{c(t)}{r_p} \tag{2.31}$$

which can be written as

$$\frac{c(t)}{r_p}dt = d\left(\frac{r_c(t)}{r_p}+\varepsilon_p(t)\right) - d\varepsilon_p(t) \tag{2.32}$$

Thus we can write

$$\sqrt{\frac{r_c(t)}{r_p}+\varepsilon_p(t)}d\left(\frac{r_c(t)}{r_p}+\varepsilon_p(t)\right) = \frac{a_0}{r_p}\sqrt{\varepsilon_p(t)}dt + \sqrt{\frac{r_c(t)}{r_p}+\varepsilon_p(t)}d\varepsilon_p(t) \tag{2.33}$$

or

$$\sqrt{\frac{r_c(t)}{r_p}+\varepsilon_p(t)}d\left(\frac{r_c(t)}{r_p}\right) = \frac{a_0}{r_p}\sqrt{\varepsilon_p(t)}dt \tag{2.34}$$

Integrating both sides yields

$$\int_1^{\frac{r_c(t)}{r_p}} \sqrt{\frac{r_c(s)}{r_p} + \varepsilon_p(s)} d\left(\frac{r_c(s)}{r_p}\right) = \frac{a_0}{r_p} \int_0^t \sqrt{\varepsilon_p(s)} ds \tag{2.35}$$

A crucial point is that $\varepsilon_p(t) \ll r_c(t)/r_p$ since $\varepsilon_p(t) \leq \varepsilon_{p,max} \ll 1$. In fact, as $\varepsilon_p(t)$ grows to $\varepsilon_{p,max}$, $r_c(t)$ grows approximately in proportion. Thus a good approximation in Eq. (2.35) is to use $\varepsilon_p(s) = \varepsilon_{p,0}$ under the square-root on the left-hand side. Thus the left-hand side becomes

$$\begin{aligned} \int_1^{\frac{r_c(t)}{r_p}} \sqrt{\frac{r_c(s)}{r_p} + \varepsilon_{p,0}} d\left(\frac{r_c(s)}{r_p}\right) &= \int_{1+\varepsilon_{p,max}}^{\frac{r_c(t)}{r_p}+\varepsilon_{p,max}} \sqrt{\frac{r_c(s)}{r_p} + \varepsilon_{p,0}} d\left(\frac{r_c(s)}{r_p} + \varepsilon_{p,0}\right) \\ &= \frac{2}{3}\left[\left(\frac{r_c(t)}{r_p} + \varepsilon_{p,0}\right)^{\frac{2}{3}} - \left(1 + \varepsilon_{p,0}\right)^{\frac{2}{3}}\right] \end{aligned} \tag{2.36}$$

Thus from Eqs (2.35) and (2.36) we have the simple result

$$\frac{2}{3}\left[\left(\frac{r_c(t)}{r_p} + \varepsilon_{p,0}\right)^{2/3} - (1 + \varepsilon_{p,0})^{2/3}\right] = \frac{a_0}{r_p} \int_0^t \sqrt{\varepsilon_p(s)} ds \tag{2.37}$$

which rearranges to

$$\frac{r_c(t)}{r_p} = \left[\frac{3}{2}\frac{a_0}{r_p} \int_0^t \sqrt{\varepsilon_p(s)} ds + (1 + \varepsilon_{p,0})^{\frac{2}{3}}\right]^{\frac{2}{3}} - \varepsilon_{p,0} \tag{2.38}$$

Next we return to Eq. (2.29), and using Eq. (2.14) we have

$$\sqrt{\varepsilon_c(t)(1 + \varepsilon_c(t))} = \kappa_c \frac{a_0 t}{r_p} \tag{2.39}$$

or

$$\varepsilon_c(t)^2 + \varepsilon_c(t) = \kappa_c \left(\frac{a_0 t}{r_p}\right)^2 \tag{2.40}$$

where for later convenience we define

$$\kappa_c \left(a_0 t / r_p\right) = \frac{1}{a_0} \frac{\cos\gamma(t)\dot{u}_c(t) + \sin\gamma(t)V(t)}{1 - \cos\gamma(t)} \tag{2.41}$$

Eq. (2.40) is a quadratic in $\varepsilon_c(t)$ that can be factored to obtain

$$\varepsilon_c(t) = \frac{-1 + \sqrt{1 + 4\kappa_c \left(a_0 t / r_p\right)}}{2} \tag{2.42}$$

Using Eq. (2.11) we also obtain

$$\varepsilon_p(t) = \frac{r_c(t)}{2r_p}\left(-1 + \sqrt{1 + 4\kappa_c(a_0 t / r_p)}\right) \tag{2.43}$$

2.1.5 Application of convolution to the unit solutions

Considering now the inflow displacement $u_c(t)$, and velocity $\dot{u}_c(t)$, we note that Eq. (2.8) and (2.10) can not be simply adopted by replacing $\varepsilon_{p,0}$ with $\varepsilon_p(t)$ since $u_c^0(t)$ and $\dot{u}_c^0(t)$ are strictly 'unit' solutions to the special case

$$\varepsilon_p(t) = \varepsilon_{p,0}, t \geq 0^+ \tag{2.44}$$

Rather we must consider the varying strain history $\varepsilon_p(s), 0 \leq s \leq t$ through Duhamel convolution integrals of the unit solutions Eqs (2.8) and (2.10) of the form

$$u_c(t) = u_c^0(0) - \int_0^t \dot{\varepsilon}_p(s) u_c^0(t - s) ds \tag{2.45}$$

and

$$\dot{u}_c(t) = \dot{u}_c^0(0) - \int_0^t \dot{\varepsilon}_p(s)\dot{u}_c^0(t-s)ds \tag{2.46}$$

which result in

$$u_c(t) = -\varepsilon_{p,0} r_p \ln\left(\frac{r_p + a_0 t}{r_c(t)}\right) - r_p \int_0^t \dot{\varepsilon}_p(s) \ln\left(\frac{r_p + a_0(t-s)}{r_c(t)}\right) ds \tag{2.47}$$

and

$$\dot{u}_c(t) = -a_0 \frac{\varepsilon_{p,0}}{1 + a_0 t/r_p} - a_0 \int_0^t \frac{\dot{\varepsilon}_p(s)}{1 + a_0(t-s)/r_p} ds \tag{2.48}$$

In Eq. (2.47), the position of evaluation is the present cone-wave front position $r_c(t)$, irrespective of the strain history.

2.1.6 Deceleration of the projectile due to membrane reaction forces

One final equation we need is the connection between deceleration of the projectile $dV(t)/dt$ and the fiber strain $\varepsilon_p(t)$, as given by Eq. (2.1). First we recall V_p as the projectile velocity before impact and let $m_p = \pi r_p^2 \rho h$ be the mass of fabric directly in contact with the projectile. Then by conservation of momentum we have $M_p V_p = \left(M_p + m_p\right) V_0$, which can be written as

$$V_0 = \frac{V_p}{1 + m_p/M_p} = \frac{V_p}{1 + \Gamma_0} \tag{2.49}$$

where $\Gamma_0 = m_p/M_p$ is the areal density ratio, that is, the mass of the fabric patch in contact with the projectile divided by the projectile mass. We also let

$$\Theta_p = \frac{2\pi r_p^2 \rho h}{M_p + \pi r_p^2 \rho h} = \frac{2\Gamma_0}{1 + \Gamma_0} \tag{2.50}$$

and then can write Eq. (2.1) as

$$\frac{dV(t)}{dt} = -\Theta_p \frac{a_0^2}{r_p} \varepsilon_p(t) \sin\gamma(t) \tag{2.51}$$

where the initial condition is $V(0) = V_0$. Integrating Eq. (2.51) we obtain

$$V(t) = V_0 - \Theta_p \frac{a_0^2}{r_p} \int_0^t \varepsilon_p(s) \sin\gamma(s) ds \tag{2.52}$$

Fortunately a numerical solution can be developed incrementally in small time steps, thus avoiding complicated numerical treatment of coupled integrals. The initial values of all quantities can be obtained from the 1D problem under constant velocity V_0, which yields an initial strain $\varepsilon_{p,0}$ over time. The relevant quantity from the 1D analysis is the exact expression

$$\varepsilon_{p,0} = \left(\frac{V_0}{\sqrt{2}a_0}\right)^{\frac{4}{3}} \left(\frac{1}{1 + \varepsilon_{p,0}}\right)^{\frac{1}{3}} \left(1 + \left(\frac{\varepsilon_{p,0} a_0}{V_0}\right)^2\right)^{\frac{2}{3}} \tag{2.53}$$

which can be solved numerically for $\varepsilon_{p,0}$ using iteration. The first approximation is

$$\varepsilon_{p,0}^{(1)} = \left(\frac{V_0}{\sqrt{2}a_0}\right)^{4/3} \tag{2.54}$$

and by substitution of Eq. (2.54) into (2.53) we obtain a second approximation as

$$\varepsilon_{p,0}^{(2)} = \left(\frac{V_0}{\sqrt{2}a_0}\right)^{\frac{4}{3}} \left(\frac{1}{1+\varepsilon_{p,0}^{(1)}}\right)^{\frac{1}{3}} \left(1+\left(\frac{\varepsilon_{p,0}^{(1)} a_0}{V_0}\right)^2\right)^{\frac{2}{3}} \tag{2.55}$$

One more iteration yields a very accurate approximation, which is

$$\varepsilon_{p,0} = \left(\frac{V_0}{\sqrt{2}a_0}\right)^{\frac{4}{3}} \left(\frac{1}{1+\varepsilon_{p,0}^{(2)}}\right)^{\frac{1}{3}} \left(1+\left(\frac{\varepsilon_{p,0}^{(2)} a_0}{V_0}\right)^2\right)^{\frac{2}{3}} \tag{2.56}$$

Other initial conditions arising from the 1D problem are

$$V(0) = V_0, \quad \delta(0) = 0, \quad \dot{u}_c(0) = -a_0\varepsilon_{p,0}, \quad u_c(0) = 0 \tag{2.57}$$

as well as

$$\cos\gamma(0) = \frac{\tilde{c}_0}{\sqrt{\tilde{c}_0^2 + V_0^2}}, \quad \sin\gamma(0) = \frac{V_0}{\sqrt{\tilde{c}_0^2 + V_0^2}}, \quad \tilde{c}_0 = a_0\sqrt{\varepsilon_{p,0}(1+\varepsilon_{p,0})} - \varepsilon_{p,0} \tag{2.58}$$

Note that in the actual programming, a dimensionless framework is utilized. The derivations are presented in Appendix A.

2.2 Multi-layer model

In addition to the assumptions made about the single layer problem, the following assumptions apply to the multi-layer problem of n layers. A two-layer

version, with different materials in each layer, is shown in Fig. 2.4. However, the cases we study shall assume that all layers are identical.

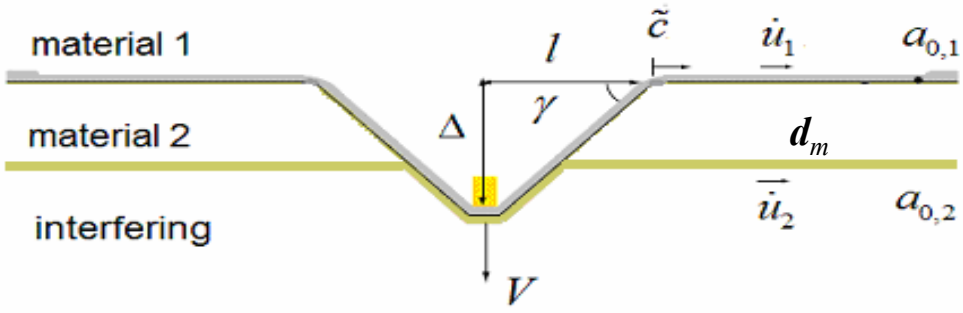

Figure 2.4: Schematic of two-layer problem with different materials for each layer and a gap between them of width d_m

Generally we assume the following:

(1) There are air gaps between the layers.

(2) There is no bonding among the layers.

(3) Sliding friction between layers is ignored (which is only significant at the cone wave-front, but otherwise the contact forces between layers are negligible).

(4) When the projectile (with its leading plug of compressed material) strikes a new layer, the initial instantaneous velocity drop is calculated using conservation of momentum.

(5) Layers are treated as incompressible so that gaps between layers reflect incremental distances the projectile must travel to sequentially engage them.

(6) When a layer fails, we assume the material of that layer is pulled out from under the projectile and so this material is no longer involved in instantaneous momentum exchange as new layers are impacted (i.e., there is not a severed material disk of radius r_p continuing on in front of the projectile).

(7) When a layer fails, its distributed mass does not interfere with other layers that have not yet failed (which might only become an issue if a layer in the sequence fails before the layer preceding it).

We assume the gaps between the n layers are of equal size totalling $G_n r_p$ so the gap per layer is $G_n r_p/(n-1)$ and we refer to G_n as the dimensionless gap sum, i.e., the sum of gaps normalized by the projectile radius, r_p.

There are two new features in the multi-layer model: (i) layers involved in decelerating the projectile are considered activated, and all the others, including those that have failed as well as those that have not yet engaged the projectile, are considered deactivated. (ii) the only common parameter shared by each layer is the current projectile speed, i.e., the layers involved are considered as having the same velocity directly under the projectile nose when calculating the projectile speed and its deceleration. Otherwise, each layer is treated as acting independently and subject to the single layer or membrane model.

There are some circumstances where these assumptions may inadequately capture actual multi-ply system behavior. For instance, plies may interfere with each other, particularly if the cone angles they form for a given projectile velocity are very different, or when plies deeper into the system fail before other plies closer to the projectile. In these circumstances some plies can have their natural cone angles altered enough to change the strain distributions within then them, and thus their likelihood of failure for a given instantaneous projectile velocity also changes. However, recent work by Phoenix et al. [3] shows that such situations require arrangements of layers that are intuitively undesirable and so should be avoided. Also, much of our focus is on studying the effects of gaps where any inter-layer interference effects would be greatly reduced.

We assume there are a total of n identical layers, and suppose that $n_1(t)$ and $n_2(t)$, respectively, represent the top (first intact) and bottom (most recently engaged) activated layers at time t (i.e., there may be some layers on top that have already been penetrated and some layers underneath not yet struck). The deceleration is caused by the forces generated by these activated membrane layers at the projectile edge. Similar to the single-ply case, Newton's second law leads to the equation

$$\left(M_p + \sum_{i=n_1(t)}^{n_2(t)} m_{c,i}(t)\right)\frac{dV(t)}{dt} = -\sum_{i=n_1(t)}^{n_2(t)} 2\pi r_{c,i}(t) E h \varepsilon_{c,i}(t)\sin\gamma_i(t), t > 0 \tag{2.59}$$

where i denotes the i-th activated layer and $m_{c,i}$ is the mass of fabric in the cone of layer i. (Henceforth we suppress the dependence of n_1 and n_2 on t through the gap spacing but this dependence will be understood throughout.) We assume V_{0,n_2} is the projectile velocity right before it strikes a new layer (i.e., layer $n_2 + 1$) and V_{0,n_2+1} is the velocity right after that, in which case $r_{p,n_2+1} = r_{c,n_2+1}$ and $m_{p,n_2+1} = m_{c,n_2+1}$ right at that instant in time. (Note that before impacting the first layer $n_1 = n_2 = 0$ and $V_{0,0} = V_p$.) Then conservation of momentum gives

$$\left(M_p + \sum_{i=n_1}^{n_2} m_{p,i}\right)V_{0,n_2} = \left(M_p + \sum_{i=n_1}^{n_2+1} m_{p,i}\right)V_{0,n_2+1} \tag{2.60}$$

since only the circles of material in the surviving layers in contact with each other and directly in the path of the projectile are involved in momentum exchange, and thus

$$V_{0,n_2+1} = \frac{\left(M_p + \sum_{i=n_1}^{n_2} m_{p,i}\right)V_{0,n_2}}{M_p + \sum_{i=n_1}^{n_2+1} m_{p,i}} \tag{2.61}$$

We define a set of dimensionless parameters as

$$\Gamma_{0,i} = \frac{m_{p,i}}{M_p} = \frac{\Gamma_0}{n} \tag{2.62}$$

$$\Gamma_{c,i}(\tau) = \frac{m_{c,i}\left(\tau t_p\right)}{M_p} \tag{2.63}$$

$$\Upsilon_c(\tau) = \frac{1 + \sum_{i=n_1}^{n_2} \Gamma_{0,i}}{1 + \sum_{i=n_1}^{n_2} \Gamma_{c,i}(\tau)} \tag{2.64}$$

$$\Theta_p = \frac{2\pi r_p E h}{M_p + \sum_{i=n_1}^{n_2} \pi r_p^2 \rho h} \frac{r_p}{a_0^2} = \frac{2\Gamma_0}{n + (n_2 - n_1)\Gamma_0} \tag{2.65}$$

Then making these substitutions and integrating Eq. (2.59) gives

$$\Psi(\tau) = \Psi_0 - \Theta_p \int_0^\tau \Upsilon_c(\zeta) \sum_{i=n_1}^{n_2} \Xi_{p,i}(\zeta) \sin \Gamma_i(\zeta) d\zeta \tag{2.66}$$

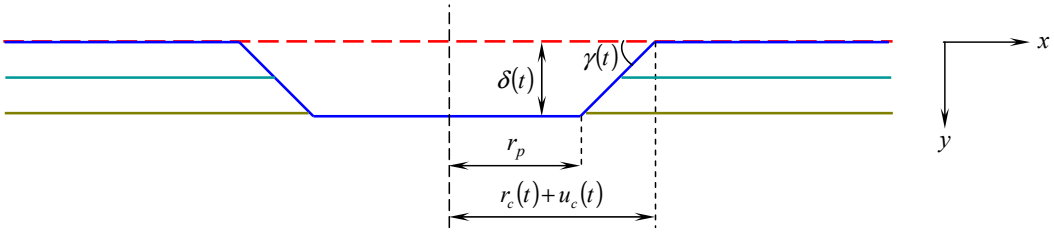

Figure 2.5: Three layer system. The cone wave speed is the same when the two layers are composed of identical materials. In reality and initially there may be a very small discrepancy, it is negligible

As stated above, only in the deceleration equation do all the activated layers act altogether as they share a common projectile velocity. Otherwise, each layer is deemed independent in the calculation. Once the common parameter, projectile velocity, has been solved for in each time step, each activated layer will be treated independently, and thus solving for all other parameters will

be based on the single-ply mode applied to each layer. With our assumptions above, there is no friction between adjacent layers, so the cone wave movement in each layer follows the single-ply rule. And the deceleration is caused by the sum of forces from all the activated layers.

2.3 Results and discussion

2.3.1 Key parameters

In our simulations, two kinds of materials are used: Kevlar 29 and Dyneema SK76. Kevlar is an aramid fiber that has a tensile stiffness of about 79 GPa and strength of 3 GPa, and a relative density of 1440 kg/m^3. Dyneema in an ultra-high molecular weight polyethylene fiber that has high molecular alignment, and has a modulus of 120 GPa, strength of 3.3 GPa and density of 0.97 kg/m^3 so it is lighter than water. Steel has a density approximately equal to 7.8 kg/m^3, and this gives a strength-to-weight ratios for these materials more than 20 times that of steel.

Some key parameters for the two materials are listed in Table 2.1.

The projectile radius r in the table is the actual projectile radius, while the effective radius r_p is the radius the projectile can impose when impacting a layer. The discrepancy is described by an effective radius factor θ, which is an experience factor that may reflect wrap around effects as layers have finite thickness.

Also m_p is the mass of the layer region covered by the projectile's effective radius r_p, and M_p is projectile mass. In our simulation study, the mass ratio

Table 2.1: A list of key parameters of Kevlar and Dyneema

Materials	Kevlar	Dyneema
Projectile radius r (mm)	2.76	
Effective radius factor θ	1.3	
Effective radius r_p (mm)	3.588	
Mass ratio m_p/M_p	0.115	
Young's modulus E (GPa)	79	120
Density ρ (kg/m^3)	1.44×10^3	0.97×10^3
Areal density a_d (kg/m^2)	0.29	0.18
Total system thickness δ_h (mm)	0.201	0.186
Dimensionless sum of layer gaps G_n	$0 \sim 8.0$	
Critical strain failure ε_{max}	0.03	

m_p/M_p is taken as constant, so changing materials will also imply either a change the projectile's mass or the layer thicknesses. One of the reasons is to make the comparison a "fair game". Each material system will have a projectile with the same mass relative to its own material mass in contact with the projectile.

The areal density a_d is the mass per unit area of the the single or multi-layer system. The total thickness δ_h is calculated as ρ/a_d. In multi-layer cases, with n plies the total compressed thickness of all the plies is ρ/a_d, and thus each ply's thickness is calculated as $\rho/(na_d)$, where n is the total number of plies. The reason to do this is that we want to determine whether it is better to use more plies with less thickness or fewer plies with larger thickness, that is, whether there is any advantage to using a system with many thin layers versus a few thick layers of the same total areal density and compressed thickness.

The dimensionless layer gap G_n is the sum of layer gaps (the cumulative distance between two adjacent layers) divided by effective projectile radius r_p. Thus, the dimensionless layer gap between two adjacent plies is $G_n/(n-1)$. Note that the effect of gaps is referenced to the projectile radius and not the compressed thickness of the multi-layer systems. This turns out to be the relevant scaling in the system affecting performance.

2.3.2 Single layer case

First, we consider a single flexible Dyneema panel and let the initial projectile velocity ve V_{ini} = 700 m/s.

Using the parameter values given in Table 2.1, Fig. 2.6 shows the calculated results of some important measures. In panel (a) of the figure,, the strain at the projectile edge $\varepsilon_p(\tau)$ first goes up and then comes down. Following the relation $\varepsilon_c(\tau) = \varepsilon_p(\tau)r_p/r_c(\tau)$, the strain at the cone wavefront $\varepsilon_c(\tau)$ reaches its peak earlier than $\varepsilon_p(\tau)$ at the projectile edge, and is much lower as well. As expected, the dimensionless projectile velocity $\Psi(\tau)$ decreases as time goes on. Comparing the strain plot (a) and velocity plot (c) in the figure, before $\varepsilon_p(\tau)$ reaches its peak versus after, the deceleration rate, $d\Psi(\tau)/d\tau$, is higher than that at later times. Since the decelerating force originates from $\varepsilon_p(\tau)$ at the projectile edge coupled to the cone angle in panel (b), a higher $\varepsilon_p(\tau)$ will lead to higher deceleration force acting on the projectile. The cone angle $\Gamma(\tau)$ actually reflects the ratio of vertical velocity $\Psi(\tau)$ and cone wave velocity $C(\tau)$. As $\Psi(\tau)$ decreases with time, $\Gamma(\tau)$ also decreases, which indicates that the cone wave-front velocity does not slow down as quickly as the velocity of the projectile. At dimensionless time,

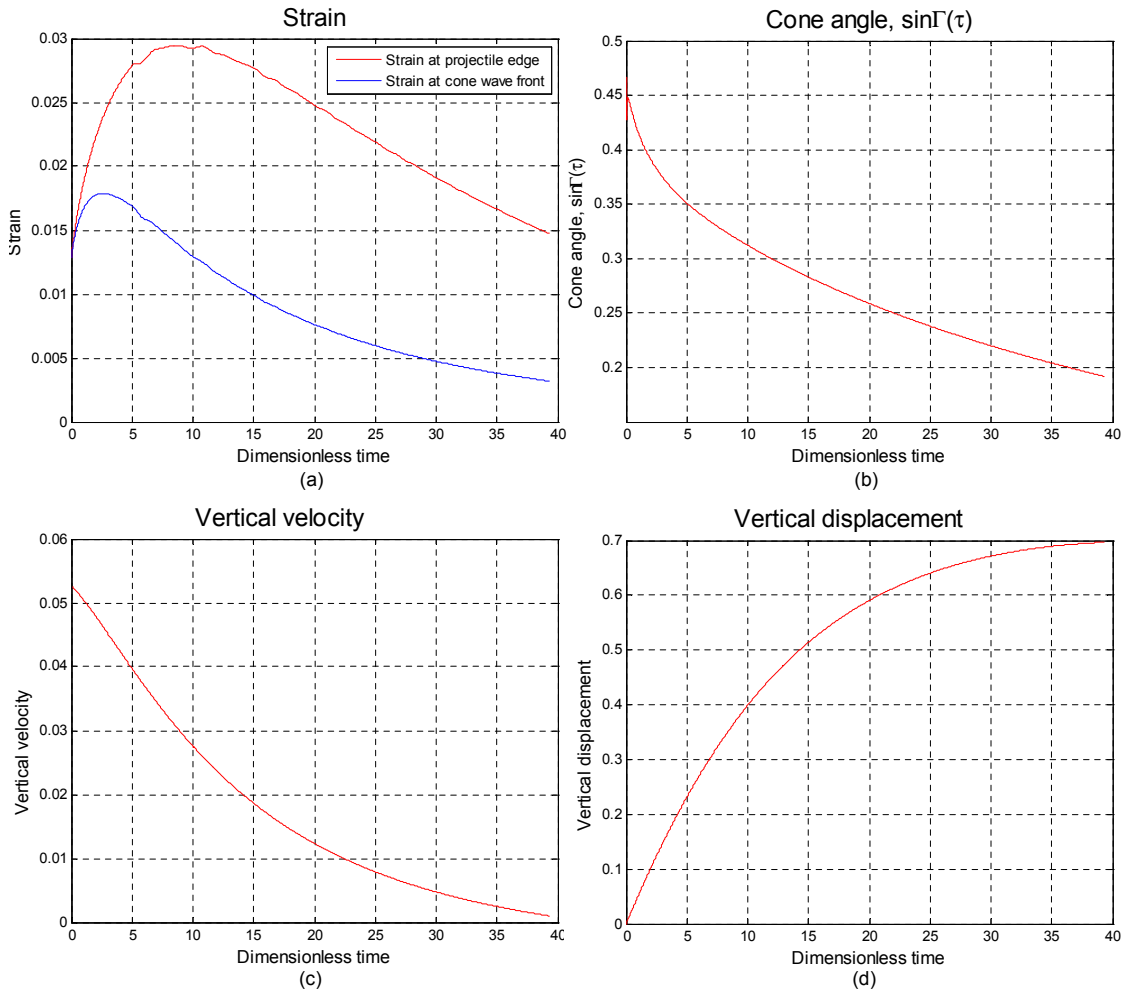

Figure 2.6: (a) strain at projectile edge and cone wave front; (b) cone angle; (c) projectile velocity; (d) vertical displacement

$\tau = 40$, we have $\sin\Gamma(\tau) \approx 0.19$ and thus $\Gamma(\tau) \approx 11°$. In panel (d) of the figure, the vertical dimensionless displacement, $\Delta(\tau)$, over time is consistent with the behavior in panel (c), as its slope everywhere is just $\Psi(\tau)$. At $\tau = 40$, $\Delta(\tau) \approx 0.7 r_p$, or 2.51×10^{-3} m.

Fig. 2.7 shows the displacement $\Delta(\tau)$ and strain $\varepsilon_p(\tau)$ at $\tau = 40$. In panel (a), the vertical displacement and cone wave angle are consistent with those seen in panels (b) and (d). Panel (b) gives an idea of vertical displacement in 3D, while in panel (c), the strain at the projectile edge $\varepsilon_p(\tau)$ is a little below 0.015, which is

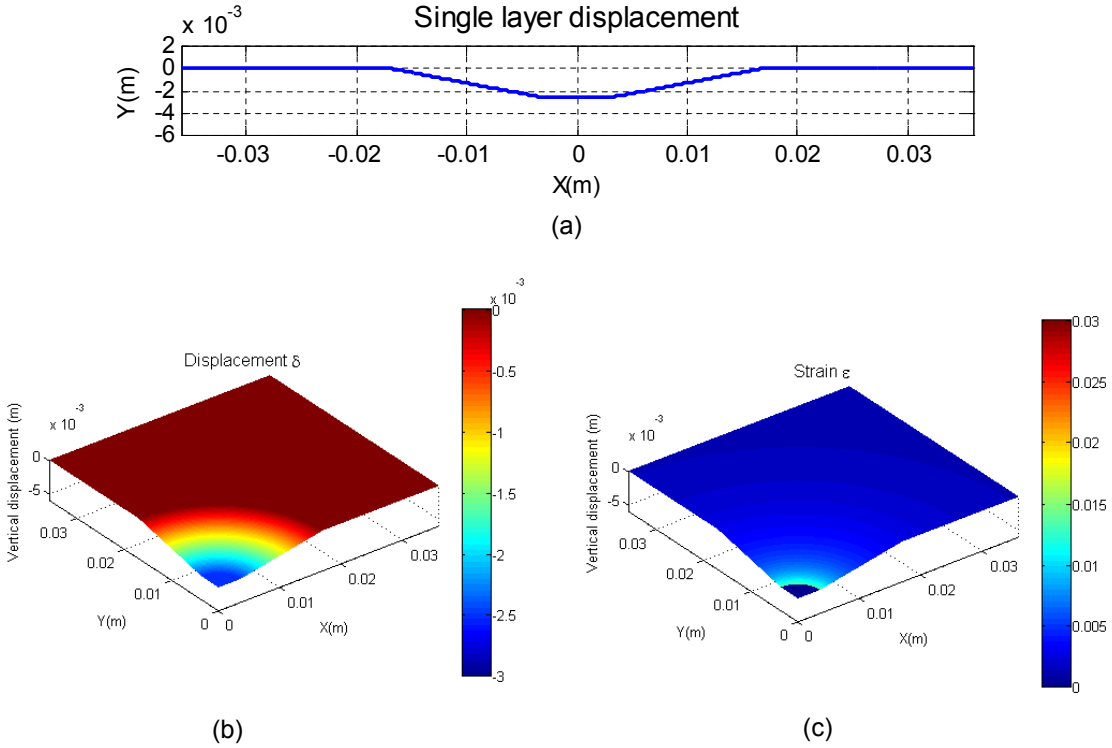

Figure 2.7: (a) Vertical displacement (2D); (b) Vertical displacement (3D); (c) Strain (3D)

consistent with panel (a).

2.3.3 Multi-layer cases

As was discussed earlier, a multi-layered system can be viewed as a single layer separated into several layers with appropriated gaps introduced between them. We shall compare the impact behavior of such a multi-layer system with its single-layer counterpart. If no layer fails, we call it ”non-penetration”. If all layers have failed, we call it ”full-penetration”. If only a portion of the layers fails, we call this “partial-penetration”.

Non-penetration cases: three layers

First, we will consider a three-ply case. The initial projectile velocity is 500m/s, the dimensionless total layer gap is $G_n = 0.5$ and each individual layer gap is $G_n/2$. The material used is Dyneema. As discussed above, the thickness of each ply is only $\delta_h/3$ of that of the single-ply case.

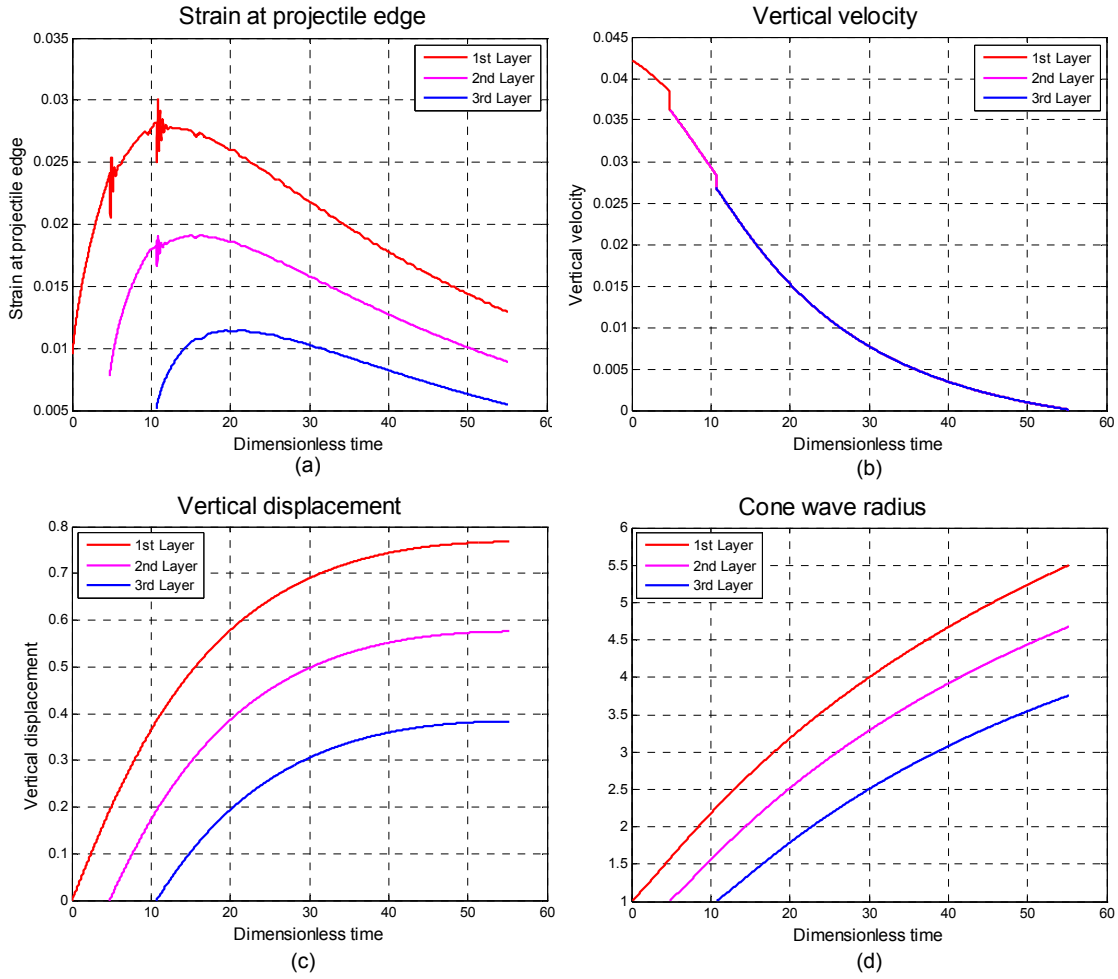

Figure 2.8: Three-ply no-failure case, initial velocity 500 m/s, layer gap $\frac{1}{2}G_n$: (a) Strain at projectile edge; (b) Projectile velocity; (c) Inflow velocity; (d) Cone wave radius.

In panel (a), the strain in all three plies is similar in shape to that of single-ply case (Fig. 2.6(a)), but there is a time-lag between them. (Note that the strain is

lower in the current example because the impact velocity is lower.) The top ply is initially loaded by the projectile and it carries most of the impact load, so the strain in the top ply is the highest throughout. With the deceleration imposed by the top layer, the impact effect on the plies underneath is diminished and thus the strains in those plies are not so high. Due to the smoothing algorithm used to treat the convolution integrals in the numerical calculations (where historically, achieving stability has proven to be problematic), when the projectile strikes a new ply, the sudden velocity drop causes numerical perturbations that are non-physical artifacts. While improvements in the code would be desirable, the results clearly show the overall effects of introducing gaps between layers.

Panel (b), shows how the projectile velocity, $\Psi(\tau)$, decays with time, τ. When striking a new ply, there is a sudden step-down in velocity due to the instantaneous momentum exchange. In this case, it is estimated that the projectile suddenly loses $\sim 6\%$ of its velocity when a new layer is impacted. Otherwise, the velocity curve is smooth everywhere. In (a), by inference from the curve trends, $\varepsilon_{p,1}(\tau)$ reaches its peak at $\tau = 12$, $\varepsilon_{p,2}(\tau)$ reaches its peak at $\tau = 15$ and $\varepsilon_{p,3}(\tau)$ peaks at $\tau = 20$. By analyzing the slope of the velocity curve in (b), we find the slope between $\tau = 12$ and $\tau = 15$ is the steepest and it starts to level off after that. Thus we can see that the largest contribution to the deceleration comes from the top plies. When the strain, which is proportional to stress and thus decelerating force, in the top plies starts to decrease, deceleration of the projectile also becomes milder.

Panel (c), shows the vertical displacement in all three layers. Note that the gap between layers is the same, so at any moment, the vertical discrepancy of the three curves is always the same. In panel (d), the cone wave radii in different

layers have been shown. The discrepancy of the three curves at a certain time is almost a constant, indicating that the cone wave speed in different layers at a certain time is the same, hence the cone wave speed is closely related to current projectile velocity but not how long the projectile has been contacting the layer.

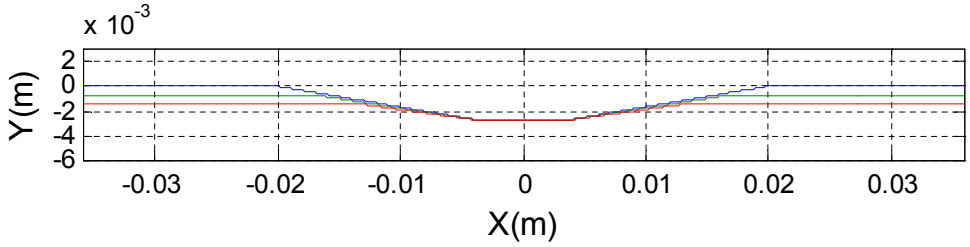

Figure 2.9: Vertical displacement in non-penetration three-ply case:, initial velocity 500 m/s, layer gap $\frac{1}{2}G_n$

In Fig. 2.9, vertical displacement is shown in 2D format. The cone wave angle in the lower layer is smaller than that in the top layer, which indicates that the projectile velocity is smaller at the time of striking the lower layers, and thus, it is smaller relative to cone wave velocity.

Non-penetration cases: ten layers

When there are ten layers in the system, each layer's thickness lowers to $\frac{1}{10}\delta h$. Since the total layer gap is still $G_n = 0.5$, individual layer gaps become smaller at $\frac{1}{9}G_n$.

Fig. 2.10(a) is very similar to Fig. 2.8(a). The strain in the top layer is almost the same in the two plots, though their thicknesses are different, e.g., the peak value is $\varepsilon_{p,1}(\tau) = 0.028$ at $\tau = 12$, and then it goes downward to $\varepsilon_{p,1}(\tau) = 0.022$ at $\tau = 30$, and lowers further to $\varepsilon_{p,1}(\tau) = 0.014$ at $\tau = 50$. Thus the impact effect on the top layer is not reduced if we separate a thicker single layer into

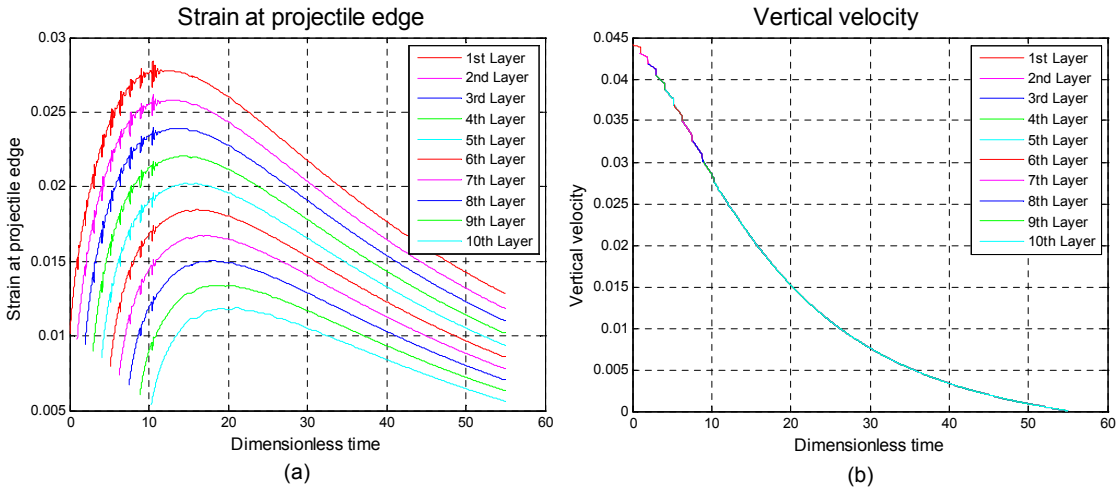

Figure 2.10: Ten-layer case where no-failure occurs since the critical strain, $\varepsilon_p = 0.030$, is not reached in any layer: (a) Strain at projectile edge; (b) Projectile velocity

several thinner layers. Similarly, the strain in the bottom layer also remains about the same. It reaches a peak of 0.012 at $\tau = 20$ and goes downward to 0.007 at $\tau = 50$, the time it takes for the tension wave to travel 50 projectile radii, r_p. The average of the strains in the $5th$ and $6th$ layers, is close to that of the second layer in Fig. 2.8(a). From the comparison above, we can see that the strains in the top, bottom and middle layers do not change much by increasing the number of layers while still holding the total gap untouched, but the strains from layer to layer are closer to each other when the number of layers increases.

There is also not much difference between Fig. 2.10(b) and Fig. 2.8(b). Because the projectile has already struck all the layers by $\tau = 10$, all the layers subsequently work in combination to decelerate the projectile, which makes no difference whether there are three layers or ten layers. Note that the down steps in velocity are much smaller in this ten-layer case, compared with the three-layer case. Recall that each layer's thickness is now $\frac{1}{10}\delta_h$ instead of $\frac{1}{3}\delta_h$, so their mass is much smaller accordingly. Thus it will lead to less velocity drop when

striking a new ply.

Full-penetration cases: ten layers

In the example that follows we again consider the case of 10 layers discussed above, but for illustrative purpose, we increase the initial projectile velocity to 636.4 m/s. The other parameters remain as they were. If one or more layers fails, we assume its tension near the projectile disappears immediately, and its strain, stress and interaction with projectile should no longer be considered. Hence if the local strain in a layer at the projectile edge reaches $\varepsilon_p = 0.030$, we clear its p

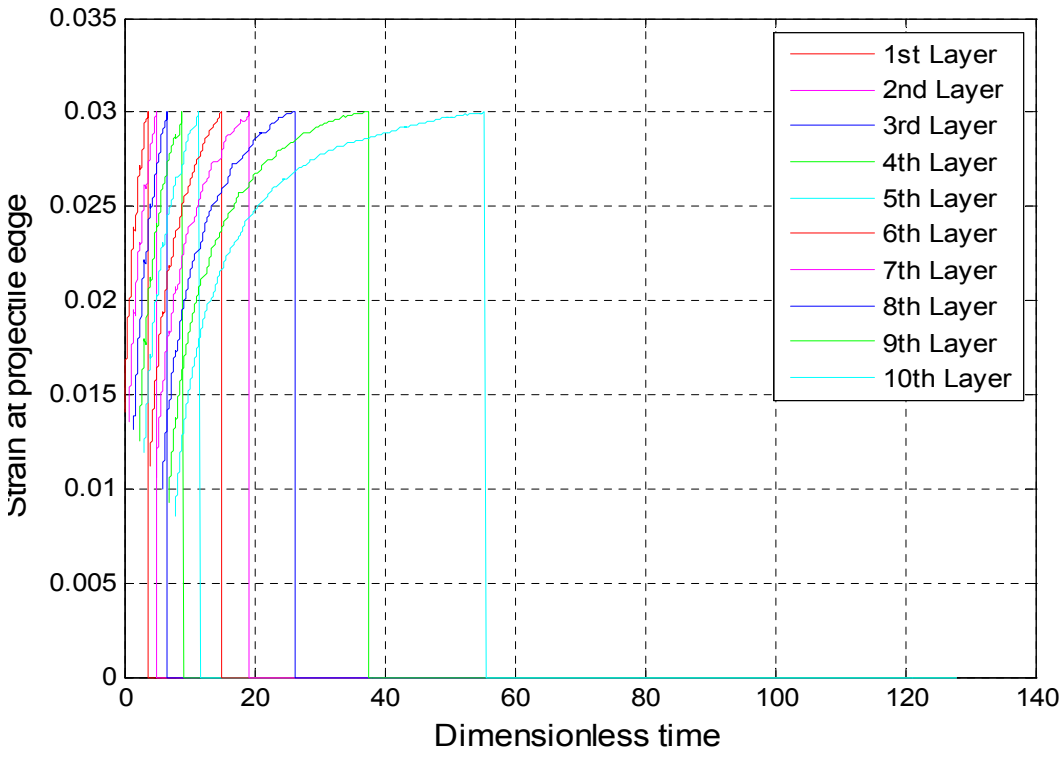

Figure 2.11: Ten layer case where all layers fail since the critical strain, $\varepsilon_p = 0.030$, is reached or exceeded in each: critical velocity 636.4 m/s

In Fig. 2.11, all the layers have been penetrated, as can be seen immediately. Four layers have failed by $\tau = 10$, and by $\tau = 20$, four more layers have failed. All remaining layers fail by $\tau = 60$, which is equivalent to $t = 3.24 \times 10^{-7}$ s, less than a microsecond. If the peak strain in a layer does not reach $\varepsilon_p = \varepsilon_{max} = 0.03$, it will never fail. However, in this case the projectile velocity is just enough to result in failure of all the layers, i.e., the peak strain in the bottom layer is just enough to reach ε_{max}. We call the corresponding velocity the "critical velocity". Actually in this case, 636.4 m/s is this "critical velocity", because, if a lower velocity is chosen, the last layer and possibly others will not fail. The "critical velocity", essentially equivalent to the V_{50} velocity, is an important measure of the material system's performance because the goal is to prevent projectiles from penetrating all the plies and thus to protect the wearer.

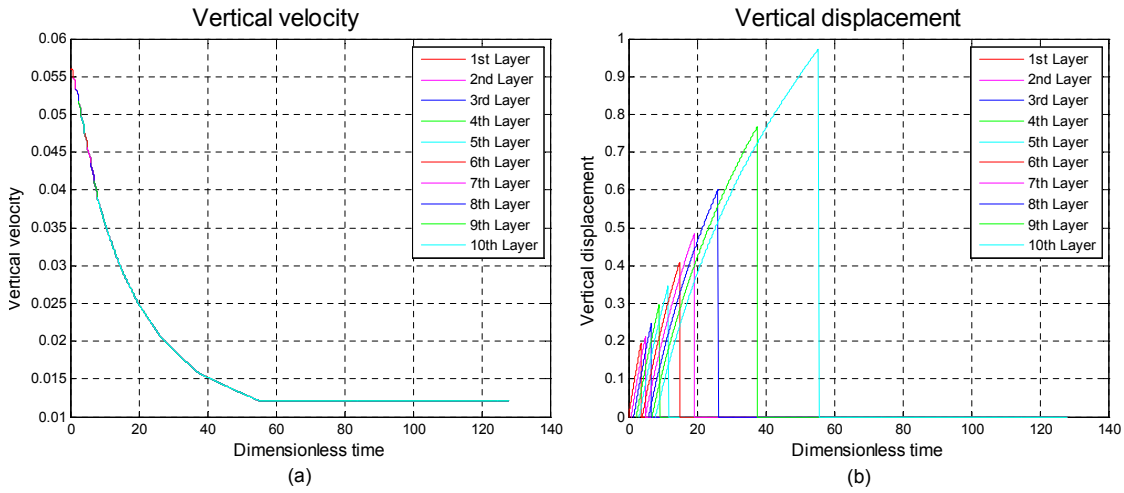

Figure 2.12: Ten layer case at critical velocity 636.4 m/s where all layers fail since the critical strain, $\varepsilon_p = 0.030$, is reached or exceeded in each: (a) Projectile velocity, (b) Vertical displacement

Fig. 2.12 shows the time evolution of projectile velocity and vertical displacement. In panel (a), the projectile velocity first decreases with time but eventually levels out, indicating all layers have been penetrated and resistance to the pro-

jectile has ended. Interestingly the projectile has lost about 80% of its velocity and 95% of its energy, but still manages to penetrate all the layers for this fairly large layer spacing. Panel (b) shows the progression of individual layer displacements, which are offset from each other because of the gaps. When a ply fails, its displacement is reset to zero implying that it is not considered any further. Note that it takes increasingly longer to penetrate subsequent plies, since the projectile speed becomes lower as penetration progresses.

Effects of changes in layer spacing and number of layers

As discussed above, "critical velocity" is important to measure the properties of impact system as it indicates whether the system will fail given a certain projectile velocity. Natural questions arise as follows: Is the "critical velocity" the same if we change the value of the dimensionless total layer gap G_n or change the number of layers, n? To answer these questions, we may want to know the relation between "critical velocity" (denoted as V_{cr} below) and these parameters.

Fig. 2.13 shows the curves of $V_{c,r}$ vs. G_n for Kevlar layers, and a comparison of our results with those obtained in Porwal and Phoenix(2005) [2]. Basically the shapes and patterns of the curves in (a) and (c) (results in this work) are very similar to those on the right side (Phoenix(2005) [2]). The main difference is that V_{cr} in the single-layer case is higher in (a) and (c) while V_{cr} in the ten-layer case is lower. This is due to a critical improvement in calculating the strain around projectile edge and cone wave front based on the model developed in Porwal and Phoenix(2005) [2].

As n increases, V_{cr} (value where the curve levels off) tends to decrease but

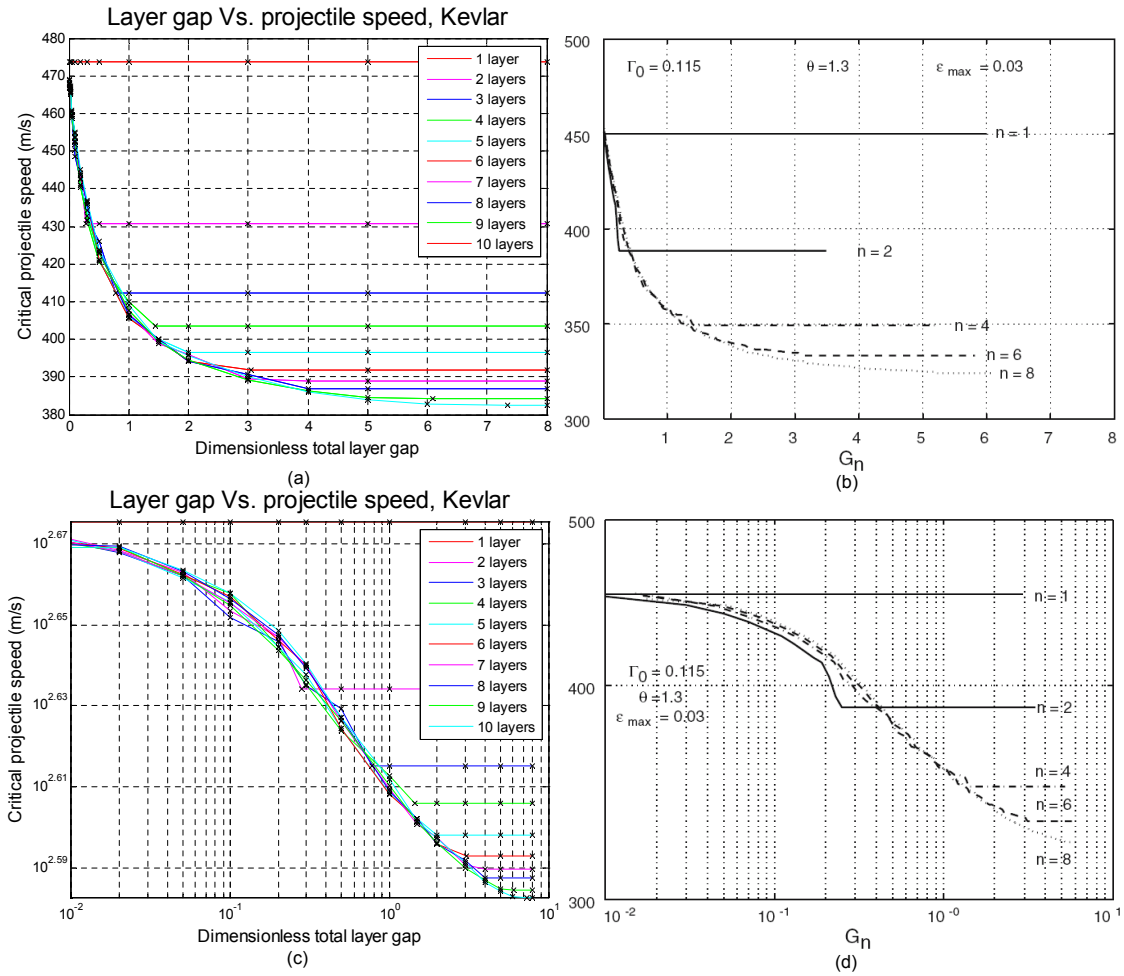

Figure 2.13: "Critical velocity" vs. dimensionless layer gap G_n for different numbers of layers: a comparison of the results in this paper with those in Porwal and Phoenix(2005) [2]. (a) Kevlar, linear scale, this paper; (b) Kevlar, linear scale, in Porwal and Phoenix(2005) [2]; (c) Kevlar, log scale, this paper; (d) Kevlar, log scale, in Porwal and Phoenix(2005) [2]

does reach a limit as n becomes large. In (a), When $n = 1$, $V_{cr} = 473$ m/s is constant because there is no layer gap. For any curve of $n > 1$, V_{cr} first decreases with increasing G_n but then levels off as the layers become fully decoupled. When $n = 3$, the limiting velocity is 412 m/s, whereas for $n = 10$, it is 383 m/s. Compared with 473 m/s for a single layer, the efficiency in terms of V_{cr} is about 87.0% and 80.7%, respectively. Therefore as n increases while G_n remains

untouched, V_{cr} decreases, while with n held fixed and G_n increasing, V_{cr} also decreases but starts to level off at a certain point, and we call this point the "critical layer gap", denoted as $G_{n,cr}$. Given n, any total layer gap larger than $G_{n,cr}$ will not lead to smaller V_{cr}.

As stated above, when $G_n = 0$, all layers are tightly coupled and are loaded simultaneously to decelerate the projectile. So actually, the projectile has to penetrate all the layers at the same time. When there are more layers in the system, each layer becomes thinner and they perform more individually. Thus it becomes easier to penetrate layers when there are gaps. Similarly, when the cumulative layer gap G_n increases, layers are placed more separately, so the projectile can penetrate one layer before it strikes another, i.e. layers cannot act in combination to decelerate the projectile and reduce the build-up of strains. Thus higher n and larger G_n will lead to lower V_{cr}.

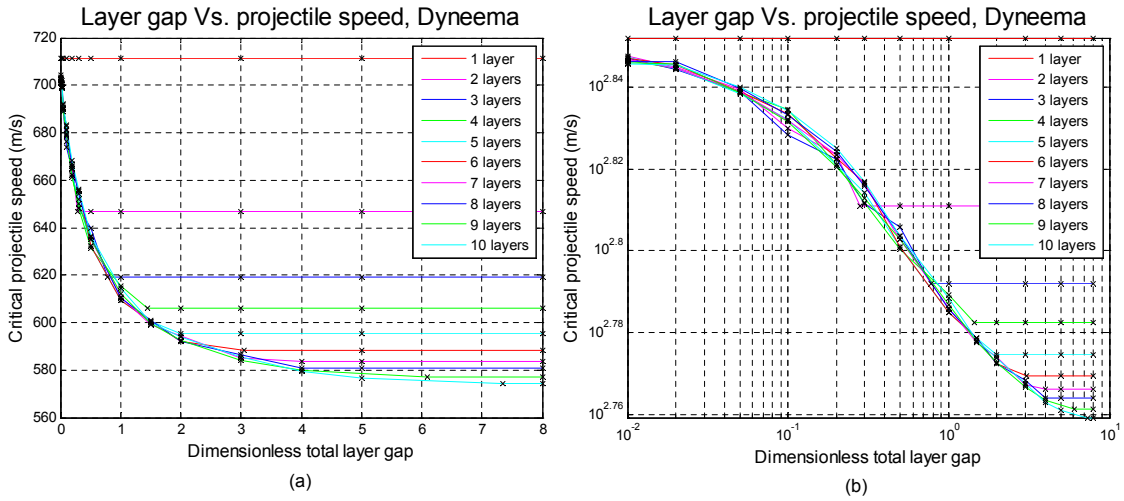

Figure 2.14: "Critical velocity" vs. layer gap G_n for different numbers of layers of Dyneema: (a) linear scale; (b) log scale

Fig. 2.14 shows the same results for Dyneema. In Fig. 2.14, the curve patterns for different numbers of layers are similar to those in Fig. 2.13(a) and (c), though

the velocity values are different. Every curve originates from $G_n = 0$, $V_{cr} = 711$ m/s when $n = 1$, and when $n = 10$, the value is 574 m/s, which also has an efficiency of 574/711 = 80.7%. If we calculate the efficiency when $n = 3$, we obtain 619/711 = 87.0%, the same as the result in Kevlar. In Table 2.2, we have listed all the critical layer gaps $G_{n,cr}$ and critical velocities $V_{n,cr}$ from $n = 1$ to 10 for both Kevlar and Dyneema.

Table 2.2: A comparison of critical layer gap $G_{n,cr}$, critical velocity $V_{n,cr}$ and relative efficiency from $n = 1$ to 10 in Kevlar and Dyneema cases

N	Kevlar	Dyneema	Kevlar	Dyneema	Kevlar	Dyneema
	$V_{n,cr}$ (m/s)		Percentage		$G_{cr,n}$	
1	473.8	711.4	100%	100%	-	-
2	430.3	646.9	90.9%	90.9%	0.28	0.28
3	412.4	619.3	87.0%	87.0%	0.78	0.78
4	403.6	606.1	85.2%	85.2%	1.44	1.44
5	396.4	595.2	83.7%	83.7%	2.0	2.0
6	391.7	588.1	82.7%	82.7%	3.05	3.05
7	388.8	583.8	82.1%	82.1%	4.0	4.0
8	386.8	580.9	81.6%	81.7%	5.0	5.0
9	384.1	577.0	81.1%	81.1%	6.1	6.1
10	382.6	574.4	80.7%	80.7%	7.35	7.35

Table 2.2 shows a comparison of the critical layer gap $G_{n,cr}$, the critical velocity $V_{n,cr}$ and the relative performance of layered systems from $n = 1$ to 10 in both Kevlar and Dyneema systems where in each case the critical strain is $\varepsilon_{max} = 0.030$. Note that the critical layer gap, $G_{n,cr}$, and velocity efficiency ($V_{n,cr}/V_{1,cr}$) for different numbers of layers are almost exactly the same for the

Kevlar and Dyneema systems. Note that in Table 2.1, the ratio m_p/M_p (layer mass under projectile divided by the projectile's mass) is set to be constant and the same for both materials (though the areal densities and projectile masses are different).

The dimensionless projectile velocity is defined as $\Psi(\tau) = V_p(t)/a_0$, where a_0 is the transverse wave velocity calculated as $a_0 = \sqrt{E/\rho}$. For Kevlar, we have Young's modulus $E = 79$ GPa, density $\rho = 1.44 \times 10^3$ Kg/m^3, so $a_{0,Ke} = 7.41 \times 10^3$ m/s. For Dyneema, we have Young's modulus $E = 120$ GPa, density $\rho = 0.97 \times 10^3$ Kg/m^3, so $a_{0,Dy} = 11.12 \times 10^3$ m/s. The ratios of tnesile wavespeed for the two materials is $a_{0,Ke}/a_{0,Dy} = 0.666$. By comparing the results in Table 2.2, we see also that $473.8/711.4 = 0.666$. Similarly, the "critical layer gap" $G_{n,cr}$ is also a dimensionless parameter we find it to be the same for the two materials, though actually their real layer gaps are distinct.

Thus Γ_0 is a key parameter in the dimensionless system of equations, and dimensionless parameters are very useful in establishing equivalence in the behavior of different systems. If Γ_0 is the same, it appears that all dimensionless calculations for the different materials lead to virtually identical results assuming the same strain to failure in each system. Given the material properties, we can predict their performance using the current approach. Note that this comparison assumes that the critical strains are not exceeded and failure does not occur. Obviously these strains will be different for different materials.

Partial-penetration

If only a portion of the layers are penetrated, we may wonder what initial projectile velocity corresponds to such a situation. As the cumulative layer gap G_n varies, the velocity to penetrate a certain number of layers is different. Thus one further question would be: how sensitive is the number of layers penetrated to the projectile velocity, i.e., how many more layers will be penetrated by a certain increase in projectile velocity? This would help us understand the reliability of body armor under different impact conditions.

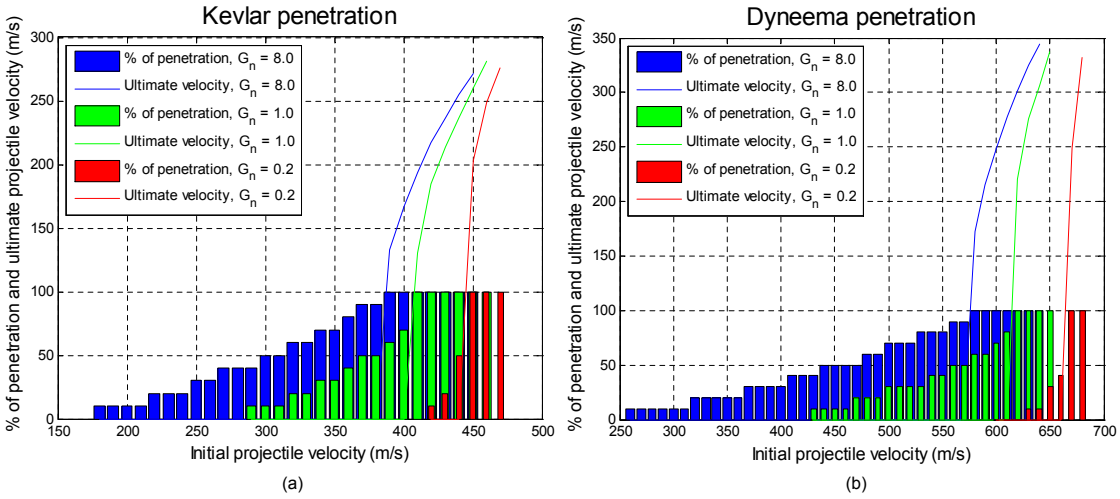

Figure 2.15: Projectile velocity vs. number of layers penetrated for various cumulative gap conditions: (a) Kevlar; (b) Dyneema

Fig. 2.15 illustrates how sensitive the number of layers penetrated (denoted as n_{ptr}) is to initial projectile velocity (denoted as V_{ini}). Note there are a total of ten layers in this case. In panel (a) (Kevlar), the number of layers penetrated, n_{ptr} becomes more sensitive to the initial velocity, V_{ini}, as G_n decreases. When G_n = 8.0, to penetrate a first layer requires only V_{ini} = 180 m/s, whereas V_{ini} = 390 m/s is required to penetrate all layers, an increase of 210 m/s, or about 116%. When G_n = 1.0, the velocity to penetrate the first layer is V_{ini} = 290 m/s whereas

V_{ini} = 410 m/s is required to penetrate them all, representing an increase of 120 m/s, or 41.4%. When G_n = 0.2, a projectile at V_{ini} = 420 m/s will break though one layer, and at V_{ini} = 430 m/s two layers, while V_{ini} = 440 m/s is needed to penetrate five of the layers!

Dyneema yields similar results. In panel (b), V_{ini} = 260 m/s and 580 m/s are needed to penetrate one ply and ten plies respectively. When G_n = 1.0, the two numbers become 430 m/s and 620 m/s respectively. And when G_n = 0.2, they are 630 m/s and 670 m/s respectively, which only have a span of 40 m/s.

The results show that small G_n will make the impact system become more sensitive to V_{ini}, which indicates that a small increase on V_{ini} will lead to the failure of the whole system. On the other side, smaller G_n will require larger V_{ini} to penetrate all layers, which is appreciated, and only a moderately lower V_{ini} will result in no layers being penetrated and back face deflection will be minimal. In both panel (a) and panel (b), we can see that if V_{ini} is large enough, the residual velocity (the projectile velocity when penetrating all layers) is lower when G_n is lower. So under the same condition, a projectile penetrating many layers under low G_n will have a lower residual velocity potentially causing less harm. With the analysis above, multiple layers with lower G_n is safer because it requires larger V_{ini} to penetrate all plies and the residual velocity is lower. But the result is sensitive to V_{ini} so a small increase on V_{ini} will lead to more layers or even the whole system being penetrated. Thus a system could have a relatively small margin of safety to guard against degradation mechanisms over time, but this might not be obvious from ballistic impact tests at a somewhat lower velocities than the critical velocity of the system.

Strain in the intact layers just prior to their failure

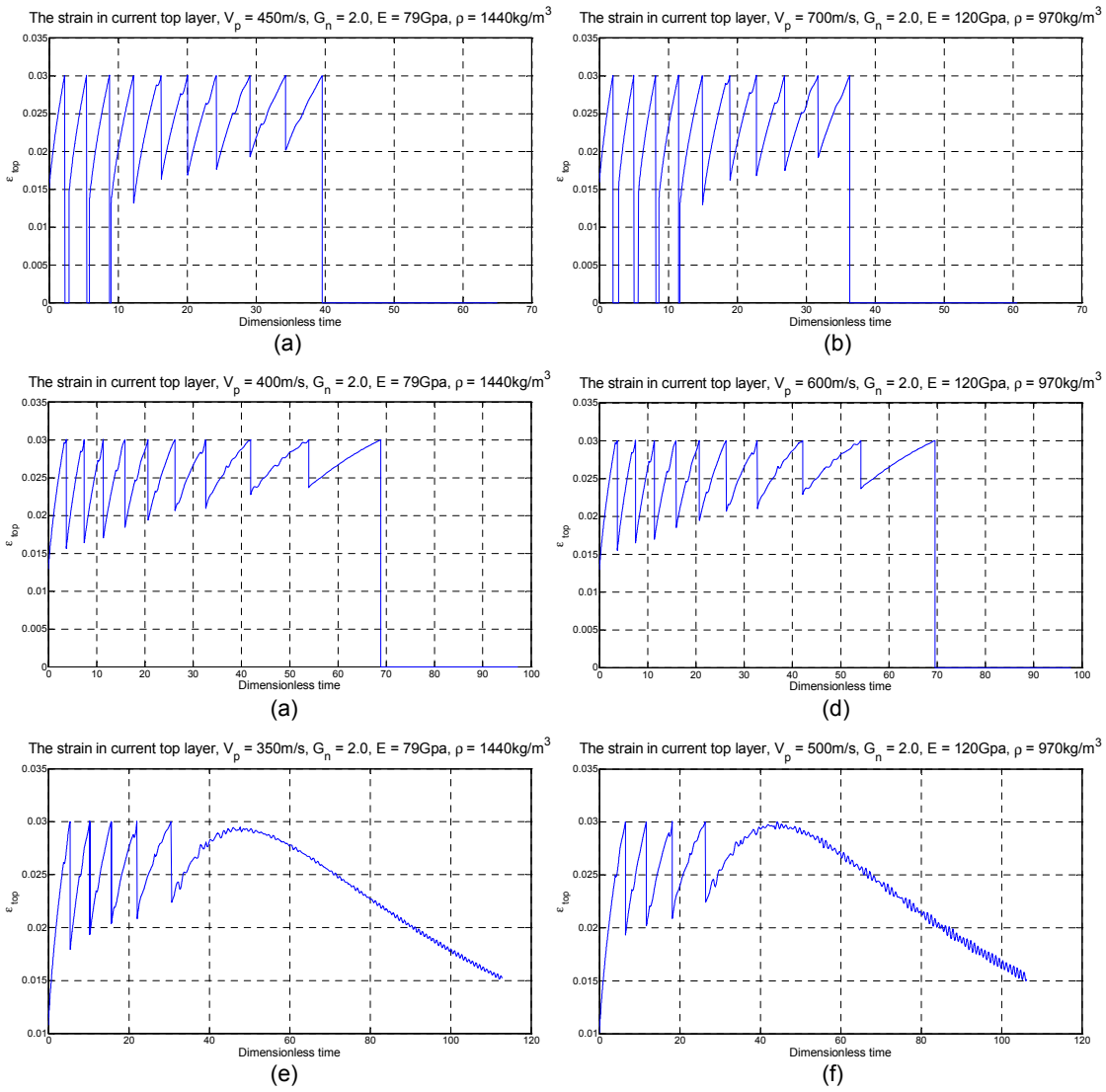

Figure 2.16: Strain in current top layer (the next layer to be penetrated). Kevlar: (a) 450 m/s; (c) 400 m/s; (d) 350 m/s. Dyneema: (b) 700 m/s; (d) 600 m/s; (e) 500 m/s

The strain in the current intact layer as time progresses is also an important parameter as it helps to see how the individual layers contribute to stopping the projectile. Fig. 2.16 shows the strain at the projectile edge ε_p on the next layer to be penetrated for different V_{ini}. In panel (a), when V_{ini} = 450 m/s, the projectile

is fast enough to penetrate all plies in a short time, and little momentum and energy are consumed during the process. As the projectile impact velocity is decreased (panel (c), V_{ini} = 400 m/s), layers are more resistant to penetration so the time staying on each layer is longer than that in panel (a). When V_{ini} is lowered to 350 m/s, only a portion of the layers are penetrated, so finally the strain curve shows a decaying pattern.

For Dyneema, the results are similar. As discussed above, the Young's modulus in Dyneema is higher but its density ρ is lower, so its "critical velocity" V_{cr} to penetrate all layers is higher. When V_{ini} is set to be 700 m/s, 600 m/s and 500 m/s (panels (b), (d) and (e)) respectively, it becomes harder to perforate layers, and the time to break layers becomes longer and finally there is no strain transition from ply to ply but just that of the first survived ply.

2.4 Summary

An improved model has been developed to study membrane performance under the impact of a flat-nosed cylindrical projectile into a flexible multi-ply body armor system with non-zero spacing between layers. An isotropic membrane system has been adopted. In our simulation, the layers are assumed to fail immediately when its strain reaches a critical strain. In particular, we considered such performance measures as critical strain in the layers, the strain in the top layers, critical layer gap, the number of layers penetrated and residual velocity when all the layers have been penetrated. A few conclusions can be made from our simulation results:

(1) In a single-layer system, as the cone wave induced by the projectile im-

pact propagates, the strain first goes up to its climax and then either goes down or levels off if the membrane layer fails at the projectile edge.

(2) In multi-layer system with non-zero spacing, if no layer fails, the strain curves in all layers are similar to that of a single-ply membrane except they appear as though there is time lag between layers.

(3) Given the mass ratio of m_p/M_p and number of layers in the system, there is always a "critical projectile velocity" which is the minimal velocity required to penetrate all the layers. Accordingly, there is a "critical layer gap" which is the minimum layer gap corresponding to the "critical projectile velocity". As the number of layers in the system increases, the "critical projectile velocity" decreases and "critical layer gap" increases. When there are ten layers, and the-gap G_n becomes large, the "critical velocity" approaches about 80% of that of a single-layer, given all the other conditions remained unchanged. This lowering percentage is only dependent on $\Gamma_0 = m_p/M_p$ but not materials.

(4) When layer gap G_n decreases, it becomes more difficult to penetrate layers, and the residual projectile velocity will be smaller, but the system becomes more sensitive to projectile velocity change, i.e. a smaller velocity increase will lead to more layers failed.

(5) As projectile velocity decreases, it becomes more difficult to penetrate layers, and the time to penetrate each layer becomes longer, and finally "current top layer strain" has no strain transition but is just the strain of the first survived layer.

CHAPTER 3

SINGLE- AND MULTI-LAYER MODELS FOR BIAXIAL MATERIALS

3.1 Introduction

In this chapter, we present results obtained from an analytical model and numerical simulation of the impact response of a right circular cylindrical (RCC) projectile into a flexible biaxial panel consisting of either a single layer or a few layers. The simulations are carried out using a newly developed semi-analytical model with some key parameters and assumptions based on a detailed study of numerical results from an extensively modified version of a spring-mass network code developed at DSM. One set of parameters chosen are for a 9 mm diameter, 8 gram mass, RCC projectile impacting a biaxial Dyneema® composite panel of areal density 3.0 Kg/m^2. In the numerical simulations, an impact velocity of 406 m/s has been modeled to compare with experimental results. Results are also presented for a fragment simulating projectile (FSP) of 5.46 mm diameter and 1.1 grams mass impacting a Dyneema® composite panel of areal density, 4.89 Kg/m^2 and traveling at 568 m/s. In the numerical simulations, our main emphasis has been on obtaining a detailed understanding of the strain, displacement, slope (the oblique angles formed by yarn with respect to the ground) and velocity fields versus time.

3.2 Introduction to single-layer model

First we describe in detail the analytical model for the response of an untensioned, balanced biaxial elastic membrane to transverse impact by a right circular cylinder (RCC) traveling with initial velocity V_p, and oriented with its axis perpendicular to the fabric plane. The projectile has radius r_p, length h_p and density ρ_p, and its mass is thus $M_p = \pi\rho_p r_p^2 h_p$. The biaxial membrane is assumed square-symmetric in plane, with thickness h, effective density ρ, and Young's modulus E, measured along the two yarn axes. The shear modulus G, relative to the two yarn axes is very small, i.e. $G << E$, so that the membrane easily deforms in shear, and as a consequence, it also has a low tensile stiffness when loaded at 45° to the main axes, as is typical of fabrics. The membrane is also assumed to have a high through-thickness modulus in compression, to avoid time delays in uniformity of fiber loading through the thickness, and it has negligible bending rigidity.

We assume that $h_p > r_p$ and $\rho_p h_p >> \rho h$, so the areal density ratio is considerably less than unity. Thus we can focus on the membrane response in terms of velocities and strains associated with in-plane tension waves and out-of-plane transverse waves, both of which involve large displacements compared to the membrane thickness. At the moment of impact, $t = 0$, instantaneous momentum exchange occurs between the projectile and the circular membrane patch it contacts, which has mass $m_p = \pi r_p^2 \rho h$. Thus by conservation of momentum we have $M_p V_p = (M_p + m_p)V_0$, and the projectile velocity at time $t = 0^+$, becomes

$$V_0 = \frac{V_p}{1 + m_p/M_p} = \frac{V_p}{1 + \Gamma_0} \tag{3.1}$$

where $\Gamma_0 = m_p/M_p$ is the mass ratio or areal density ratio in the problem. After this time, the membrane deforms around the projectile forming a deepening truncated cone, and the velocity of the projectile $V(t)$, continuously decreases over time $t > 0$, as a result of reaction forces applied to it from tension induced in the membrane and acting at angle γ, which may vary with position and time.

3.2.1 Review of projectile impact into 1D tape

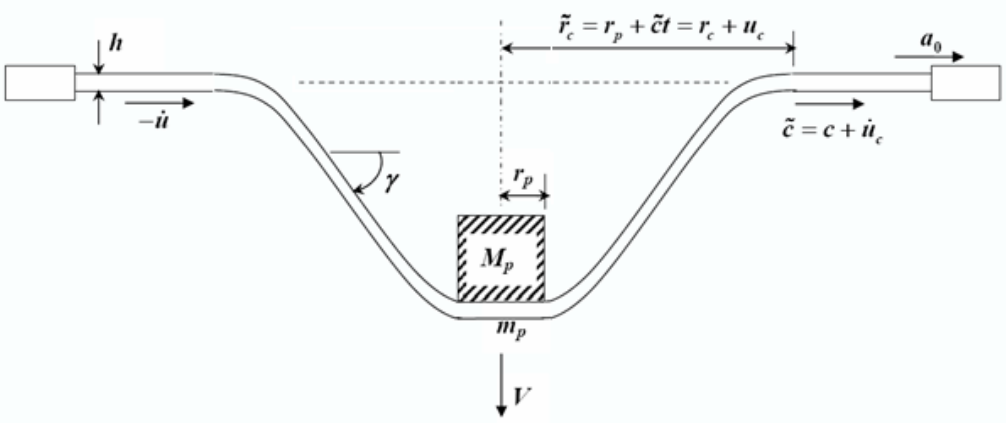

Figure 3.1: Cross-sectional geometry of projectile impact into a 1D tape.

The transverse, cone-shaped deformation evolving after projectile impact has some features similar to those observed following impact of an untensioned tape of width $2r_p$, by a right square prismatic projectile of the same width (a useful idealization), so the impacted area is a square. Illustration of this behavior is seen in Fig. 3.1, which shows a cross-section of a deformed tape under impact, where the angle γ is fixed in the tape, though in the biaxial membrane we find the surface to be somewhat curved so that $\gamma = \gamma(t, r)$. The deformation behavior in the tape is simplest to describe if we first assume constant velocity $V_0 = V_p$, which would imply infinite projectile mass $M_p = \infty$. In this case very few of the

key quantities are time-dependent.

Because of projectile impact, a tensile wave is initiated in the tape that travels symmetrically away from the impact zone along the tape in both directions, and at velocity $a_0 = \sqrt{E/\rho}$. Henceforth we describe the behavior on the right-hand half of the tape in Cartesian coordinates. Behind this wave-front, the tensile wave draws tape material horizontally inward (along the x-axis), towards the impact region at velocity $\dot{u} = \partial u/\partial t = -\varepsilon_p a_0$, where u is the horizontal displacement of a membrane point from its original position, and ε_p is the induced strain in the tape, being constant everywhere behind the tensile wave-front. This material inflow provides most of the additional length or tape 'slack' closer to the projectile that allows a deformation cone (actually two triangles in the case of the 1D tape) to form with a fairly large cone angle γ. The stretching of the tape itself within the cone makes only a small contribution to allowing this angle. The distance, δ, traveled by the projectile follows $\delta(t) = V_0 t$, $t > 0$, and the growing cone is actually a transverse wave, which has a fixed wave-front velocity $\tilde{c}$, with respect to ground and c, in material coordinates (the speed with which the cone wave-front consumes tape material points with reference to their original positions in the unstretched state). Thus the cone angle is given simply by $\tan(\gamma) = V_0/\tilde{c}$.

To provide some insight into what is involved in such an impact problem, several well-known relationships among the various key variables are briefly summarized as follows:

Distance traveled by the projectile after impact

$$\delta(t) = V_0 t \tag{3.2}$$

Inflow velocity of material behind the tensile wave front

$$\dot{u} = \partial u/\partial t = -\varepsilon_p a_0 \tag{3.3}$$

Material strain behind the tensile wave front

$$\varepsilon_p = \left(\frac{1}{4(1+\varepsilon_p)}\right)^{1/3} \left(\left(\frac{V_0}{a_0}\right)^2 + \varepsilon_p^2\right)^{2/3} \tag{3.4}$$

which for light and stiff membranes with small failure strain approximates as

$$\varepsilon_p \approx \left(\frac{V_0}{\sqrt{2}a_0}\right)^{4/3} \tag{3.5}$$

Velocity of the cone wave front in material coordinates

$$\tilde{c} = c(1+\varepsilon_p) + \dot{u} \tag{3.6}$$

and

$$r_c(t) = r_p + ct \tag{3.7}$$

Thus for a given projectile velocity we can first calculate the strain and from that all the other quantities, some of which change linearly with time.

3.2.2 Difficulties in extending results from 1D tape impact to impact into a biaxial membrane

The above analysis is straightforward and is known to apply extremely well to the behavior of yarns and tapes, whether experimentally or through numerical simulation. In biaxial membrane, the yarns are interwoven in two perpendicular directions. The yarns will carry the load from the projectile and the tensions

will propagate only in the yarns. Since the biaxial membrane has negligible shear modulus, i.e. $G << E$, one might be tempted to think that the 1D tape analysis will carry over to the membrane with little modification, unlike the case of impact into an in-plane, isotropic membrane, which is known to be very different. While impact into a biaxial membrane has several features that appear much closer to impact into a tape than into the isotropic membrane studied in previous chapters, many crucial features do not carry over. In particular, the 1D tape model predicts fixed strain under constant velocity (and decreasing strain under decreasing velocity), whereas in a biaxial membrane, numerical simulations show increasing strain under constant velocity and the development of a local strain concentration peaking at about $\pm 45^\circ$ to the projectile axes, unless the projectile deceleration is sufficiently fast to prevent strain build-up.

3.2.3 In-plane tension wave and out-of-plane cone wave profiles of deformation

Earlier we described the system of equations that model projectile impact into a 1D tape. Here we describe the behavior of various quantities only in the x-axis set of yarns (though the effects of coupling with the y-axis set of yarns are captured) since behavior associated with the y-axis set of yarns follows from symmetry. In fact, when calculating certain averages we will focus specifically on only one quadrant of the $x - y$ plane, since there is also symmetry above and below the x-axis as there is on the right and left of the y-axis. Eventually, when calculating projectile deceleration, we will have two sets of yarns and four quadrants each leading to a factor of 8 in calculating the deceleration force.

From extensive study of simulation results from the Cornell-modified DSM code, we know that just after impact, the tensile strains in the few yarns passing under the projectile very close to the center are given by the 1D tape result $\varepsilon_{p,0}$, as shown in Eq. (3.4). Very early in time, the strain at the centerline of x-axis increases almost step-wise to a steady value, and at first the strain profile diminishes traveling laterally around the projectile from the centerline of the x-axis to where the y-axis intersects the projectile edge. Thus the strain profile going from negative y-axis to positive y-axis begins as a hump. After a short time period, however, the strain at the edge of the projectile on the y-axis grows rapidly to be come dominant, and the strain profile from the negative y-axis to the positive y-axis along the projectile edge now changes from a hump-shape to a valley shape, whereas the value on the x-axis grows very little. We shall capture this phenomenon working with at first with a circular shape that rapidly changes to a a parabolic shape whose governing parameters change with time.

We define $\varepsilon_p(y)$ as the x-direction yarn strain measured at the projectile edge where y is the lateral position of the yarn relative to the x-axis. Also we define $\varepsilon_p = \varepsilon_p(0)$ as the strain on the x-axis, and let $\bar{\varepsilon}_p$ be the average yarn strain around the projectile edge so that

$$\bar{\varepsilon}_p = \frac{1}{r_p} \int_0^{r_p} \varepsilon_p(y) dy \tag{3.8}$$

We also consider the strains $\varepsilon_c(y)$, in x-direction yarns measured at locations around the tip of the cone wave-front (pyramid base with rounded noses) and along the sides out to the cone wave tip along the y-axis, where again y gives the lateral location in material coordinates. Note that where they intersect with the main axes, the rounded tips are at distance r_c from the origin. The virtual tips of the pyramid base, from which the straight portions of the cone sides emanate,

are at distance $r_c + r_p\left(\sqrt{2}-1\right)$ from the origin along the yarn axes.

We then define $\varepsilon_c = \varepsilon_c(0)$ for the yarn along the x-axis where it intersects with the cone, and let

$$\bar{\varepsilon}_c = \frac{1}{r_p}\int_0^{r_p} \varepsilon_c(y)dy \tag{3.9}$$

be the average yarn strain at the cone wave tip in the band of yarns that pass under the projectile. Between the projectile edge and the cone wave front, and at specified elevations in the cone, we envision nested, roughly diamond-shaped contours with rounded tips of radius, r_p, and with farthest points along the axes being at locations r, where $r_p < r < r_c$. The virtual tips are at distance $r+r_p\left(\sqrt{2}-1\right)$ measured along the yarn axes. Thus we let $\varepsilon(r,y)$ be the x-direction yarn strains at points around a closed contour, where r is the farthest point in the direction of the x- or y-axis. Note that when $r = r_p$ the rounded tip diamond simply collapses to the impact circle with no straight side portions. Also, in our abbreviated notation, we have $\varepsilon_p(y) = \varepsilon(r_p, y)$ and $\varepsilon_c(y) = \varepsilon(r_c, y)$.

Next we develop a profile for the strain ratio $\varepsilon/\varepsilon_0$, versus radius ratio r/r_c, as well as the force to decelerate the projectile calculated around fixed elevation contours through the cone surface. Just after initial impact, when the tension wave and transverse cone wave have only begun to grow, numerical simulations indicate that the initial profile of x-direction yarn strains at the cone wavefront has an approximately circular profile

$$\frac{\varepsilon_c(y)}{\varepsilon_c} = \sqrt{1-\left(\frac{y}{r_p}\right)^2} \approx 1 - \frac{1}{2}\left(\frac{y}{r_p}\right)^2 - \frac{1}{8}\left(\frac{y}{r_p}\right)^4 - \ldots \tag{3.10}$$

where $\varepsilon_c(y)$ is the strain in the yarn at lateral distance y away from the x-axis and $\varepsilon_c = \varepsilon_c(0)$ is the strain in the yarn lying along the x-axis.

As the cone wave grows, the circular shape does not persist because at $\theta = 45°$ the yarns are spaced further apart and the actual membrane tension normal to the circle is initially only $1/\sqrt{2}$ times the value along the axes (and eventually it becomes just $1/2$ of this value as the cone wave speed becomes $1/\sqrt{2}$ times the value along the axes). Thus the strain profile very quickly evolves a shape in the coordinate y that is approximately parabolic. Thus we assume a rapid transition to a parabolic shape soon after impact with the same asymptotic behavior in y as the circle (that is, $4th$ and higher order terms in Eq. (3.10) are neglected). (Later we will introduce a transition effect on the average strain since at the very beginning the averaged difference between the parabola and the circle is noticeable in very fine scale simulations.)

Beyond this brief transition there appear to be two regimes, one where the deformation cone has advanced a distance less than one projectile radius $r_p < r_c < 2r_p$, and one for larger cones where $r_c > 2r_p$.

Regime 1 ($r_p < r_c < 2r_p$)

As r_c/r_p grows, but the cone has advanced less than one projectile radius, i.e., $r_p < r_c < 2r_p$, numerical simulations show that the scale in y of this initial parabolic profile also grows but transitions on the sides outside the projectile radius to approximately a straight line, which decays to zero by $y = r_c$. Thus we model the profile as

$$\frac{\varepsilon_c(y)}{\varepsilon_c} = \begin{cases} 1 - \frac{1}{2}\left(\frac{y}{r_c}\right)^2, \ 0 < y < r_p \\ S_{p,c,1}\frac{r_c - y}{r_p}, \ r_p < y < r_c \end{cases} \tag{3.11}$$

where the slope is

$$S_{p,c,1} = \frac{1 - \frac{1}{2}\left(\frac{y}{2r_p}\right)^2}{\frac{r_c}{r_p} - 1} \tag{3.12}$$

and is dependent on r_c. This provides a rapidly expanding parabola as the cone-wave grows. Then we have

$$\frac{\bar{\varepsilon}_c}{\varepsilon_c} = \frac{1}{r_p}\int_0^{r_p}\left(1 - \frac{1}{2}\left(\frac{y}{r_c}\right)^2\right)dr = 1 - \frac{1}{6}\left(\frac{r_p}{r_c}\right)^2 \tag{3.13}$$

and note that for $r_c = r_p$ we obtain $\bar{\varepsilon}_c/\varepsilon_c = 5/6 = 0.833$, which is slightly higher than the value $\pi/4 \approx 0.785$, calculated using the circular profile applying immediately after impact. Also for $r_c = 2r_p$ we have

$$\frac{\bar{\varepsilon}_c}{\varepsilon_c} = 1 - \frac{1}{6}\left(\frac{r_p}{2r_p}\right)^2 = \frac{23}{24} \tag{3.14}$$

It turns out that this small difference is noticeable in very fine scale simulations around the projectile, so in the numerical code we use a transitional form

$$\frac{\bar{\varepsilon}_c}{\varepsilon_c} = 1 - \frac{1}{6}\left(\frac{r_p}{r_c}\right)^2 + \left(\frac{\pi}{4} - \frac{5}{6}\right)\left(\frac{r_p}{r_c}\right)^{14} \tag{3.15}$$

Thus by $r_c = 3r_p/2$, the correction is only 0.039 times the initial difference.

Regime 2 ($r_c > 2r_p$)

At longer times, when the cone has grown by at least one projectile radius, $r_c > 2r_p$, a second regime emerges where the parabolic portion stops broadening in scale and remains steady at its size at the end of the first regime. Again the profile portion outside the parabolic region decays linearly from the value of the parabola at the projectile radius $y = r_p$ to zero by $y = r_c$. Thus we have

$$\frac{\varepsilon_c(y)}{\varepsilon_c} = \begin{cases} 1 - \frac{1}{2}\left(\frac{y}{2r_p}\right)^2, & 0 < y < r_p \\ S_{p,c,2}\frac{r_c - y}{r_p}, & r_p < y < r_c \end{cases} \tag{3.16}$$

where the slope now is

$$S_{p,c,2} = \frac{1 - \left(\frac{1}{2}\right)^3}{\frac{r_c}{r_p} - 1} \tag{3.17}$$

Thus we have a parabola up to $y = r_p$, but a linear decay out to r_c with a slope that exhibits shallowing as r_c continues to grow. Overall, these features capture well the behavior seen in the numerical simulations.

An important quantity is the average strain along the cone wave-front $\bar{\varepsilon}_c$, where the averaging is in y only out to the projectile radius r_p, that is, considering only yarns that pass directly under the projectile. Then we have

$$\frac{\bar{\varepsilon}_c}{\varepsilon_c} = \frac{1}{r_p}\int_0^{r_p}\left(1 - \frac{1}{2}\left(\frac{y}{2r_p}\right)^2\right)dr = \frac{23}{24} = 0.95833 \tag{3.18}$$

so this ratio never quite reaches unity, which is consistent with the numerical simulations.

3.2.4 Vertical forces acting to decelerate the projectile

A very important aspect is to determine the vertical forces acting on the projectile to decelerate it, and first we determine these by integrating around contours in the cone at fixed elevations where r satisfies $r_p < r < r_c$. A major assumption, supported by numerical simulation, is that the yarn slopes $\gamma(r_c, y)$ do not vary along the cone wave-front, except very close to the tip at distance r_c in the y-direction, and also along elevation profiles not too distant from the cone edge. This means that much of the integration does not involve a changing cone angle around the edge. However, simulation does reveal that when $r_c > 2r_p$ and $r_p < r - r_p < y < r$, i.e., within a distance r_p of the furthest extent of the contour in the y-direction, the slope decays to zero approximately linearly in y, but the effect proves inconsequential since the strains have also become very small. When $r_p < r_c < 2r_p$, this linear decay actually occurs over the whole range $r_p < y < r$. In what follows we use the notation $\bar{\gamma}(r)$ to refer to an effective yarn or cone angle along the specific path of integration to obtain the net vertical force. Decays in slope within a distance r_p of the furthest extent of the contour in the y-direction, will be introduced as special decay factors in the integrands.

Regime 1

For $r_p < r_c < 2r_p$, we thus have

$$F(r) = \sin(\bar{\gamma}(r))\,\varepsilon_c \left[\int_0^{r_p} \left(1 - \frac{1}{2}\left(\frac{y}{r_c}\right)^2 + (K(r,r_c) - 1)\right) dy + S_{p,c,1} \int_{r_p}^{r} \left(\frac{r_c - y}{r_p}\right)\left(\frac{r-y}{r-r_p}\right) dy \right]$$
$$= \sin(\bar{\gamma}(r))\,\varepsilon_c r_p \left[K(r,r_c) - \frac{1}{6}\left(\frac{r_p}{r_c}\right) + \frac{S_{p,c,1}}{r_p} I(r) \right] \tag{3.19}$$

where $K(r,r_c) = \varepsilon(r)/\varepsilon_c$ is the strain enhancement (calculated later) for an elevation contour with tip at r along the x-axis ($K(r,r_c) = 1$), and the second integral accounts for both the strain decay and the slope decay. Also

$$\begin{aligned} I(r) &= \int_{r_p}^{r} \left(\frac{r_c - y}{r_p}\right)\left(\frac{r-y}{r-r_p}\right) dy \\ &= \frac{r_p^2}{r-r_p} \int_1^{r/r_p} \left(\frac{r_c}{r_p} - \eta\right)\left(\frac{r}{r_p} - \eta\right) d\eta \\ &= \frac{r_p^2}{r-r_p} \left[\frac{r_c r}{r_p^2}\eta - \left(\frac{r_c + r}{r_p}\right)\frac{\eta^2}{2} + \frac{\eta^3}{3} \right]_1^{r/r_p} \\ &= \frac{r_p^2}{r-r_p} \left[\frac{r_c}{r_p}\left(\frac{r}{r_p}\right)^2 - \frac{1}{2}\left(\frac{r_c + r}{r_p}\right)\left(\frac{r}{r_p}\right)^2 + \frac{1}{3}\left(\frac{r}{r_p}\right)^3 - \frac{r_c}{r_p}\frac{r}{r_p} + \frac{1}{2}\left(\frac{r_c + r}{r_p}\right) - \frac{1}{3} \right] \end{aligned} \tag{3.20}$$

which upon factoring and further rearranging yields

$$I(r) = \frac{r_p}{2}\left[\left(\frac{r_c}{r_p} - 1\right)\left(\frac{r}{r_p} - 1\right) - \frac{1}{3}\left(\frac{r}{r_p} - 1\right)^2 \right] \tag{3.21}$$

Thus from Eq. (3.19), we have for an arbitrary elevation contour

$$F(r) = \sin(\bar{\gamma}(r))\,\varepsilon_c r_p \vartheta(r) \tag{3.22}$$

where

$$\vartheta(r) = K(r,r_c) - \frac{1}{6}\left(\frac{r_p}{r_c}\right)^2 + \frac{1}{2}\left[1 - \frac{1}{2}\left(\frac{r_p}{r_c}\right)^2\right] \left[\left(\frac{r}{r_p} - 1\right) - \frac{1}{3}\frac{\left(\frac{r}{r_p} - 1\right)^2}{\left(\frac{r_c}{r_p} - 1\right)} \right] \tag{3.23}$$

Around the cone wave-front $r = r_c$ we get the important result

$$F_c = \sin(\bar{\gamma}_c)\,\varepsilon_c r_p \vartheta(r_c) \tag{3.24}$$

where

$$\vartheta(r_c) = 1 - \frac{1}{6}\left(\frac{r_p}{r_c}\right)^2 + \frac{1}{3}\left(1 - \frac{1}{2}\left(\frac{r_p}{r_c}\right)^2\right)\left(\frac{r_c}{r_p} - 1\right) \tag{3.25}$$

For $r = r_p$ we have

$$F_p = \sin\left(\bar{\gamma}_p\right)\varepsilon_c r_p \vartheta(r_p) \tag{3.26}$$

where

$$\vartheta(r_p) = K(r_p, r_c) - \frac{1}{6}\left(\frac{r_p}{r_c}\right)^2 \tag{3.27}$$

as is shown by taking limits as $r_c \to r_p$. This result, however, ignores the initial circular nature of the strain profile around the projectile at very early times. Thus to reflect this feature, a small correction shall be applied to the main results at the end of the theoretical development of the model, to avoid cluttering the equations along the way unnecessarily. At the end, we use instead the modified versions

$$\vartheta(r_p) = K(r_p, r_c) - \frac{1}{6}\left(\frac{r_p}{r_c}\right)^2 + \left(\frac{\pi}{4} - \frac{5}{6}\right)\left(\frac{r_p}{r_c}\right)^{14} \tag{3.28}$$

and

$$\vartheta(r_c) = 1 - \frac{1}{6}\left(\frac{r_p}{r_c}\right)^2 + \left(\frac{\pi}{4} - \frac{5}{6}\right)\left(\frac{r_p}{r_c}\right)^{14} + \frac{1}{3}\left(1 - \frac{1}{2}\left(\frac{r_p}{r_c}\right)^2\right)\left(\frac{r_c}{r_p} - 1\right) \tag{3.29}$$

where the added term makes the adjustment from the circular to parabolic profile of strain.

Explicit relationship for Regime 1

For $r_p < r_c < 2r_p$, we can rewrite Eq. (3.23) as

$$\vartheta(r) = K(r, r_c) - \frac{1}{6}\left(\frac{r_p}{r_c}\right)^2 + \Theta(r) \tag{3.30}$$

where

$$\Theta(r) = \frac{1}{2}\left[1 - \frac{1}{2}\left(\frac{r_p}{r_c}\right)^2\right]\left[\left(\frac{r}{r_p} - 1\right) - \frac{1}{3}\frac{\left(\frac{r}{r_p} - 1\right)^2}{\left(\frac{r_c}{r_p} - 1\right)}\right], \quad r_p < y < r_c \tag{3.31}$$

and from Eq. (3.30)

$$\Theta(r_p) = 0 \tag{3.32}$$

and

$$\Theta(r_c) = \frac{1}{3}\left[1 - \frac{1}{2}\left(\frac{r_p}{r_c}\right)^2\right]\left(\frac{r_c}{r_p} - 1\right) \tag{3.33}$$

Thus

$$\vartheta(r_c) = 1 - \frac{1}{6}\left(\frac{r_p}{r_c}\right)^2 + \Theta(r_c) \tag{3.34}$$

and

$$\vartheta(r_p) = K(r_p, r_c) - \frac{1}{6}\left(\frac{r_p}{r_c}\right)^2 \tag{3.35}$$

as is shown by taking limits as $r_c \to r_p$. This result, however, ignores the initial circular nature of the strain profile around the projectile at very early times. Thus to reflect this feature, a small correction shall be applied to the main results

at the end of the theoretical development of the model, to avoid cluttering the equations along the way unnecessarily. Therefore instead, we use the modified versions

$$\vartheta(r_p) = K(r_p, r_c) - \frac{1}{6}\left(\frac{r_p}{r_c}\right)^2 + \left(\frac{\pi}{4} - \frac{5}{6}\right)\left(\frac{r_p}{r_c}\right)^{14} \tag{3.36}$$

and

$$\vartheta(r_c) = 1 - \frac{1}{6}\left(\frac{r_p}{r_c}\right)^2 + \left(\frac{\pi}{4} - \frac{5}{6}\right)\left(\frac{r_p}{r_c}\right)^{14} + \frac{1}{3}\left(1 - \frac{1}{2}\left(\frac{r_p}{r_c}\right)^2\right)\left(\frac{r_c}{r_p} - 1\right) \tag{3.37}$$

where the added term makes the adjustment from the circular to parabolic profile of strain.

Regime 2

For $r_c > 2r_p$, there are two cases to consider depending on the value of r. The first case is when $2r_p < r < r_c$, and we have

$$\begin{aligned} F(r) &= \sin(\bar{\gamma}(r))\,\varepsilon_c \left\{ \int_0^{r_p} \left(1 - \frac{1}{2}\left(\frac{y}{r_c}\right)^2 + (K(r, r_c) - 1)\right) dy \right. \\ &\quad \left. + S_{p,c,2}\left[\int_{r_p}^{r-r_p} \frac{r_c - y}{r_p} dy + \int_{r-r_p}^{r} \frac{(r_c - y)(r - y)}{r_p^2} dy \right] \right\} \\ &= \sin(\bar{\gamma}(r))\,\varepsilon_c r_p \left[K(r, r_c) - \frac{1}{24} + \frac{S_{p,c,2}}{r_p}\left(I_1(r) + I_2(r)\right) \right] \end{aligned} \tag{3.38}$$

where

$$\begin{aligned} I_1(r) &= \int_{r_p}^{r-r_p} \left(\frac{r_c - y}{r_p}\right) dy \\ &= r_c\left(\frac{r_c}{r_p}\right)\left[\left(\frac{r - r_p}{r_c}\right) - \frac{1}{2}\left(\frac{r - r_p}{r_c}\right)^2 - \left(\frac{r_p}{r_c}\right) + \frac{1}{2}\left(\frac{r_p}{r_c}\right)^2\right] \\ &= r_p\left(\frac{r_c}{r_p}\frac{r}{r_p} - \frac{1}{2}\left(\frac{r}{r_p}\right)^2 + \frac{r}{r_p} - 2\frac{r_c}{r_p}\right) \end{aligned} \tag{3.39}$$

and

$$
\begin{aligned}
I_2(r) &= \int_{r-r_p}^{r} \left(\frac{r_c - y}{r_p}\right)\left(\frac{r - y}{r_p}\right) dy \\
&= r_p \int_0^1 \left(\frac{r_c - r}{r_p} + 1 - \zeta\right)(1 - \zeta) d\zeta \\
&= r_p \int_0^1 \left(\frac{r_c - r}{r_p} + \omega\right) \omega d\omega \\
&= r_p \left(\frac{1}{2}\left(\frac{r_c - r}{r_p}\right) + \frac{1}{3}\right)
\end{aligned} \tag{3.40}
$$

Thus

$$
\begin{aligned}
I_1(r) + I_2(r) &= r_p \left(\frac{r_c r}{r_p^2} - \frac{1}{2}\left(\frac{r}{r_p}\right)^2 + \frac{r}{r_p} - 2\frac{r_c}{r_p} + \frac{1}{2}\left(\frac{r_c - r}{r_p}\right) + \frac{1}{3}\right) \\
&= r_p \left(\frac{r_c r}{r_p^2} - \frac{1}{2}\left(\frac{r}{r_p}\right)^2 + \frac{1}{2}\frac{r}{r_p} - \frac{3}{2}\frac{r_c}{r_p} + \frac{1}{3}\right) \\
&= r_p \left(\frac{r_c}{r_p}\left(\frac{r}{r_p} - 1\right) - \frac{1}{2}\left(\frac{r}{r_p} - 1\right)^2 - \frac{1}{2}\left(\frac{r}{r_p} - 1\right) - \frac{1}{2}\left(\frac{r_c}{r_p} - 1\right) - \frac{1}{6}\right)
\end{aligned} \tag{3.41}
$$

Hence we have

$$
F(r) = \sin(\bar{\gamma}(r)) \varepsilon_c r_p \vartheta(r) \tag{3.42}
$$

where

$$
\begin{aligned}
\vartheta(r) = K(r, r_c) - \frac{1}{24} + \frac{7/8}{r_c/r_p - 1}\Bigg[&\frac{r_c}{r_p}\left(\frac{r}{r_p} - 1\right) - \frac{1}{2}\left(\frac{r}{r_p} - 1\right)^2 \\
&- \frac{1}{2}\left(\frac{r}{r_p} - 1\right) - \frac{1}{2}\left(\frac{r_c}{r_p} - 1\right) - \frac{1}{6}\Bigg]
\end{aligned} \tag{3.43}
$$

Note that for $r = r_c$, we have the important result

$$
F_c = \sin(\bar{\gamma}_c) \varepsilon_c r_p \vartheta(r_c) \tag{3.44}
$$

and since $K(r_c, r_c) = 1$, we have

$$\vartheta(r_c) = \frac{23}{24} + \frac{7}{16}\left[\left(\frac{r_c}{r_p} - 1\right) - \frac{1}{3\left(\frac{r_c}{r_p} - 1\right)}\right] \tag{3.45}$$

For the second case, $r_p < r < 2r_p < r_c$, we have a change in the region of integration and must calculate

$$\begin{aligned} F(r) &= \sin(\bar{\gamma}(r))\,\varepsilon_c r_p \left(K(r, r_c) - \frac{1}{24} + \frac{S_{p,c,2}}{r_p}\int_{r_p}^{r}\left(\frac{r_c - y}{r - r_p}\right)\left(\frac{r - y}{r_p}\right)dy\right) \\ &= \sin(\bar{\gamma}(r))\,\varepsilon_c r_p \left(K(r, r_c) - \frac{1}{24} + \frac{S_{p,c,2}}{r_p} I(r)\right) \end{aligned} \tag{3.46}$$

where in this case

$$\begin{aligned} I(r) &= \int_{r_p}^{r}\left(\frac{r_c - y}{r - r_p}\right)\left(\frac{r - y}{r_p}\right)dy \\ &= \frac{r_p}{r/r_p - 1}\int_1^{r/r_p}\left(\frac{r_c r}{r_p^2} - \frac{r_c + r}{r_p}\eta + \eta^2\right)d\eta \\ &= \frac{r_p}{r/r_p - 1}\left[\frac{r_c r}{r_p^2}\eta - \frac{r_c + r}{r_p}\frac{\eta^2}{2} + \frac{\eta^3}{3}\right]_1^{r/r_p} \\ &= \frac{r_p}{r/r_p - 1}\left[\frac{1}{2}\frac{r_c}{r_p}\left(\frac{r}{r_p} - 1\right)^2 - \frac{1}{6}\left(\frac{r}{r_p}\right)^3 + \frac{1}{2}\left(\frac{r}{r_p}\right) - \frac{1}{3}\right] \end{aligned} \tag{3.47}$$

which can be shown to be equivalent to

$$I(r) = r_p\left[\frac{1}{2}\left(\frac{r_c}{r_p} - 1\right)\left(\frac{r}{r_p} - 1\right) - \frac{1}{6}\left(\frac{r}{r_p} - 1\right)^2\right] \tag{3.48}$$

Thus we have

$$F(r) = \sin(\bar{\gamma}(r))\,\varepsilon_c r_p \vartheta(r) \tag{3.49}$$

where

$$\vartheta(r) = K(r, r_c) - \frac{1}{24} + \frac{7/8}{\frac{r_c}{r_p} - 1}\left[\frac{1}{2}\left(\frac{r_c}{r_p} - 1\right)\left(\frac{r}{r_p} - 1\right) - \frac{1}{6}\left(\frac{r}{r_p} - 1\right)^2\right]$$

$$= K(r, r_c) - \frac{1}{24} + \frac{7}{16}\left[\left(\frac{r}{r_p} - 1\right) - \frac{1}{3}\frac{\left(\frac{r}{r_p} - 1\right)^2}{\left(\frac{r_c}{r_p} - 1\right)}\right] \tag{3.50}$$

For the special case $r = r_p$, this reduces to

$$F_p = \sin\left(\bar{\gamma}_p\right)\varepsilon_c r_p \vartheta(r_p) \tag{3.51}$$

where

$$\vartheta(r_p) = K(r_p, r_c) - \frac{1}{24} \tag{3.52}$$

as is obtained by taking limits as $r \to r_p$. This last result for F_p gives the force to decelerate the projectile itself, whereas Eq. (3.44) and Eq. (3.45) ultimately involve both the projectile and the membrane material inside the cone.

Explicit relationship for Regime 2

From Eq. (3.43) and Eq. (3.50)

$$\vartheta(r) = K(r, r_c) - \frac{1}{24} + \Theta(r) \tag{3.53}$$

where

$$\Theta(r) = \begin{cases} \dfrac{7}{16}\left[\left(\dfrac{r}{r_p}-1\right) - \dfrac{1}{3}\dfrac{\left(\dfrac{r}{r_p}-1\right)^2}{\left(\dfrac{r_c}{r_p}-1\right)}\right], & r_p < r < 2r_p \\ \dfrac{7/8}{\dfrac{r_c}{r_p}-1}\left[\dfrac{r_c}{r_p}\left(\dfrac{r}{r_p}-1\right) - \dfrac{1}{2}\left(\dfrac{r}{r_p}-1\right)^2 \right. \\ \left. -\dfrac{1}{2}\left(\dfrac{r}{r_p}-1\right) - \dfrac{1}{2}\left(\dfrac{r_c}{r_p}-1\right) - \dfrac{1}{6}\right], & 2r_p < r < r_c \end{cases} \tag{3.54}$$

and the special cases are

$$\Theta(r_c) = \frac{7}{16}\left[\left(\frac{r_c}{r_p}-1\right) - \frac{1}{3\left(\dfrac{r_c}{r_p}-1\right)}\right] \tag{3.55}$$

and

$$\Theta(r_p) = 0 \tag{3.56}$$

3.2.5 Angles at the cone wave front and ratio of strains at the projectile and the cone wave front

A crucial task is to calculate $\sin(\bar{\gamma}_c)$ and for this we must consider the slope change from the cone wave front back to the projectile edge. First we note that

$$\delta = \int_{r_p}^{\hat{r_c}} \tan\left(\bar{\gamma}\left(r\left(\hat{r}\right)\right)\right) d\hat{r} \tag{3.57}$$

where $\hat{r}$ is position in the cone (along the x-axis) in ground coordinates. However, we have

$$d\hat{r} = \cos\left(\bar{\gamma}\left(r\right)\right) dr \tag{3.58}$$

as well as

$$\sin\left(\bar{\gamma}\left(r\right)\right) = \sin\left(\bar{\gamma}_c\right) \frac{\varepsilon_c}{\varepsilon(r)} \frac{\vartheta\left(r_c\right)}{\vartheta\left(r\right)} \tag{3.59}$$

and

$$\cos\left(\bar{\gamma}\left(r\right)\right) = \cos\left(\bar{\gamma}_c\right) \frac{\varepsilon_c}{\varepsilon(r)} \tag{3.60}$$

We have

$$\begin{aligned} \delta &= \int_{r_p}^{\hat{r}_c} \tan\left(\bar{\gamma}\left(r\left(\hat{r}\right)\right)\right) d\hat{r} \\ &= \int_{r_p}^{r_c} \tan\left(\bar{\gamma}(r)\right) \cos\left(\bar{\gamma}\left(r\right)\right) dr \\ &= \int_{r_p}^{r_c} \sin\left(\bar{\gamma}(r)\right) dr \end{aligned} \tag{3.61}$$

Note also that

$$\frac{\delta}{r_p} = \sin\left(\hat{\gamma}_c\right) \left(\frac{r_c - r_p}{r_p} \right) \tag{3.62}$$

so that

$$\sin\left(\hat{\gamma}_c\right) \left(\frac{r_c - r_p}{r_p} \right) = \frac{1}{r_p} \int_{r_p}^{r_c} \sin\left(\bar{\gamma}\left(r\right)\right) dr \tag{3.63}$$

From the equations above, there are two of the integral to work with. The first is

$$\int_{r_p}^{r_c} \sin\left(\bar{\gamma}\left(r\right)\right) dr = \sin\left(\bar{\gamma}_c\right) \int_{r_p}^{r_c} \frac{\varepsilon_c}{\varepsilon(r)} \frac{\vartheta(r_c)}{\vartheta(r)} dr \tag{3.64}$$

so that

$$\sin\left(\bar{\gamma}_c\right) = \frac{\sin\left(\hat{\gamma}_c\right)}{\frac{1}{r_c - r_p} \int_{r_p}^{r_c} \frac{\varepsilon_c}{\varepsilon(r)} \frac{\vartheta(r_c)}{\vartheta(r)} dr} \tag{3.65}$$

There are various approaches to evaluating this integral. First we note that upon letting

$$A\left(r_c\right) = \begin{cases} 1 - \dfrac{1}{6}\left(\dfrac{r_p}{r_c}\right)^2, & r_p < r_c < 2r_p \\ 1 - \dfrac{1}{24}, & r_c > 2r_p \end{cases} \tag{3.66}$$

which differs little from unity, we can write

$$\begin{aligned} \frac{\vartheta(r_c)}{\vartheta(r)} &= \frac{1 + (A(r_c) - 1) + \Theta(r_c)}{\dfrac{\varepsilon(r)}{\varepsilon_c} + (A(r_c) - 1) + \Theta(r)} \\ &= \frac{\varepsilon_c}{\varepsilon(r)} \frac{A(r_c) + \Theta(r_c)}{1 + \dfrac{\varepsilon_c}{\varepsilon(r)}\left(A(r_c) - 1 + \Theta(r)\right)} \end{aligned} \tag{3.67}$$

and thus

$$\sin(\bar{\gamma}_c) = \frac{\sin(\hat{\gamma}_c)}{\dfrac{1}{r_c - r_p}\displaystyle\int_{r_p}^{r_c} \left(\frac{\varepsilon_c}{\varepsilon(r)}\right)^2 \frac{A(r_c) + \Theta(r_c)}{1 + \dfrac{\varepsilon_c}{\varepsilon(r)}\left(A(r_c) - 1 + \Theta(r)\right)} dr} \tag{3.68}$$

A simplifying approximation

Towards simplifying the integral, a useful approximation is obtained upon noting that deviation of $\varepsilon_c/\varepsilon(r)$ from unity in the denominator is generally modest and occurs in the region of r closer to r_p. However $\Theta(r) = 0$ at $r = r_p$, when $\varepsilon_c/\varepsilon(r)$ is smallest and the growth in $\varepsilon_c/\varepsilon(r)$ towards unity with increasing r is initially rapid. Furthermore, our main interest in such calculations (where $\sin(\bar{\gamma}_c)$ begins to differ from $\sin(\hat{\gamma}_c)$) is when $r_c \geq 2r_p$. Thus

$$\begin{aligned} \left(1 + \frac{\varepsilon_c}{\varepsilon(r)}\left(A(r_c) - 1 + \Theta(r)\right)\right)_{r=r_p} &= A(r_c) + (1 - A(r_c))\left(1 - \frac{\varepsilon_c}{\varepsilon_p}\right) \\ &\approx A(r_c) \end{aligned} \tag{3.69}$$

since $1 - A(r_c) = 1/24$ and generally $1 - \dfrac{\varepsilon_c}{\varepsilon_p} > 0.25$ so the error is of the order of 1%. Also

$$\left(1 + \frac{\varepsilon_c}{\varepsilon(r)}\left(A(r_c) - 1 + \Theta(r)\right)\right)_{r=r_c} = A(r_c) + \Theta(r_c) \tag{3.70}$$

Thus a good approximation for the denominator for all $r_p < r < r_c$ is

$$1 + \frac{\varepsilon_c}{\varepsilon(r)}\left(A(r_c) - 1 + \Theta(r)\right) \approx A(r_c) + \Theta(r_c) \tag{3.71}$$

and thus

$$\frac{\vartheta(r_c)}{\vartheta(r)} \approx \frac{\varepsilon_c}{\varepsilon(r)} \frac{A(r_c) + \Theta(r_c)}{A(r_c) + \Theta(r)} \tag{3.72}$$

Thus our first expression that might be used for calculating $\sin(\bar{\gamma}_c)$ is

$$\sin(\bar{\gamma}_c) = \frac{\sin(\hat{\gamma}_c)}{\dfrac{1}{r_c - r_p}\displaystyle\int_{r_p}^{r_c} \left(\frac{\varepsilon_c}{\varepsilon(r)}\right)^2 \frac{A(r_c) + \Theta(r_c)}{A(r_c) + \Theta(r)} dr} \tag{3.73}$$

This result requires knowing $\varepsilon_c/\varepsilon(r)$ but its evaluation also involves $\Theta(r)$, which is known but not easily treated if one wants a closed from result to avoid numerical integration.

On the other hand we have

$$\begin{aligned} \int_{r_p}^{r_c} \sin\left(\bar{\gamma}(r)\right) dr &= \int_{r_p}^{r_c} \sqrt{1 - \cos^2\left(\bar{\gamma}(r)\right)} dr \\ &= \int_{r_p}^{r_c} \sqrt{1 - \cos^2\left(\bar{\gamma}_c\right)\left(\frac{\varepsilon_c}{\varepsilon(r)}\right)^2} dr \end{aligned} \tag{3.74}$$

and thus we have

$$\frac{1}{r_c - r_p} \int_{r_p}^{r_c} \sqrt{1 - \cos^2\left(\bar{\gamma}_c\right)\left(\frac{\varepsilon_c}{\varepsilon(r)}\right)^2} dr = \sin\left(\hat{\gamma}_c\right) \tag{3.75}$$

which avoids the involvement of $A(r_c)$ and $\Theta(r_c)$, and associated approximations above. Either way, we must determine $(\varepsilon_c/\varepsilon(r))$ in order to carry out the integration. Our approach in this case will be to develop an approximate functional form for $(\varepsilon_c/\varepsilon(r))^2$ in terms of $\left(\varepsilon_c/\varepsilon_p\right)^2$ and r_p/r_c.

Nonetheless we explore certain relationships, from which we can also calculate $\varepsilon_p/\varepsilon_c$ and $\bar{\gamma}_p$ from $\bar{\gamma}_c$. We have

$$\begin{aligned}
\frac{\varepsilon_c}{\varepsilon(r)} &= \frac{\sin\left(\bar{\gamma}(r)\right)}{\sin\left(\bar{\gamma}_c\right)}\frac{\vartheta(r)}{\vartheta(r_c)} \\
&= \frac{\sqrt{1-\cos^2\left(\bar{\gamma}(r)\right)}}{\sin\left(\bar{\gamma}_c\right)}\frac{\vartheta(r)}{\vartheta(r_c)} \\
&\approx \frac{\sqrt{1-\cos^2\left(\bar{\gamma}_c\right)\left(\dfrac{\varepsilon_c}{\varepsilon(r)}\right)^2}}{\sin\left(\bar{\gamma}_c\right)}\frac{\varepsilon(r)}{\varepsilon_c}\frac{A(r_c)+\Theta(r)}{A(r_c)+\Theta(r_c)}
\end{aligned} \tag{3.76}$$

so

$$\sin(\bar{\gamma}_c) \approx \frac{\varepsilon(r)}{\varepsilon_c}\sqrt{\left[\left(\frac{\varepsilon(r)}{\varepsilon_c}\right)^2-\cos^2(\bar{\gamma}_c)\right]\left[\frac{A(r_c)+\Theta(r)}{A(r_c)+\Theta(r_c)}\right]^2} \tag{3.77}$$

and

$$\left(\frac{\varepsilon(r)}{\varepsilon_c}\right)^2\left(\left(\frac{\varepsilon(r)}{\varepsilon_c}\right)^2-\cos^2(\bar{\gamma}_c)\right) \approx \sin^2(\bar{\gamma}_c)\left(\frac{A(r_c)+\Theta(r_c)}{A(r_c)+\Theta(r)}\right)^2 \tag{3.78}$$

or

$$\left(\frac{\varepsilon(r)}{\varepsilon_c}\right)^4-\cos^2(\bar{\gamma}_c)\left(\frac{\varepsilon(r)}{\varepsilon_c}\right)^2-\sin^2(\bar{\gamma}_c)\left(\frac{A(r_c)+\Theta(r_c)}{A(r_c)+\Theta(r)}\right)^2 \approx 0 \tag{3.79}$$

so

$$\left(\frac{\varepsilon(r)}{\varepsilon_c}\right)^2 \approx \frac{\cos^2(\bar{\gamma}_c)}{2}\left(1+\sqrt{1+4\frac{\tan^2(\bar{\gamma}_c)}{\cos^2(\bar{\gamma}_c)}\left(\frac{A(r_c)+\Theta(r_c)}{A(r_c)+\Theta(r)}\right)^2}\right) \tag{3.80}$$

or

$$\left(\frac{\varepsilon(r)}{\varepsilon_c}\right)^2 \approx \sin(\bar{\gamma}_c)\frac{1-\sin^2(\bar{\gamma}_c)}{2\sin(\bar{\gamma}_c)}\left(1+\sqrt{1+\left(\frac{2\sin(\bar{\gamma}_c)}{1-\sin^2(\bar{\gamma}_c)}\right)^2\left(\frac{A(r_c)+\Theta(r_c)}{A(r_c)+\Theta(r)}\right)^2}\right) \tag{3.81}$$

as well as

$$\left(\frac{\varepsilon_p}{\varepsilon_c}\right)^2 \approx \sin(\bar{\gamma}_c)\frac{1-\sin^2(\bar{\gamma}_c)}{2\sin(\bar{\gamma}_c)}\left(1+\sqrt{1+\left(\frac{2\sin(\bar{\gamma}_c)}{1-\sin^2(\bar{\gamma}_c)}\right)^2\left(\frac{A(r_c)+\Theta(r_c)}{A(r_c)}\right)^2}\right) \tag{3.82}$$

This result is very valuable and accurate because for $r = r_p$ the maximum strain ratio $\varepsilon_p/\varepsilon_c$ is directly related to $\bar{\gamma}_c$ and to $\Theta(r_c)$, which is completely known.

Key set of formulas

For $r = r_p$ we have the key relationships

$$\frac{1}{r_c - r_p}\int_{r_p}^{r_c}\sqrt{1-\cos^2(\bar{\gamma}_c)\left(\frac{\varepsilon_c}{\varepsilon(r)}\right)^2}\,dr = \sin(\hat{\gamma}_c) \tag{3.83}$$

together with the earlier results

$$\left(\frac{\varepsilon_p}{\varepsilon_c}\right)^2 \approx \frac{\cos^2(\bar{\gamma}_c)}{2}\left(1+\sqrt{1+4\frac{\tan^2(\bar{\gamma}_c)}{\cos^2(\bar{\gamma}_c)}\left(\frac{A(r_c)+\Theta(r_c)}{A(r_c)}\right)^2}\right) \tag{3.84}$$

and

$$\sin(\bar{\gamma}_p) = \sin(\bar{\gamma}_c)\left(\frac{\varepsilon_c}{\varepsilon_p}\right)^2\left(\frac{A(r_c)+\Theta(r_c)}{A(r_c)}\right) \tag{3.85}$$

where

$$A(r_c) = \begin{cases} 1-\dfrac{1}{6}\left(\dfrac{r_p}{r_c}\right)^2, & r_p < r_c < 2r_p \\ 1-\dfrac{1}{24}, & r_c > 2r_p \end{cases} \tag{3.86}$$

and again

$$\Theta(r_c) = \begin{cases} \frac{1}{3}\left[1 - \frac{1}{2}\left(\frac{r_p}{r_c}\right)^2\right]\left(\frac{r_c}{r_p} - 1\right), & r_p < r_c < 2r_p \\ \\ \frac{7}{16}\left[\left(\frac{r_c}{r_p} - 1\right) - \frac{1}{3\left(\frac{r_c}{r_p} - 1\right)}\right], & r_c > 2r_p \end{cases} \tag{3.87}$$

Thus the key is to evaluate the integral involving $(\varepsilon_c/\varepsilon(r))^2$ and to do this we must understand how the strain ratio $(\varepsilon_c/\varepsilon(r))^2$ behaves. Fig. 3.2 below illustrates the behavior of this quantity and shows that at larger values of r_c and for $r < r_c - r_p$ back from the cone-wave tip the behavior is approximately linear. This feature breaks down however for $r_c < 2r_p$. However in this regime $\sin(\bar{\gamma}_c)$ and $\sin(\hat{\gamma}_c)$ are not so different and a simple approximation may suffice.

3.2.6 Calculating the key integral directly using an accurate expansion

The above approximate approach relies on the observed behavior of the strain within the cone region using numerical simulations. However, a more direct approach may be more desirable. Returning to Eq. (3.74), i.e.,

$$\sin(\bar{\gamma}_c) = \frac{\sin(\hat{\gamma}_c)}{\frac{1}{r_c - r_p}\int_{r_p}^{r_c}\left(\frac{\varepsilon_c}{\varepsilon(r)}\right)^2 \frac{A(r_c) + \Theta(r_c)}{A(r_c) + \Theta(r)} dr} \tag{3.88}$$

we obtained Eq. (3.82) earlier, i.e.,

$$\left(\frac{\varepsilon(r)}{\varepsilon_c}\right)^2 \approx \sin(\bar{\gamma}_c)\frac{1 - \sin^2(\bar{\gamma}_c)}{2\sin(\bar{\gamma}_c)}\left(1 + \sqrt{1 + \left(\frac{2\sin(\bar{\gamma}_c)}{1 - \sin^2(\bar{\gamma}_c)}\right)^2\left(\frac{A(r_c) + \Theta(r_c)}{A(r_c) + \Theta(r)}\right)^2}\right) \tag{3.89}$$

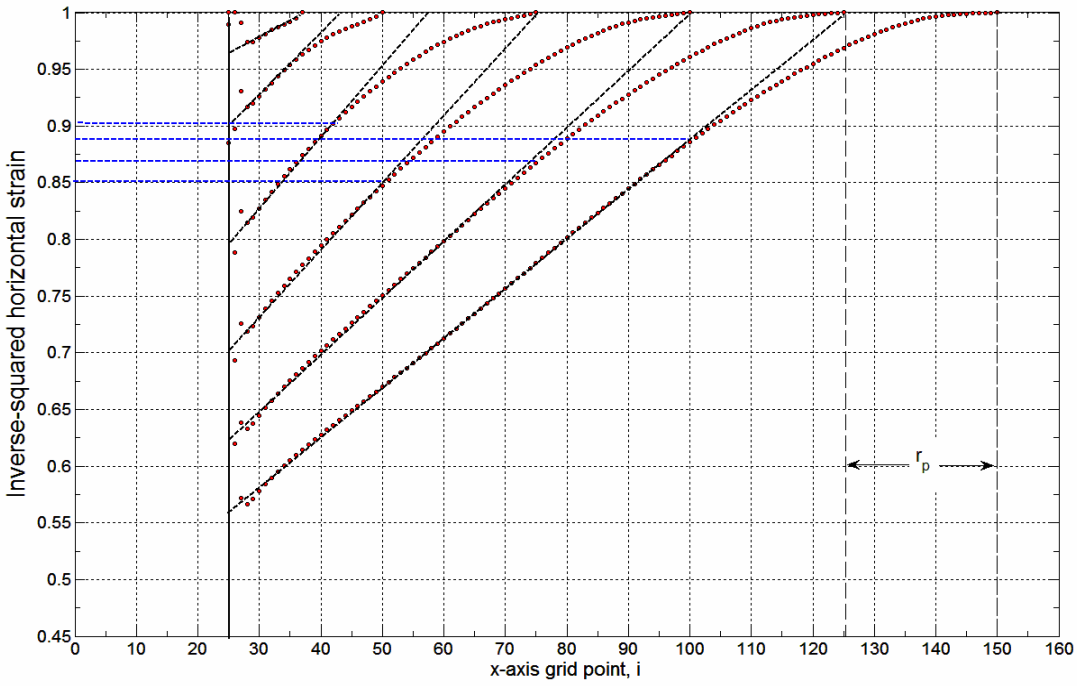

Figure 3.2: Behavior of the inverse of the square of the strain ratio along the yarn axis inside the cone region using the DSM simulation code at approximately constant strain at the cone wave-front.

and thus

$$\sin(\hat{\gamma}_c) = \sin(\bar{\gamma}_c)\frac{1}{r_c - r_p}\int_{r_p}^{r_c}\left(\frac{\varepsilon_c}{\varepsilon(r)}\right)^2\left(\frac{A(r_c)+\Theta(r_c)}{A(r_c)+\Theta(r)}\right)dr \tag{3.90}$$

or

$$\sin(\hat{\gamma}_c) = \frac{2\sin(\bar{\gamma}_c)}{1-\sin^2(\bar{\gamma}_c)}\frac{1}{r_c - r_p}\int_{r_p}^{r_c}\frac{\frac{A(r_c)+\Theta(r_c)}{A(r_c)+\Theta(r)}}{1+\sqrt{1+\left(\frac{2\sin(\bar{\gamma}_c)}{1-\sin^2(\bar{\gamma}_c)}\right)^2\left(\frac{A(r_c)+\Theta(r_c)}{A(r_c)+\Theta(r)}\right)^2}}dr \tag{3.91}$$

Letting

$$C(\bar{\gamma}_c) = \frac{2\sin(\bar{\gamma}_c)}{1-\sin^2(\bar{\gamma}_c)} \tag{3.92}$$

and

$$\eta = \frac{A(r_c) + \Theta(r)}{A(r_c) + \Theta(r_c)} \tag{3.93}$$

we see that

$$d\eta = \frac{1}{A(r_c) + \Theta(r_c)} \frac{d\Theta(r)}{dr} dr \tag{3.94}$$

or

$$dr = \frac{A(r_c) + \Theta(r_c)}{\dfrac{d\Theta(r)}{dr}} d\eta \tag{3.95}$$

We thus have

$$\sin(\hat{\gamma}_c) = C(\bar{\gamma}_c) \frac{A(r_c) + \Theta(r_c)}{r_c - r_p} \int_{\frac{A(r_c)}{A(r_c)+\Theta(r_c)}}^{1} \frac{1/\eta}{1 + \sqrt{1 + C(\bar{\gamma}_c)^2/\eta^2}} \frac{1}{d\Theta(r)/dr} d\eta \tag{3.96}$$

Now by inversion

$$\Theta(r) = (A(r_c) + \Theta(r_c))\, \eta - A(r_c) \tag{3.97}$$

so

$$\frac{d\Theta(r)}{dr} = (A(r_c) + \Theta(r_c)) \frac{d\eta}{dr} \tag{3.98}$$

and thus

$$\sin(\hat{\gamma}_c) = C(\bar{\gamma}_c) \frac{1}{r_c - r_p} \int_{\frac{A(r_c)}{A(r_c)+\Theta(r_c)}}^{1} \frac{1/\eta}{1 + \sqrt{1 + C(\bar{\gamma}_c)^2/\eta^2}} \frac{1}{d\eta(r)/dr} d\eta \tag{3.99}$$

In Regime 1, we have

$$\Theta(r) = \Theta(r_c) \frac{3}{2} \left(\frac{r - r_p}{r_c - r_p} \right) \left[1 - \frac{1}{3} \left(\frac{r - r_p}{r_c - r_p} \right) \right], \quad r_p < r < r_c < 2r_p \tag{3.100}$$

or

$$\Theta(r) = \Theta(r_c) \frac{3}{2} \zeta \left(1 - \frac{1}{3} \zeta \right), \quad 0 < \zeta < 1,\ r_c < 2r_p \tag{3.101}$$

In Regime 2 we can show that

$$\Theta(r) = \Theta(r_c)\begin{cases} \dfrac{\left(\dfrac{r-r_p}{r_c-r_p}\right) - \dfrac{1}{3}\left(\dfrac{r-r_p}{r_c-r_p}\right)^2}{1-\dfrac{1}{3}\left(\dfrac{r_p}{r_c-r_p}\right)}, & r_p < r < 2r_p \\ \dfrac{2\left(\dfrac{r-r_p}{r_c-r_p}\right) - \left(\dfrac{r-r_p}{r_c-r_p}\right)^2 + \left(\dfrac{r_p}{r_c-r_p}\right)\left[\left(\dfrac{r-r_p}{r_c-r_p}\right)-1\right] - \dfrac{1}{3}\left(\dfrac{r_p}{r_c-r_p}\right)^2}{1-\dfrac{1}{3}\left(\dfrac{r_p}{r_c-r_p}\right)^2}, & \\ & 2r_p < r < r_c \end{cases} \tag{3.102}$$

or

$$\Theta(r) = \frac{\Theta(r_c)}{1-\dfrac{D^2}{3}}\begin{cases} \zeta - \dfrac{\zeta^2}{3}, & 0 < \zeta < D \\ 2\zeta - \zeta^2 + D(\zeta - 1) - \dfrac{D^2}{3}, & D < \zeta < 1 \end{cases} \tag{3.103}$$

where

$$D = \frac{r_p}{r_c - r_p} \tag{3.104}$$

and

$$\zeta = \frac{r - r_p}{r_c - r_p} \tag{3.105}$$

Letting

$$\hat{D} = \min\left(\frac{r_p}{r_c - r_p}, 1\right) \tag{3.106}$$

both regimes are handled using

$$\Theta(r) = \Theta(r_c) \begin{cases} \dfrac{\zeta - \dfrac{\zeta^2}{3}}{1 - \dfrac{\hat{D}^2}{3}}, & 0 < \zeta < \hat{D} \\ \dfrac{2\zeta - \zeta^2 + \hat{D}(\zeta - 1) - \dfrac{\hat{D}^2}{3}}{1 - \dfrac{\hat{D}^2}{3}}, & \hat{D} < \zeta < 1 \end{cases} \tag{3.107}$$

or

$$\Theta(r) = \Theta(r_c)\, f\left(\zeta, \hat{D}\right) \tag{3.108}$$

where

$$f\left(\zeta, \hat{D}\right) = \begin{cases} \dfrac{\zeta - \dfrac{\zeta^2}{3}}{1 - \dfrac{\hat{D}^2}{3}}, & 0 < \zeta < \hat{D} \\ \dfrac{2\zeta - \zeta^2 + \hat{D}(\zeta - 1) - \dfrac{\hat{D}^2}{3}}{1 - \dfrac{\hat{D}^2}{3}}, & \hat{D} < \zeta < 1 \end{cases} \tag{3.109}$$

We let

$$\begin{aligned} \eta &= \frac{A(r_c) + \Theta(r)}{A(r_c) + \Theta(r_c)} \\ &= 1 + \frac{\Theta(r) - \Theta(r_c)}{A(r_c) + \Theta(r_c)} \\ &= 1 + \frac{\Theta(r_c)}{A(r_c) + \Theta(r_c)} \left(f\left(\zeta, \hat{D}\right) - 1 \right) \end{aligned} \tag{3.110}$$

or

$$\eta = 1 + \chi\left(\frac{r_c}{r_p}\right) \begin{cases} \dfrac{(\zeta - 1)\left(\zeta^2 - \hat{D}^2\right)}{3}, & 0 < \zeta < \hat{D} \\ \hat{D}(\zeta - 1) - (\zeta - 1)^2, & \hat{D} < \zeta < 1 \end{cases} \tag{3.111}$$

or

$$1-\eta=\chi\left(\frac{r_c}{r_p}\right)\begin{cases}\dfrac{(1-\zeta)\left(\hat{D}^2-\zeta^2\right)}{3}, & 0<\zeta<\hat{D}\\ \hat{D}(1-\zeta)+(1-\zeta)^2, & \hat{D}<\zeta<1\end{cases} \tag{3.112}$$

where

$$\chi\left(\frac{r_c}{r_p}\right)=\left(\frac{\Theta(r_c)}{A(r_c)+\Theta(r_c)}\right)\left(\frac{1}{1-\hat{D}^2/3}\right) \tag{3.113}$$

Now

$$\frac{d\eta}{dr}=\frac{d\eta}{d\zeta}\frac{d\zeta}{dr}=\frac{1}{r_c-r_p}\frac{d\eta}{d\zeta} \tag{3.114}$$

and thus

$$\sin(\hat{\gamma}_c)=C(\bar{\gamma}_c)\int_{\frac{A(r_c)}{A(r_c)+\Theta(r_c)}}^{1}\frac{1/\eta}{1+\sqrt{1+C(\bar{\gamma}_c)^2/\eta^2}}\frac{1}{d\eta/d\zeta}d\eta \tag{3.115}$$

In Regime 1, namely $r_p < r < r_c \leq 2r_p$, we have $\hat{D} = 1$ so only the top expression in Eq. (3.109) applies. In Regime 2, namely $r_c > 2r_p$, we have $0 < \hat{D} < 1$ so both expressions in Eq. (3.109) are involved.

To understand what is involved in evaluating this integral we consider the behavior of

$$\eta=\frac{A(r_c)+\Theta(r)}{A(r_c)+\Theta(r_c)} \tag{3.116}$$

versus r/r_p which is shown in Fig. 3.3. The first line at the top corresponds to the end of Regime 1 and there is no 'kink' in the behavior of η since $r_c/r_p = 2$. For $r_c/r_p > 2$ a kink in η always appears at $r/r_p = 2$ corresponding to $\zeta = (2r_p - r_p)/(r_c - r_p)$. Thus in Regime 2 we must evaluate the integral both for $0 < \zeta \leq \hat{D}$ and $\hat{D} < \zeta \leq 1$.

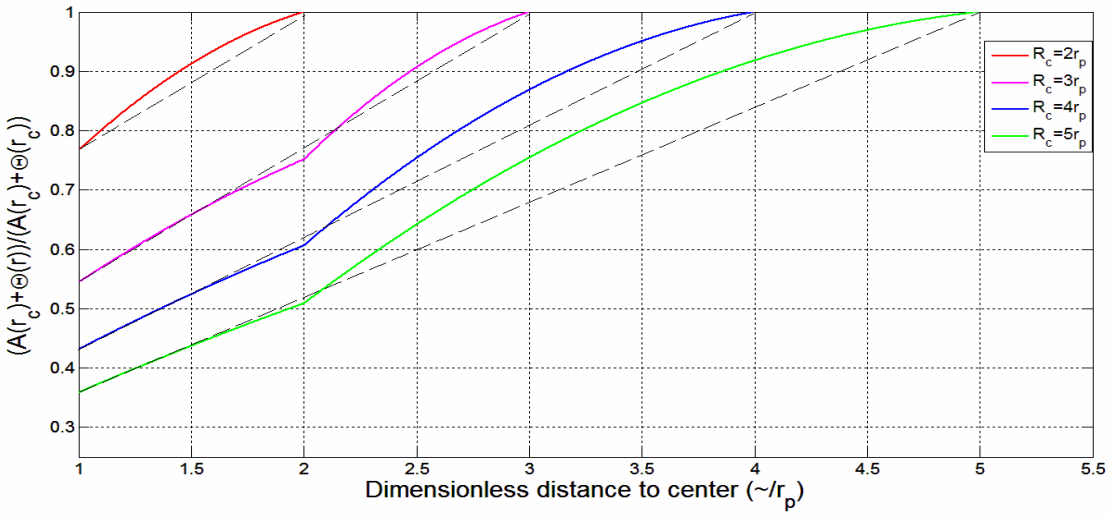

Figure 3.3: Behavior of a key ratio η in the analysis.

Regarding Regime 2, we can write Eq. (3.112) as

$$1-\eta=\chi\left(\frac{r_c}{r_p}\right)\begin{cases}\dfrac{\left((1-\zeta)^2+(1-\zeta)-(\hat{D}^2-1)\right)}{3}, & 0<\zeta<D\\ \hat{D}(1-\zeta)+(1-\zeta)^2, & D<\zeta<1\end{cases} \tag{3.117}$$

and thus

$$\frac{d\eta}{d\zeta}=\frac{d(1-\eta)}{d(1-\zeta)}\approx\chi\left(\frac{r_c}{r_p}\right)\begin{cases}1/3+\dfrac{2(1-\zeta)}{3}, & 0<\zeta<D\\ \hat{D}+2(1-\zeta), & D<\zeta<1\end{cases} \tag{3.118}$$

For $\hat{D}<\zeta\leq 1$ we obtain the inversion

$$(1-\zeta)^2+\hat{D}(1-\zeta)-\frac{1-\eta}{\chi(r_c/r_p)}=0 \tag{3.119}$$

given

$$1-\zeta=\frac{\hat{D}}{2}\left(\sqrt{1+\frac{4(1-\zeta)}{\hat{D}^2\chi(r_c/r_p)}}-1\right) \tag{3.120}$$

Thus

$$\frac{d\eta}{d\zeta}=\chi(r_c/r_p)\hat{D}\sqrt{1+\frac{4(1-\zeta)}{\hat{D}^2\chi(r_c/r_p)}}=2\sqrt{\chi(r_c/r_p)}\sqrt{\frac{\hat{D}^2\chi(r_c/r_p)+4}{4}-\eta} \tag{3.121}$$

For the case $0 < \zeta \leq \hat{D}$ we have the inversion

$$(1-\zeta)^2 + (1-\zeta) - \left((\hat{D}^2 - 1) + \frac{3(1-\eta)}{\chi(r_c/r_p)}\right) = 0 \tag{3.122}$$

giving

$$1 - \zeta = -\frac{1}{2}\left(1 - \sqrt{1 + 4\left((\hat{D}^2 - 1) + \frac{3(1-\eta)}{\chi(r_c/r_p)}\right)}\right) \tag{3.123}$$

Thus

$$\begin{aligned}
\frac{d\eta}{d\zeta} &= \frac{\chi(r_c/r_p)}{3}\left(1 + 2(1-\zeta)\right) \\
&= \frac{\chi(r_c/r_p)}{3}\sqrt{1 + 4\left((\hat{D}^2 - 1) + \frac{3(1-\eta)}{\chi(r_c/r_p)}\right)} \\
&= \frac{2}{\sqrt{3}}\sqrt{\chi(r_c/r_p)}\sqrt{\frac{(4\hat{D}^2 - 3)\chi(r_c/r_p) + 12}{12} - \eta}
\end{aligned} \tag{3.124}$$

The transition value $\hat{\eta} = \eta(\zeta = \hat{D})$ separating the case $\hat{D} < \zeta \leq 1$ from $0 < \zeta \leq \hat{D}$ is

$$\begin{aligned}
\hat{\eta} &= 1 + \frac{\Theta(r_c)}{A(r_c) + \Theta(r_c)}\left(\frac{\hat{D} - \hat{D}^2/3}{1 - \hat{D}^2/3} - 1\right) \\
&= \frac{A(r_c) + \Theta(r_c)(\hat{D} - \hat{D}^2/3)/(1 - \hat{D}^2/3)}{A(r_c) + \Theta(r_c)}
\end{aligned} \tag{3.125}$$

Regime 2, where $0 < \hat{D} < 1$, or $r_c > 2r_p$

In Regime 2, $0 < \hat{D} < 1$. thus for Regime 2 we have

$$\begin{aligned}
\sin(\hat{\gamma}_c) = \Bigg[&\int_{\frac{A(r_c)}{A(r_c)+\Theta(r_c)}}^{\frac{A(r_c)+\Theta(r_c)(\hat{D}-\hat{D}^2/3)/(1-\hat{D}^2/3)}{A(r_c)+\Theta(r_c)}} \frac{1/\eta}{1 + \sqrt{1 + \frac{C(\bar{\gamma}_c)^2}{\eta^2}}} \frac{\sqrt{3}}{\sqrt{\frac{(4\hat{D}^2-3)\chi(r_c/r_p)+12}{12} - \eta}} d\eta \\
&+ \int_{\frac{A(r_c)+\Theta(r_c)(\hat{D}-\hat{D}^2/3)/(1-\hat{D}^2/3)}{A(r_c)+\Theta(r_c)}}^{1} \frac{1/\eta}{1 + \sqrt{1 + \frac{C(\bar{\gamma}_c)^2}{\eta^2}}} \frac{1}{\sqrt{\frac{\hat{D}^2\chi(r_c/r_p)+4}{4} - \eta}} d\eta \Bigg] \frac{C(\bar{\gamma}_c)}{2\sqrt{\chi(r_c/r_p)}}
\end{aligned} \tag{3.126}$$

Letting

$$B = \frac{\hat{D}^2\chi(r_c/r_p) + 4}{4} = 1 + \left(\frac{\hat{D}}{2}\right)^2 \chi(r_c/r_p) \tag{3.127}$$

$$\hat{B} = \frac{(4\hat{D}^2 - 3)\chi(r_c/r_p) + 12}{12} = 1 + \frac{(4\hat{D}^2 - 3)\chi(r_c/r_p)}{12} \tag{3.128}$$

$$C = C(\bar{\gamma}_c) \tag{3.129}$$

$$E = \frac{A(r_c)}{A(r_c) + \Theta(r_c)} \tag{3.130}$$

$$F = \frac{A(r_c) + \Theta(r_c)(\hat{D} - \hat{D}^2/3)/(1 - \hat{D}^2/3)}{A(r_c) + \Theta(r_c)} \tag{3.131}$$

and

$$G = \frac{1}{2\sqrt{\chi(r_c/r_p)}} \tag{3.132}$$

we have

$$\sin(\hat{\gamma}_c) = CG\left(\int_E^F \frac{1/\eta}{1 + \sqrt{1 + C^2/\eta^2}} \frac{\sqrt{3}}{\sqrt{\hat{B} - \eta}} + \int_F^1 \frac{1/\eta}{1 + \sqrt{1 + C^2/\eta^2}} \frac{1}{\sqrt{B - \eta}}\right) \tag{3.133}$$

or

$$\sin(\hat{\gamma}_c) = CG\left(\sqrt{3}\int_E^F \frac{1/\eta}{1 + \sqrt{1 + C^2/\eta^2}} \frac{1}{\sqrt{\hat{B} - \eta}} + \int_F^1 \frac{1/\eta}{1 + \sqrt{1 + C^2/\eta^2}} \frac{1}{\sqrt{B - \eta}}\right) \tag{3.134}$$

or

$$\sin(\hat{\gamma}_c) = \frac{G}{C}\left(\sqrt{3}\int_E^F \frac{\sqrt{\eta^2 + C^2}}{\sqrt{\hat{B} - \eta}} d\eta - \sqrt{3}\int_E^F \frac{\eta}{\sqrt{\hat{B} - \eta}} d\eta + \int_F^1 \frac{\sqrt{\eta^2 + C^2}}{\sqrt{B - \eta}} d\eta + \int_F^1 \frac{\eta}{\sqrt{B - \eta}} d\eta \right) \tag{3.135}$$

or

$$\sin(\hat{\gamma}_c) = \frac{G}{C}\left(\sqrt{3}\hat{J}_{21} - \sqrt{3}\hat{J}_{22} + J_{21} + J_{22} \right) \tag{3.136}$$

where

$$\hat{J}_{21} = \int_E^F \frac{\sqrt{\eta^2 + C^2}}{\sqrt{\hat{B} - \eta}} d\eta \tag{3.137}$$

$$\hat{J}_{22} = \int_E^F \frac{\eta}{\sqrt{\hat{B} - \eta}} d\eta \tag{3.138}$$

$$J_{21} = \int_F^1 \frac{\sqrt{\eta^2 + C^2}}{\sqrt{B - \eta}} d\eta \tag{3.139}$$

and

$$J_{22} = \int_F^1 \frac{\eta}{\sqrt{B - \eta}} d\eta \tag{3.140}$$

Regime 1, where $\hat{D} = 1$, or $r_p < r_c < 2r_p$

For Regime 1, we have $\hat{D} < \zeta \leq 1$ so that

$$F = \frac{A(r_c) + \Theta(r_c)}{A(r_c) + \Theta(r_c)} = 1 \tag{3.141}$$

Thus

$$\sin(\hat{\gamma}_c) = \sqrt{3}\frac{G}{C}\left(\int_E^1 \frac{\sqrt{\eta^2 + C^2}}{\sqrt{\hat{B} - \eta}} d\eta - \int_E^1 \frac{\eta}{\sqrt{\hat{B} - \eta}} d\eta\right) \tag{3.142}$$

or

$$\sin(\hat{\gamma}_c) = \sqrt{3}\frac{G}{C}\left(\hat{J}_{11} - \hat{J}_{12}\right) \tag{3.143}$$

where

$$\hat{J}_{11} = \int_E^1 \frac{\sqrt{\eta^2 + C^2}}{\sqrt{\hat{B} - \eta}} \tag{3.144}$$

and

$$\hat{J}_{12} = \int_E^1 \frac{\eta}{\sqrt{\hat{B} - \eta}} \tag{3.145}$$

3.2.7 Strain decay along tension wave arms by wave induced drag of crossing yarns

We now consider effects on the unit solution caused by drag effects on the main tension wave arms from induced secondary tension and transverse waves in the crossing yarns. Under the unit solution, where $\varepsilon_c = \varepsilon_{p,0}$ (i.e., the strain at the cone wave front is held fixed over time at the initial strain upon impact), we nominally (following the 1D tape solution) would have a tensile wave occurring in the x-direction set of yarns with strain $\varepsilon_x(r) = \varepsilon_c$ and a constant 'in-flow' velocity behind the tensile wave-front as $\dot{u}_x(r) = -a_0\varepsilon_c$. As the tension wave passes position r, this causes a tension wave in the crossing y-direction yarns

but at a much lower strains $\varepsilon_y(r)$ (about 4% of those in the main tension waves) since $\dot{u}_x(r) << V_0$. It also causes a corresponding transverse wave in the crossing yarns at each location, r, (provided r is significantly back from the tensile wave-front to allow sequential transverse kinks in the yarns to develop). The sequence of transverse yarn tensions applied at a kink angle to the $2r_p$ wide band of x-direction yarns in the tension wave, loads the edge of the band all the way from the cone edge r_c, out to within about $6r_p$ of the tensile wave-front at r_{a_0}. (The effect is analogous to how the original yarns exert a decelerating force on the projectile, except that the loading acts like a distributed shear force along the two edges of the band of x-direction yarns.)

After investigating various possibilities and comparing the results with the numerical simulations it has been found that by far the most effective way to capture the influence of secondary drag on the inflow is to consider a blend of 1D tape impact behavior and that for a 2D axisymmetric membrane that has in-plane isotropic properties. In the latter case the axisymmetry itself and resulting radial spreading of the tensile wave-front means that the tension at this front (and yarn strain) must decay roughly inversely with its location at $r_{a_0} = r_p + a_0 t$. Behind it the tension builds back up to its constant value at the cone wave-front. Thus we 'blend' the 1D and axisymmetric unit solutions to yield the unit solution forms for the biaxial membrane given by

$$\dot{u}_c^0(t) = a_0 \varepsilon_{p,0} \frac{1 - \exp(-t/t_0)}{t/t_0} \tag{3.146}$$

$$u_c^0(t) = \int_0^t a_0 \dot{u}_c^0(s) ds \tag{3.147}$$

where superscripts '0' have been added to prevent confusion of these 'unit' quantities with their more general counterparts discussed in the next subsection, and where t_0 is a time constant of the order of the time it takes for the cone wave to advance about four projectile radii and the tension wave to advance about 30 projectile radii. In other words, $t_0 \approx 75 r_p/a_0$, which means the inflow velocity takes considerable time to decay as a result of drag from the crossing yarns. These two equations have features which transition from those for the 1D tape impact problem to something closer to the 2D axisymmetric, isotropic problem. In most practical applications, since the characteristic time $t_0 \approx 75 r_p/a_0$ is a rather long time compared to the time it takes to reach maximum strain, the behavior is driven mostly by the 1D behavior rather than the 2D behavior which requires even more time to fully dominate. Nevertheless the effects become noticeable for problems involving lower fabric to projectile areal density ratios, and longer times to decelerate the projectile.

Thus decay in strain at the cone wave-front is ostensibly treated as influencing immediately the inflow velocity behavior all the way out to the tensile wave-front. In reality the timescale for the decay in strain and projectile velocity is very long compared to the tensile wave-speed in typical materials so this assumption poses very little risk to computational accuracy and is no worse in effect than the assumption behind Eq. (3.146), which itself is mitigated as the strain at the cone wave-front diminishes. The result of this is that we have integrals for which closed forms are not available, but the stepwise numerical integration is easily performed. In any case these 2D type effects are only relevant when the peak strain around the projectile occurs at relatively long times, i.e., when the projectile mass is relatively large and the areal density ratio of the fabric to the projectile is small.

One possible additional difficulty with our assumptions is that the transient behavior for short times, when the cone wave-front is still primarily a circle, may not be accurately reflected once the pyramid-shaped cone emerges. However, numerical simulations show no slowdown in inflow velocity with time or state of evolution of the pyramid in terms of the ratio $r_c(t)/r_p$. Thus, other than the effect already accommodated, there is no reason to impose any additional decrease in the inflow velocity along the yarn axes because of the transition to pyramid-shaped cone behavior.

3.2.8 Application of Duhamel convolution to unit solutions to obtain general solutions

In the actual problem, all important quantities will depend on time as the projectile decelerates and the strain at the cone wave-front will not be constant, so we must acknowledge that $\varepsilon_c = \varepsilon_c(t)$, and this affects all quantities that depend on it directly. Evaluation of various expressions that arise later, requires knowing the inflow displacement at the cone wave-front, denoted $u_c(t)$, and the associated velocity of material, $\dot{u}_c(t) = \partial(t, r_c(t))/\partial t)$, flowing towards the projectile, particularly for the band of yarns that actually pass under the projectile. We have 'unit solution' results described above in Eq. (3.146) and Eq. (3.147) for the special case

$$\varepsilon_c(t) = \varepsilon_c, \ t \geq 0 \tag{3.148}$$

(where we recall that $\varepsilon_p(t)$ and $\varepsilon_c(t)$ without over-bars refer to strains measured

in the material along the main axes). Conversely, in the actual problem, eventually $\varepsilon_c(t)$ decreases with time even when the strain around the projectile, $\varepsilon_p(t)$, is increasing.

Our approach is to treat the varying strain history, $0 \leq s \leq t$ up to time t, through Duhamel convolution integrals of the unit solutions, $\dot{u}_c^0(t)$ and $u_c^0(t)$, in the form

$$\dot{u}_c(t) = \dot{u}_c^0(0) - \int_0^t \dot{\varepsilon}_c(t-s)\dot{u}_c(s)ds \tag{3.149}$$

Similar to Eq. (3.146) and Eq. (3.147), we have

$$\dot{u}_c(t) = a_0\varepsilon_c(t)\frac{1-\exp(-t/t_0)}{t/t_0} \tag{3.150}$$

and

$$u_c(t) = \int_0^t a_0\dot{u}_c(s)ds \tag{3.151}$$

3.2.9 Yarn length compatibility along the yarn axis in the cone

In order to relate various quantities like strain level, cone wave-speed and projectile travel, must we consider length compatibility or matching along the x-axis yarns passing under the projectile center. We let

$$\hat{\lambda}_c(t) = \sqrt{\left(r_c(t) + u_c(t) - r_p\right)^2 + \delta(t)^2} \tag{3.152}$$

be the straight line distance in ground coordinates between the cone wave front and the projectile edge. (Here and in the following discussion, we explicitly

acknowledge the dependence of the various quantities on time, t). In this expression

$$r_c(t) = r_p + \int_0^t c(s)ds \tag{3.153}$$

is the position of the pyramid corner (or wave-front at the tip of the diagonal along the yarn axis) in material coordinates, and $u_c(t)$ is the in-flow in ground coordinates of those yarn material points at the cone wave front towards the projectile due to the outgoing tension wave, and lastly

$$\delta(t) = \int_0^t V(s)ds \tag{3.154}$$

is the displacement of the projectile.

Upon taking derivatives of $\hat{\lambda}_c(t)$ with respect to t, after some manipulation we arrive at

$$c(t)(1+\varepsilon_c(t)) = \frac{\left(r_c(t)+u_c(t)-r_p\right)\left(c(t)\left(1+\varepsilon_c(t)\right)+\dot{u}_c(t)\right)+\delta(t)V(t)}{\sqrt{\left(r_c(t)+u_c(t)-r_p\right)^2+\delta(t)^2}} \tag{3.155}$$

We let $\hat{\gamma}_c(t)$ be the effective cone angle with respect to ground as defined by the hypotenuse $\hat{\lambda}_c(t)$, and this angle follows the relationships

$$\sin\left(\hat{\gamma}_c(t)\right) = \frac{\delta(t)}{\sqrt{\left(r_c(t)+u_c(t)-r_p\right)^2+\delta(t)^2}} \tag{3.156}$$

$$\cos\left(\hat{\gamma}_c(t)\right) = \frac{r_c(t)+u_c(t)-r_p}{\sqrt{\left(r_c(t)+u_c(t)-r_p\right)^2+\delta(t)^2}} \tag{3.157}$$

and

$$\tan\left(\hat{\gamma}_c(t)\right) = \frac{\delta(t)}{r_c(t) + u_c(t) - r_p} \tag{3.158}$$

Thus

$$c(t)\left(1 + \varepsilon_c(t)\right) = \cos\left(\hat{\gamma}_c(t)\right)\left(c(t)\left(1 + \varepsilon_c(t)\right) + \dot{u}_c(t)\right) + \sin\left(\hat{\gamma}_c(t)\right) V(t) \tag{3.159}$$

Since the cone wave-speed with respect to ground (at the tips on the axis) is

$$\tilde{c} = c(t)\left(1 + \varepsilon_c(t)\right) + \dot{u}_c(t) \tag{3.160}$$

we also have

$$c(t)\left(1 + \varepsilon_c(t)\right) = \cos\left(\hat{\gamma}_c(t)\right)\tilde{c}(t) + \sin\left(\hat{\gamma}_c(t)\right) V(t) \tag{3.161}$$

and

$$\tilde{c}(t) = \cos\left(\hat{\gamma}_c(t)\right)\tilde{c}(t) + \sin\left(\hat{\gamma}_c(t)\right) V(t) + \dot{u}_c(t) \tag{3.162}$$

We can also write directly from Eq. (3.159)

$$c(t)\left(1 + \varepsilon_c(t)\right) = \frac{\cos\left(\hat{\gamma}_c(t)\right)\dot{u}_c(t) + \sin\left(\hat{\gamma}_c(t)\right) V(t)}{1 - \cos\left(\hat{\gamma}_c(t)\right)} \tag{3.163}$$

3.2.10 Fundamental formula for strain at the cone wave-front and other key variables

Similar to the 1D tape behavior, the cone wave speed is

$$c(t) = a_0 \sqrt{\frac{\varepsilon_c(t)}{1 + \varepsilon_c(t)}} \tag{3.164}$$

From Eq. (3.163) and (3.164), we obtain

$$\sqrt{\varepsilon_c(t)(1+\varepsilon_c(t))} = \kappa_c(t) \tag{3.165}$$

where

$$\begin{aligned}\kappa_c(t) &= \frac{1}{a_0}\left(\frac{\cos(\hat{\gamma}_c(t))\,\dot{u}_c(t) + \sin(\hat{\gamma}_c(t))\,V(t)}{1-\cos(\hat{\gamma}_c(t))}\right) \\ &= \frac{\cos(\hat{\gamma}_c(t))\,\dot{u}_c(t)/a_0 + \sin(\hat{\gamma}_c(t))\,V(t)/a_0}{1-\cos(\hat{\gamma}_c(t))}\end{aligned} \tag{3.166}$$

or

$$\varepsilon_c(t)^2 + \varepsilon_c(t) = \kappa_c(t)^2 \tag{3.167}$$

Since this is a quadratic in $\kappa_c(t)$ we can solve it to obtain

$$\varepsilon_c(t) = \frac{-1 + \sqrt{1+4\kappa_c(t)^2}}{2} \tag{3.168}$$

3.2.11 Deceleration of the projectile due to membrane reaction forces

One additional relationship we need is the connection between deceleration of the projectile $dV(t)/dt$ and the average fiber strain $\bar{\varepsilon}_p(t)$ around the projectile. This can also be written in terms of the average fiber strain $\bar{\varepsilon}_p(t)$ at the cone wave front. The mass of the projectile is M_p and the membrane mass under the projectile is

$$m_p = \pi r_p^2 \rho h \tag{3.169}$$

and we define $\Gamma_0 \equiv m_p/M_p$ as the areal density ratio, i.e., the ratio of these two masses so that

$$\Gamma_0 \equiv \frac{\pi r_p^2 \rho h}{M_p} \tag{3.170}$$

Since this analysis applies to $t > 0$, it assumes that the velocity drop from instantaneous momentum exchange at impact has already occurred. That is, if the original projectile velocity just before impact is V_p then the velocity in the instant after impact is

$$V_0 = V_p \frac{M_p}{M_p + m_p} = \frac{V_p}{1 + \Gamma_0} \tag{3.171}$$

We also note that $\bar{\varepsilon}_p(t)$ is an average or effective yarn strain around the projectile and $\bar{\gamma}_p(t)$ is the average cone angle of the yarns passing under the projectile. In addition, $\bar{\gamma}_c(t)$ is an effective angle at which the same yarns enter the cone at the cone wave front (although the angle remains nearly the same for all yarns entering the cone). We also recall the angle $\hat{\gamma}_c(t)$ as defined earlier in connection with the hypotenuse spanning from $r_c(t)$ to r_p, although expressed in ground coordinates. Lastly, we recall that $E = \rho a_0^2$.

We must account for the need to decelerate the membrane mass that is already within the pyramid-like cone. The propagating cone wave causes the velocity of material entering the cone to change from having horizontal velocity $\dot{u}_c$ directed in plane towards the original impact point, to a vertical velocity close to the velocity of the projectile, $V_p(t)$, and in the same direction. We have found

(as will be shown in a later section) that the material velocity in the direction of motion of the projectile is actually distributed approximately as

$$V(\zeta,t) = V_p(t)\left((1-\zeta) + \zeta\frac{\sin(\bar{\gamma}_c(t))}{\sin(\hat{\gamma}_c(t))}\right),\ \zeta = \frac{r-r_p}{r_c-r_p} \tag{3.172}$$

where for transparency we use the notation $V(\zeta,t) = \dot{w}(r,t)$, where w is the out-of-plane displacement. This means that some of the cone material is lagging in out-of-plane velocity and for a rapidly decelerating projectile does not ever reach the same velocity as the projectile, so conversely requires less deceleration. It is also very important to realize that the distribution of the material at a given velocity grows linearly in radius r, away from the projectile. Thus three times as much cone material exists between $r = r_c/2$ to r_c, as between $r = 0$ to $r = r_c/2$. Thus the velocity of the material closer to the cone wave front than to the projectile, is by far the most important to model.

We construct a linear momentum density distribution (incremental mass times velocity) in terms of material corresponding to radius r, and for this purpose we assume

$$\begin{aligned}\mathsf{m}_c(\zeta) &= A_c\left(\frac{r_c}{r_p}\right)V(\zeta,t)\rho h 2\pi\left(r_p + (r_c-r_p)\zeta\right)\\ &= A_c\left(\frac{r_c}{r_p}\right)V(\zeta,t)\rho h 2\pi r_p\left(1+\left(\frac{r_c}{r_p}-1\right)\zeta\right)\end{aligned} \tag{3.173}$$

where $A_c(r_c/r_p)$ is a shape factor to account for the changing shape of the cone 'foot-print' from a circle to a diamond that has rounded corners at $r = r_c$. For this momentum effect to become important, the cone radius must be considerably

larger than the radius of the projectile, and thus, the area is approximately that of a rotated square or diamond with diagonals of length $2r_c$. This area is $2r_c^2$, and is smaller than the area of an equivalent circle, πr_c^2, when the cone first starts to develop. Thus we take the area factor to be the ratio of the two, that is, $A_c(r_c/r_p) = 2/\pi$. Combining Eq. (3.169) and Eq. (3.173), we obtain

$$\begin{aligned}
\mathsf{m}_c(\zeta) &= \frac{m_p V_p(t)}{r_p}\frac{4}{\pi}\left(1+\left(\frac{r_c}{r_p}-1\right)\zeta\right)\frac{V(\zeta,t)}{V_p(t)} \\
&= \frac{m_p V_p(t)}{r_p}\frac{4}{\pi}\left[1+\left(\frac{r_c}{r_p}-1\right)\zeta\right]\left[(1-\zeta)+\zeta\frac{\sin(\bar{\gamma}_c(t))}{\sin(\hat{\gamma}_c(t))}\right] \\
&= \frac{m_p V_p(t)}{r_p}\frac{4}{\pi}\left[1+\left(\frac{r_c}{r_p}-1\right)\zeta\right]\left[1+\left(\frac{\sin(\bar{\gamma}_c(t))}{\sin(\hat{\gamma}_c(t))}-1\right)\zeta\right]
\end{aligned} \tag{3.174}$$

The total momentum is obtained by integrating over r_p to r_c, or

$$\begin{aligned}
\mathsf{M}_c\left(\frac{r_c}{r_p}\right) &= m_p V_p(t) + \int_{r_p}^{r_c} \mathsf{m}_c(\zeta(r)) \\
&= m_p V_p(t)\left[1+\frac{4}{\pi}\left(\frac{r_c}{r_p}-1\right)I\left(\frac{r_c}{r_p}\right)\right]
\end{aligned} \tag{3.175}$$

where

$$I\left(\frac{r_c}{r_p}\right) = \int_0^1 \left[1+\left(\frac{r_c}{r_p}-1\right)\zeta\right]\left[1+\left(\frac{\sin(\bar{\gamma}_c(t))}{\sin(\hat{\gamma}_c(t))}-1\right)\zeta\right]d\zeta \tag{3.176}$$

and includes the momentum of the circular membrane patch under the projectile. In general

$$\begin{aligned}
\int_0^1 (1+P\zeta)(1+Q\zeta)\,d\zeta &= \int_0^1 (1+(P+Q)\zeta+PQ\zeta^2)d\zeta \\
&= 1+\int_0^1 (P+Q)\zeta d\zeta + \int_0^1 PQ\zeta^2 d\zeta \\
&= 1+\frac{P+Q}{2}+\frac{PQ}{3}
\end{aligned} \tag{3.177}$$

Thus we have

$$
\begin{aligned}
I\left(\frac{r_c}{r_p}\right) &= 1 + \frac{1}{2}\left[\left(\frac{r_c}{r_p} - 1\right) + \left(\frac{\sin\left(\bar{\gamma}_c(t)\right)}{\sin\left(\hat{\gamma}_c(t)\right)} - 1\right)\right] + \frac{1}{3}\left(\frac{r_c}{r_p} - 1\right)\left(\frac{\sin\left(\bar{\gamma}_c(t)\right)}{\sin\left(\hat{\gamma}_c(t)\right)} - 1\right) \\
&= \frac{1}{3}\frac{r_c}{r_p}\frac{\sin\left(\bar{\gamma}_c(t)\right)}{\sin\left(\hat{\gamma}_c(t)\right)} + \frac{1}{3} + \frac{1}{6}\frac{r_c}{r_p} + \frac{1}{6}\frac{\sin\left(\bar{\gamma}_c(t)\right)}{\sin\left(\hat{\gamma}_c(t)\right)} \\
&= \frac{1}{3}\left(\frac{r_c}{r_p} + 1\right)\left(\frac{\sin\left(\bar{\gamma}_c(t)\right)}{\sin\left(\hat{\gamma}_c(t)\right)} + 1\right) - \frac{1}{6}\left(\frac{\sin\left(\bar{\gamma}_c(t)\right)}{\sin\left(\hat{\gamma}_c(t)\right)} + \frac{r_c}{r_p}\right)
\end{aligned}
\tag{3.178}
$$

Thus, dropping the dependence on time, t, which is understood, we have

$$
\mathsf{M}_c\left(\frac{r_c}{r_p}\right) = m_p V_p \left\{1 + \frac{4}{\pi}\left(\frac{r_c}{r_p} - 1\right)\left[\frac{1}{3}\left(\frac{r_c}{r_p} + 1\right)\left(\frac{\sin\left(\bar{\gamma}_c(t)\right)}{\sin\left(\hat{\gamma}_c(t)\right)} + 1\right) - \frac{1}{6}\left(\frac{\sin\left(\bar{\gamma}_c(t)\right)}{\sin\left(\hat{\gamma}_c(t)\right)} + \frac{r_c}{r_p}\right)\right]\right\}
\tag{3.179}
$$

Note that for $\sin(\hat{\gamma}_c) = \sin(\bar{\gamma}_c)$ this result reduces as expected to

$$
\begin{aligned}
\mathsf{M}_{c,0}\left(\frac{r_c}{r_p}\right) &= m_p V_p \left[1 + \frac{2}{\pi}\left(\frac{r_c}{r_p} - 1\right)\left(\frac{r_c}{r_p} + 1\right)\right] \\
&= m_p V_p \left\{1 + \frac{2}{\pi}\left[\left(\frac{r_c}{r_p}\right)^2 - 1\right]\right\}
\end{aligned}
\tag{3.180}
$$

The mass of the material involved in the cone wave is thus

$$
m_c(t) = \frac{\mathsf{M}_c\left(\frac{r_c}{r_p}, t\right)}{V_p(t)}
\tag{3.181}
$$

which is

$$
m_c(t) = m_p \left\{1 + \frac{4}{\pi}\left(\frac{r_c}{r_p} - 1\right)\left[\frac{1}{3}\left(\frac{r_c}{r_p} + 1\right)\left(\frac{\sin\left(\bar{\gamma}_c(t)\right)}{\sin\left(\hat{\gamma}_c(t)\right)} + 1\right) - \frac{1}{6}\left(\frac{\sin\left(\bar{\gamma}_c(t)\right)}{\sin\left(\hat{\gamma}_c(t)\right)} + \frac{r_c}{r_p}\right)\right]\right\}
\tag{3.182}
$$

Recalling Eq. (3.36), Eq. (3.37), Eq. (3.44) and Eq. (3.45), the out-of-plane reaction force acting around the base of the pyramid, which decelerates the projectile of mass, M_p, as well as the target material mass, $m_c(t)$, inside the cone can be written as

$$F_c(t) = 8\varepsilon_c(t) r_p \vartheta\left(r_c(t)\right) \sin\left(\bar{\gamma}_c(t)\right) \tag{3.183}$$

where

$$\vartheta(r_c) = \begin{cases} 1 - \dfrac{1}{6}\left(\dfrac{r_p}{r_c}\right)^2 + \left(\dfrac{\pi}{4} - \dfrac{5}{6}\right)\left(\dfrac{r_p}{r_c}\right)^{14} + \dfrac{1}{3}\left(1 - \dfrac{1}{2}\left(\dfrac{r_p}{r_c}\right)^2\right)\left(\dfrac{r_c}{r_p} - 1\right), \\ \qquad r_p < r_c < 2r_p \\ \dfrac{23}{24} + \dfrac{7}{16}\left[\left(\dfrac{r_c}{r_p} - 1\right) - \dfrac{1}{3\left(\dfrac{r_c}{r_p} - 1\right)}\right], \qquad r_c > 2r_p \end{cases} \tag{3.184}$$

The factor 8 arises because the quantity $r_p \vartheta\left(r_c(t)\right)$ involved integration over yarns within the width $0 < r < r_c(t)$, and for each set of yarns, in the x-direction and y-direction, there are four such regions all contributing to the projectile deceleration, giving a total of 8. Balancing these forces we have

$$\left(M_p + m_c(t)\right) \frac{dV(t)}{dt} = -8 r_p E h \varepsilon_c(t) \vartheta(r_c(t)) \sin(\bar{\gamma}_c(t)) \tag{3.185}$$

In view of the above equation we let

$$\Theta_p = \frac{8 r_p^2 \rho h}{M_p + m_p} = \left(\frac{8}{\pi}\right) \frac{\Gamma_0}{1 + \Gamma_0} \tag{3.186}$$

and let

$$\bar{\omega}_c(t) = \frac{M_p + m_p}{M_p + m_c(t)} = \frac{1 + \Gamma_0}{1 + \left(m_c(t)/m_p\right)\Gamma_0} \tag{3.187}$$

and thus we can write this equation as

$$\frac{dV(t)}{dt} = -\Theta_p \bar{\omega}_c(t) \frac{a_0^2}{r_p} \varepsilon_c(t) \sin(\bar{\gamma}_c(t)) \vartheta(r_c(t)) \tag{3.188}$$

Note that the deceleration force on the projectile itself is

$$F_p(t) = M_p \frac{dV(t)}{dt} \tag{3.189}$$

Since the initial condition is $V(0) = V_0$, we can integrate either of the above equations to obtain

$$V(t) = V_0 - \Theta_p \frac{a_0^2}{r_p} \int_0^t \bar{\omega}_c(s)\varepsilon_c(s)\sin(\bar{\gamma}_c(s))\vartheta(r_c(s))ds \tag{3.190}$$

3.2.12 Average and peak strains around the projectile edge and at the cone wave-front nose

Fig. 3.4 shows curves of the peak strain, $\varepsilon_{p,\max}$, around the projectile edge and the strain, ε_p, at the intersection of the x-axis and the projectile edge, with respect to dimensionless time, τ, and for different projectile masses, M_p. Around dimensionless time $\tau = 17$, the ratios $\varepsilon_{p,\max}/\varepsilon_p$ in the three cases are 1.325, 1.326 and 1.326 respectively. Actually, at any specified time the strain ratio, $\varepsilon_{p,\max}/\varepsilon_p$, appears to be independent of M_p, and thus of the deceleration of the projectile. Upon obtaining ε_p, based on the procedures discussed above (that is, the strain along the axis at the intersection with the projectile edge), it is therefore feasible to calculate the peak strain around the edge, $\varepsilon_{p,\max}$, due to the strain concentration, as long as the ratio, $\varepsilon_{p,\max}/\varepsilon_p$, at different times is known or can be modeled.

Fig. 3.5 shows a 2D overview of the strain distribution in the $x - y$ plane when $\tau = 5$ and using 150 grids per projectile radius r_p. (Note that the yarns are aligned along the vertical axis, labeled x.) The peak strain appears on the

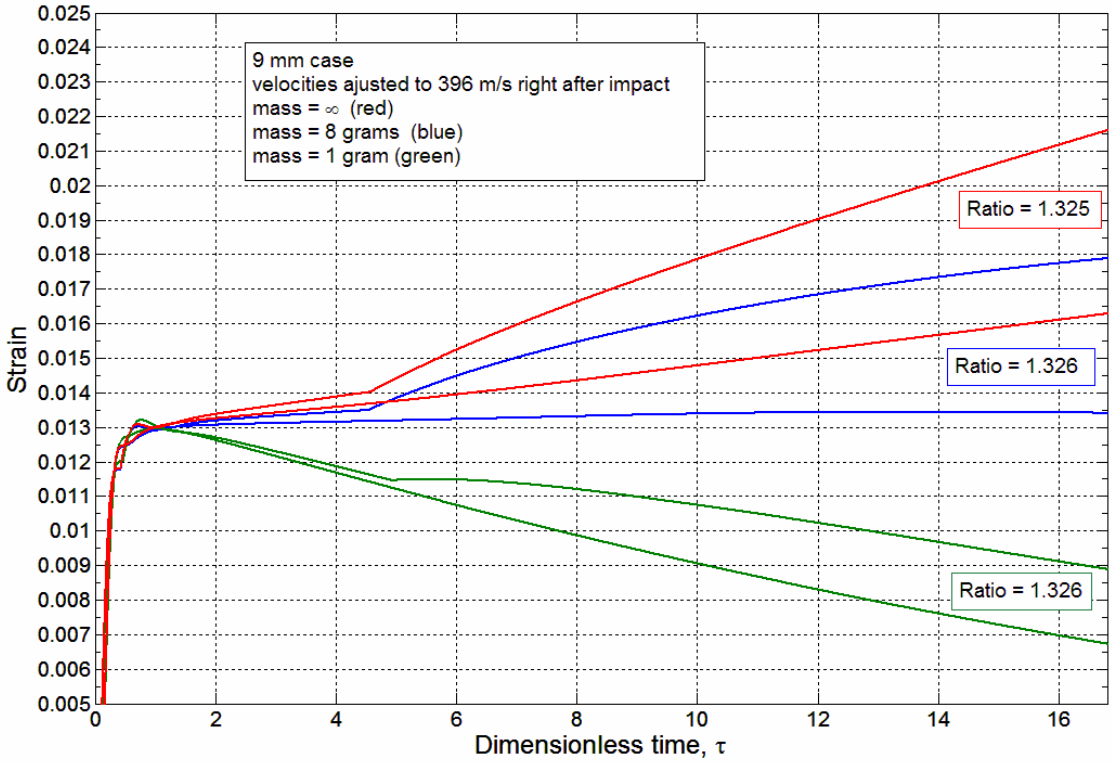

Figure 3.4: Comparison of peak strain $\varepsilon_{p,max}$ and strain at the centerline of x-axis ε_p with projectile mass $M_p = \infty$(red), 8.0gram(blue) and 1.1gram(green)

projectile edge at a position of about $0.9r_p$ in the y-direction. To explain why we note that based on previous simulation results, the rounded tip of the front of the tensile wave has a similar profile to the projectile shape and the yarns start to stretch from that position. At the other end, the yarns stop stretching at the projectile edge, since all the yarn portions under the projectile itself are assumed to be non-deformed (in the case of no slip). Therefore the total integrated stretching from the rounded tip of the tensile wave front to the projectile edge along the yarns in the x-direction should be about the same for all yarns passing under the the projectile. However, this stretching involves two contributions: (1) in-flow of yarns along the x-direction into the cone, and (2) the local yarn strain within the cone.

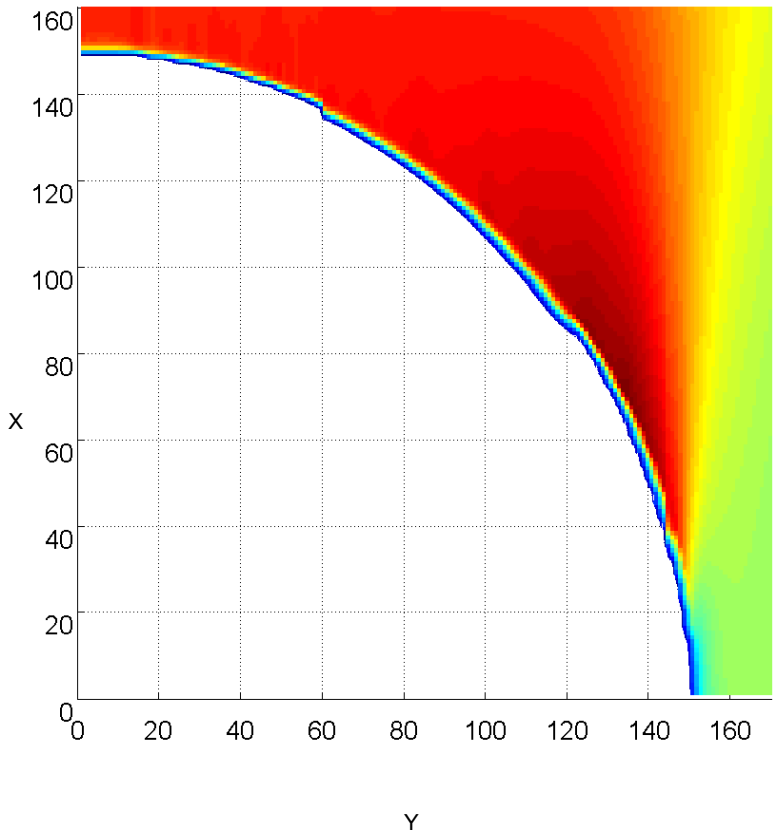

Figure 3.5: 2D strain overview in $x - y$ plane (150 grid points per unit distance, r_p) at $\tau = 5$, as obtained from the Cornell modified DSM code.

Previous simulation results have shown that the highest inflow velocity and inflow displacement occur in the yarn lying right along the x-axis, but for parallel yarns laterally further way from the x-axis but still within distance r_p, and especially in the region closer to the tensile wave-front, the strains are lower (reminiscent of the parabolic roll-off early in the development and propagation of the tension wave) and the inflow is somewhat diminished. Hence in order to recover the same total stretching for these more distant yarns, the local strain approaching the projectile edge has to be increased enough to compensate for the slight insufficiency of the inflow displacement.

In the case of no yarn slip under the projectile, and at locations around the

projectile approaching the y-axis, the yarns approach the projectile increasingly tangentially (the angle between the yarn and the tangent to the projectile edge where it intersects, becomes smaller and smaller). Thus for these yarns the rigid projectile increasingly has a constraining effect (manifest through increasing shear displacements and imposed shear loads from crossing yarns) that prevents the last few yarns at lateral distance beyond about $0.9r_p$ from fully stretching. Thus the strain in these yarns begins to decay coming into the projectile edge rather than to reach a peak, and hence, the strain concentration peaks at about $0.9r_p$.

In the case of near frictionless yarn slip under the projectile, the situation is somewhat different. For parallel yarns closer to the x-axis, there will be some strain relief due to the additional length from stretching the yarns under the projectile. However this extra length disappears for the most distant yarns of the group intersecting the projectile closest to where it intersects the y-axis. Also, yarn slip under the projectile means that the rigid boundary of the projectile has no constraining effect on the strain development there. Thus, in the case of slip, the peak yarn strain occurs in the yarn right where the projectile ege intersects the y-axis.

Fig. 3.6 shows the behavior for the no slip case at a much longer time ($\tau = 35$) and with a coarser mesh (38 grid points per projectile radius, r_p). As time goes on, and consistent with our previous analysis, the peak strain position does not "converge" to y-axis but stays at about the same position at $y = 0.9r_p$ as seen in Fig. 3.5. The only difference is the strain distribution is less uniform due to having a coarser mesh and the contour eventually is almost perpendicular to y-axis.

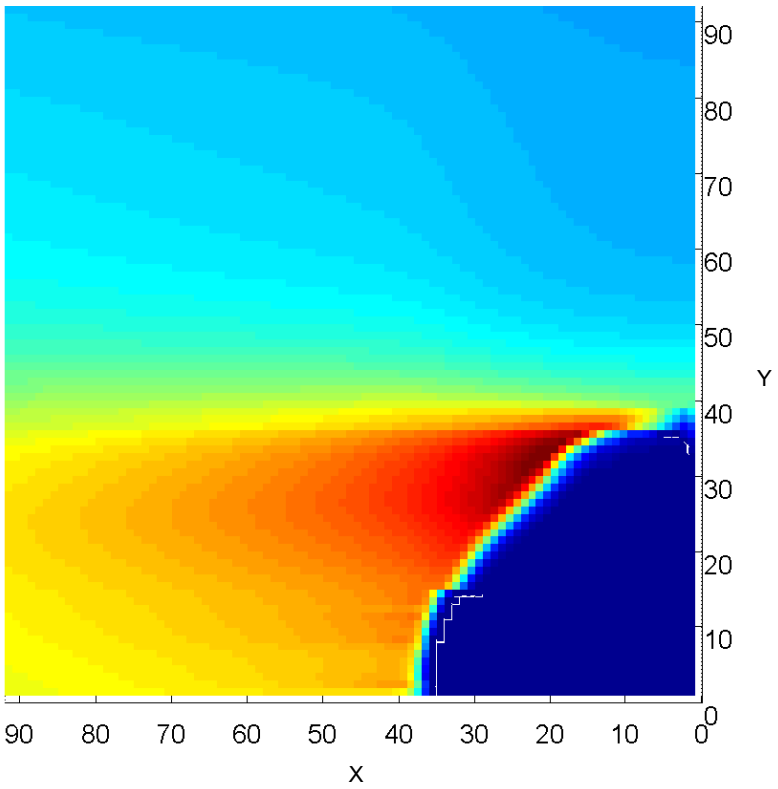

Figure 3.6: 2D strain overview in the $x-y$ plane (38 grid points per distance r_p), where $\tau = 35$, as obtained from the Cornell-modified DSM code.

Fig. 3.7 shows the same behavior in 3D indicating the strain magnitude in color intensity ranging from from blue(low) to red (high). The strain is higher around the projectile edge compared with that at cone wave front and tensile wave front. The strains in yarns where they intersect the projectile edge are always higher than at other locations. This is consistent with the previous analysis.

Based on all the results obtained from the Cornell-modified DSM code and all the analysis above, we propose the following form for the strain distribution around projectile edge, given by

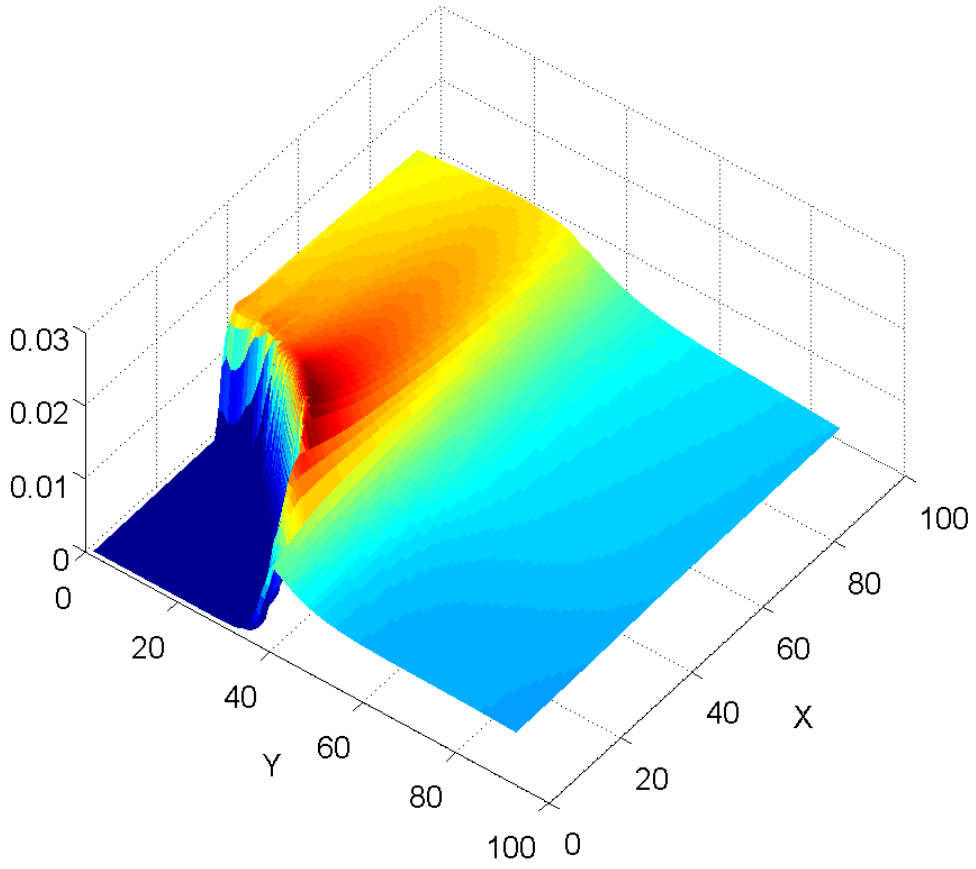

Figure 3.7: 3D strain distribution (38 grid points per r_p) for $\tau = 35$, as obtained from the Cornell-modified DSM code.

$$\varepsilon_p(Y, R_c) = \varepsilon_p(0, R_c)\left[1 + Y^2 g(R_c) - \min\left(1 - \sqrt{1 - Y^2}, f(R_c)Y^2\right)\right], \quad 0 \leq Y < 1 \tag{3.191}$$

where $\varepsilon_p(Y, R_c)$ is the strain in the yarn at lateral position $Y = y/r_p$ where it passes under the projectile edge and $R_c = r_c/r_p$. This form gives us the circular shape we observe shortly after impact and beyond, which then rapidly transitions to becomes parabolic. This transition is governed by the function $f(R_c)$ over the early portion of Regime 1 ($0 < \tau < 2$), and this function is taken as.

$$f(R_c) = \left(\frac{1}{R_c}\right)^6 \tag{3.192}$$

Counteracting the roll-off is the strain buildup, which we represent using

$$g(R_c) = \frac{1 + \kappa_{\max}(R_c - 1)}{1 + \kappa_0(R_c - 1)} - 1 \tag{3.193}$$

where κ_{max} is an amplification factor applying to $Y = 1$ (the lateral edge of the projectile) and where κ_0 is an amplification factor applying to the x-axis yarns, i.e., at $Y = 0$. For instance, for the 9 mm projectile traveling at 406m/s we calculate $\kappa_{max} = 0.410$ and $\kappa_0 = 0.147$. These values were calculated through study of strain evolution profiles under constant projectile velocity over time, V_{const}, (i.e. infinite projectile mass) where the strain at the cone wave front grows only very slowly (equivalent to about $\kappa_0/3$). The advantage of choosing V_{const} is that the strains grow virtually linearly from the same initial strain point, once the transition region up to $R_c = 1$ has passed, as suggested in Fig. 3.4.

It can be seen that as soon as $R_c = \sqrt[6]{2}$, the influence of the circular profile ceases since the parabola envelopes it. Thus we can see that

$$\varepsilon_p(Y, R_c) = \varepsilon_p(0, R_c)\left[1 + Y^2 H(R_c)\right],\ 0 \le Y < 1 \tag{3.194}$$

where

$$H(R_c) = \frac{1 + \kappa_{\max}(R_c - 1)}{1 + \kappa_0(R_c - 1)} - 1 - \left(\frac{1}{R_c}\right)^6 \tag{3.195}$$

Note that the strain profile is essentially flat for $R_c = \bar{R}_c$ satisfying $H(\bar{R}_c) = 0$. This happens at about $\bar{R}_c \approx 1.45$.

The average strain over $0 \leq Y < 1$ is obtained by integrating the parabolic form over Y and this yields

$$\varepsilon_{p,\text{avg}}(R_c) = \varepsilon_p(0, R_c)\left[1 + \frac{H(R_c)}{3}\right] \tag{3.196}$$

However, for very small $0 < R_c - 1 \ll 1$ this turns out not to reflect well the observed fact that, immediately after impact, the strain profile is actually circular, so we make an adjustment using the transitional form

$$\varepsilon_{p,\text{avg}}(R_c) = \varepsilon_p(0, R_c)\left[1 + \frac{H(R_c)}{3} + \left(\frac{\pi}{4} - \frac{1}{3}\right)\left(\frac{1}{R_c}\right)^6\right] \tag{3.197}$$

3.2.13 Out-of-plane velocity profile in the cone wave

The out-of-plane velocity profile is now modeled as follows. We have the out of plane displacement, $w(r, t)$, given by

$$w(r, t) = \int_r^{r_c(t)} \sin\left(\bar{\gamma}\left(r, t\right)\right) dr \tag{3.198}$$

and taking derivatives with respect to time gives

$$\begin{aligned}
\dot{w}(r,t) &= \frac{\partial}{\partial t}\int_r^{r_c(t)} \sin\left(\bar{\gamma}\left(\eta,t\right)\right) d\eta \\
&= \sin\left(\bar{\gamma}\left(r,t\right)\right)\frac{dr_c(t)}{dt} + \int_r^{r_c(t)} \frac{\partial}{\partial t}\sin\left(\bar{\gamma}\left(\eta,t\right)\right) d\eta \\
&= \sin\left(\bar{\gamma}\left(r,t\right)\right)c(t) + \int_r^{r_c(t)} \cos\left(\bar{\gamma}\left(\eta,t\right)\right)\frac{\partial}{\partial t}\bar{\gamma}\left(\eta,t\right) d\eta \\
&= \sin\left(\bar{\gamma}\left(r,t\right)\right)c(t) + \int_r^{r_c(t)} \sqrt{1-\sin^2\left(\bar{\gamma}\left(\eta,t\right)\right)}\dot{\bar{\gamma}}\left(\eta,t\right) d\eta
\end{aligned} \tag{3.199}$$

We know that $\sqrt{1-\sin^2\left(\bar{\gamma}\left(\eta,t\right)\right)} \simeq 1$ and $\dot{\bar{\gamma}}\left(\eta,t\right)$ changes relatively slowly with time. However we also have the boundary condition that $\dot{w}(r_p,t) = V(t)$ and we know

$$\sin\left(\bar{\gamma}\left(r_p,t\right)\right) > \sin\left(\hat{\gamma}_c(t)\right) = \frac{r_c(t)-r_p}{\delta(t)} \tag{3.200}$$

and

$$\sin\left(\bar{\gamma}\left(r_c,t\right)\right) < \sin\left(\hat{\gamma}_c(t)\right) = \frac{r_c(t)-r_p}{\delta(t)} \tag{3.201}$$

This means that, in general, one must be careful about neglecting the second term. However as $r \to r_c(t)$, the second term vanishes and since $\bar{\gamma}\left(r_c(t),t\right) = \bar{\gamma}_c(t)$, we have

$$\dot{w}\left(r_c(t),t\right) = \sin\left(\bar{\gamma}_c(t)\right)c(t) \tag{3.202}$$

Making the approximation $c(t) = V(t)/\sin\left(\hat{\gamma}_c(t)\right)$ and restating the boundary condition at $r = r_p$ we obtain the key results

$$\dot{w}\left(r_c(t),t\right) = V(t)\frac{\sin\left(\bar{\gamma}_c(t)\right)}{\sin\left(\hat{\gamma}_c(t)\right)} \tag{3.203}$$

and

$$\dot{w}(r_p, t) = V(t) \tag{3.204}$$

For purposes of estimating the out of plane velocity distribution in r over $r_p \leq r \leq r_c$, study of numerical simulations using the DSM code strongly suggests that its behavior is very close to linear over this region. Thus we can write

$$\dot{w}(r, t) = V(t)\left((1 - \zeta) + \zeta \frac{\sin(\bar{\gamma}_c(t))}{\sin(\hat{\gamma}_c(t))}\right) \tag{3.205}$$

where again

$$\zeta = \frac{r - r_p}{r_c - r_p} \tag{3.206}$$

This also explains how Eq. (3.172) was derived.

3.2.14 Explicit formulas for initial strains, velocities and angles upon the impact of projectile

For initial values at time, $t = 0$, from 1D analysis we have the initial velocity, V_0 (after instantaneous momentum exchange as described below), and the initial strain at the projectile edge, $\varepsilon_{p,0} = \varepsilon_p(0)$, which satisfies

$$\varepsilon_{p,0} = \left(\frac{1}{4\left(1 + \varepsilon_{p,0}\right)}\right)^{1/3} \left(\left(\frac{V_0}{a_0}\right)^2 + \varepsilon_{p,0}^2\right)^{2/3} \tag{3.207}$$

A first approximation is

$$\varepsilon_{p,0}^{(1)} = \left(\frac{V_0}{2^{1/2} a_0}\right)^{4/3} \tag{3.208}$$

and by substitution of this result into the previous equation, we obtain a second approximation as

$$\varepsilon_{p,0}^{(2)} = \left(\frac{1}{4\left(1+\varepsilon_{p,0}^{(1)}\right)}\right)^{1/3}\left(\left(\frac{V_0}{a_0}\right)^2+\left(\varepsilon_{p,0}^{(1)}\right)^2\right)^{2/3} \tag{3.209}$$

One more iterative substitution yields a third refinement and the approximation that we use, which is

$$\varepsilon_{p,0} \approx \varepsilon_{p,0}^{(3)} = \left(\frac{1}{4\left(1+\varepsilon_{p,0}^{(2)}\right)}\right)^{1/3}\left(\left(\frac{V_0}{a_0}\right)^2+\left(\varepsilon_{p,0}^{(2)}\right)^2\right)^{2/3} \tag{3.210}$$

Note that the initial strain at the cone wave-front is

$$\varepsilon_c(0) = \varepsilon_{p,0} \tag{3.211}$$

Other initial conditions arising from this approach are

$$V(0) = V_0, \quad \delta(0) = 0, \quad \dot{u}_c(0) = -a_0\varepsilon_{p,0}, \quad u_c(0) = 0 \tag{3.212}$$

Also

$$\sin(\bar{\gamma}_c(0)) = \sin(\hat{\gamma}_c(0)) = \frac{V_0}{\sqrt{\tilde{c}_0^2+V_0^2}} \tag{3.213}$$

$$\cos(\bar{\gamma}_c(0)) = \cos(\hat{\gamma}_c(0)) = \frac{\tilde{c}_0}{\sqrt{\tilde{c}_0^2+V_0^2}} \tag{3.214}$$

where

$$\tilde{c}_0 = a_0\left(\sqrt{\varepsilon_{p,0}(1+\varepsilon_{p,0})}-\varepsilon_{p,0}\right) \tag{3.215}$$

In Appendix B the above expressions are cast in terms of a convenient set of dimensionless parameters.

3.3 Multi-layer model for biaxial materials

The assumptions that must be made in the case of the multi-layer model are very similar to those introduced in the multi-layer model for isotropic materials as described in Chapter 2. Thus we will skip several of the steps (though these can be referred to there) and move forward to the momentum function for multiple layers, which can be written as

$$(M_p + \sum_{i=n_1}^{n_2} m_{c,i}(t))\frac{dV(t)}{dt} = -8r_pEh\sum_{i=n_1}^{n_2}\varepsilon_{c,i}\vartheta\left(r_{c,i}(t)\right)\sin(\bar{\gamma}_{c,i}(t)) \tag{3.216}$$

where i denotes the *ith* activated layer, and $m_{c,i}$ is the mass of fabric in the cone of layer i. We assume V_{0,n_2} is the projectile velocity right before it strikes a new layer (i.e., layer $n_2 + 1$) and V_{0,n_2+1} is the velocity right after that, in which case $r_{p,n_2+1} = r_{c,n_2+1}$ and $m_{p,n_2+1} = m_{c,n_2+1}$ right at that instant in time. (Note that before impacting the first layer $n_1 = n_2 = 0$ and $V_{0,0} = V_p$.) Then conservation of momentum gives

$$(M_p + \sum_{i=n_1}^{n_2} m_{p,i})V_{0,n_2} = (M_p + \sum_{i=n_1}^{n_2+1} m_{p,i})V_{0,n_2+1} \tag{3.217}$$

and thus

$$V_{0,n_2+1} = \frac{(M_p + \sum_{i=n_1}^{n_2} m_{p,i})V_{0,n_2}}{M_p + \sum_{i=n_1}^{n_2+1} m_{p,i}} \tag{3.218}$$

We define a set of dimensionless parameters as

$$\Gamma_{0,i} = \frac{m_{p,i}}{M_p} = \frac{\Gamma_0}{n} \tag{3.219}$$

$$\Gamma_{c,i}(\tau) = \frac{m_{c,i}(\tau t_p)}{M_p} \tag{3.220}$$

$$\Upsilon_c(\tau) = \frac{1 + (n_2 - n_1)\,\Gamma_0/n}{1 + \sum_{i=n_1}^{n_2} \Gamma_{c,i}(\tau)} \tag{3.221}$$

and

$$\Theta_p = \frac{8 r_p E h}{M_p + \sum_{i=n_1}^{n_2} \pi r_p^2 \rho h} \frac{r_p}{a_0^2} = \left(\frac{8}{\pi}\right) \frac{\Gamma_0/n}{1 + (n_2 - n_1)\,\Gamma_0/n} \tag{3.222}$$

Then Eq. (3.216) becomes

$$\Psi(\tau) = \Psi_0 - \Theta_p \int_0^\tau \Upsilon_c(\zeta) \sum_{i=n_1}^{n_2} \Xi_{c,i}(\zeta) \sin \Gamma_{c,i}(\zeta) d\zeta \tag{3.223}$$

where $\Psi(\tau) = V(\tau t_p)/a_0$, $\Xi_{c,i}(\tau) = \varepsilon_{c,i}(\tau t_p)$ and $\Gamma_{c,i}(\tau) = \gamma_{c,i}(\tau t_p)$. (For reference, Appendix B describes the full set of dimensionless parameters.)

As stated above, only in the deceleration equation do all the activated layers act altogether as they share a common projectile velocity. Otherwise, each layer is deemed independent in the calculation. Once the common parameter, the projectile velocity, $V(t)$, has been solved for in each time step, each activated layer can be treated independently insofar as the reaction it imposes on the projectile and cones of activated material around it, and thus solving for all other parameters will be based on the single-ply model applied to each layer. With our assumptions above, there is no friction between adjacent layers, so the cone wave movement in each layer follows the single-ply rule,and the deceleration is caused by the sum of forces from all the activated layers at any given time.

3.4 Results and discussions

3.4.1 Verification and comparisons

We now present a case study where we compare results from the Cornell semi-analytical model of this thesis with those from numerical simulations using the Cornell-modified version of the DSM code. While the main focus is on the results of the semi-analytical model it is important to first point out the improvements made in the Cornell-modified version of the DSM code in order to control some numerical artifacts that became increasingly conspicuous once comparisons were made. Specifically modifications were made to introduce limited out-of-plane, angle or bending damping at mass nodes (to suppress transverse standing waves and resonances), smoothing of strain disturbances around the projectile edge particularly at protruding square corners (where if un-smoothed, the magnitudes of disturbances appear fixed and only the length-scale of the disturbance decays with refining of the mesh), and finally controllable viscous sliding of yarns under the projectile. These adjustments led to a much more informed interpretation of the results.

Simulation conditions have been listed in Fig. 3.8, which shows strain results from the current analytical model versus dimensionless time for the average strain $\varepsilon_{p,avg}$ around the projectile edge, the peak strain $\varepsilon_{p,max}$ around the projectile edge, and the strain ε_p at the intersection of the x-axis (centerline) and the projectile edge. In the revised DSM code three levels of mesh refinement were used, namely $n_p = 100$, 80 and 33 grid points per projectile radius r_p. Note that $\tau = t/t_p$ where $t_p = r_p/a_0$, that is, $\tau = 1$ corresponds to the time it takes for the tension wave to travel one projectile radius, r_p, whereas recall that one unit of

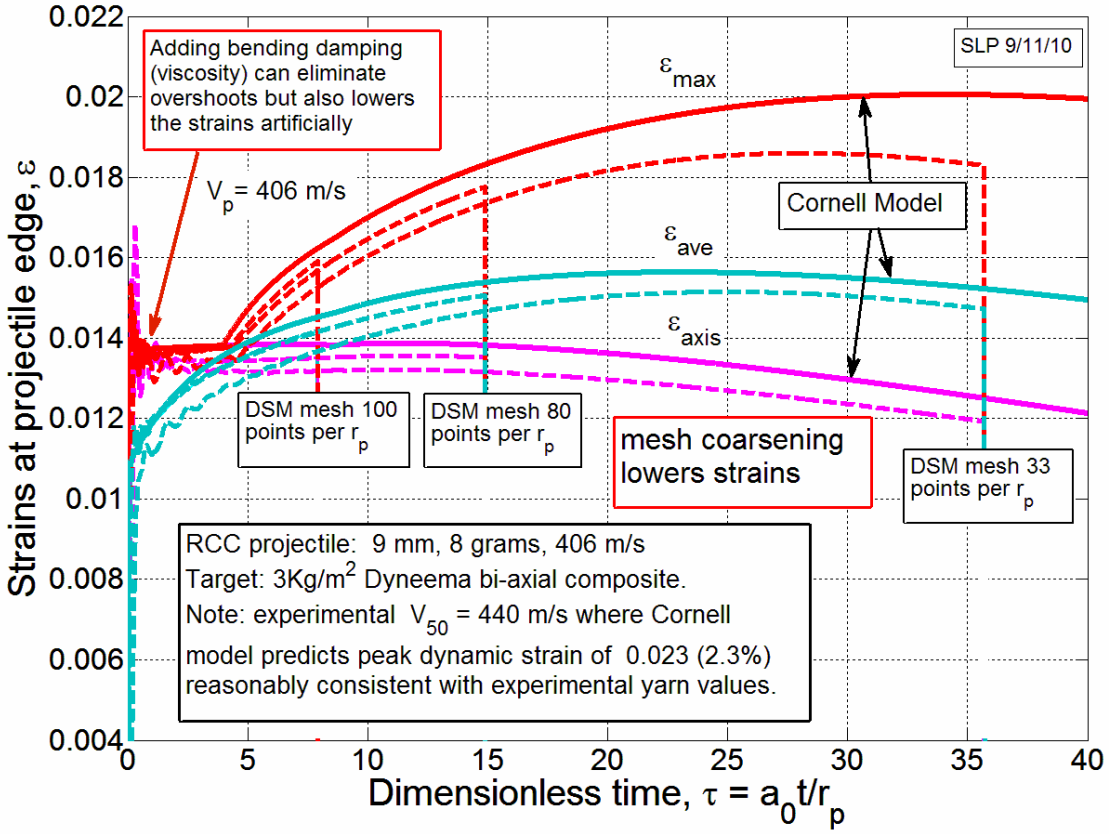

Figure 3.8: Comparison of semi-analytical model of the thesis with Cornell-modified DSM code results in terms of $\varepsilon_{p,Avg}$, $\varepsilon_{p,max}$ and ε_p, with three mesh sets in the DSM code: 100, 80 and 33 grid points per projectile radius r_p.

dimensionless time, $\tau \approx 7$ corresponds to an advance of the cone wave front along the x-axis by about distance r_p.

In Fig. 3.8, the solid lines are from Cornell model while the dashed lines are from the modified DSM code. In the Cornell-modified DSM code, we found that increasing the bending damping viscosity to eliminate overshoot in the initial buildup of tensile strain for $0 < \tau << 1$, tended to artificially lower the strain, ε_p, along the x-axis center-line, especially during the initial period right after projectile impact. On the other hand less damping resulted in more initial oscillation over $0 < \tau < 3$ depending on the level of mesh refinement before the

strains settled down.

Note that increasing the fineness of the mesh leads to results closer to the ones given by Cornell model (which are certainly the correct values in the very early regime), but unfortunately, with an enormous cost in computational time. This is why results are shown only over a very limited time-span. In the Cornell model, ε_p reaches its peak at $\tau \approx 10$, while it takes a considerably longer time ($\tau \approx 33$) for the peak strain $\varepsilon_{p,\max}$ to go to its maximum. When the initial projectile velocity $V_p = 440$ m/s (before it strikes the layer), the Cornell semi-analytical model predicts a peak strain of 0.023, which as it turns out is reasonably consistent with experimental results.

More simulations and results (not shown here) of the DSM code suggest that a mesh of at least $n_p = 400$, and possibly larger, is needed to truly test the full accuracy of the Cornell analytical model, but unfortunately even getting to $\tau = 2$ takes 12 hours and occupies too much memory on a small workstation, and $\tau = 30$ requires a far more efficient machine or refinement of the calculation algorithm.

Fig. 3.9 shows the velocity decay associated with Fig. 3.8. There is strain oscillation and delay when building up strain in DSM code results and this causes a small time lag in velocity decay, which is barely noticeable. The velocity decay in the DSM code is very slightly slower than for Cornell semi-analytical model, but they coincide again after $\tau \approx 30$. A finer mesh does lead to slightly better agreement with Cornell model, though the agreement is already excellent. The error is less than 1% in velocity decay even for 33 grid points per projectile radius r_p.

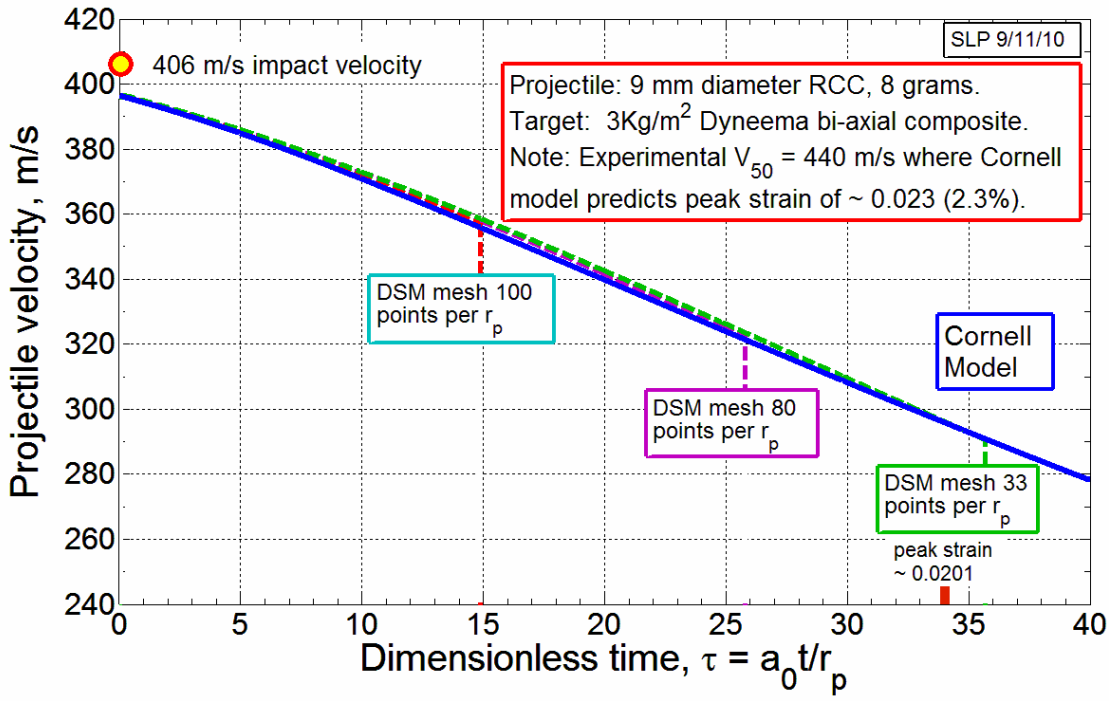

Figure 3.9: Evolution of velocity decay versus dimensionless time for the 9mm projectile comparing results from the Cornell semi-analytical model versus numerical simulations using the Cornell-modified DSM code with two levels of square mesh refinement.

3.4.2 Key parameters

Table 3.1 lists the simulation conditions for the single-layer cases. The material used is Dyneema SK76, and two types of projectiles are simulated: 9 mm and FSP, whose main differences are the radius, mass and initial velocity. The FSP has a higher initial velocity (568 m/s) than the 9 mm projectile (406 m/s).

Table 3.1: A list of key parameters implemented in the Kevlar and Dyneema cases (Dyneema SK76 is assumed in all the following simulations)

Projectile type	9 mm	FSP
Projectile mass M_p(g)	8.0	1.1
Projectile radius r(mm)	4.5	2.73
Initial projectile velocity (m/s)	406	568
Dyneema density ρ(kg/m^3)	0.98	
Areal density a_d(kg/m^2)	3×10^{-3}	4.89×10^{-3}
Single-ply thickness δ_h(mm)	3.06	4.99
Vertical displacement allowance (mm)	8.0, 12.0	8.0
Young's modulus E(GPa)	101.26	
Layer gap (mm) (multi-layer)	0.444, 0.667(10 layers), 2, 3 (3 layers)	
Strain failure criterion ε_{max}	0.02	

3.4.3 Single-layer results: analysis and verification

Results from impact of a 9 mm projectile

Next we study results of the Cornell semi-analytical model presented in this thesis, beginning with the case of impact by a 9 mm projectile. The initial projectile velocity is $V_0 = 406$ m/s. Fig. 3.10 shows the strain ε_r along x-axis at $\tau = 10, 20, 30$ and 40 respectively. Note that X is distance from the projectile axis to the cone wave-front, measured in number of projectile radii. ε_r curves decrease as the distance to the projectile increases at different times. From $X = 1$ to $X = 2$ (from the projectile edge to twice the projectile radius from the center), ε_r decreased by 5.1%, 7.0%, 7.8% and 9.1% respectively. At a longer time, ($\tau = 40$),

the strain close to the cone wave front gradually levels off, showing the strain gradient converges to zero as time goes on.

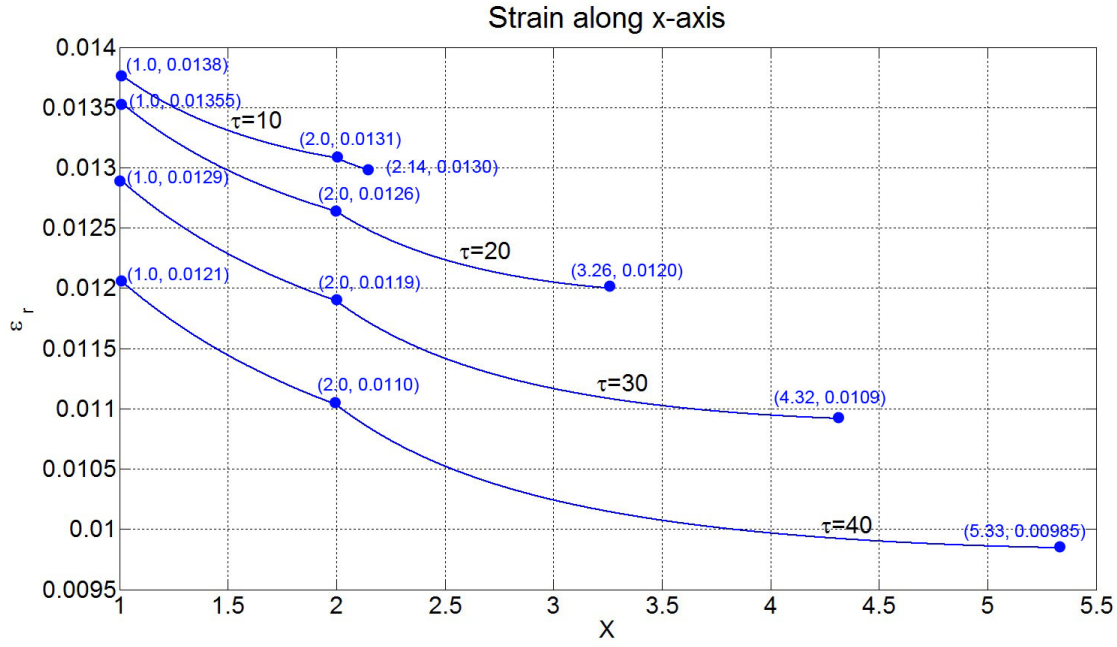

Figure 3.10: Strain along the centerline of the x-axis at $\tau = 10,\ 20,\ 30,\ 40$ respectively (9 mm).

Note that ε_r follows Eq. (3.81), in which both $A(r_c)$ and $\Theta(r)$ follow different functions transiting at $r = 2r_p$. This explains why the curve in Fig. 3.10 is continuous but not differentiable. At $\tau = 40$, the strain decreases to 0.011, or $91\%\varepsilon_p$ at $X = 2$, and decreases further to 0.00985, or $18.6\%\varepsilon_p$ when the cone wave-front arrives at $5.4r_p$.

Fig. 3.11 shows the strain distribution along projectile edge from $\tau = 0$ to $\tau = 40$. At $\tau = 0$, the peak strain around the projectile is located at $Y = 0$. The strain at $Y = 1$ is only about 36% of the peak strain. When $\tau = 5$, the strain curve becomes almost flat, showing a uniform strain distribution along the projectile edge. $\varepsilon_{p,\max}$, $\varepsilon_{p,\text{ave}}$ and ε_p are almost the same at this time. When times goes further to $\tau = 10$, the strain at $Y = 1$ becomes dominant, and its advance keeps

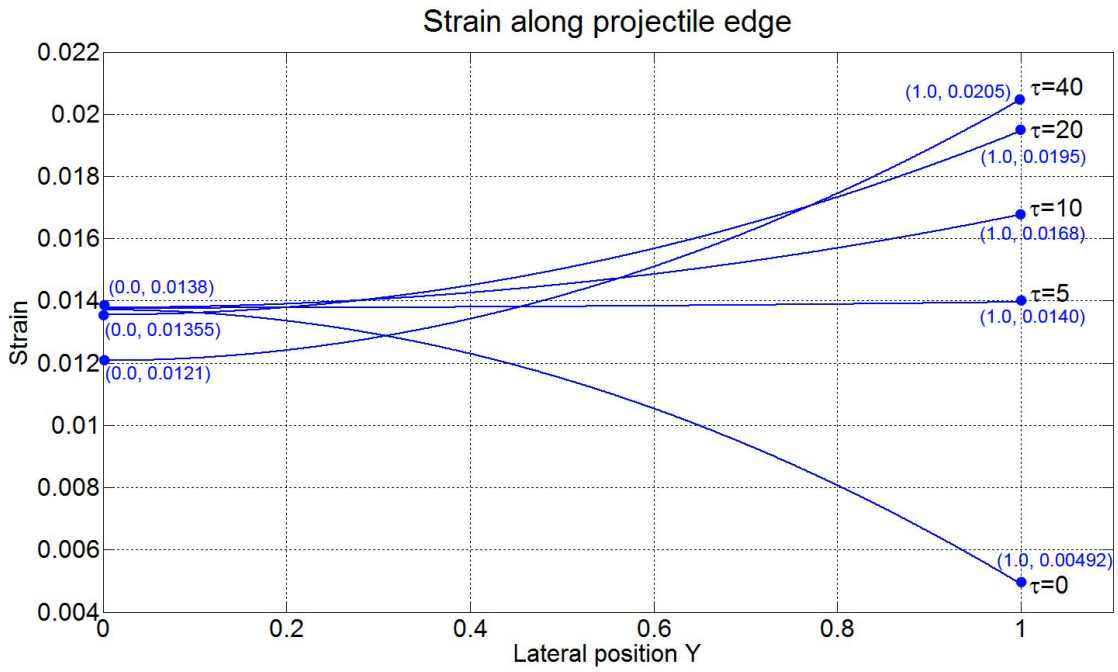

Figure 3.11: Strain distribution along projectile edge at $\tau = 0,\ 5,\ 10,\ 20,\ 40$ respectively (9 mm).

increasing, so we can see a similar pattern when $\tau = 20$. Up to this point, the strain, ε_p, at $Y = 0$ didn't change much, since the initial strike of the projectile. However, when $\tau = 40$, ε_p becomes lower (about 88% of its initial value), while $\varepsilon_{p,\max}$ at $Y = 1$ becomes higher. We can expect that this trend will continue as the cone wave radius increases. As discussed in previous sections, within slip boundary, the peak strain $\varepsilon_{p,\max}$ will occur on the y-axis at the projectile edge. At $\tau = 40$, $\varepsilon_{p,\max} \simeq 1.7\varepsilon_p$, which is consistent with the result obtained from the DSM code.

Fig. 3.12 shows five strain curves at the cone wave front and projectile edge, namely, the strain ε_p at the centerline of the x-axis, the average strain $\varepsilon_{p,\text{avg}}$ and peak strain $\varepsilon_{p,\max}$ around the projectile edge, the strain ε_c at the centerline and the average strain $\varepsilon_{c,\text{avg}}$ at cone wave front.

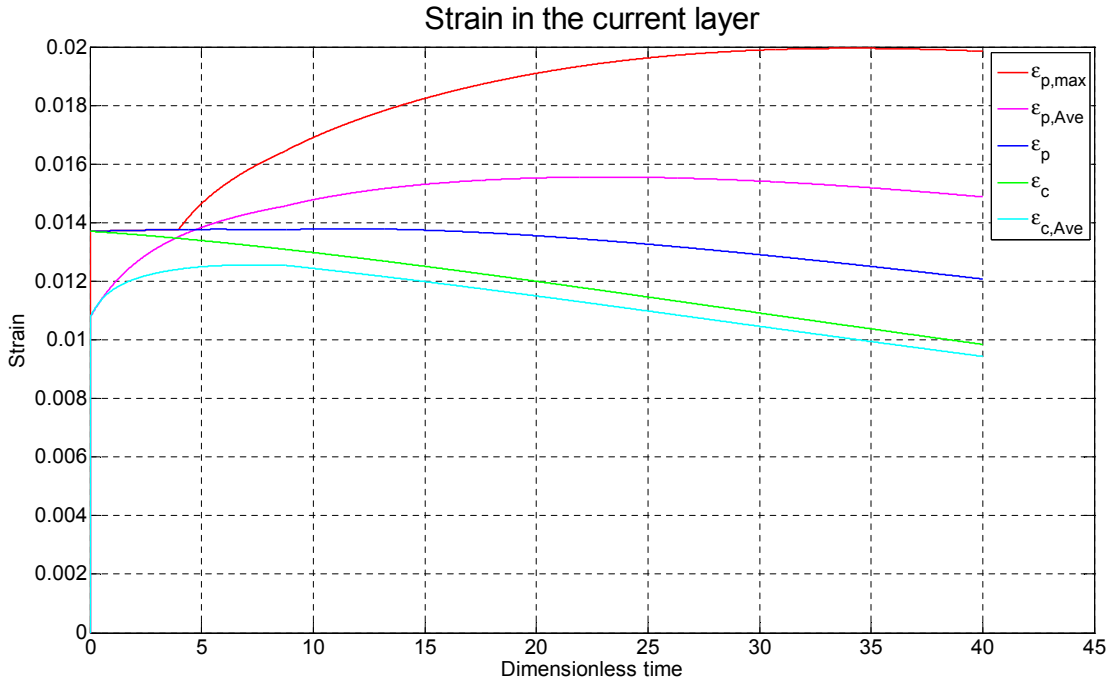

Figure 3.12: Curve of strain at cone wave front and projectile edge, 9 mm.

Consistent with the results shown in Fig. 3.10 and Fig. 3.11, the maximum strain in the whole region is $\varepsilon_{p,\max}$. As discussed in the previous section, the strain around the projectile (denoted as $\varepsilon_{p,Y}$) has a "hump" distribution initially, i.e. the peak strain is at the centerline along the x-axis and decays along the projectile edge towards the y-axis. After a short period, a peak strain position develops gradually moving towards y-axis and thus the strain closer to y-axis becomes dominant as a strain concentration.

During the transition of peak strain position departing from the intersection of the x-axis and the projectile edge, there is a moment when the strain distribution along the projectile edge is relatively uniform, i.e. the strain is almost the same at every place around projectile edge, and thus $\varepsilon_{p,\text{avg}}$ is roughly equal to both $\varepsilon_{p,\max}$ and ε_p at that moment. This has also been confirmed in Fig. 3.12 (the three variables ε_p, $\varepsilon_{p,\text{avg}}$ and $\varepsilon_{p,\max}$ are approximately equal to each other at

$\tau \approx 4$). Before $\tau \approx 4$, $\varepsilon_p = \varepsilon_{p,\max}$. At $\tau \approx 4$, the strain distribution is uniform, so $\varepsilon_p = \varepsilon_{p,\max} \approx \varepsilon_{p,\text{avg}}$. After that, $\varepsilon_p < \varepsilon_{p,avg} < \varepsilon_{p,\max}$, indicating the peak strain has moved to approximately $Y = 1$.

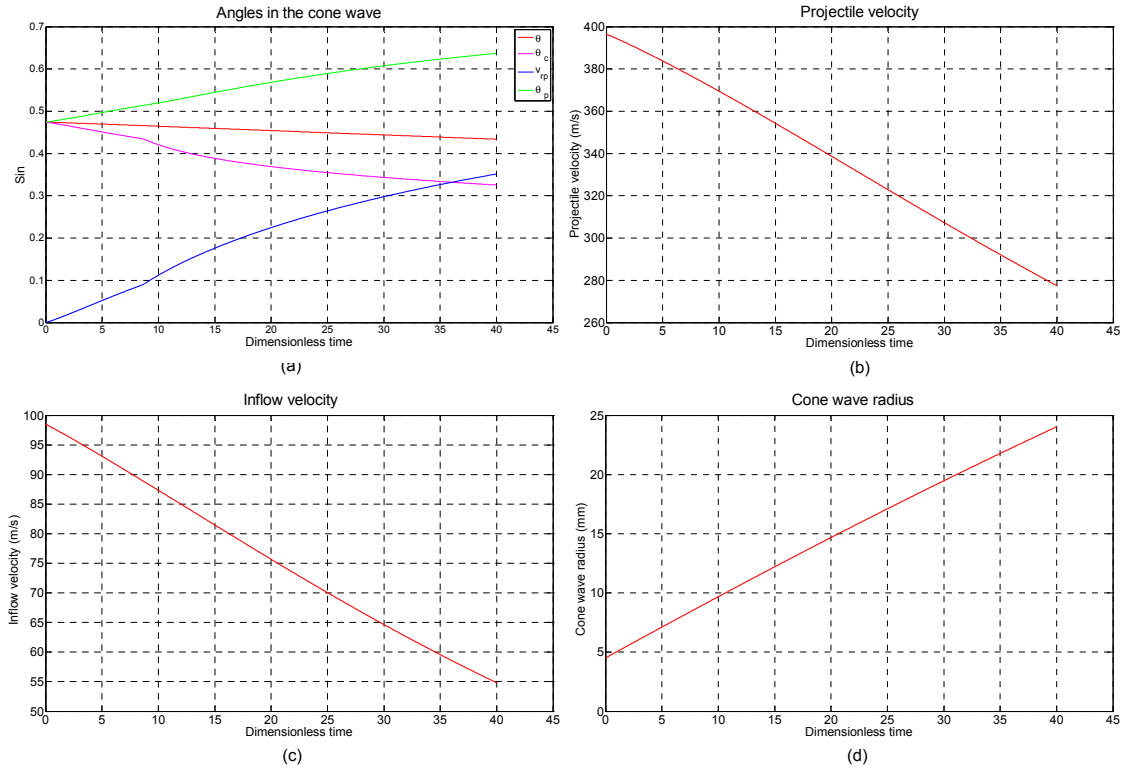

Figure 3.13: Results for some important parameters: (a) Angles at cone wave front (θ_c) and projectile edge (θ_p), effective cone wave angle (θ) and $V_{cp} = |\theta_c - \theta_p|$; (b) Projectile velocity decaying with time; (c) Inflow velocity and (d) Cone wave radius r_c.

Upon impact of the projectile, ε_c keeps decreasing as time goes on, showing the projectile velocity V_0 is not large enough to cause a strain sustainable over time. While $\varepsilon_{c,\text{avg}}$ goes up first and then decreases at the same rate as that of ε_c, we suspect that beyond the initial region where the strain around the cone wave-front rolls off like the strain around the projectile, later on the strain will be seen to be approximately the same around the cone wave-front and decreases at the same rate.

Fig. 3.13 shows the results of some key model parameters. In panel (a), the angle θ_p at the projectile edge is greater than all the other angles, while the effective angle θ is greater than θ_c at the cone wave front, indicating that the angle decreases gradually from the projectile edge to the cone wave front. The difference between θ_p and θ_c amplifies as time goes on. In panels (b) and (c), the projectile velocity V_p is shown to decrease from 395 m/s to 278 m/s, or about 30.6%, while the inflow velocity $\dot{u}_c$ decreases from 99 m/s to 55 m/s, or about 44.4%. Thus the inflow velocity decays faster than the projectile velocity. In panel (d), the cone wave radius is about 24mm, or 4 times of the projectile radius (4.5mm).

Fig. 3.14 shows the contours of the out-of-plane displacements of the pyramid pocket at $\tau = 40$. The contour lines of vertical displacement are geometrically shaped as follows: (i) when $x < \sqrt{2}r_p/2$ or $y < \sqrt{2}r_p/2$, they are arcs of radius r_p. (ii) when $x \geq \sqrt{2}r_p/2$ and $y \geq \sqrt{2}r_p/2$, they are straight lines 45° oblique to the y-axis. From the inner to the outer circumference, the contour lines look as if they are transforming from a circle to a square with rounded corners and straight sides.

Note that the pyramid diagonals are aligned with the two sets of orthogonal yarns passing beneath the projectile, and that the corners of the pyramid base are actually rounded also with virtually the same radius as the projectile. The distance from the center of the projectile to the tips of the rounded noses in Fig. 3.14, denoted as r_c, is about $5r_p$. Therefore the cone wave has actually progressed the distance $r_c - r_p = 4r_p$ (in material coordinates) away from the projectile edge, but only about $3.0r_p$ in the direction ±45° to the yarn axes, where as time passes its speed of growth is only $1/\sqrt{2}$ of that along the yarn axes.

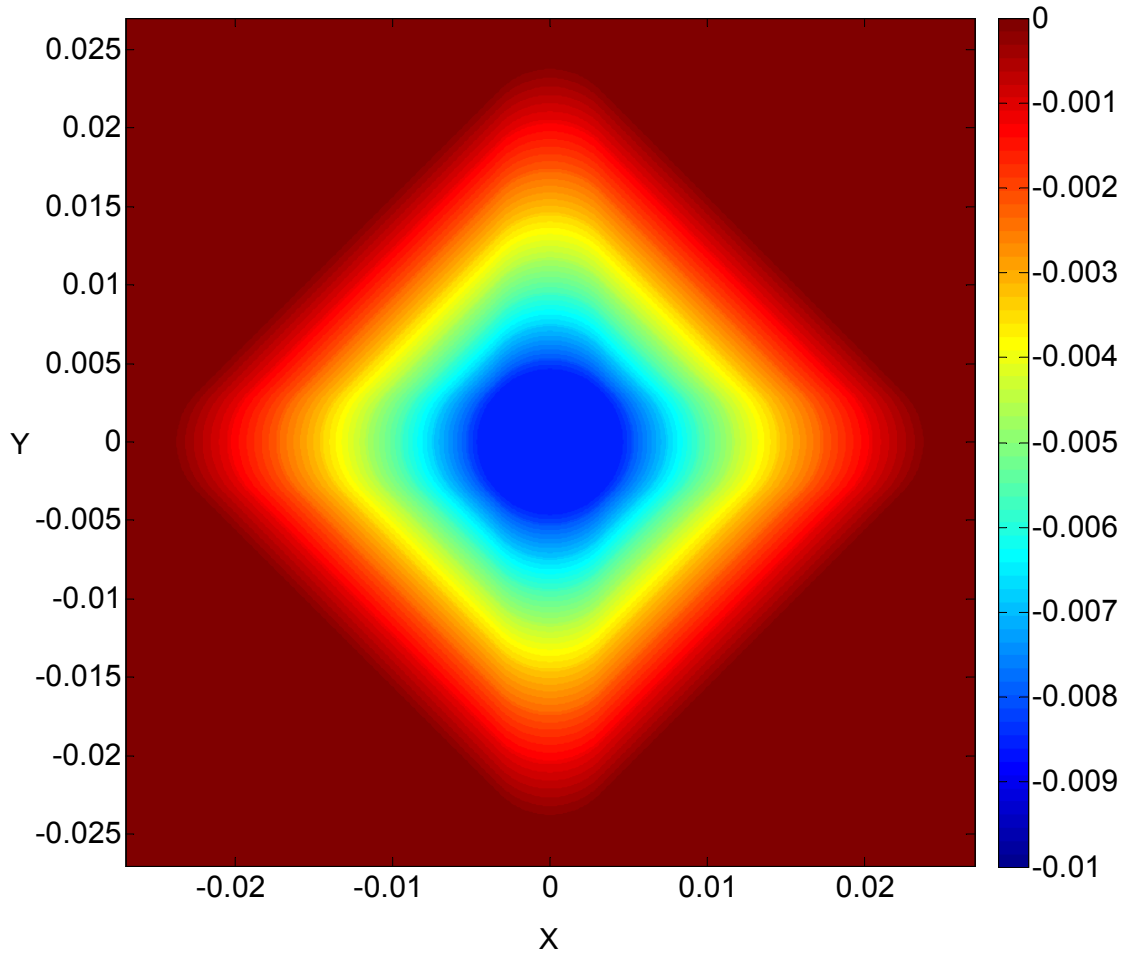

Figure 3.14: Contours of vertical displacement, top view, 9mm.

Fig. 3.15 shows a quarter region of the pyramid pocket at $\tau = 40$. The elevation contours have round edges when $x < \sqrt{2}r_p/2$ or $y < \sqrt{2}r_p/2$ while having straight sides outside the region.

Up to now we have been discussing the behavior of yarns in x-direction. Although helpful, the features seen thus far are not sufficient to motivate precise refinement of the analytical model. A major component in gaining further insight, however, is obtained from the study of the slope patterns in yarns within the pyramid-shaped cone. The slope of a certain point on an x-yarn is defined here by the sine of the angle with respect to the ground rather than the tangent.

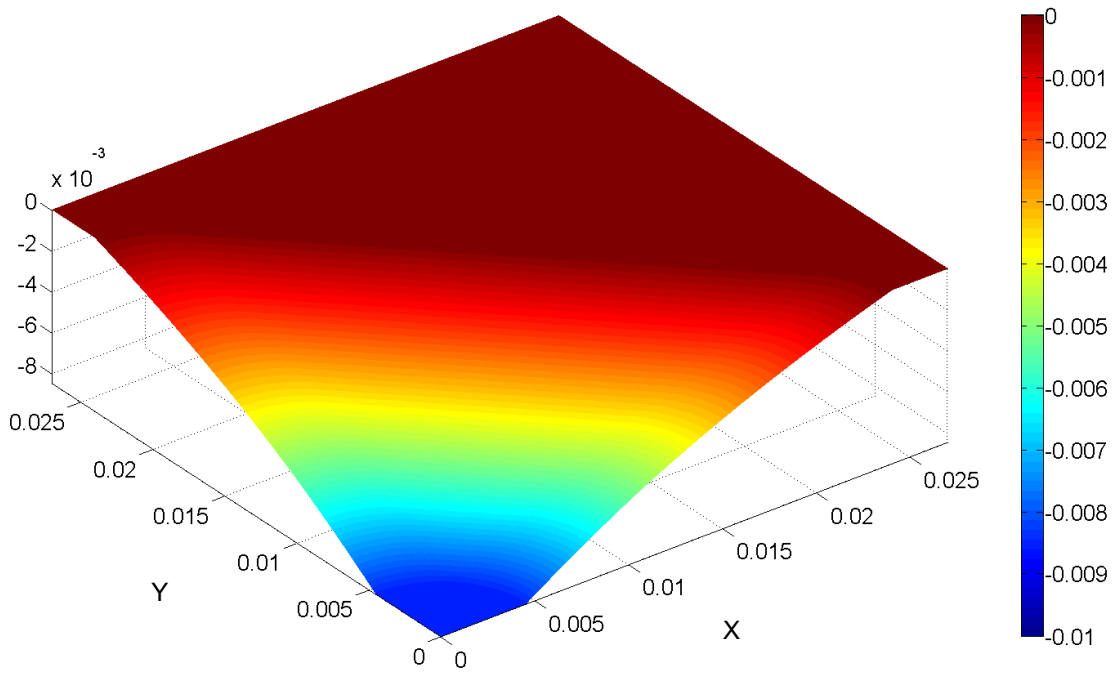

Figure 3.15: One quarter region of the cone wave, maximum displacement around 8mm.

Fig. 3.16 shows the angle sine distribution within the cone wave. The first and most important observation is that the slopes of the x-direction yarns entering the cone at its wave-front have approximately the same value along this wave front spanning from the nose region on the x-axis, all the way out to the extremities near the y-axis nose region. In fact, even along shorter diagonal lines parallel to the cone wave-front but somewhat closer to the projectile, i.e., at elevation contours that are some modest fraction of the projectile displacement, δ, the slopes are also fairly uniform.

A second important observation in Fig. 3.16 is that, on average, the yarn slopes increase traveling from the cone wave-front back to the projectile edge. The cause of this steepening, also discussed earlier, is very important to model since it affects the membrane strain (and tension) distribution at various elevations in the cone, in order to yield approximately the same net force resolved

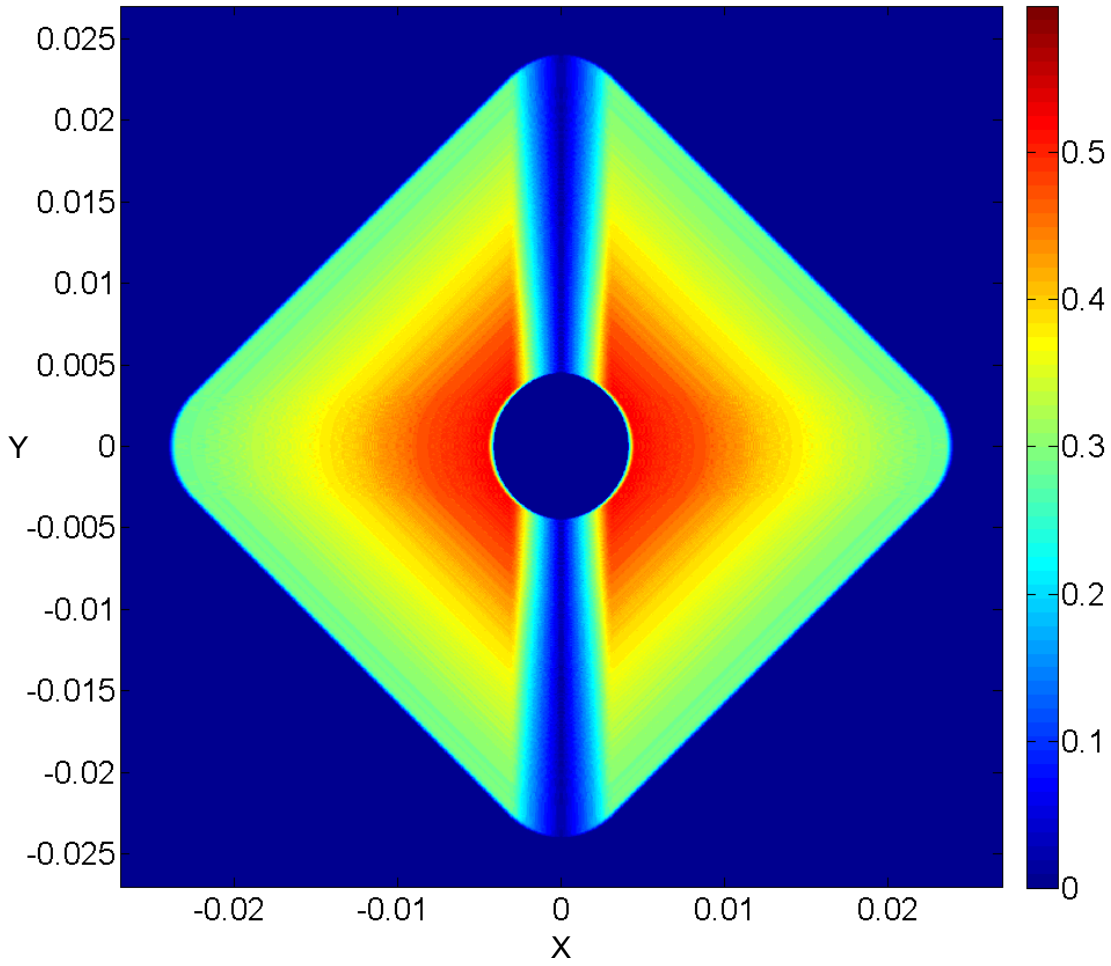

Figure 3.16: Slope distribution of yarns in the x-direction.

perpendicular to the membrane plane as the decelerating force on the projectile. Note that membrane inertia forces within the cone while relatively small will be accounted for. This feature is very important in revising the analytical model to reflect how the strains and slopes interactively increase approaching the edge of the projectile.

Fig. 3.17 shows the strain distribution in the x-direction yarns as calculated using the Cornell semi-analytical model presented in this thesis. The tensile wave front causes tension in the yarns, which then leads to an inflow velocity

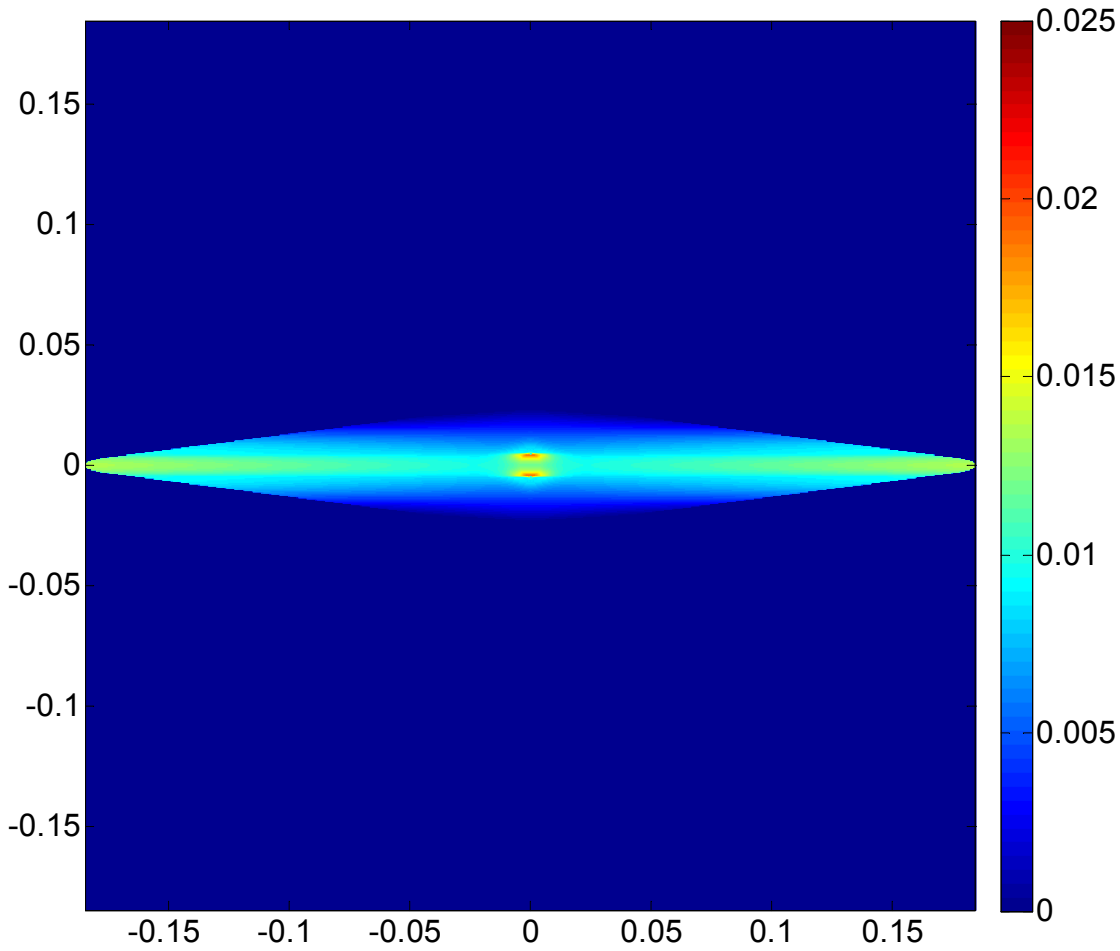

Figure 3.17: Strain distribution in the x-direction yarns, single layer, 9 mm.

increase. When the tensile wave travels outward, the tension at the tip of the "strain finger" of the tension wave will remain approximately as it was upon the impact of projectile, and thus the strain is just the initial strain close to that caused at the moment of striking by the projectile. With the analysis of the results obtained from the Cornell-modified DSM code, we have determined that the strain profile from the cone wave-front to the "finger tips" of the tensile wave-front is approximately linear in position. However depending on the deceleration of the projectile the gradient of the strain profile may be positive or negative.

When the cone-wave proceeds in the y-direction, it intersects x-direction yarns and emits in them new tensile 'wavelets'. This occurs because the cone wave induces a sudden vertical velocity of magnitude to that initially induced by the projectile when impacting the yarns passing underneath. The tensile wavelet speed is the same in all yarns once a wavelet is emitted. Therefore the tensile wave front in each yarn can be calculated in terms of the time when the cone wave front first intersects that particular yarn.

Based on our analysis of the modified DSM code results for the current case under study, the strain decreases almost linearly from the cone wave front to the tensile wave front in x-direction yarns. At $y = r_p$ (or 4.5mm), the strain gradient in the y-direction is roughly the inverse of the distance to the centerline of the x-axis, starting from $x = 0$ to the tensile wave front in each yarn. Thus the strain gradient is much steeper at $x = 0$ than that at the cone wave front and the tensile wave front. In the strain distribution plot, we can see that there is a sharp strain plunge in x-direction yarns traveling along the y-axis away from the projectile edge at $y = r_p$. At $y = 2r_p$ (or 9 mm), the strain along x-direction yarns has almost a uniform distribution, and thus, the strain gradient decreases to zero everywhere from $x = 0$ to the tensile wave front in each yarn. In cases of yarn slip under the projectile, the x-direction yarns at around $y = r_p$ are the last that stretch to very high tensions. All the yarns beyond that point have no contact with the projectile and thus have much less tensile strain.

Up to now we have only analyzed the mechanical loads, strains, displacements and velocities of x-direction yarns without considering y-direction yarns. When interwoven together, y-direction yarns are symmetric to x-direction yarns and thus the strain distribution will be symmetric to that in x-direction yarns.

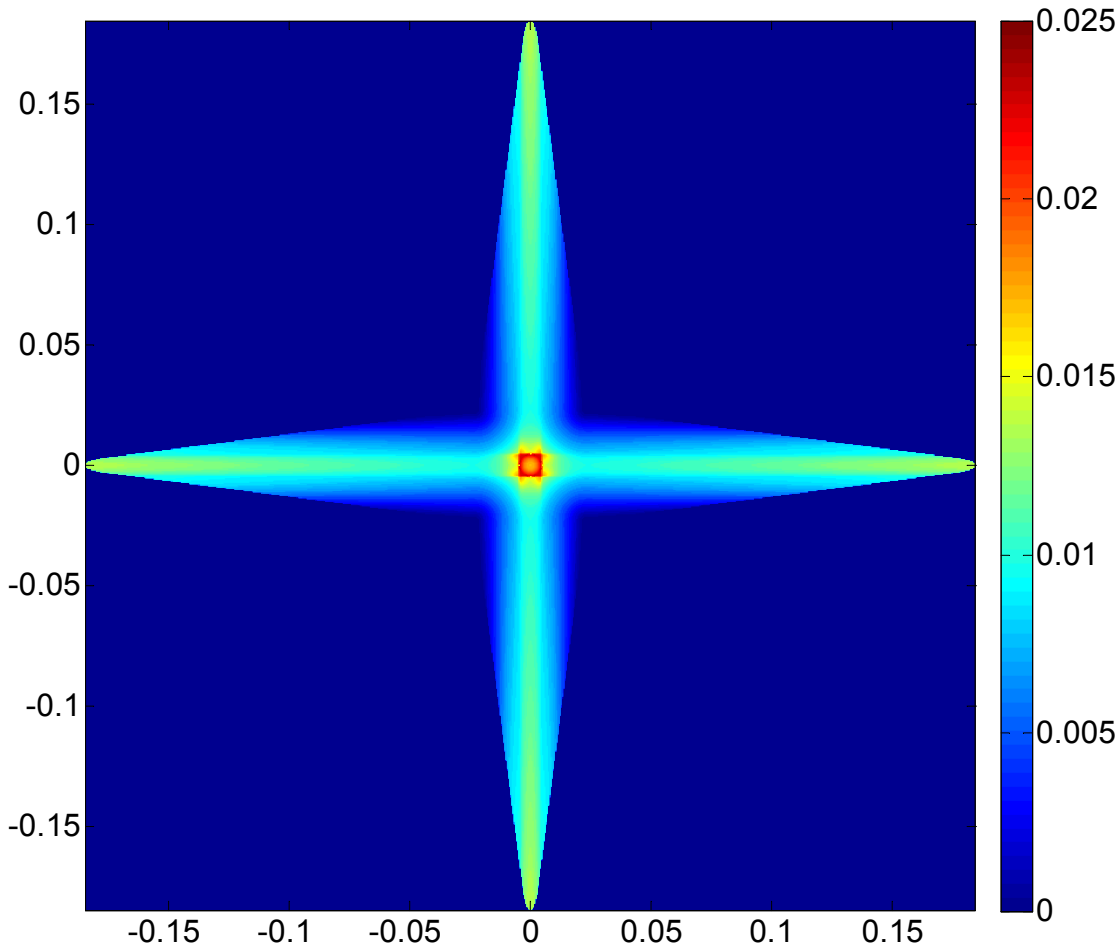

Figure 3.18: Slope distribution of yarns in the x-direction.

Fig. 3.18 shows the plot for $\varepsilon_{\text{eff}} = \sqrt{\varepsilon_x^2 + \varepsilon_y^2}$, where ε_x and ε_y are the strains in the two orthogonal sets of yarns at each location. (We shall use a Cartesian $x - y$ axis system to describe the primary yarn directions.) As in a tape, the tension waves still travel at the speed of sound in the material, $a_0 = \sqrt{E/\rho}$, but several new features emerge. First, the tips of the tension waves show a curved shape (the simulations from the Cornell-modified DSM code will also show slight dispersion induced by the finite mesh as discussed later) with radius similar to the projectile, r_p. Second, for waves traveling outward from the projectile at ±45° from the yarn axes, the propagation speed is not only slower by the factor $1/\sqrt{2}$,

but the strains induced are very small. Strains are shown to be zero in the dark blue regions. In reality, and as shown later, there are actually second order induced strains that are only about 4% of those shown in yellow regions of the star arms, and thus prove to be negligible for modeling purposes. This feature is certainly in keeping with the negligible shear modulus, G. A third and crucial observation in Fig. 3.18 is that the widths of the arms increase approximately linearly from the tensile wave tips back to the projectile impact point. This is the result of the growth of the cone-wave emitting wavelets in yarns it intersects as discussed previously. Fourth, along the arms away from the projectile, one notes a modest but progressive decrease in strain intensity approaching the tip of the cone wave front. Fifth, ε_{eff} has it peak around projectile edge, especially along $\pm 45^{\circ}$ from the yarn axes. Outside the projectile edge and within the cone wave-front, the strain contour becomes like a diamond with its diagonals along yarn axes. The strains in regions close to $x-y$ axes are higher than the strains in yarns further from the yarn axes where the strain profile is almost constant. At the tensile wave front, the strain becomes higher again, showing the influence of the original impact as it has propagated at the front of the tension wave.

Fig. 3.19 shows the evolution of strain distribution in the $x-y$ plane. At the beginning (panel (a), $\tau = 10$), the tensile wave front is still close to the projectile edge, and the strain distribution around the projectile edge is still uniform. so the area around the projectile is totally red, and the average strain within the tensile wave front is relatively high. When $\tau = 20$ and 30, the strain around the projectile edge starts to bifurcate, and the peak strain has clearly moved to the centerline of the y-axis. With the tensile wave going farther, in regions of $y \geq r_p$, the strain distribution going from the center to the edge of the front "finger" is uniform. At $y = 0$, the strain at the tensile wave tip remains almost as the initial

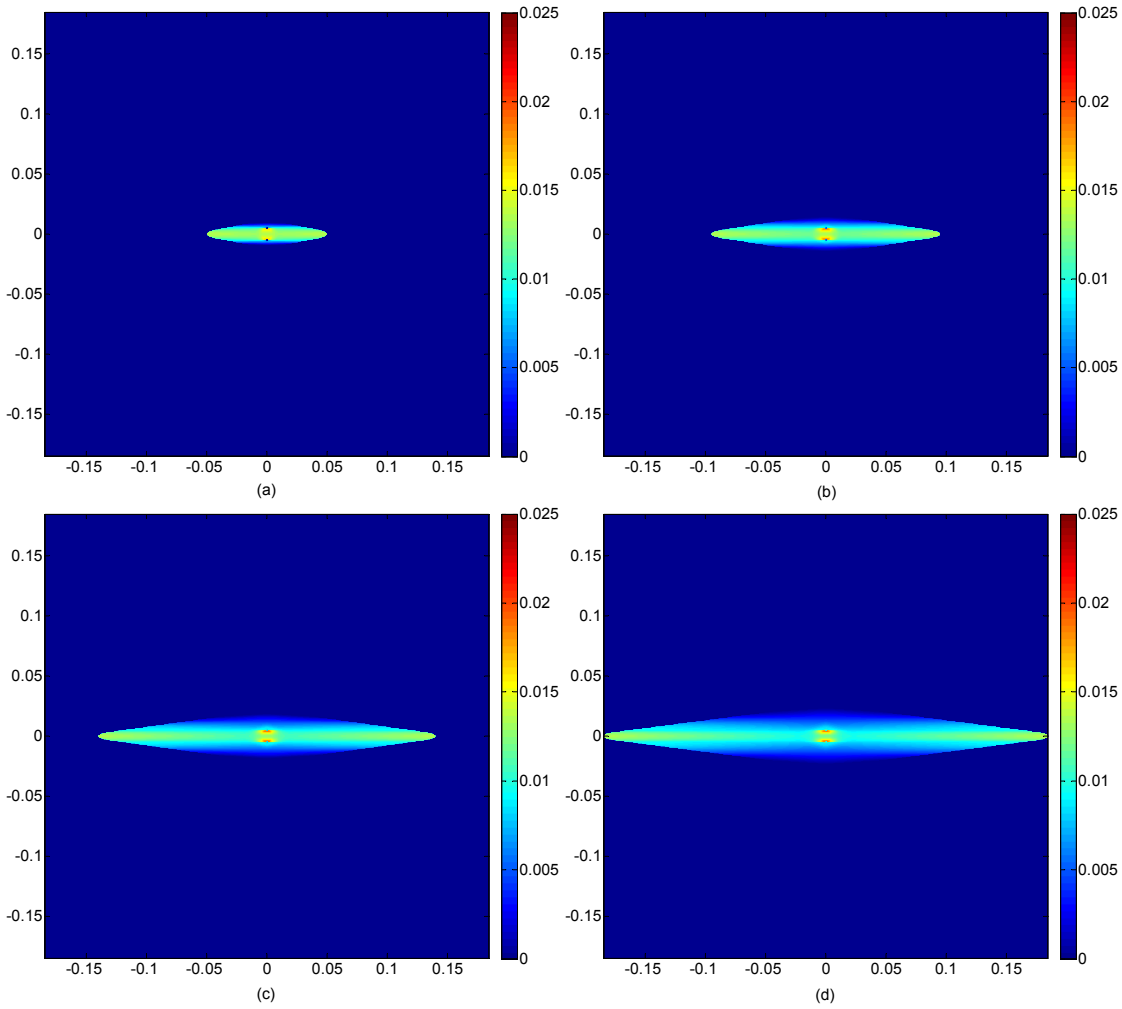

Figure 3.19: The evolution of strain over time in the x-direction yarns: (a) $\tau = 10$; (b) $\tau = 20$; (c) $\tau = 30$; (d) $\tau = 40$.

strain upon the impact of projectile. When $\tau = 40$, the tendency described above continues, and the middle area becomes more uniform.

Fig. 3.20 shows the effective strain distribution by involving the strain in both the x-direction and the y-direction yarns, which in biaxial fabrics, is symmetric. In panel (a), the strain pattern is affected by the initial impact and thus the strain within the projectile is highly intensified and the average within the tensile wave front is high. Later on, when $\tau = 20$, the strain at the root of four

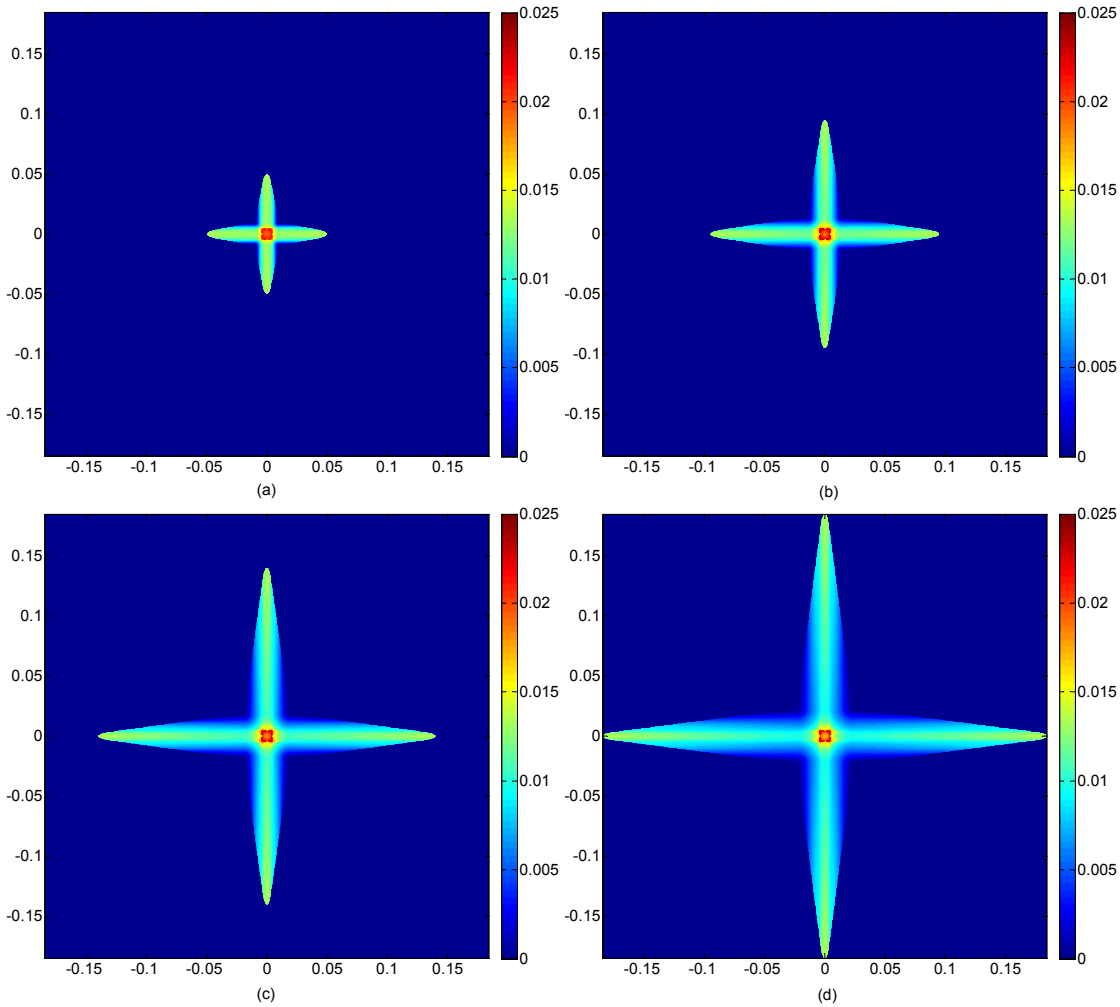

Figure 3.20: The evolution of effective strain $\sqrt{\varepsilon_x^2 + \varepsilon_y^2}$ in x-direction yarns and y-direction yarns: (a) $\tau = 10$; (b) $\tau = 20$; (c) $\tau = 30$; (d) $\tau = 40$.

branches starts to dampen, and the strains along the x-axis and y-axis centerlines are higher but uniform. When $\tau = 30$, the strain at the roots of the four fingers keeps decreasing and there has been a noticeable difference between the strain at the tensile wave front and that at the roots of the four fingers. The strain within the projectile starts to decrease and the intensified part is only located around the projectile edge. Between the projectile edge and the cone wave front, which can be indicated by the position where the lowest strain is located

along the x-axis and the y-axis centerlines, the strain pattern transforms from a square to a diamond with its diagonal lines along the x-axis and the y-axis. When $\tau = 40$, the tendency described above becomes more distinct.

Results from impact of an FSP projectile

Next we study results of the Cornell semi-analytical model presented in this thesis, considering now the case of impact by an FSP projectile, the parameters for which are given in Table 3.1. Fig. 3.21 shows the strain distribution along the x-axis centerline at different times. The patterns of the curves are similar to those shown in Fig. 3.10. From $X = 1$ to $X = 2$ (within one projectile radius of the projectile edge) the strain has decreased by 4.8%, 7.0%, 7.7% and 8.3% at $\tau = 10$, $\tau = 20$, $\tau = 30$ and $\tau = 40$ respectively, very close to the results in Fig. 3.21. When $\tau = 40$, the strain levels out at the cone wave front ($X = 5$) and thus the strain gradient along x-axis is almost zero.

At $\tau = 40$, the strain at the projectile edge on the projectile centerline (x-axis) is $\varepsilon_p = 0.00638$, while the strain at the cone wave front is $\varepsilon_c = 0.0053$. At $X = 2$, the strain is 0.00586. The strain decreased by 8.3% from $X = 1$ to $X = 2$ and by 17.1% to the cone wave front. In 9 mm case, the numbers are 9.1% and 18.6% respectively at $\tau = 40$. Considering that the cone wave front is $r_c(\tau) = 5.4r_p$ in 9 mm case, and that $r_c(\tau) = 4.98r_p$ in FSP case, the specific mass and initial velocity values of the projectile have relatively little effect on the strain distribution from the projectile edge to the cone wave front. The strain values at different positions, $X = 1$, $X = 2$ and $X = r_c/r_p$ and at different times from $\tau = 10$ to $\tau = 40$ are listed in Table 3.2.

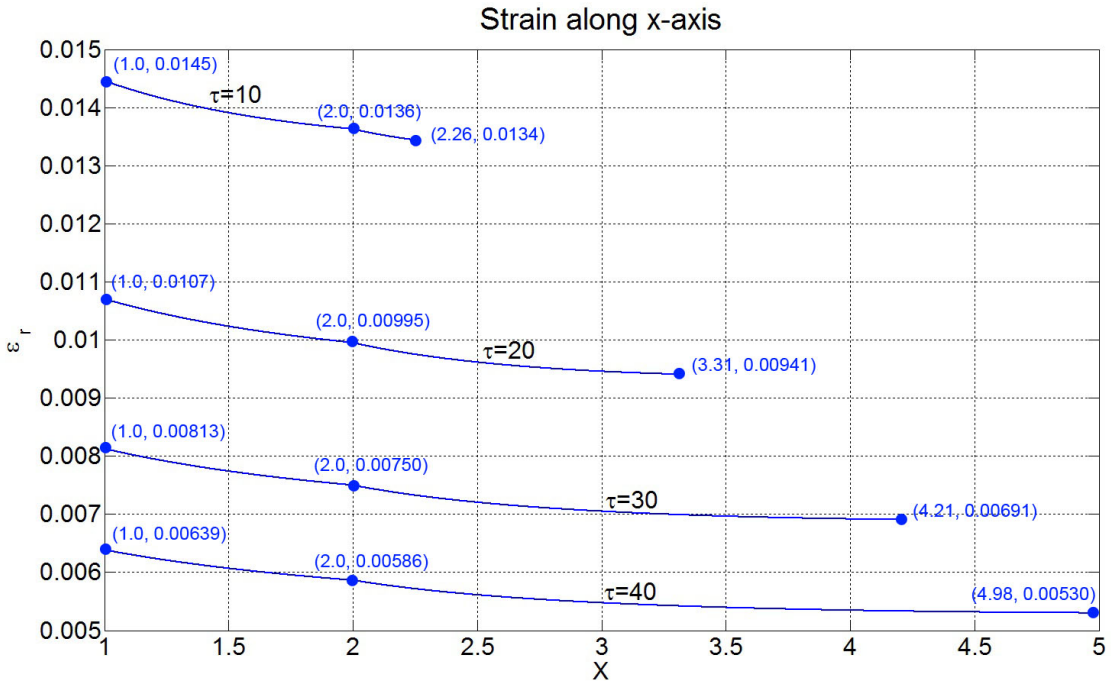

Figure 3.21: Strain profile along the x-axis centerline at $\tau = 10,\ 20,\ 30,\ 40$ respectively (FSP).

The strain distribution is obtained from Eq. (3.81), in which the quantities $\Theta(r)$, $A(r_c)$ and $\Theta(r_c)$ are only dependent on the dimensionless distance r/r_p from the projectile center. The angle measure, $\sin(\bar{\gamma}_c)$, is obtained from Eq. (3.88) and Eq. (3.96), so it is only related to $\sin(\hat{\gamma}_c)$. Therefore, the strain distribution along the x-axis is determined by $\sin(\hat{\gamma}_c)$, the local angle relative to the horizontal line where the material travels into the pyramid pocket. The variation of $\sin(\hat{\gamma}_c)$ and $\sin(\bar{\gamma}_c)$ will be discussed in more detail later, however, we note here that they do not vary much over the different cases, i.e. they are quantities highly dependent on material properties but much less so on projectile properties (mass or velocity), and thus, the strain distribution along the x-axis center-line is almost the same in both the 9 mm and FSP cases.

Fig. 3.22 shows the strain around the FSP projectile edge at different times.

Table 3.2: A comparison of the strain decrease from $X = 1$ to $X = 2$ and then to $X = R_c(\tau)$ at different times.

	Position									
τ	$\varepsilon_{X=1}$		$\varepsilon_{X=2}$				$\varepsilon_{R_c(\tau)}$			
	9 mm	FSP	9 mm	$\downarrow$ %	FSP	$\downarrow$ %	9 mm	$\downarrow$ %	FSP	$\downarrow$ %
10	0.0138	0.0145	0.0131	5.1	0.0136	4.8	0.0130	5.8	0.0134	7.6
20	0.0136	0.0107	0.0126	7.0	0.0010	7.0	0.0120	11.4	0.0094	12.1
30	0.0129	0.0081	0.0119	7.8	0.0075	7.7	0.0109	15.5	0.0069	15.0
40	0.0121	0.0064	0.0110	9.1	0.0059	8.3	0.0099	18.6	0.0053	17.1

The pattern of the curves is a little bit different from that of the 9 mm case shown in Fig. 3.11. At $\tau = 0$, the strain is 0.0195 at $Y = 0$, and 0.00698 at $Y = 1$, so has decreased by 35.8% from $Y = 0$ to $Y = 1$, which is almost the same as 9 mm result. However, when $\tau = 5$, the curve has transitioned beyond having a flat profile and the curvature of the profile has reversed. While ε_p at $Y = 0$ decreased by about 14%, the position of the peak strain moved to $Y = 1$ and is about 5.4% higher than ε_p at at $Y = 0$. As time goes on, both ε_p and $\varepsilon_{p,\max}$ decrease, but $\varepsilon_{p,\max}$ decreases more slowly and is about 24%, 45% and 66% higher than ε_p at times, $\tau = 10$, $\tau = 20$ and $\tau = 40$, respectively. These results are also listed in Table 3.3.

The strain distribution along the projectile edge is calculated using Eq. (3.194), so the strain profile at $Y = 1$ should be the same for various cases given the same dimensionless cone wave front position $R_c(\tau)$. T he velocity of the FSP projectile is larger at the beginning than for the 9 mm case, and therefore, the cone wave travels faster at that point in time. However, the velocity of the FSP projectile decays more rapidly, so by $\tau = 40$ the peak strain $\varepsilon_{p,max}$ is about 66% higher than ε_p in the FSP case as compared to being 69% higher in

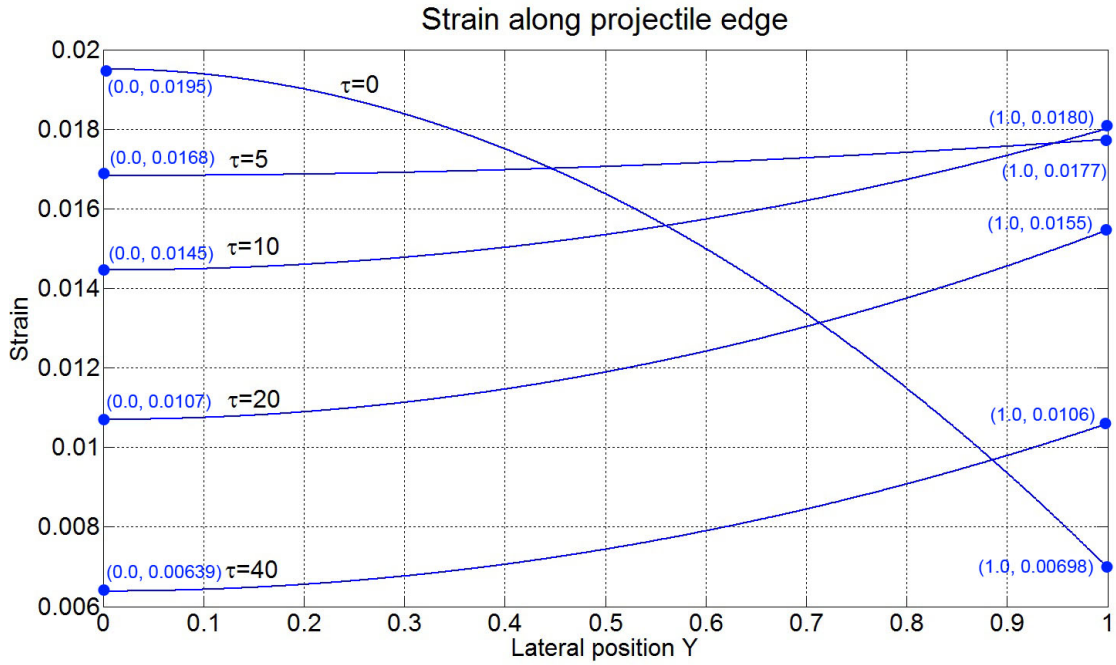

Figure 3.22: Strain distribution around projectile edge at $\tau = 0,\ 5,\ 10,\ 20,\ 40$ respectively (FSP).

the 9 mm case. Thus the strain concentration around the projectile diminishes more rapidly in the FSP case.

The progression of strain versus dimensionless time is quite different in the case of the FSP (shown in Fig. 3.23) as compared to the 9 mm case (shown in Fig. 3.12). In the 9 mm case, with impact velocity of $V_0 = 406$ m/s, the strain initially builds and the maximum strain appears at a later time after the impact of the projectile (around $\tau = 30$). The the maximum strain, $\varepsilon_{p,\max}$, reaches its climax at about $\tau = 35$, and for $\varepsilon_{p,\text{avg}}$ and ε_p the largest values occur at $\tau = 22$ and $\tau = 10$, respectively. Also the strain distribution around projectile edge is relatively uniform by about $\tau = 4$ in the 9 mm case. For the FSP,with impact velocity of $V_0 = 568$ m/s, however, $\varepsilon_{p,\max}$ reaches its peak much earlier at about $\tau = 6$, and for $\varepsilon_{p,\text{avg}}$ and ε_p the corresponding times are $\tau = 3$ and $\tau = 0$, respectively.

Table 3.3: A comparison of the strain decrease from $X = r_p$ to $X = 2r_p$ and $X = r_c$ at different time

	Position					
τ	$\varepsilon_{Y=0}$		$\varepsilon_{Y=1}$		$\frac{(\varepsilon_{Y=1}-\varepsilon_{Y=0})}{\varepsilon_{Y=0}} \times 100\%$	
	9 mm	FSP	9 mm	FSP	9 mm	FSP
0	0.0138	0.0195	0.00492	0.00698	-64.3	-64.2
5	0.0138	0.0168	0.0140	0.0177	1.4	5.4
10	0.0138	0.0145	0.0168	0.0180	21.7	24.1
20	0.01356	0.0107	0.0195	0.0155	43.8	44.9
40	0.0121	0.00639	0.0205	0.0106	69.4	65.9

In other words, ε_p begins decreasing almost immediately after the impact of the projectile. Therefore with the FSP projectile, the membrane will either be perforated immediately after the impact or will let the cone wave develop for a long time. The mass of FSP projectile is only 1.1 gram (compared to 8.0 gram of the 9 mm projectile), so the projectile cannot sustain for very long in dimensionless time high tension and thus high strain in the membrane.

The initial strain in the 9 mm case is about 0.0136, while in the FSP case, it is about 0.019. Although the FSP mass is much less than that of the 9 mm, the initial velocity is much higher (568 m/s vs. 406 m/s). As shown in Eq. (3.208)-(3.210), the initial strain is only dependent on the ratio of projectile velocity to tensile wave speed, hence a higher initial velocity will lead to a higher initial strain, both at the projectile edge and at the cone wave front, which are the same upon the impact. However, in the FSP case, after $\tau = 15$, all curves decrease at almost the same rate, while in the 9 mm case, they increase and decrease at quite different rates.

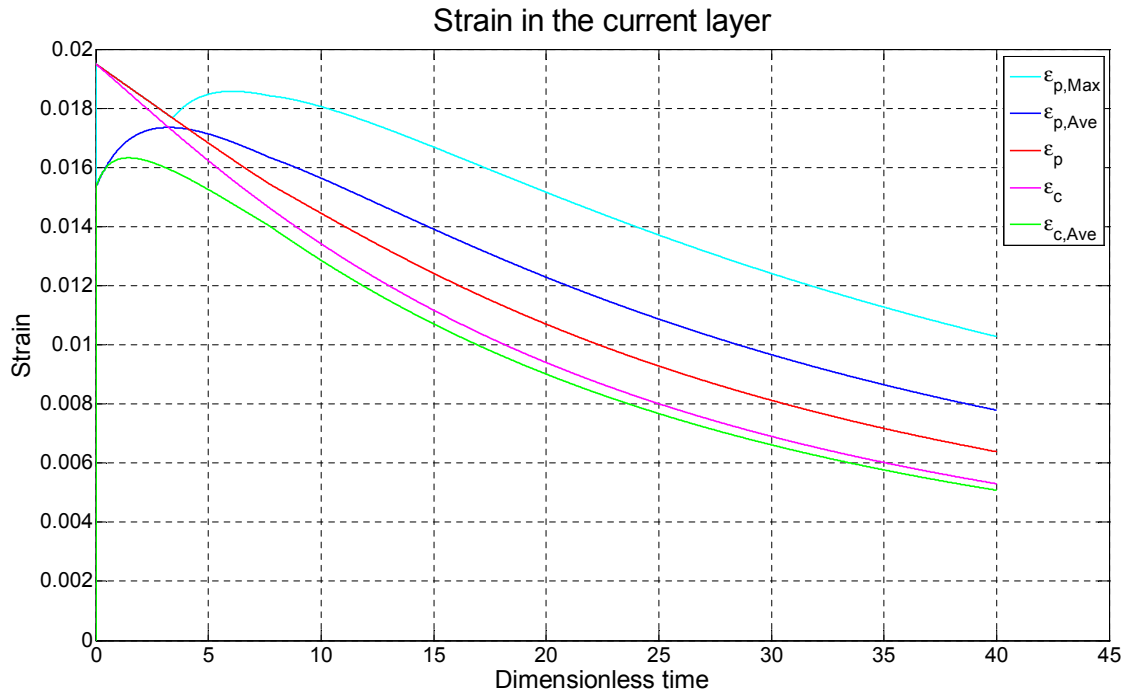

Figure 3.23: Profiles of strain around the cone wave front and the projectile edge, FSP projectile.

Fig. 3.24 shows the behavior of some important quantities in the FSP case. In panel (a), the angles at the projectile edge and the cone wave front are almost the same as those in the 9 mm case (shown in Fig. 3.13(a)). In the 9 mm case, both the projectile velocity and inflow velocity decrease almost linearly with time. In the FSP case, however, the deceleration rate is higher at the beginning, but then decreases noticeably when τ approaches 40. This reflects a decrease in the deceleration force around the cone wave and thus a decreased strain concentration as well, which has been clearly reflected in Fig. 3.23. The cone wave radius growth curve is similar to that in the 9 mm case, but nonetheless, the rate of increase is fast initially and then becomes slower later on.

Fig. 3.25 shows the displacement of the projectile. Compared to the 9 mm case, although the FSP projectile started with a higher velocity (568 m/s), the

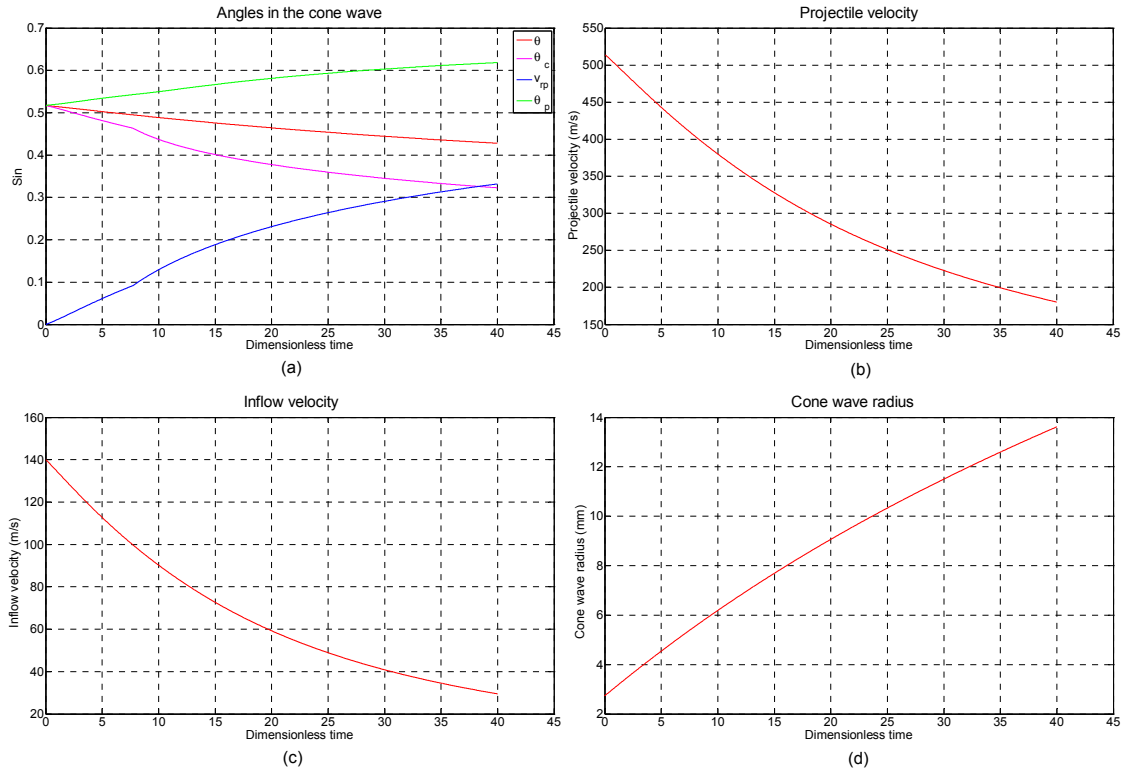

Figure 3.24: Results of some important parameters, FSP projectile: (a) Angles at cone wave front (θ_c) and projectile edge (θ_p), effective cone wave angle (θ and $V_{rp} = |\theta_c - \theta_p|$; (b) Projectile velocity decaying with time; (c) Inflow velocity and (d) Cone wave radius R_c.

deceleration is much faster early on (see Fig. 3.24(b)), so the FSP projectile velocity drops below 350 m/s by $\tau = 15$, while in Fig. 3.13(b), the 9 mm projectile velocity is still above 350 m/s at $\tau = 15$. Thus the total vertical displacement by $\tau = 40$ is smaller for the FSP than for the 9 mm projectile. The FSP projectile travels no more than 0.005 m after striking the membrane. From the colors of the contours, we can see that the profile of displacement goes from a circle to a diamond with rounded corners and with its diagonal lines aligned along the axes, which is similar to what we have seen in Fig. 3.14.

Fig. 3.26 shows the slope distribution within the cone wave front. The dis-

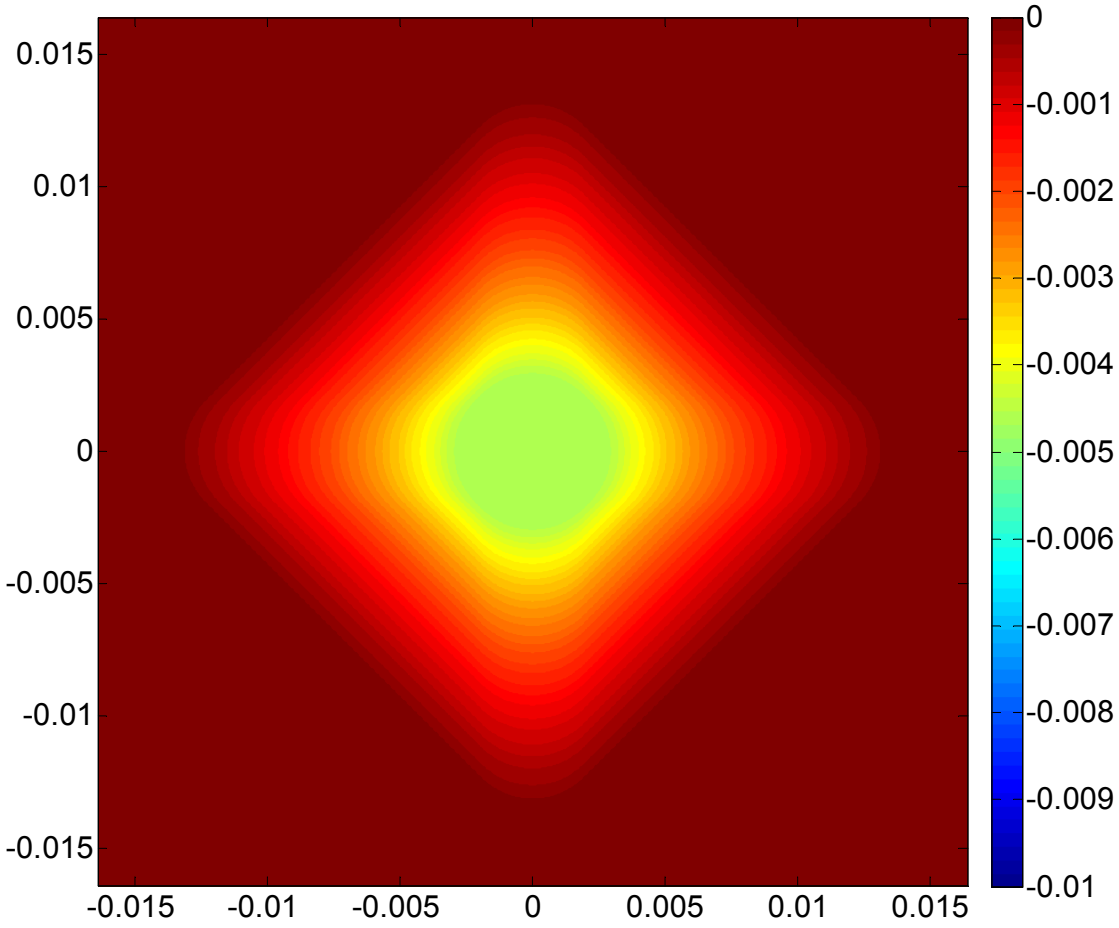

Figure 3.25: Vertical displacement profile within the cone wave, FSP.

placement pattern in the FSP case (Fig. 3.25) is similar to that in 9 mm case (Fig. 3.14), though the values are different due to the differences in the average projectile velocities. In Fig. 3.26, the slope pattern is similar to Fig. 3.15 as well, in terms of the effective angle θ, the angle at the projectile edge, and at the cone wave front, as well as the contour distribution within the pyramid pocket. The slope distribution is uniform along the contours of the cone wave displacement except around the centerline of the y-axis. As discussed above, the angles at the projectile edge and cone wave front are independent of projectile mass and velocity but depend on material properties, and here the rule can be generalized to the whole region within the cone wave front, i.e. the angle distribution is also

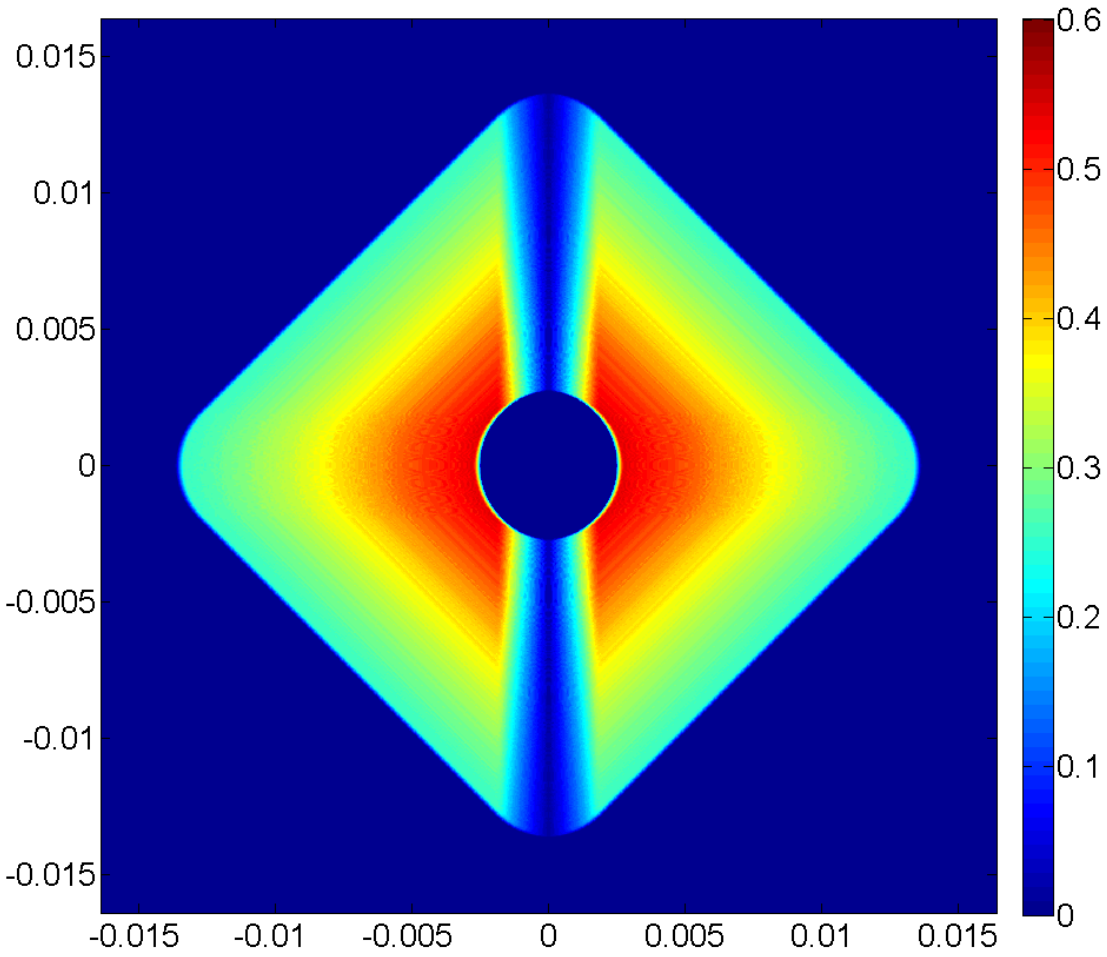

Figure 3.26: The slope distribution within the cone wave, FSP.

independent of variables other than the properties of the membrane.

Fig. 3.27 shows the strain distribution at $\tau = 40$ in the x-direction yarns out to the tensile wave fronts on each side. The pattern of the strain distribution is a somewhat different from that of the 9 mm case. In the 9 mm case, the maximum strain is located at the projectile edge ($Y = 1$), while in the FSP case, the maximum strain is located at the tensile wave front. In Fig. 3.23, we know that the maximum strain occurred right after the impact of the projectile. After that, the local tension will propagate together with the tensile wave-front and therefore the tension at the finger tips is larger than that any anywhere else

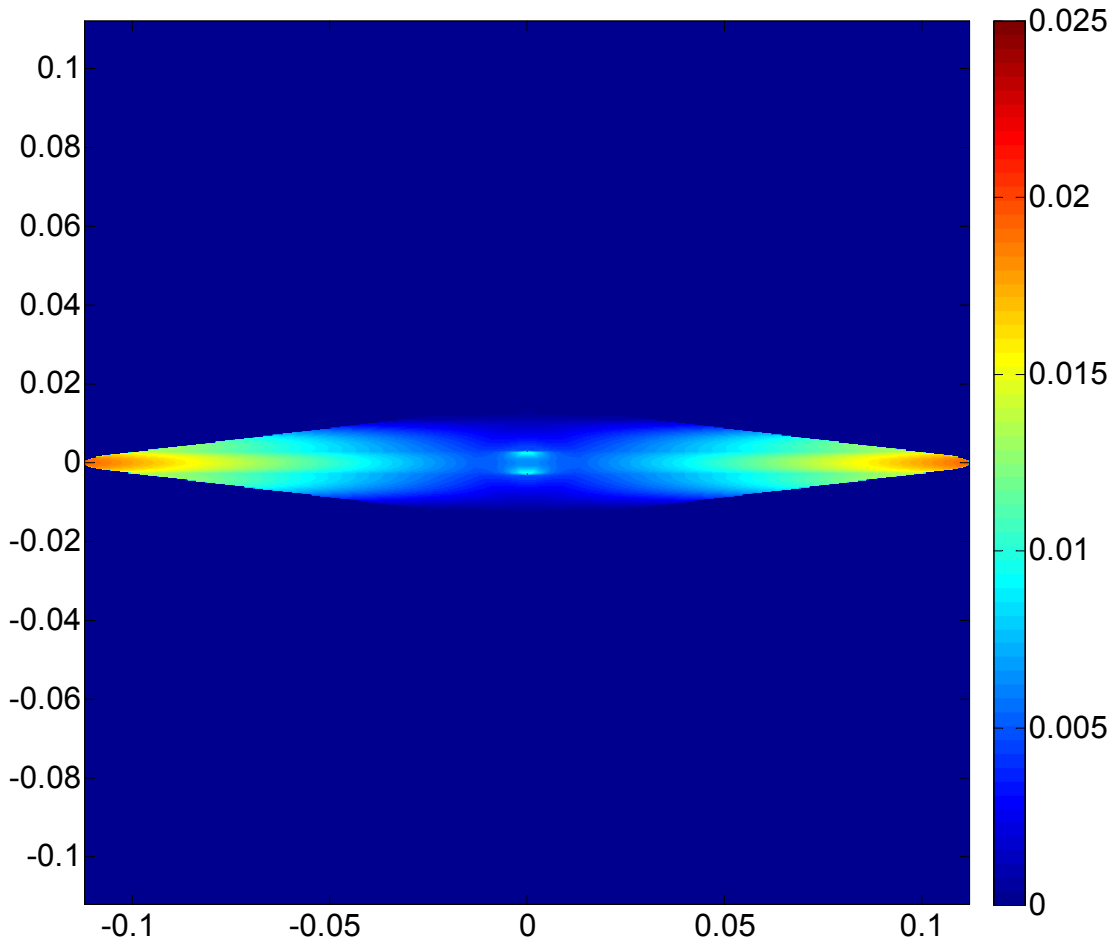

Figure 3.27: Strain distribution in x-yarns within tensile wave front, FSP projectile.

further back, which leads to the maximum strain occurring there. However, once surviving impact, the strains do not increase at the tensile wave-front and the membrane will not fail there. The tensile wave and cone wave will keep growing, however. Compared to the case of the 9 mm projectile, it is easier to establish the safe performance of the body armor since the peak strain occurs very early after projectile impact.

Fig. 3.28 shows the effective strain distribution behind the tensile wave tips calculated as the square-root of the the sum of the squares of x-direction and

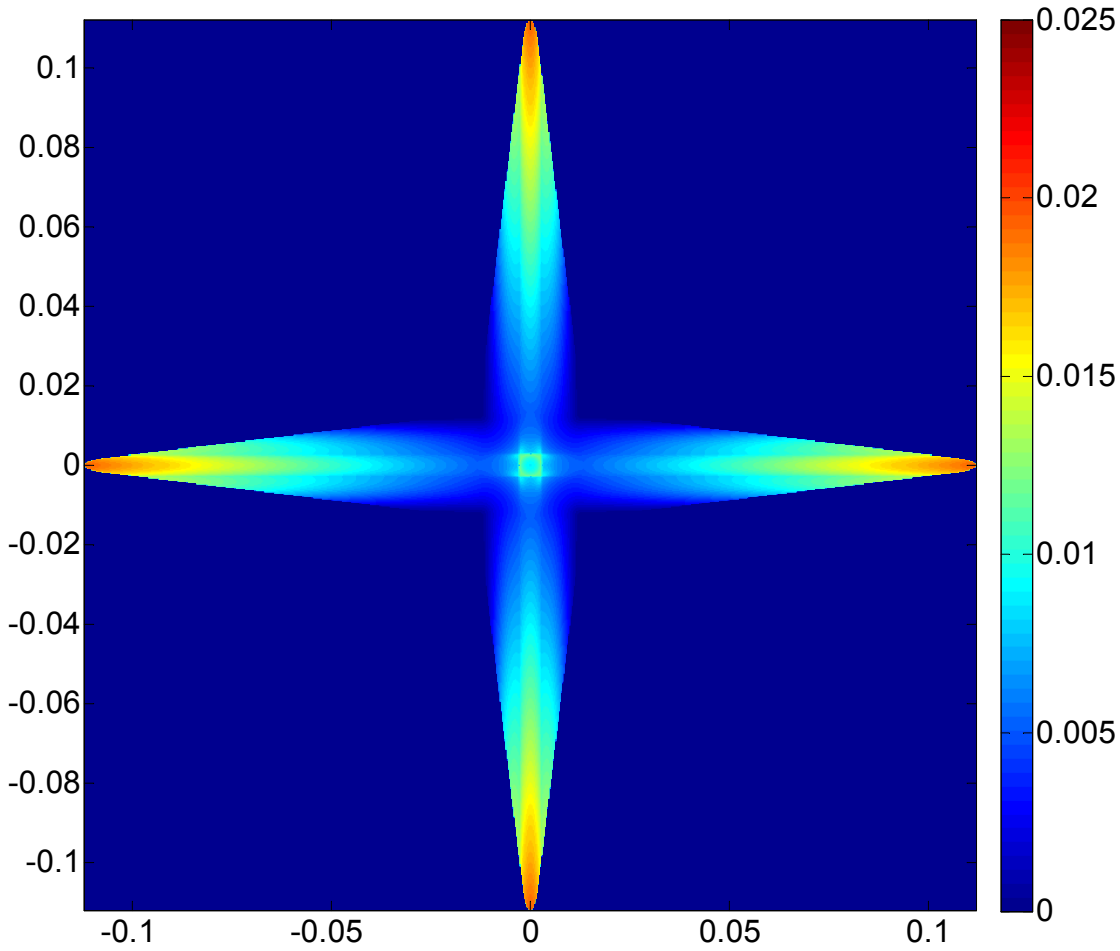

Figure 3.28: The effective strain ($\sqrt{\varepsilon_x^2 + \varepsilon_y^2}$), FSP projectile.

y-direction yarn strains. Compared to Fig. 3.20, the disparity is similar to what we explained above in Fig. 3.27 . The peak strain is still located at the four finger tips of the tensile wave front. In the center, there is a local square area of intensified strain with length $\sqrt{2}r_p$, showing the projectile's effect on strains, around the projectile, in the interwoven yarns before passing underneath.

Fig. 3.29 shows the evolution of strain in x-yarns in FSP case. When $\tau = 10$, the strains at tensile wave front and around the projectile edge are the highest, showing a strong effect of the projectile at the beginning. When $\tau = 20$, 30 and 40, the strains at projectile edge and cone wave front keep decreasing and thus

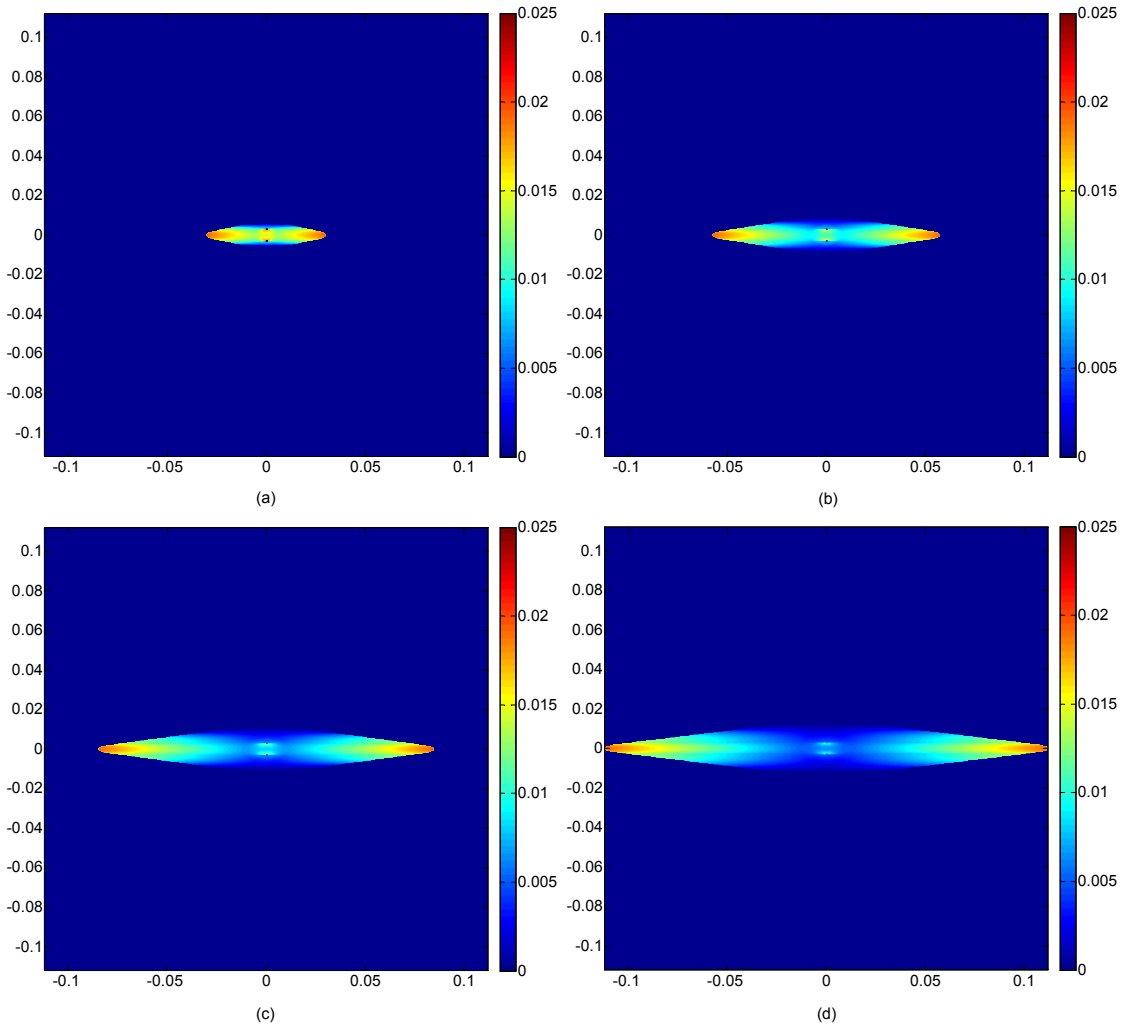

Figure 3.29: The evolution of strain in x-yarns, FSP projectile: (a) $\tau = 10$; (b) $\tau = 20$; (c) $\tau = 30$; (d) $\tau = 40$.

the strain within cone wave front become lower and lower (in dark blue), while the strain at the tensile wave front remains roughly constant. Within the cone wave front itself, the strain around projectile edge is the highest at any given moment.

Fig. 3.30 shows the effective strain $\sqrt{\varepsilon_x^2 + \varepsilon_y^2}$ in the whole region. similar to what we have seen in Fig. 3.29, the peak strain is located at the tensile wave front. When $\tau = 10$, the strain at projectile edge is much higher than that at later

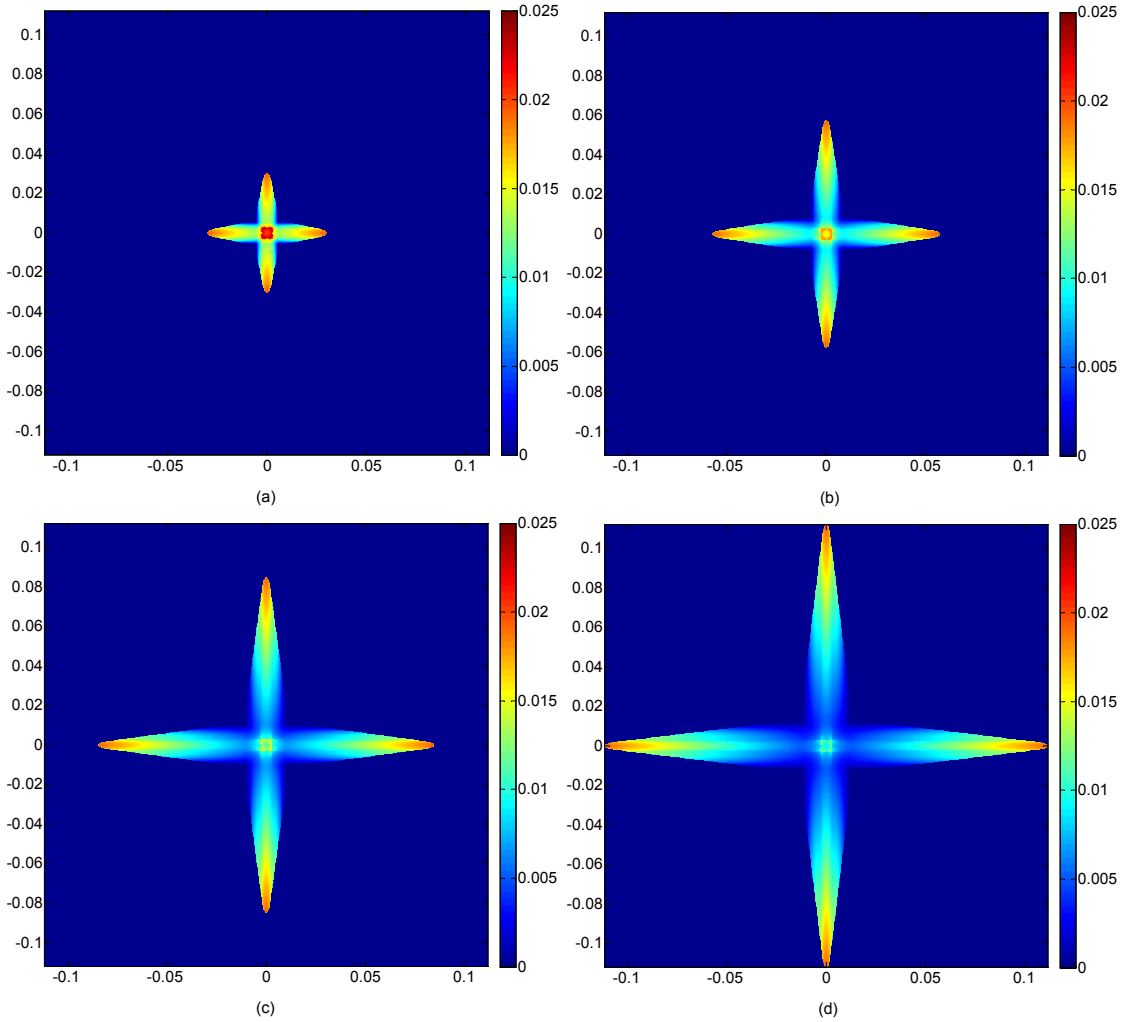

Figure 3.30: The evolution of effective strain $\sqrt{\varepsilon_x^2 + \varepsilon_y^2}$, FSP projectile: (a) $\tau = 10$; (b) $\tau = 20$; (c) $\tau = 30$; (d) $\tau = 40$.

times. When $\tau = 20$, the strain around projectile edge decreases quickly, and the square high-tension red region around the projectile at $\tau = 10$ has diminished substantially by $\tau = 20$. Approaching the cone wave-front, the strain contour becomes a diamond with diagonals along the axes. By $\tau = 40$, however, there are two yarn sets with the width of $\sqrt{2}r_p$ going underneath the projectile and extending up to the tensile wave front. The strain pattern in the center now looks like a "#" sign.

Comparison with DSM results

As further validation of the Cornell semi-analytical model, Figs. 3.31-3.33 shows a comparison between the Cornell model and DSM-based model of the slope distribution, strain distribution in the x-direction yarns, and effective strain $\sqrt{\varepsilon_x^2 + \varepsilon_y^2}$ behind the tensile wave fronts. In the slope comparison, the high slope region in the Cornell model has slightly lower slopes than in DSM model. This is due to the approximation used calculate the vertical displacement at each point in the region. The displacement is not continuous and thus the slope at each point is not continuous, either. Actually when we check the results at some key points, such as the cone wave front or projectile edge, as shown in Fig. 3.24(a), the results are consistent with the DSM results.

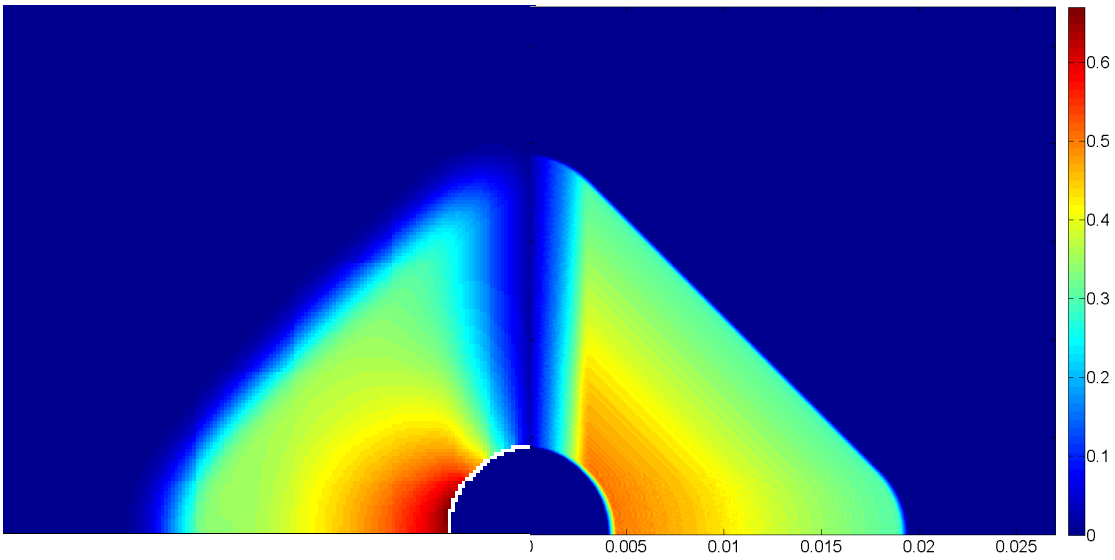

Figure 3.31: Comparison of slope (local cone wave obliqueness with respect to the ground) distribution, 9 mm projectile: left, DSM model; right, Cornell model.

In the Cornell model, we have a sharp strain boundary at the tensile wave front in each yarn. Beyond the tensile wave front in a certain yarn, the strain

steps down to zero immediately. In the DSM model, the calculation is executed on each grid point in the domain, and the strain transformation across the tensile wave front is intermittent but relatively smooth, so there is always a light blue "buffering" region before the strain goes to zero in DSM plots.

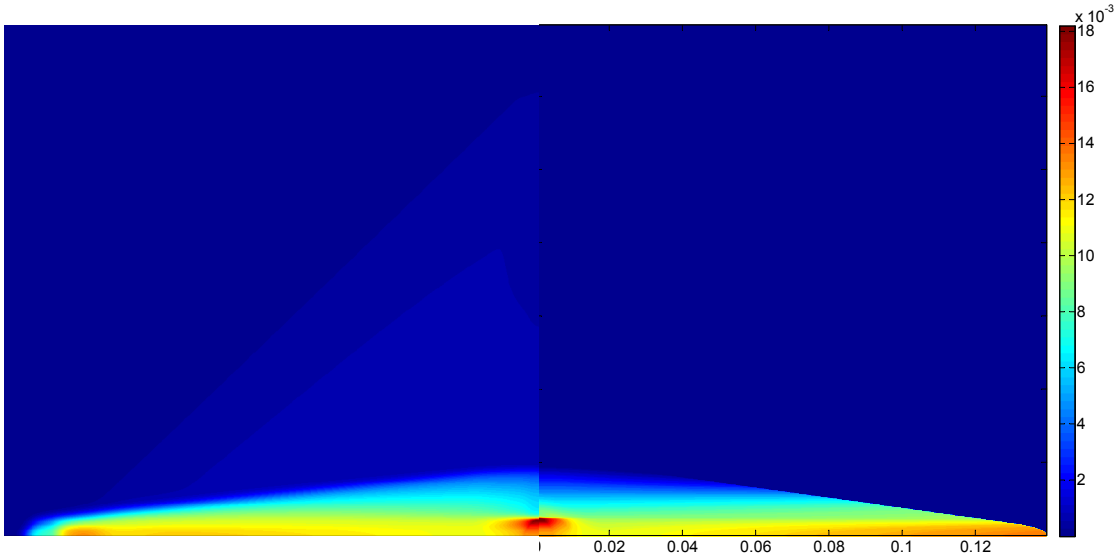

Figure 3.32: Horizontal strain ε_x, 9 mm projectile: left, DSM model; right, Cornell model.

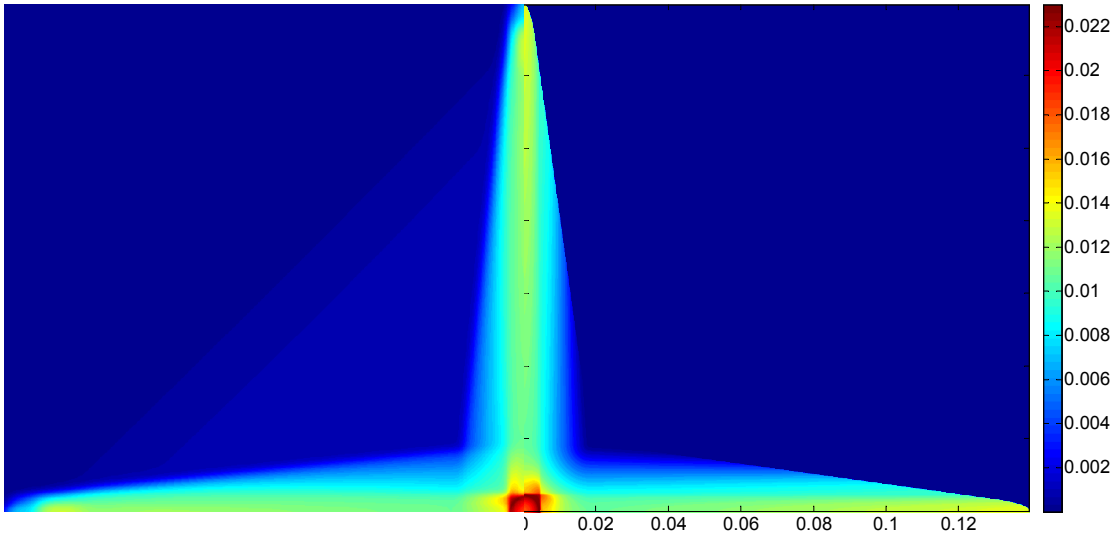

Figure 3.33: Effective strain $\sqrt{\varepsilon_x^2 + \varepsilon_y^2}$, 9 mm: left, DSM model; right, Cornell model.

The three groups of comparison are consistent with each other, indicating our assumptions, implementations of key phenomena seen in the DSM simulations and the analytical model itself has been successful. The simulation results are exactly as expected and have reflected the mechanical behavior of the membrane after the impact of the projectile. Using a semi-analytical approach based on some assumptions constructed from the DSM simulation results, we have been able to develop a much faster, computationally effective and accurate model that can be further expanded to multi-layer cases.

Summary

We have studied and contrasted the behavior of several key quantities of importance in characterizing the impact of 9 mm and FSP projectile int a bia-axial fabric. Regarding the comparison, there are several points that should be made:

(1) The strain distribution from the projectile edge to the cone wave front is not dependent on the projectile mass, radius, and initial velocity, but rather it depends on the material properties on the material properties.

(2) The strain variation with time is mostly dependent on projectile mass through the areal density ratio. A projectile with high mass induces an initially growing strain in the membrane ,which eventually can peak at a large value compared to the initial value on impact, and then decays. A low mass projectile can induce a high strain initially but that strain may increase only modestly over a short time before decreasing fairly rapidly.

(3) Related to the second poinht, is the fact that the displacement of the projectile over time is not just dependent on its initial velocity, but also on its mass,

with lower mass projectiles generating less displacement.

(4) When impacted by a heavy projectile (9 mm), the membrane may survive initially but fail much later, while in the case of a light projectile (FSP), it will fail almost immediately after impact at a strain close to that on impact or will not fail at all.

(5) The location of critical yarn failures can differ for a high mass versus a low mass projectile. For a high mass projectile the critical yarn failures will be transversely off axis at a lateral distance of about 90 percent of the projectile radius, whereas for a very low mass projectile the critical yarn failures will occur along the main yarn axes.

(6) If the membrane doesn't fail, at later times the peak strain is at projectile edge if the projectile is heavy (9 mm), but occurs at the tensile wave front if the projectile is light (FSP).

(7) The Cornell semi-analytical model is very accurate and much more efficient in calculation time than the Cornell-modified DSM model.

3.4.4 Further exploration of the single-ply model

We investigate further some key parameter relationships after impact, and for this we consider how we might define the safety of body armors insofar as projecting the wearer. There are two aspects affecting whether the body armor is effective: (1) How powerful the projectile is. (2) How robust the membrane behavior is.

Assuming the masses of the 9 mm and FSP projectiles are constant, then the energy is only dependent on its initial velocity. If we could estimate the peak strain caused by a specific projectile at a certain speed, it would be easy to determine whether the membrane would fail.

For a given material, the membrane effectiveness mainly depends on the membrane's thickness. In the Cornell model, the thickness of the armor membrane is reflected by the material's density and areal density, and thus, we adopt areal density as the key variable in the following analysis. Note that in the 9 mm and FSP cases, we have used different 'membrane' panels with areal densities 3.0 kg/m^2 and 4.89 kg/m^2, respectively, even though the 9 mm projectile has the higher mass.

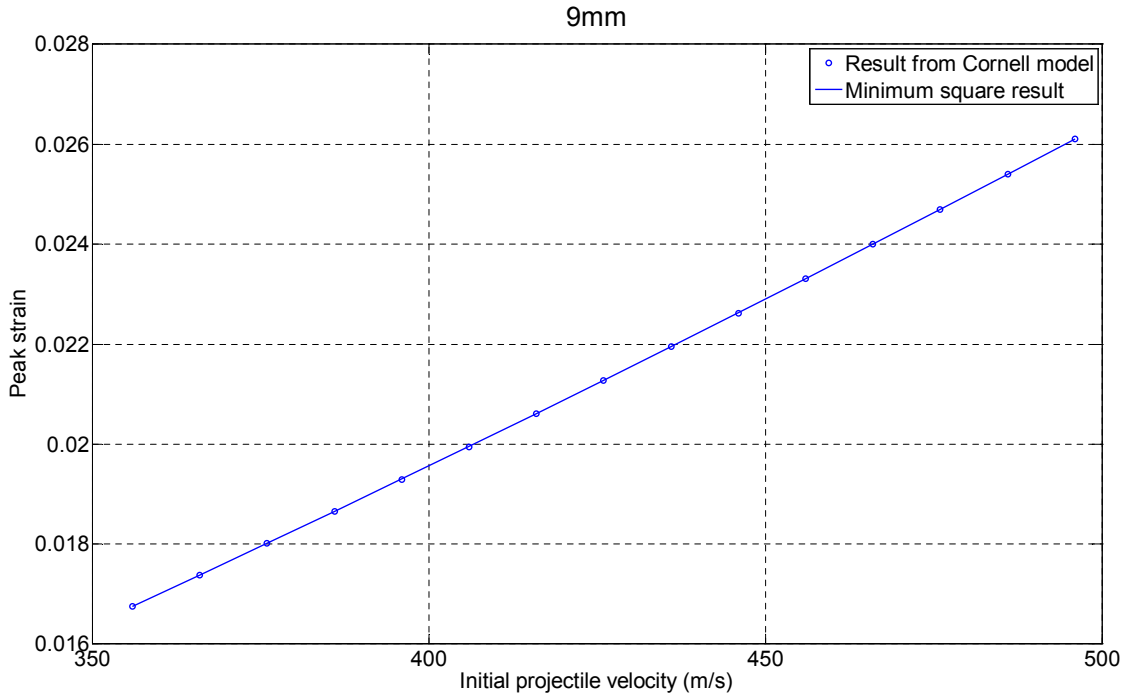

Figure 3.34: The effect of initial projectile velocity on peak strain, 9 mm.

Figs. 3.34 and 3.35 show the effect of initial projectile velocity on peak strain in the 9 mm and FSP cases. For the Cornell semi-analytical model, in both cases

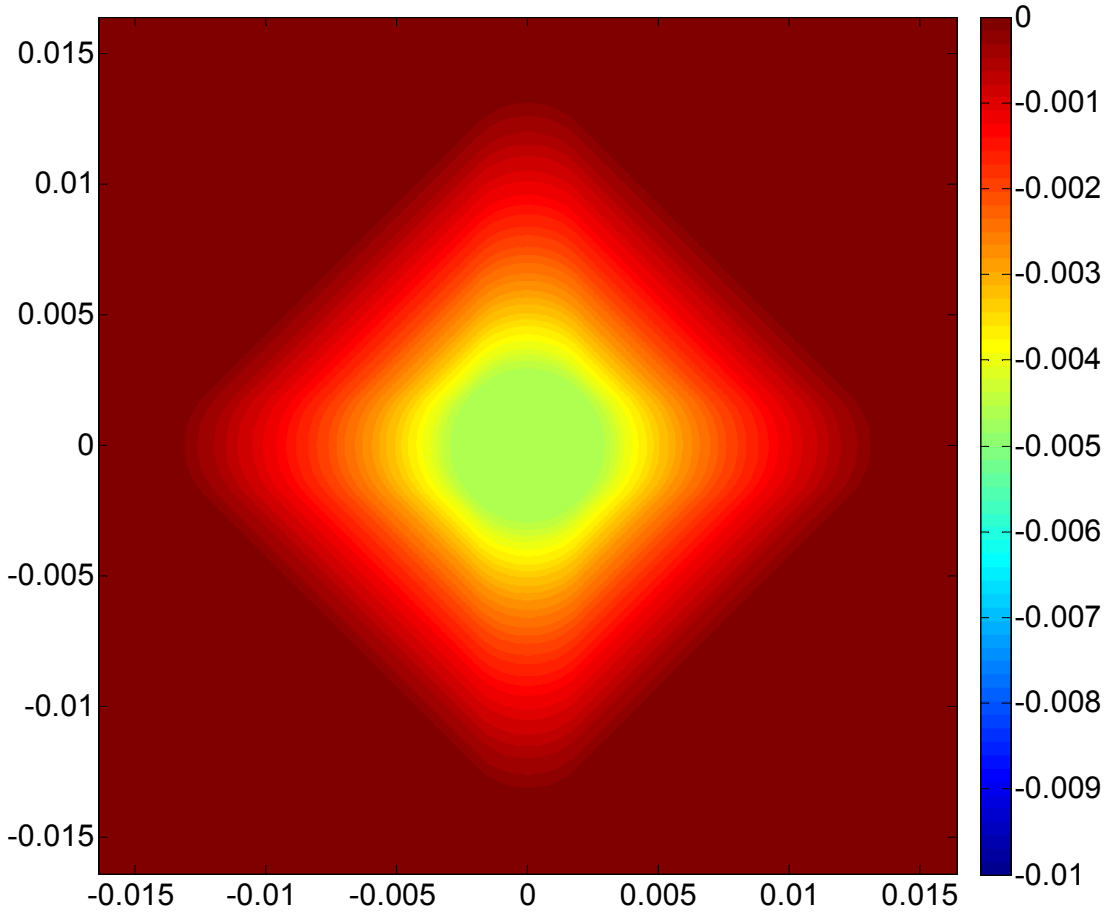

Figure 3.35: The effect of initial projectile velocity on peak strain, FSP.

the the peak strain increases fairly linearly with initial projectile velocity, though the curve is actually a complicated function. In the 9 mm case, when the initial projectile velocity increases from 356 m/s to 496 m/s, or an increment of about 40%, the peak strain goes from 0.01675 to 0.0261, an increase of 56%. In the FSP case, however, when the projectile velocity is increased from 518 m/s to 658 m/s (27% increment), the peak strain increases from 0.0172 to 0.0238, or about a 38% increment. If we compare the increment ratio of strain/velocity, in the 9 mm case it is 56%/40% = 1.4, and in the FSP case, it is 38%/27% = 1.4, so virtually the same. Therefore, the increment ratio of strain over projectile velocity is apparently fairly independent of details such as projectile speed, mass, front

nose radius, and material thickness etc.

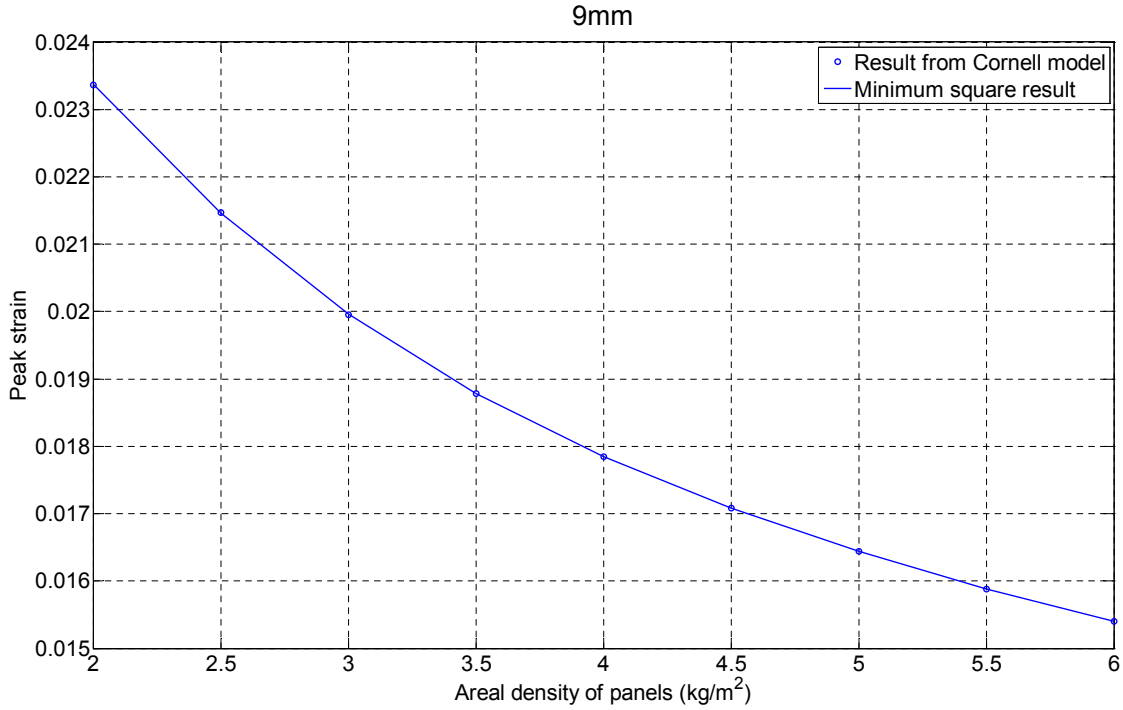

Figure 3.36: The effect of areal density on peak strain, 9 mm.

Figs. 3.36 and 3.37 show the effect of the armor panel's areal density on peak strain. As shown in Table 3.1, the areal densities for the 9 mm and FSP projectiles are different, namely 3.00 kg/m^2 and 4.89 kg/m^2 respectively. This is due to the latter having more fiber layers than the former, although we treat them both as membranes. In the Cornell model, the membrane's thickness is calculated from its areal density, divided by its density, which is constant, so the areal density is again proportional to the membrane's thickness.

In the 9 mm case at 406 m/s (Fig. 3.36), the peak strain decreases with areal density smoothly but nonlinearly, again as a complicated function. In the FSP case at 568 m/s (Fig. 3.37), the peak strain in terms of areal density shows two fairly linear regimes with a kink in between, depending on whether the areal density is above or below about 4.0 kg/m^2. The reason for this behavior is

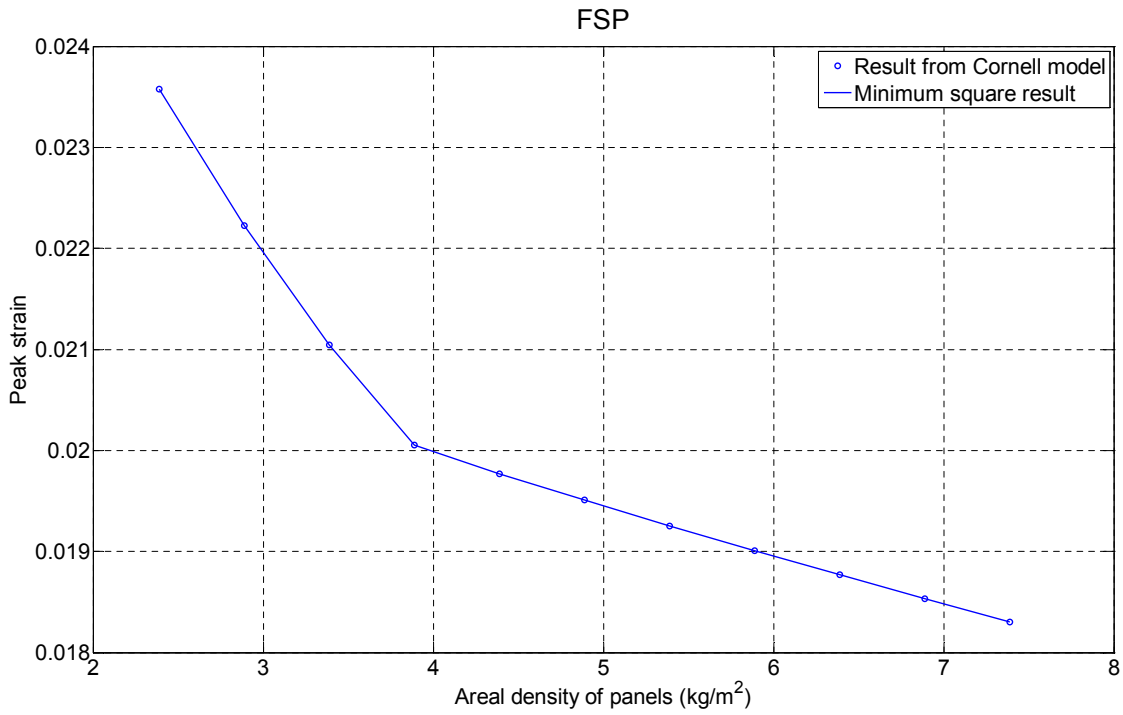

Figure 3.37: The effect of areal density on peak strain, FSP.

related to the fact that at an impact velocity of $V_0 = 568$ m/s and nominal areal density of 4.89 kg/m^2, the peak strain nominally occurs fairly soon after impact, so is very close to the strain on impact, as shown in Fig. 3.23. This situation remains the same for higher areal densities. However as the areal density is reduced below about, 4.0 kg/m^2, the peak strain starts to occur later and later and involves an increasingly large build-up of strain beyond the initial strain generated at impact. For this reason, the peak strain starts to grow rapidly as the areal density is decreased whereas the initial strain would follow an extension of the line for higher areal densities.

From the discussions above, we can see that the peak strain is highly affected by the initial projectile velocity and membrane thickness, or its areal density. The peak strain and initial projectile velocity have a near-linear relation (in the range studied), whereas the relation between the membrane's thickness and

peak strain is more complicated.

3.4.5 Three-layer system with gaps

We now consider the behavior of multi-layer systems that consist of several individual single layers with small air gaps between them. The objective is to investigate the effect of having gaps between these layers on the peak strain and other strain curves with respect to time. The projectile velocity deceleration and cone wave development in each layer are also of interest. The results will be compared with their single-layer counterparts, i.e. the single-layer case with the membrane's thickness equal to the total thickness of all three layers. If one or more layers are penetrated after impact, we will refer to such a case as a "penetration case"; otherwise, we will call such case a "non-penetration case". We first consider a three-layer system.

Non-penetration cases: 9 mm

In the 9 mm case, we use the same parameters as listed in Table 3.1. The gap between layers 1 and 2 and between layers 2 and 3 is 2 mm. The maximum distance allowed is 8 mm, which is about the same vertical displacement as obtained in the single-layer, 9 mm case above. The motivation is to investigate how the projectile is decelerated throughout a certain vertical displacement, over which the projectile has traveled. Note that in the single-layer case, the time consumed to reach an 8 mm displacement is about $\tau = 37$. When comparing to the behavior in the single-layer case below, we refer to the behavior at $\tau = 37$.

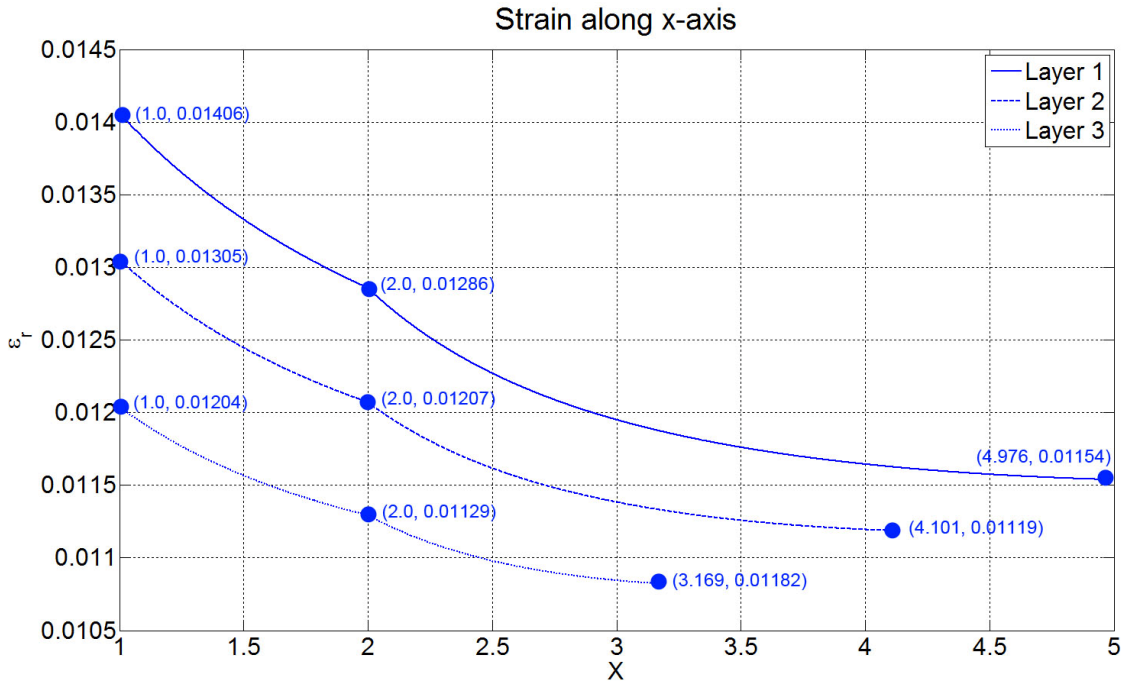

Figure 3.38: Strain distribution along the x-axis from the projectile edge to the cone wave front in a three layer system, with a layer gap of: 2 mm, vertical displacement: 8 mm, projectile type: 9 mm.

Fig. 3.38 shows the strain distribution along the x-axis from the projectile edge to the cone wave front in each of the three layers. From the pairs of values given in Fig. 3.38, we can see that at $X = 1$, $X = 2$ and cone wave front, the strain in Layer 2 is always approximately the average of those in Layer 1 and Layer 3. Therefore it is reasonable to infer that the behavior of in the middle layer is roughly the average of all the all the layers in the multi-layer case.

Fig. 3.39 shows the various strain profiles over time in the 9 mm case. The solid lines are the results of the 1st layer, the dashed lines are for the 2nd layer and the dotted lines are for the 3rd layer. Line colors have been shown in the legend and correspond to the various strains, ε_p, $\varepsilon_{p,\max}$, $\varepsilon_{p,\text{avg}}$, ε_c and $\varepsilon_{c,\text{avg}}$.

Early on when the projectile has displaced only the first layer ($\tau < 8$), the

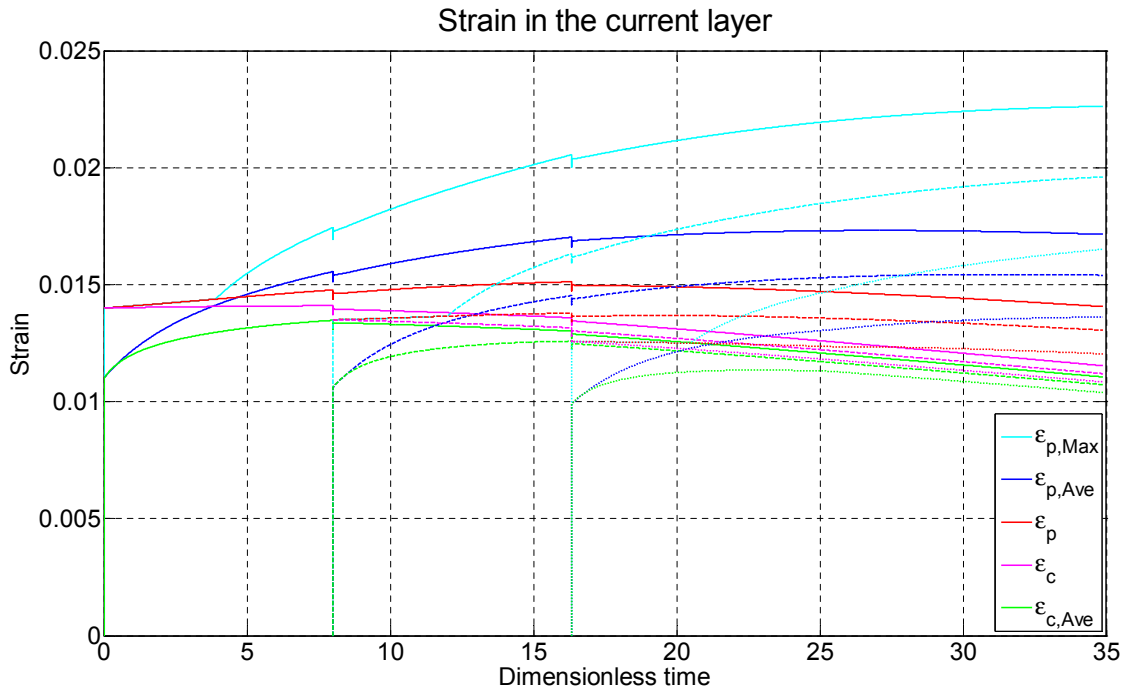

Figure 3.39: Various strains versus time in the three layers, layer gaps: 2 mm, vertical displacement: 8 mm, projectile type: 9 mm.

curves are exactly the same as those shown in Fig. 3.12. However, when the projectile has traveled just far enough for the second layer to feel the impact and to suddenly begin moving with the projectile, there is a small but sudden drop in projectile velocity (Fig. 3.40) governed by conservation of momentum, and consequently there is also a sudden drop in local strain around the projectile. Nonetheless, the peak strain $\varepsilon_{p,\max}$ and average strain around projectile $\varepsilon_{p,\text{avg}}$ continue to increase in the 1st layer, as happened in Fig. 3.12. Note that $\varepsilon_{p,\max}$ in the 1st layer reaches a higher value than that in Fig. 3.12, since each layer has only 1/3 of the original thickness and so there is a delay in engaging all the layers and in decelerating the projectile. Thus it is reasonable that $\varepsilon_{p,\max}$ in the 1st layer, and possibly the 2nd layer, are higher than $\varepsilon_{p,\max}$ in the single-layer counterpart, as long as the average of the three layers is similar to the behavior of the single-layer counterpart with three times the thickness.

When the projectile strikes the 3rd layer, the process is similar. There is a sudden, small drop in projectile velocity, and after small corresponding drops, the strains $\varepsilon_{p,\max}$ and $\varepsilon_{p,\text{avg}}$ in the 1st and 2nd layer continue increasing for some time. Note that $\varepsilon_{p,\max}$ and $\varepsilon_{p,\text{avg}}$ in the 3rd layer are lower than the average, and thus lower than for a single-layer having three times the thickness.

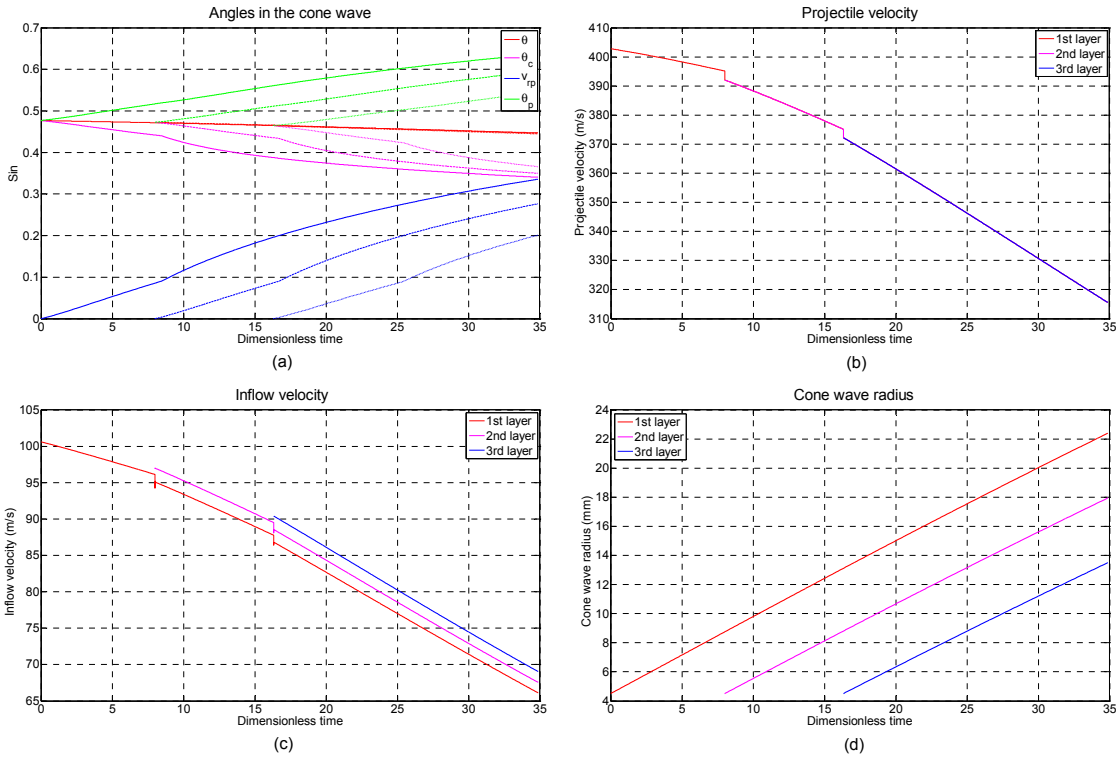

Figure 3.40: Results for some important model quantities for layer gap: 2 mm, final vertical displacement: 8 mm and projectile type: 9 mm: (a) Angles at the cone wave front (θ_c) the projectile edge (θ_p), the effective cone wave angle θ and the angle difference $V_{rp} = |\theta_c - \theta_p|$; (b) projectile velocity; (c) inflow velocity and (d) cone wave radius R_c.

Fig. 3.40 shows some key parameters in the 3-layer 9 mm case with a gap between layers of 2 mm. The solid, dashed and dotted lines correspond to behavior in 1st, 2nd and 3rd layers, respectively, as in the previous figures. In panel (a), the effective angle θ, the obliqueness of a virtual line connecting the

cone wave front and projectile edge at $Y = 0$, is almost the same in the three layers at any given time. Therefore there is no interference between layers outside of the contact patch, when the projectile strikes a new layer. Furthermore, we have $\theta_{p,1} > \theta_{p,2} > \theta_{p,3}$ and $\theta_{c,1} < \theta_{c,2} < \theta_{c,3}$ (the numbers 1, 2 and 3 denote different layers), and the curvature in the 3rd layer is the highest among the three layers, which again is consistent with previous analysis since the times since impact is the longest.

In panel (b), the velocity curve has two sudden drops each time when the projectile strikes a new layer. Also the deceleration becomes faster as more layers are engaged. In panel (c), the inflow velocity in the 1st layer also has two sudden drops and the deceleration is faster as time goes on. Whenever the projectile strikes a new layer, the inflow velocity in the new layer becomes higher than that in the previous layer because of the effective time-lag, so finally we have $\dot{u}_{c,1} < \dot{u}_{c,2} < \dot{u}_{c,3}$. Their average is almost an extension of the line of the inflow velocity before the projectile strikes the 2nd layer.

In panel (d), the cone wave radius grows linearly with time, and the difference in radius between Layer 1 vs. Layer 2 and Layer 2 vs. Layer 3 is almost the same, indicating that the cone wave speed is almost constant over time and among layers, and it is fairly insensitive to projectile deceleration.

Fig. 3.41 shows the vertical displacement of the three layers. As discussed above, the curvature becomes higher from top to bottom so there is no interference between layers when striking a new layer. The effective angles of the three layers are almost the same, and thus, the cone wave front in the three layers and the projectile edge are on the same line.

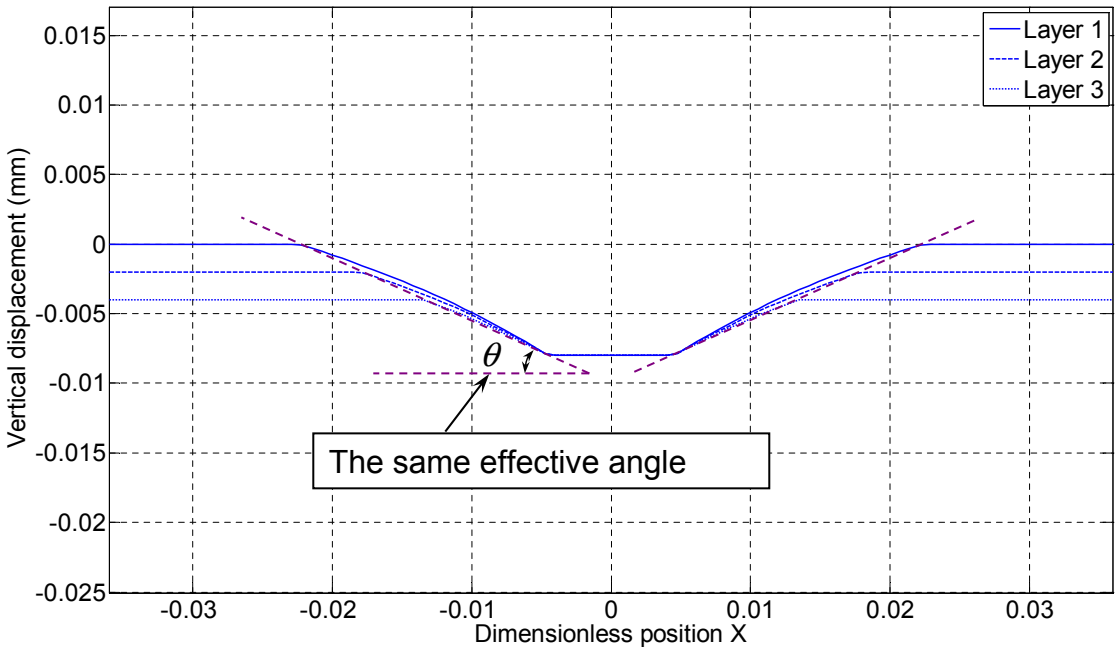

Figure 3.41: Vertical displacements of the three layers, layer gap: 2 mm, vertical displacement: 8 mm, and projectile type: 9 mm.

Next we consider the effect of the the layer gap size on the projectile deceleration, various strains and certain other key quantities. We consider the case of a 9 mm projectile and assume a layer gap of 3 mm, but the values of all the other parameters are held fixed. Fig. 3.42 shows the strain curves versus time for this situation, and upon comparing the behavior to that seen in Fig. 3.39, several differences are noted:

(1) The differences in the layer strains ($\varepsilon_{p,\max}$ and $\varepsilon_{p,\text{avg}}$ etc.) for the three layers are larger than for the case having 2 mm layer gaps, i.e. the strain in Layer 1 becomes higher while the strain in Layer 3 becomes lower. When the layer gap is increased, Layer 1 must carry the load by itself for a longer time and Layer 3 does not become involved until an even later time.

(2) The time required to reach a certain displacement (8 mm in our calcu-

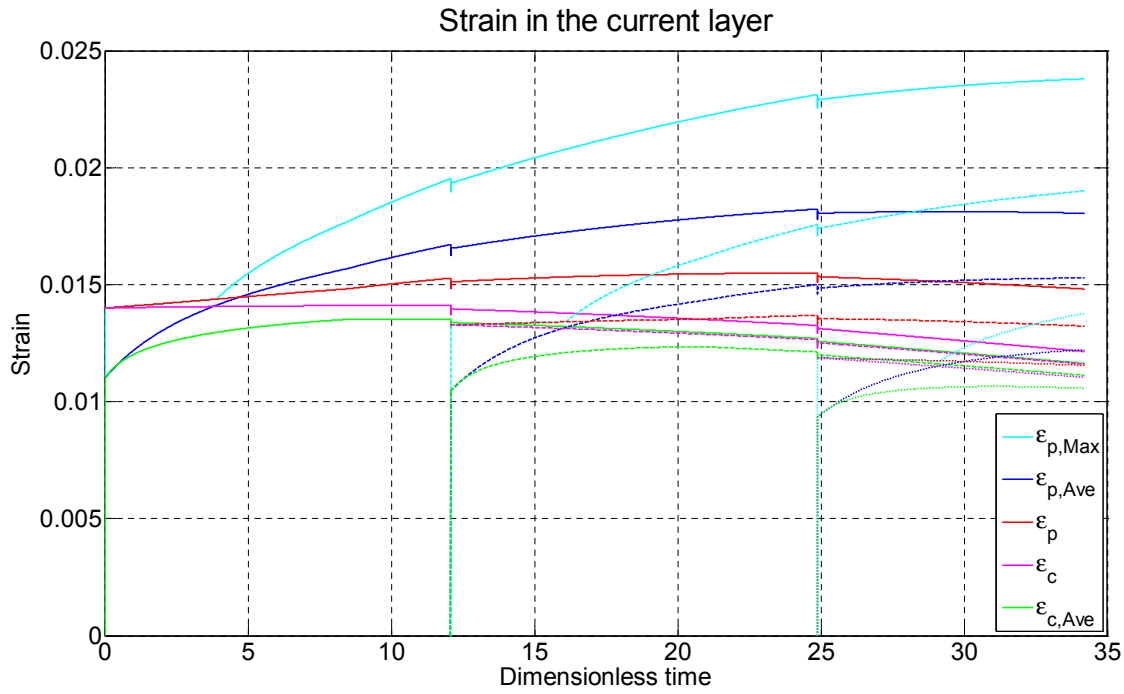

Figure 3.42: The strain curves in the three layers, with layer gap: 3 mm, vertical displacement: 8 mm, and projectile type: 9 mm.

lation) becomes slightly shorter, being $\tau = 34.5$ when the layer gaps are 3 mm versus $\tau = 35$ when the layer gap is just 2 mm. The reason is similar to the discussion in (1). Layers 2 and 3 join in the projectile deceleration later in time, so the projectile deceleration is smaller and the velocity is higher throughout the impact and deceleration process.

(3) At a certain vertical displacement, the final average strain ($\varepsilon_{p,\max}$, $\varepsilon_{p,\text{avg}}$ etc.) is almost the same, though it appears at a later time in the case of 3 mm layer gaps. However the strain in Layer 1 reaches a higher value than in the case of 2 mm layer gaps.

Fig. 3.43 shows the behavior of several important quantities when the layer to layer gap is 3 mm. In panel (a), compared with Fig. 3.40(a), the differences in (θ_c and θ_p), from layer to layer are now larger, but the effective angles of the

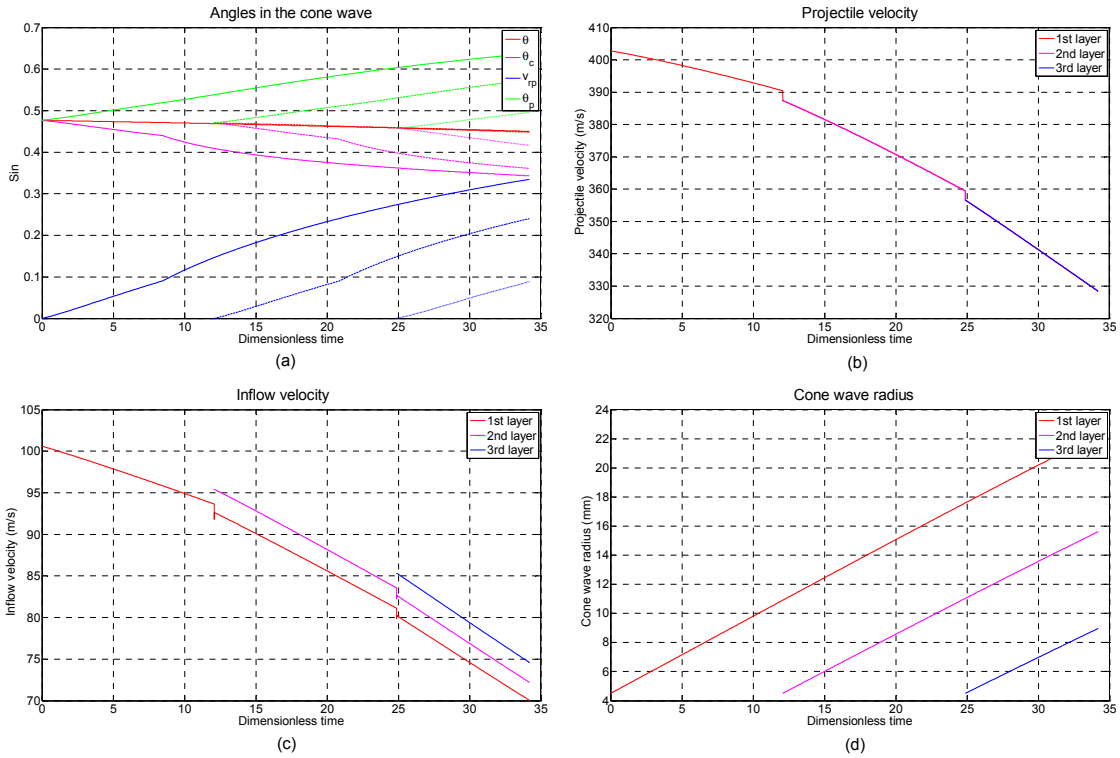

Figure 3.43: Behavior over time after impact of several important quantities for the case layer gap: 3 mm, and projectile type: 9 mm: (a) Angles at the cone wave front (θ_c), the projectile edge (θ_p), and the effective cone wave angle θ as well as the angle difference $V_{rp} = |\theta_c - \theta_p|$; (b) the projectile velocity; (c) inflow velocity and (d) cone wave radius R_c.

three layers are about the same at any time, as we saw also in the case of 2 mm gaps. In panel (b), the residual projectile velocity is about 329 m/s, while in Fig. 3.40(b), it was about 315 m/s. In panel (c), similar to what we saw in panel (b), the residual inflow velocity is higher than that in Fig. 3.40(c), and the disparity among the different layers also becomes higher. Therefore larger layer gaps lead to larger residual projectile velocity and a larger disparity in inflow velocity between the different layers. In panel (d), as compared with panel (d) in Fig. 3.40(d), the time lag between layer engagement becomes larger, but the cone wave velocities (the slopes of the curves) do not change and are about the

same as for 2 mm gaps.

Non-penetration cases: FSP

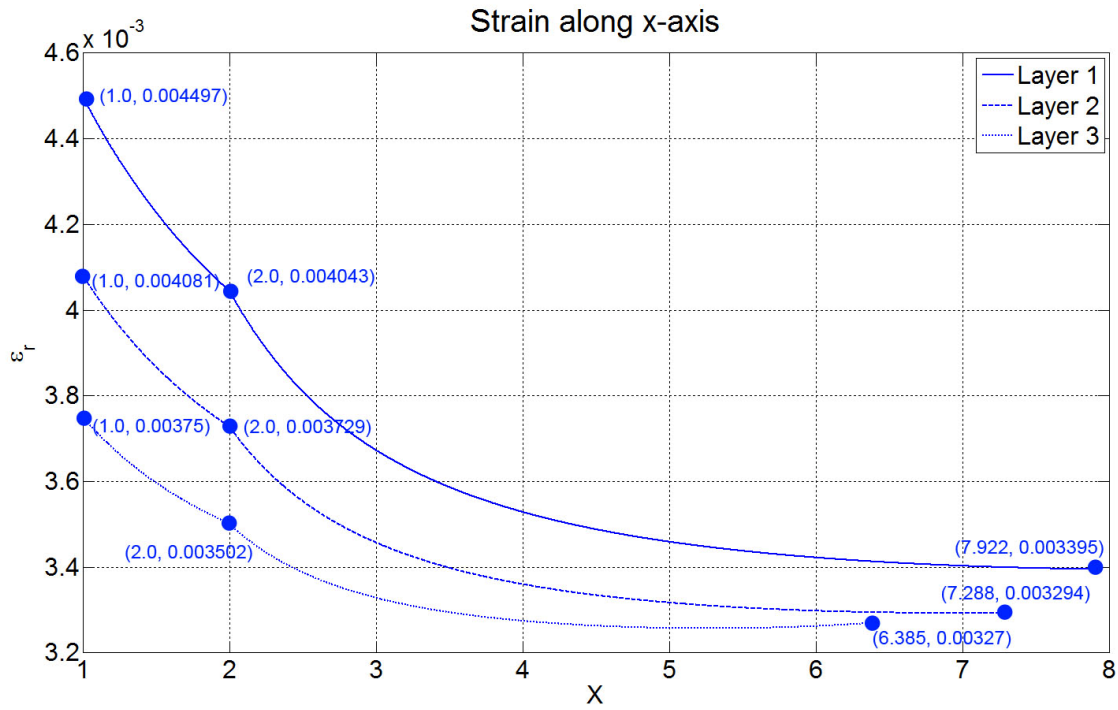

Figure 3.44: Strain distribution along the x-axis from the projectile edge to the cone wave front in the three layers for layer to layer gap: 2 mm, vertical displacement: 8 mm, and projectile type: FSP.

Next we consider the behavior of key quantities in the case of an FSP projectile. Fig. 3.44 shows the strain distribution along the x-axis from the projectile edge to the cone wave front in the three layers. The numerical strain values for the middle layer, Layer 2, are no longer the average of the other two. After being decelerated by Layer 1, the projectile doesn't have enough remaining velocity to induce a high strain in subsequent layers. The strain at the cone wave front in all the layers levels out when the displacement of the projectile approaches 8 mm, the point where the plots terminate.

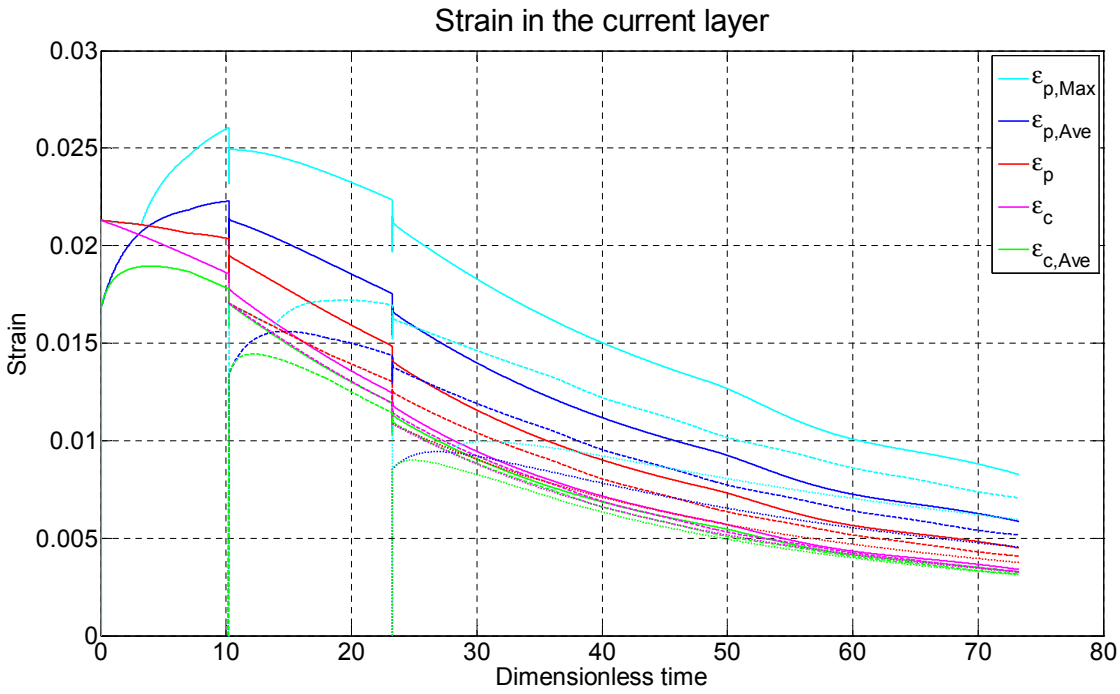

Figure 3.45: Various strains versus time in the three layers for a layer gap: 2 mm, maximim vertical displacement: 8 mm, and projectile type: FSP.

Fig. 3.45 shows strain curves for the three-layer case of an FSP projectile and with a 2 mm layer to layer gap. Unlike the single-layer counterpart, the peak strain $\varepsilon_{p,\max}$ in Layer 1 significantly increases after the impact of the projectile. When the projectile hits Layer 2, there is a sudden velocity drop, and the corresponding drop in the strains is much larger than that in the 9 mm projectile case. Note that the FSP projectile's mass is much lower than that of the 9 mm projectile (1.1 g vs. 8.0 g), but each layer's thickness is larger (4.89/3 = 1.63 mm vs. 3.00/3 = 1.00 mm), so when the velocity is decreased early on, the projectile can no longer sustain high strains any more. After that, all key strains in Layer 1 decrease. The strains in Layer 2 have a similar pattern, though starting from lower values. When the projectile hits Layer 3, similar but smaller strain patterns can be observed.

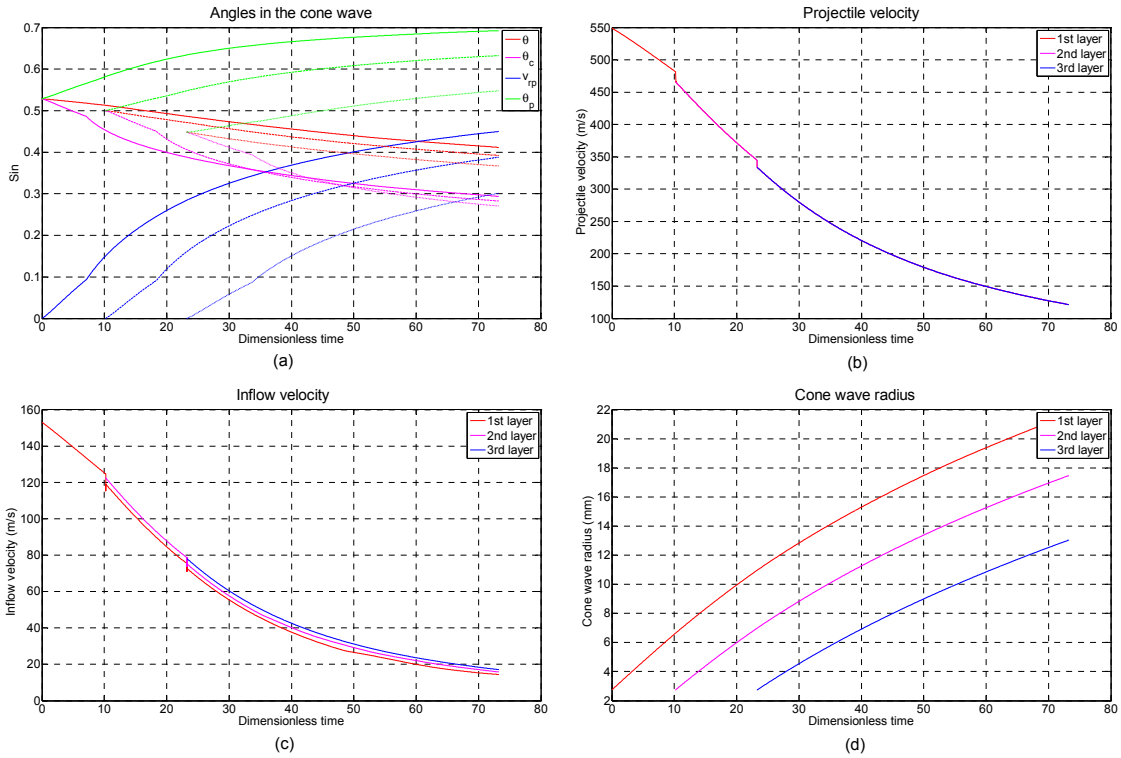

Figure 3.46: Results of some important parameters. Layer gap: 2 mm, vertical displacement: FSP: (a) Angles at cone wave front (θ_c) and projectile edge (θ_p), effective cone wave angle θ and $V_{rp} = |\theta_c - \theta_p|$; (b) projectile velocity; (c) inflow velocity and (d) cone wave radius R_c.

Fig. 3.46 shows some important parameters in the case of an FSP projectile. In panel (a), similar to what occurred in the 9 mm case, we have $\theta_{p,1} > \theta_{p,2} > \theta_{p,3}$ and $\theta_{c,1} < \theta_{c,2} < \theta_{c,3}$, indicating that there is again no interference when the projectile strikes a new layer. However, we also have $\theta_1 > \theta_2 > \theta_3$, different from what we saw in Fig. 3.40(a) where the effective angles in different layers were roughly equal to each other. In panel (b), different from the convex deceleration curve seen in the 9 mm case (Fig. 3.40(b)), the deceleration curve in the FSP case is concave upward. The projectile has decelerated faster initially, but the deceleration slows later on. The inflow velocity in panel (c) has a similar pattern to the vertical velocity. In panel (d), different from 9 mm case, the cone wave

curve is convex, indicating the cone wave velocity is faster initially and then slows down due to the low strain in the membrane. Note that the total distance the projectile has traveled is 8 mm, the same as in 9 mm case, but the time consumed is much longer ($\tau > 70$ vs. $\tau = 35$).

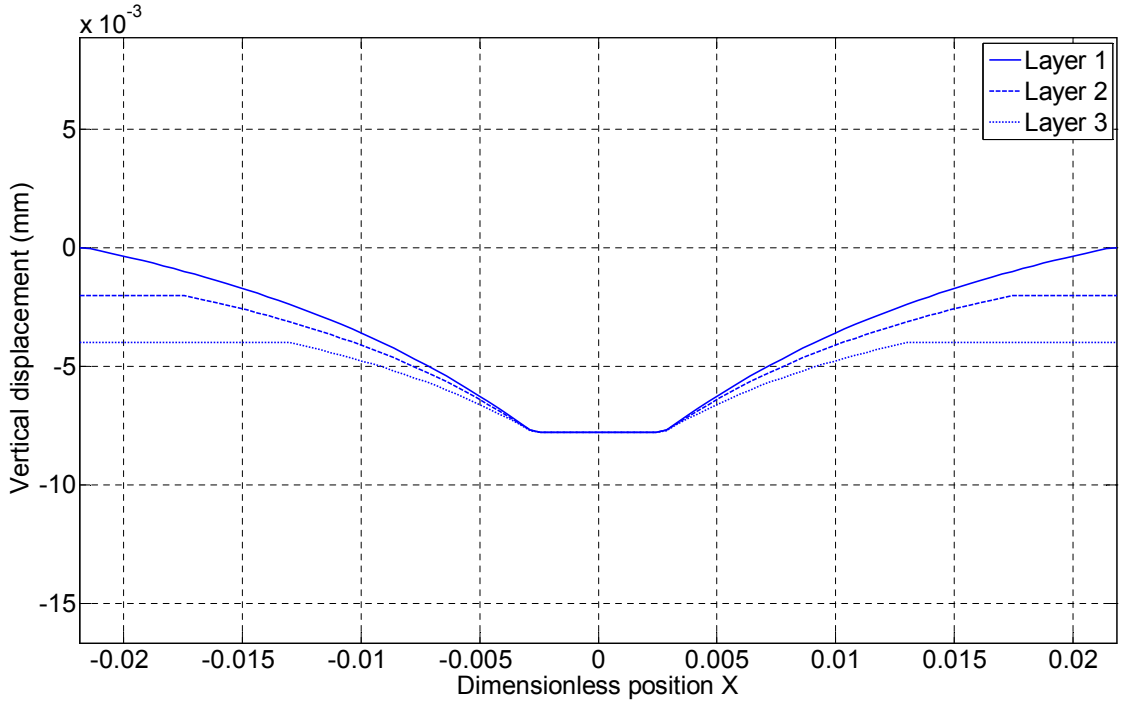

Figure 3.47: Vertical displacements in the three layers with layer gap: 2 mm, vertical displacement: 8 mm, and for projectile type: FSP.

Fig. 3.47 shows the vertical displacement in the FSP three-layer case. Unlike the 9 mm case, the profiles of the cone waves in the three layers are much more curved, indicating a loss of tension and thus an insufficient strain in the membrane. Consistent with Fig. 3.46(a), the effective angles in different layers are no longer equal. We still have $\theta_{p,1} > \theta_{p,2} > \theta_{p,3}$ and $\theta_{c,1} < \theta_{c,2} < \theta_{c,3}$, indicating there is no interference between layers outside the projectile contact zone.

We now consider the effect of layer gaps on impact behavior in the case of an FSP projectile where key parameters are listed in Table 3.1 and the membrane

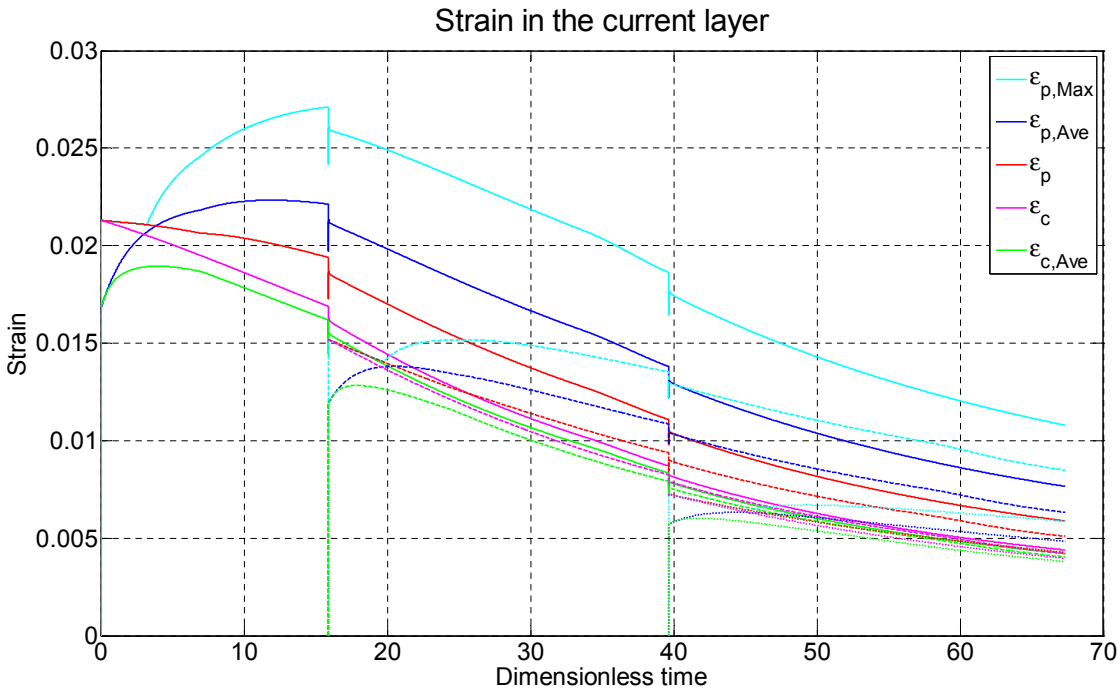

Figure 3.48: Strain versus dimensionless time in three layers. Layer gap: 3 mm, maximum vertical displacement: 8 mm, projectile type: FSP

target has been subdivided into three layers. We assume the layer to layer gap is 3 mm. Fig. 3.48 shows the strain curves versus dimensionless time for this case. Basically the observations found in the 9 mm cases are also applicable in this FSP case. However, compared to results in Fig. 3.45, for 2 mm gaps the strain in Layer 1 is higher while the strain is Layer 3 is lower, and the initial strains in Layer 2 and Layer 3 are lower. The time consumed to reach a vertical displacement of 8 mm becomes shorter as well, i.e., $\tau = 68$ vs. $\tau = 72$.

Fig. 3.49 shows some key quantities characterizing FSP impact in the case of 3 mm layer gaps. In panel (a), the effective layer angles, θ, do not change much as compared to those in Fig. 3.48(a) for the 2 mm case while θ_p values for the three layers are much lower than those in Fig. 3.48(a) when the projectile reaches a displacement of 8 mm. In panel (b), the residual projectile velocity is

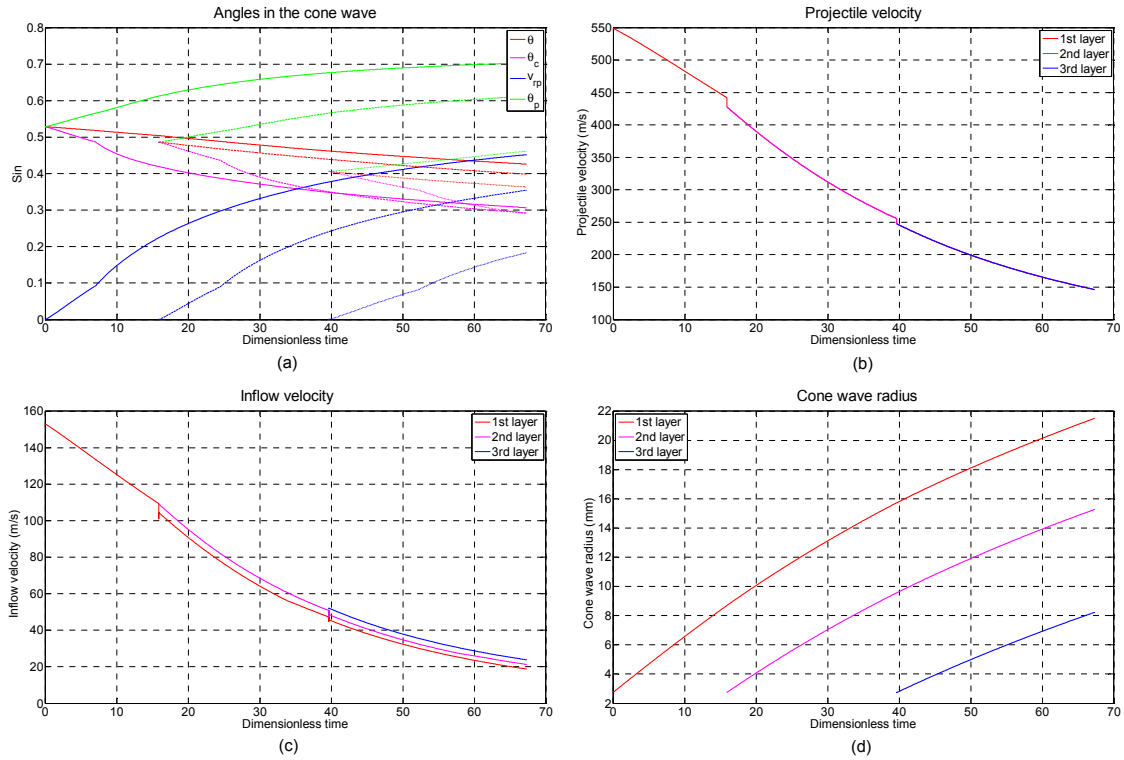

Figure 3.49: Plots over dimensionless time of some important quantities describing impact behavior. Layer gap: 3 mm, maximum vertical displacement: 8 mm, projectile type: FSP: (a) Angles at the cone wave front (θ_c) and the projectile edge (θ_p) as well as the effective cone wave angle θ and angle difference $V_{rp} = |\theta_c - \theta_p|$; (b) projectile velocity; (c) inflow velocity and (d) cone wave radius R_c.

about 150 m/s compared to 125 m/s for the case of 2 mm layer gaps or about 20% higher. In panel (c), the residual inflow velocity is a little above 24 m/s, compared to 16 m/s in Fig. 3.48(c). In panel (d), the cone wave radius grows about the same as in Fig. 3.48(d) except the starting times for Layers 2 and 3 are delayed. Increasing the layer gap thus leads to larger residual projectile velocity and inflow velocity.

Penetration cases: 9 mm

As stated earlier if one or more layers fail, we refer to such a case as a "penetration case". We assume the failure criterion is that failure occurs when the layer strain anywhere reaches 0.02 or 2 percent. We fist consider behavior for a 9 mm projectile. As with non-penetration, we consider two cases with different layer gaps, 2 mm and 3 mm, respectively. The allowance for total vertical displacement is now taken as 12 mm. All other variables remain the same.

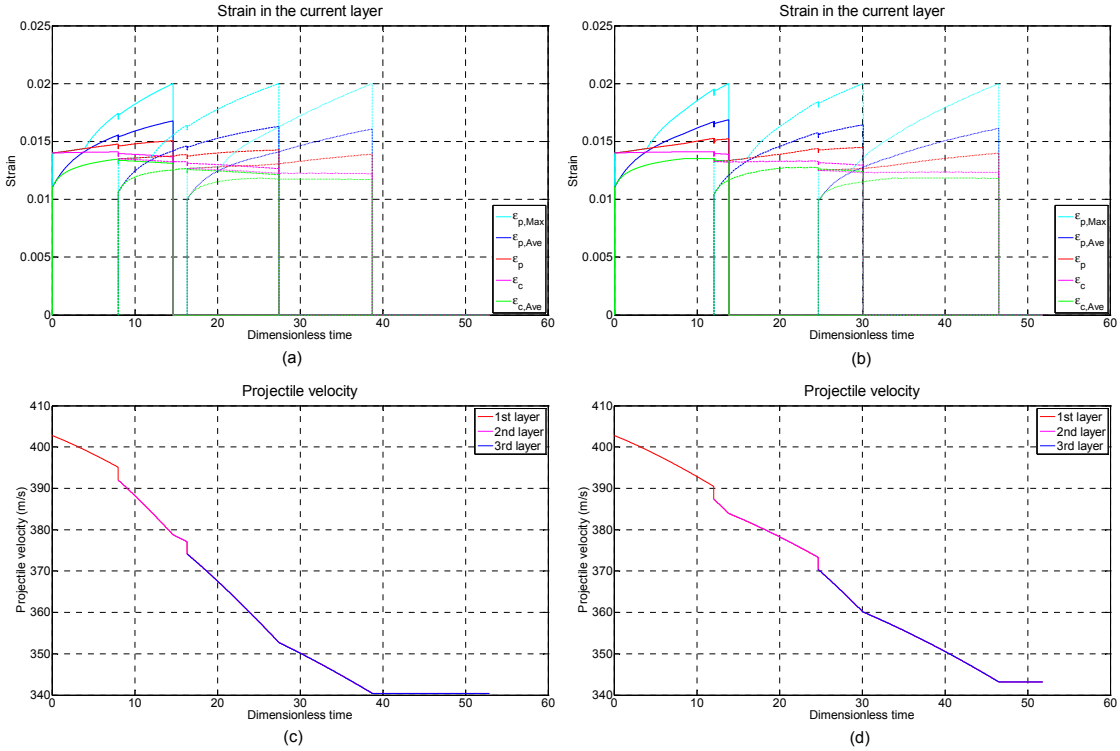

Figure 3.50: The effect of layer gap size on strain variation and projectile deceleration with time for a 9 mm projectile: (a) strain for layer gap 2 mm; (b) strain for layer gap 3 mm; (c) projectile velocity for layer gap 2 mm; (d) projectile velocity for layer gap 3 mm.

Fig. 3.50 shows results for both 2 mm and 3 mm layer gaps and a 9 mm projectile. In all cases the three layers were penetrated. Comparing panel (a) and

panel (b), we can see that the total time consumed to proceed to a certain distance (12 mm) is longer when the layer gap is smaller (τ = 55 vs. τ = 51). The reason is similar to that given above, i.e. more layers are involved in decelerating at an early stage so the projectile is decelerated more quickly. Comparing panel (c) and panel (d), the final projectile velocity in the 2 mm case, after penetrating all layers, is lower than that in the 3 mm case. Therefore, in order to lower the projectile velocity as much as possible within a certain distance, it is better to have multiple layers with no gaps and let them decelerate the projectile together, though there is a possibility that the layers would fail at the same time in this case. On the other hand, the perforation of the bullet through the first layer may involve bullet blunting. If there is at least one layer remaining unperforated in the end, it would be beneficial for safeguard the wearer. Hence when designing the body armor system, we might wish to balance considerations of decelerating the projectile within a certain distance versus having layers not penetrated by the projectile. As it turns out increasing the gap size leads to lower velocities for perforation of all layers.

Penetration cases: FSP

Next we consider penetration cases for an FSP projectile. As we know, in the FSP single-layer case, the membranes will either fail almost immediately after impact, or will not fail at all, because the FSP projectile has a mass too low to result in a large buildup in strain around its edge over time. To provide a case where not all layers fail we adjust the failure criterion whereby failure occurs whenever the strain reaches 0.025 or 2.5 percent, which is higher than the previous 0.02 value in Fig. 3.50. In panels (a) and (b) of Fig. 3.51, the first

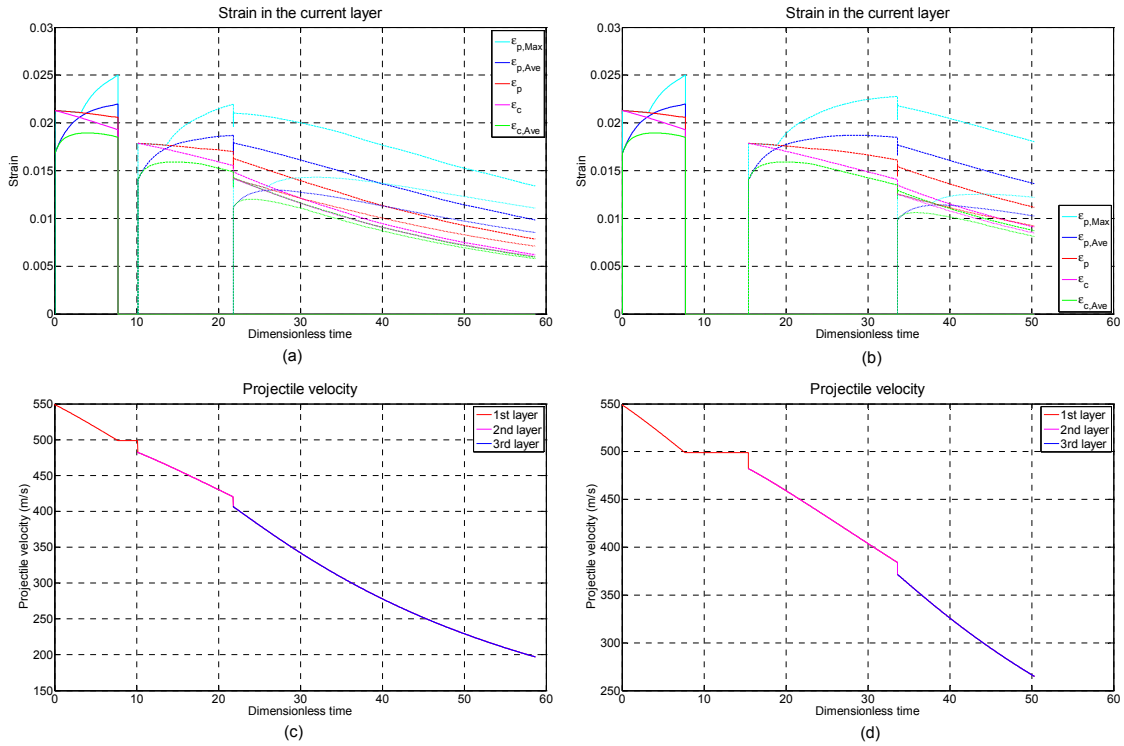

Figure 3.51: The effect of layer gap size on strain variation and projectile deceleration with time for an FSP projectile: (a) strain for layer gap 2 mm; (b) strain for layer gap 3 mm; (c) projectile velocity for layer gap 2 mm; (d) projectile velocity for layer gap 3 mm.

layer fails before the projectile strikes the second layer, so everything in the two panels is the same till the projectile hits Layer 2. After that, the patterns are similar to what we have seen before in the non-penetration case as the Layers 2 and 3 are not penetrated as the strain does not reach the value achieved by Layer 1. In panels (c) and (d), the final velocity for the 2 mm layer gap is about 200 m/s, while it is above 250 m/s for a 3 mm layer gap.

Summary

To summarize, in these three-layer cases, there are several new features in the curves plotting strain vs. dimensionless time.

(1) In order to decelerate the projectile velocity to a lower velocity within a certain distance, it is best to have a layer gap of zero, i.e. to combine all layers together. It takes longer for the projectile to reach a certain distance when the layer gap is smaller - the consequence of increased deceleration.

(2) The strain induced by the projectile in the bottom layers is higher when layer gap is larger.

(3) If no layer fails, in the case of a 9 mm projectile, the effective angles of the three layers are approximately the same at any time. However, in the case of an FSP projectile, the effective angles decrease progressively from top layer to bottom layer. The angles at the projectile edge θ_p decrease from top to bottom, and the angles at the cone wave fronts, θ_c, have the opposite order, but still indicating there is no interference between layers when striking new layers.

3.4.6 A ten-layer system with gaps

We now consider the behavior of ten-layer systems that consist of 10 individual layers with small air gaps between them. Again the objective is to investigate the effect of the layer gaps on the various strains versus time as well as the projectile velocity, deceleration and cone wave development in each layer. Again the results will be compared with their three and single-layer counterparts where the total thickness is the same in all cases. If one or more layers are penetrated after impact, we call such a case as a "penetration case"; otherwise, such a case will be a "non-penetration case". Two layer to layer gaps will be considered, 0.444 mm and 0.667 mm, so that the total layer gap is 4 mm and 6 mm respectively, and thus equal to total gap for the three-layer cases. All other

parameters remain the same as in the single and three-layer cases.

Non-penetration case: 9 mm

Again we consider behavior until the projectile travels 8 mm, the same value as used in the three-layer and single-layer cases. In the single-layer case, the time consumed to reach a 8 mm displacement is about $\tau = 37$, so in making comparisons among multi-layered cases we consider behavior at $\tau = 37$.

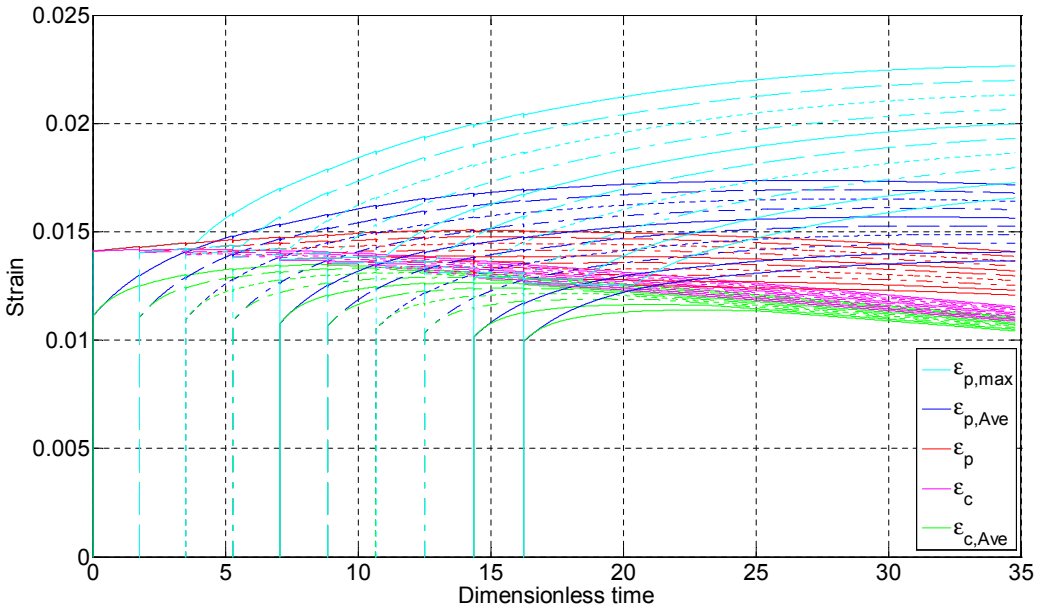

Figure 3.52: Various strains vs. time for the case of ten layers. Layer gap: 0.444 mm, vertical displacement: 8 mm, projectile type: 9 mm.

Fig. 3.52 shows the various strain curves over time for the ten-layer system gaps of 0.444 mm. Compared to the three-layer result (shown in Fig. 3.39), the strain patterns for quantities such as $\varepsilon_{p,\max}$, and $\varepsilon_{p,\text{avg}}$ do not change much. The time consumed to reach 8 mm is about $\tau = 35$, almost the same as three-layer case, and again less than for the single-layer case ($\tau = 37$). The strain $\varepsilon_{\max}$ in Layer 1 is close to that in Layer 1 in three-layer case, and the strain in Layer 10

is close to that in Layer 3 in three-layer case. The average of $\varepsilon_{\max}$ for the ten-layer and three-layer cases are roughly the same and are close to single-layer result (Fig. 3.12). However the strains in the first layer are highest. Similar correlations can be found for the other strain quantities. As was hypothesized in the case involving three-layers, in an n-layer system, the strain in the middle layer is roughly equal to the average of all the layers and equal to single-layer result, provided the time is long enough after all layers have been engaged.

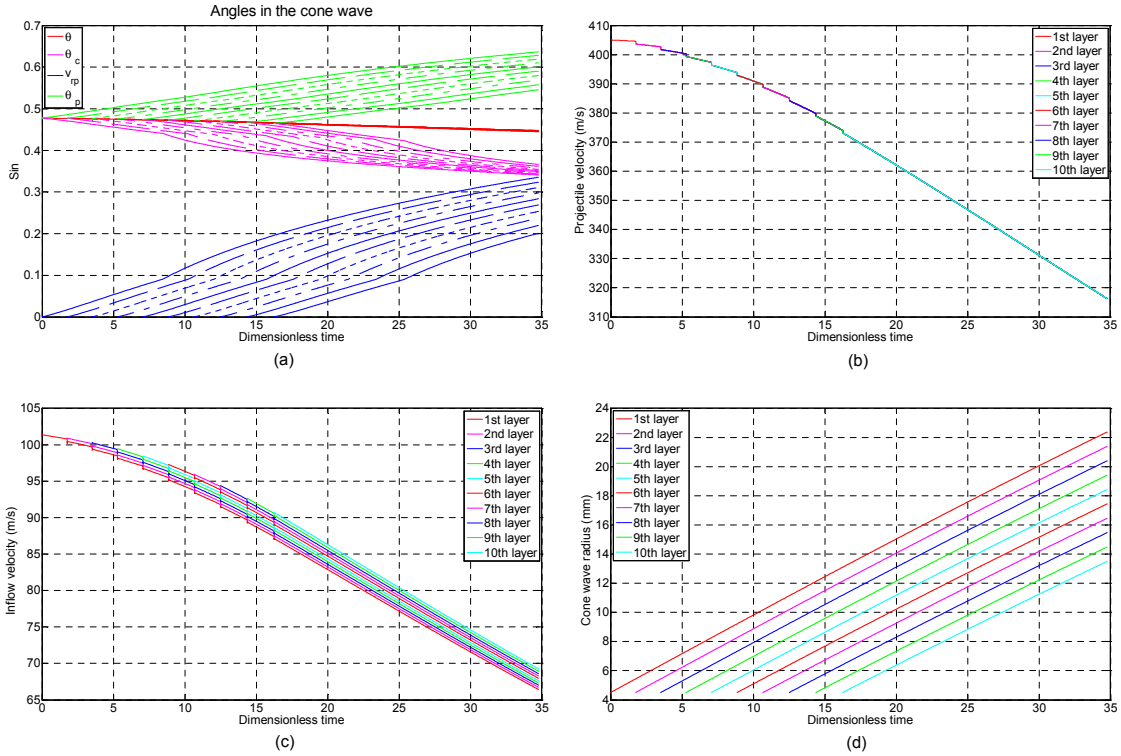

Figure 3.53: Behavior of various key quantities (0.444 mm layer gap): (a) Angles at the cone wave front, θ_c, and the projectile edge, θ_p, as well as the effective cone wave angle, θ, and the angle difference, $V_{rp} = |\theta_c - \theta_p|$; (b) projectile velocity; (c) inflow velocity and (d) cone wave radius R_c.

Fig. 3.53 shows the behavior of some important quantities following impact into 10 layers. In panel (a), the patterns and values are quite close to those shown in Fig. 3.39(a). The effective angles, θ_n, in all the layers are almost the

same, going from 0.48 to 0.45, the same as for the three-layer case. Also, $\theta_{p,1}$, the angle at the projectile edge in Layer 1, is almost the same as $\theta_{p,1}$ in Fig. 3.39(a) at any given time, while $\theta_{p,10}$ is consistent with $\theta_{p,3}$ in Fig. 3.39(a) at any given time. Additionally, θ_c in the different layers follow the same type of behavior. By analyzing the results and the various curves, we find that the average of $\theta_{p,i}$ or $\theta_{c,i}$,i = 1 to 10, in the ten-layer case is the same as the average of $\theta_{p,j}$ or $\theta_{c,j}$,j = 1 to 3, in the three-layer case. If we plot the "average" curves of all the layers, the curves would be very close to those in Fig. 3.13(a) for the single layer case. Thus, provided the time is much longer than the time to engage all layers, by splitting a single-layer membrane into multiple layers, the angles, θ, θ_p and θ_c,will vary from layer to layer, but the average of them will be affected very little, and they are approximately equal to the corresponding angles obtained in single-layer case.

In Fig. 3.53(b), at τ = 35, the residual projectile velocity is about 317 m/s, almost the same as 316 m/s in the three-layer case shown in Fig. 3.39(b), and higher than 285 m/s in the single-layer case in Fig. 3.13(b). Thus by splitting a single layer into many layers, the deceleration of the projectile is affected, but whether there are three layers or 10 layers, the behavior doesn't change much, i.e., as long as the membrane has been split into layers, the deceleration is not very dependent on the actual number of layers.

Panel (c) in Fig. 3.53 shows similar tendencies as were seen in panel (b). The average inflow velocity in the the ten-layer system is about 68 m/s, approximately the same as 67 m/s in the three-layer system, and higher than 58 m/s in single-layer case. We can infer that the inflow velocity will be affected to the same degree as the vertical velocity. Fig. 3.53(d) reveals little that is new, except

that all the cone wave radii increase approximately linearly with time and the radius differences between adjacent layers are almost the same.

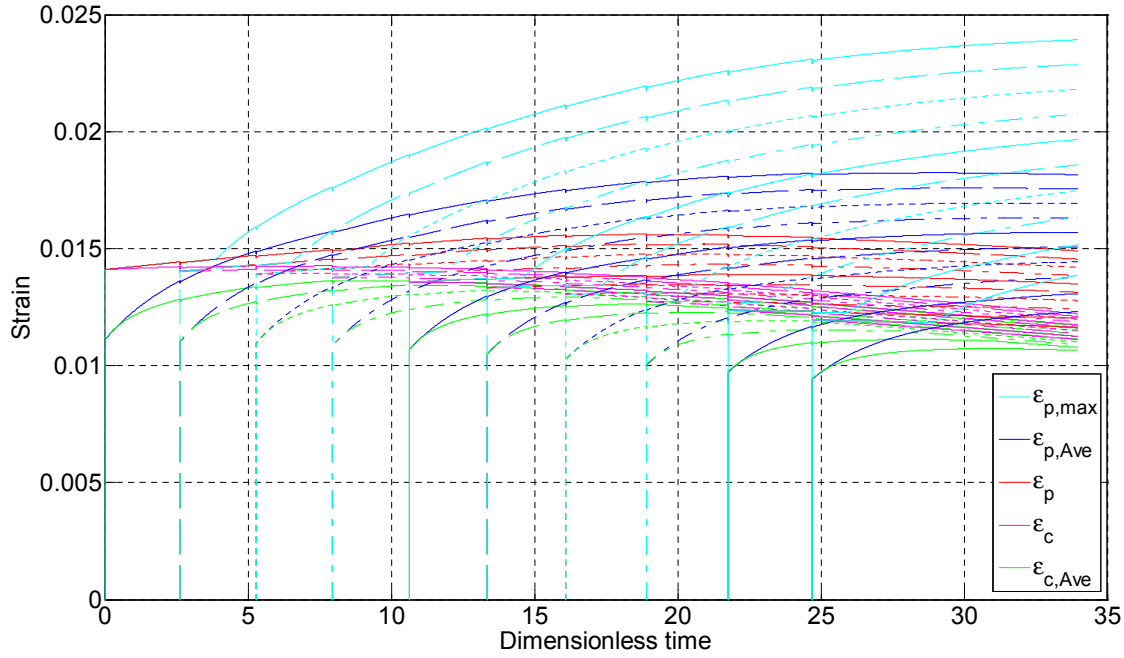

Figure 3.54: Various strains versus dimensionless time in a 10-layer system. Layer gap: 0.667 mm, vertical displacement: 8 mm, projectile type: 9 mm

We now consider the effect of increasing the layer to layer gap size in the ten-layer case. Fig. 3.54 shows the strain versus time curves when the layer gap is 0.666 mm (and thus total layer gap is 6 mm). Similar to what we have found in the three-layer case, by increasing the layer to layer gap, the behavioral differences among all the layers has increased, i.e., the top layers have higher strain while the bottom layers have lower strain. Also average strain of all layers becomes lower at given moment. The strain in all the layers except Layer 1 starts at a lower value compared to those in the 2 mm layer gap case.

Fig. 3.55 shows the behavior of key quantities after projectile impact obtained for the case of a layer to layer gap of 0.667 mm. In panel (a), compar-

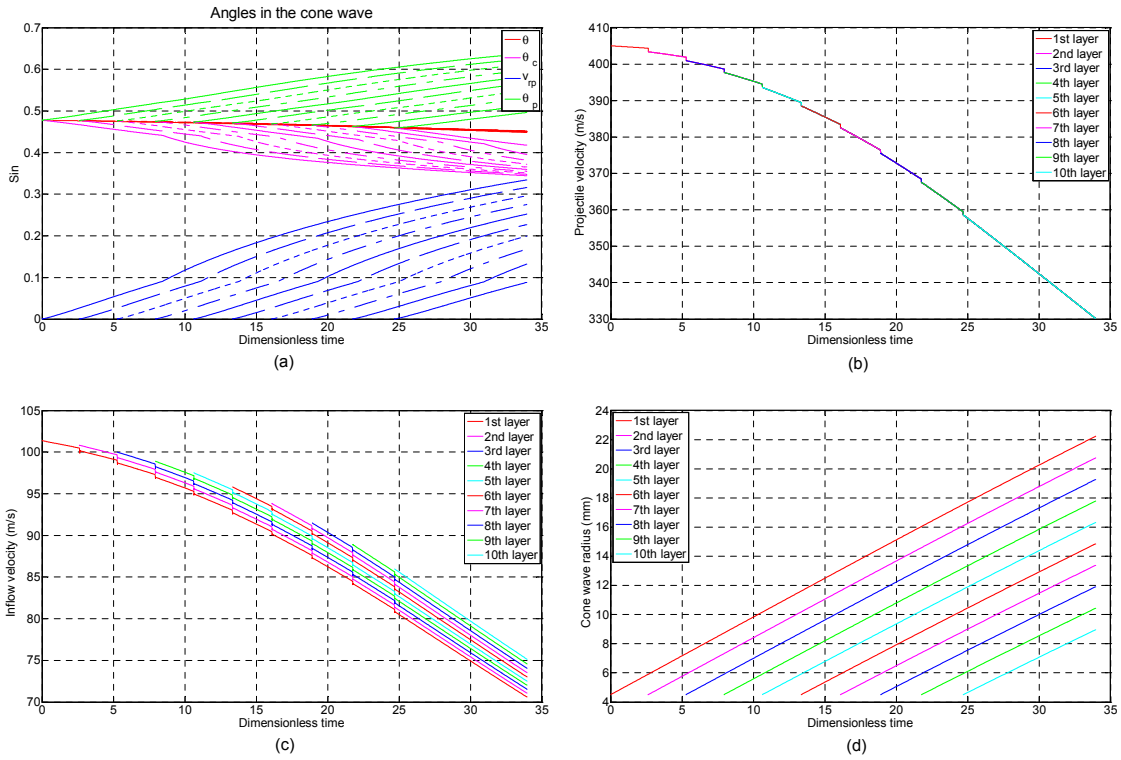

Figure 3.55: Behavior of various key quantities (0.666 mm layer to layer gaps): (a) Angles at the cone wave front, θ_c, and the projectile edge, θ_p, as well as the effective cone wave angle, θ, and the angle difference, $V_{rp} = |\theta_c - \theta_p|$; (b) projectile velocity; (c) inflow velocity and (d) cone wave radius R_c.

ing with Fig. 3.53(a), the effective angle θ is almost the same, going from 0.48 to 0.45. The discrepancy of angles in the layers has been enlarged compared with what is seen in Fig. 3.53(a). In panels (b) and (c), the remaining vertical velocity and inflow velocity are 330 m/s and 73 m/s respectively, while in in the case of 0.444 mm layer to layer gaps, the corresponding values are 317 m/s and 68 m/s respectively. Panel (d), once again shows the linear relation between time and cone wave radii in the different layers.

Table 3.4 summarizes some important results obtained from the single-layer, three-layer and ten-layer cases. From these results, we can see that: (1) The ef-

Table 3.4: Comparison of some important quantities calculated from study of the single-layer, three-layer and ten-layer cases.

Parameters	1 layer	3 layers		10 layers	
Layer gap (mm)	N/A	2.0	3.0	0.444	0.667
Time consumed	37	35	34	35	34
Average final $\varepsilon_{p,\max}$	0.020	0.0195	0.019	0.0195	0.019
$\max(\varepsilon_{p,\max})$ in top layer	0.020	0.0225	0.024	0.023	0.024
$\max(\varepsilon_{p,max})$ in bottom layer	0.020	0.01625	0.01375	0.016	0.014
Effective angle $\sin\theta$	0.44	0.45	0.45	0.45	0.45
Average $\sin\theta_p$	0.62	0.595	0.585	0.59	0.58
$\sin\theta_p$ in top layer	0.62	0.63	0.63	0.63	0.63
$\sin\theta_p$ in bottom layer	0.62	0.55	0.50	0.54	0.50
Average $\sin\theta_c$	0.32	0.35	0.38	0.36	0.38
$\sin\theta_c$ in top layer	0.32	0.34	0.34	0.34	0.34
$\sin\theta_c$ in bottom layer	0.32	0.37	0.42	0.37	0.42
Residual velocity (m/s)	286	316	329	316	330
Residual inflow velocity (m/s)	58	68	72.5	68	72.5

fective or average of a certain quantities in all the layers is actually close to that for the single-layer case, such as θ, average $\varepsilon_{p,\max}$ etc. (2) The layer to layer gap has a larger effect on the results than the number of layers. If we compare the corresponding results in the three-layer and ten-layer cases, we find the results in the 1st column labeled "3 layers" are close to those in the 1st column labeled "10 layers", and the results in the 2nd columns labeled "3 layers" and "10 layers" are close to each other as well. Thus having more layers in the system that are each thinner will not change the behavior very much, but will consume

more time in calculation and post processing. Thus we place more effort on investigating the size of the layer to layer gap and initial parameters such as initial projectile velocity, rather than adding more layers into calculation.

Non-penetration cases: FSP

We now consider the behavior of key quantities after impact into a ten-layer system by an FSP projectile. The layer to layer gaps used are 0.444 mm and 0.667 mm, respectively, the same as used in the ten-layer cases involving a 9 mm projectile, and also preserving the same total layer gaps used in the three-layer cases.

For an FSP projectile impacting a single layer, the peak strain, $\varepsilon_{p,max}$, occurs almost immediately after the impact of the projectile due to the low ratio of projectile mass over membrane density. However, when split into multi-layers, the strain pattern will be changed as the peak strain $\varepsilon_{p,max}$ will appear at a later time, so the results in multi-layer cases will not be comparable with that of single-layer case. Therefore, ten-layer results will only be compared with three-layer results.

Fig. 3.56 shows the various strain curves for FSP impact into the ten-layer system. The main difference between Fig. 3.56 and Fig. 3.48 is that the strain drop when striking a new layer is much smaller in a ten-layer system. The strain curves are more continuous and smooth in Fig. 3.56. As discussed above, the FSP projectile mass is much less than that of the 9 mm projectile, and the target thickness is larger, so the mass ratio of membrane to projectile is higher in the FSP. Therefore, whether one considers a three-layer or a ten-layer system,

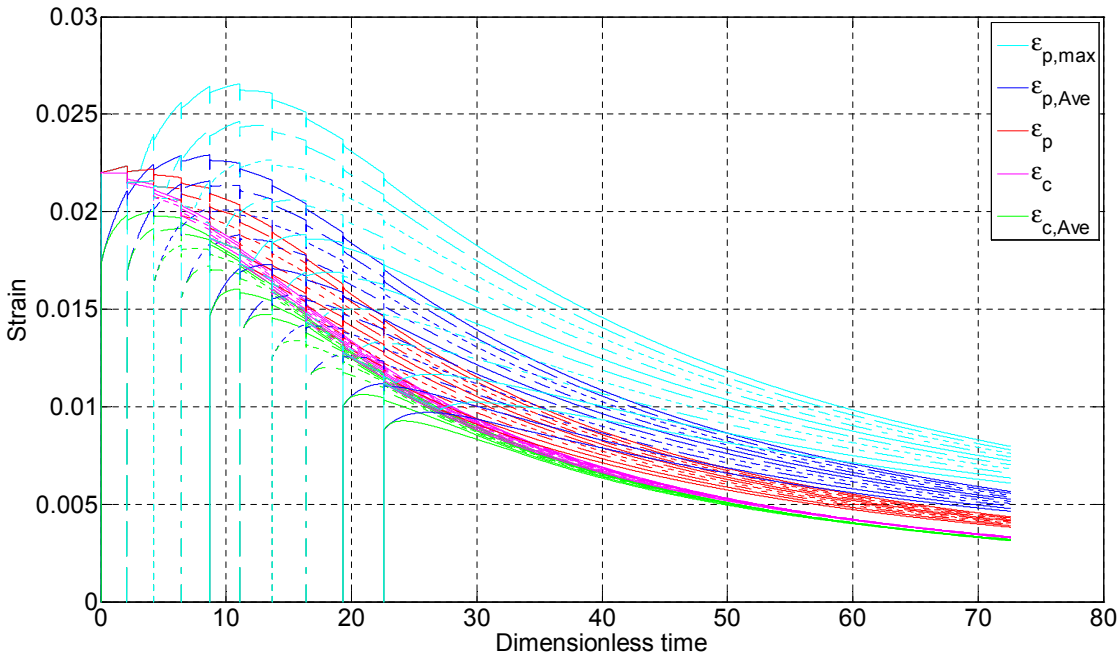

Figure 3.56: The strain curves in ten layers. Layer gap: 0.444 mm, vertical displacement: 8 mm, projectile type: FSP

the layer to layer effects have a larger effect on the FSP projectile's velocity. In Fig. 3.48, $\varepsilon_{p,\max}$ in Layer 1 starts to decrease immediately after it hits Layer 2, while in Fig. 3.56, that didn't happen until Layer 6 was engaged. Also $\varepsilon_{p,\max}$ in Layers 1 and 10 started with and ended up with the same values in Fig. 3.56 as Layer 1 and Layer 3 did in Fig. 3.48, and the average of $\varepsilon_{p,\max}$ in the ten-layer case is also close to that in the three-layer case. The same thing can be seen for all the other strain variables.

Fig. 3.57 shows the behavior of various important quantities obtained for the ten-layer system impacted by an FSP projectile and with 0.444 mm layer to layer gaps. In panel (a), all the angles in Layer 1 and Layer 10 are equal to those in Layer 1 and Layer 3 in Fig. 3.46(a) respectively, and therefore the average is also approximately the same. Such behavior is consistent with what we have found in the 9 mm case. In panel (b), the velocity curves are concave, and the residual

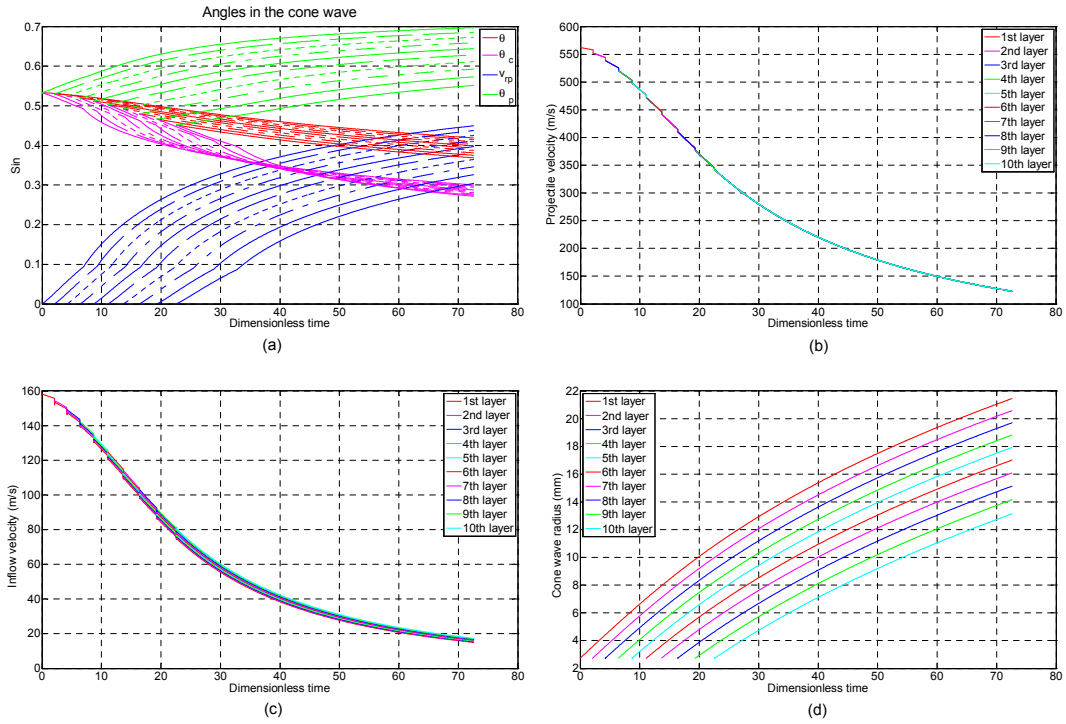

Figure 3.57: Behavior of various key quantities (0.444 mm layer to layer gaps) for the case of an FSP projectile impacting a 10-layer system: (a) Angles at the cone wave front, θ_c, and the projectile edge, θ_p, as well as the effective cone wave angle, θ, and the angle difference, $V_{rp} = |\theta_c - \theta_p|$; (b) projectile velocity; (c) inflow velocity and (d) cone wave radius R_c.

velocity is about 120 m/s, the same as that in Fig. 3.46(b). The average residual inflow velocity shown in panel (c) is about 17 m/s, the same as Fig. 3.46(c). In panel (d), we find that the cone waves in Layer 1 and Layer 10 start and end up with the same radii as those of Layer 1 and Layer 3 in Fig. 3.46(d). As we discussed in the 9 mm case, once a single-layer membrane is split into multiple layers with gaps, the differences between one system and another are almost independent of the number of layers, provided the gap sums are the same.

Fig. 3.58 shows the various strains versus time when the layer to layer gap is increased 0.667 mm in the ten-layer system. Compared to the behavior in

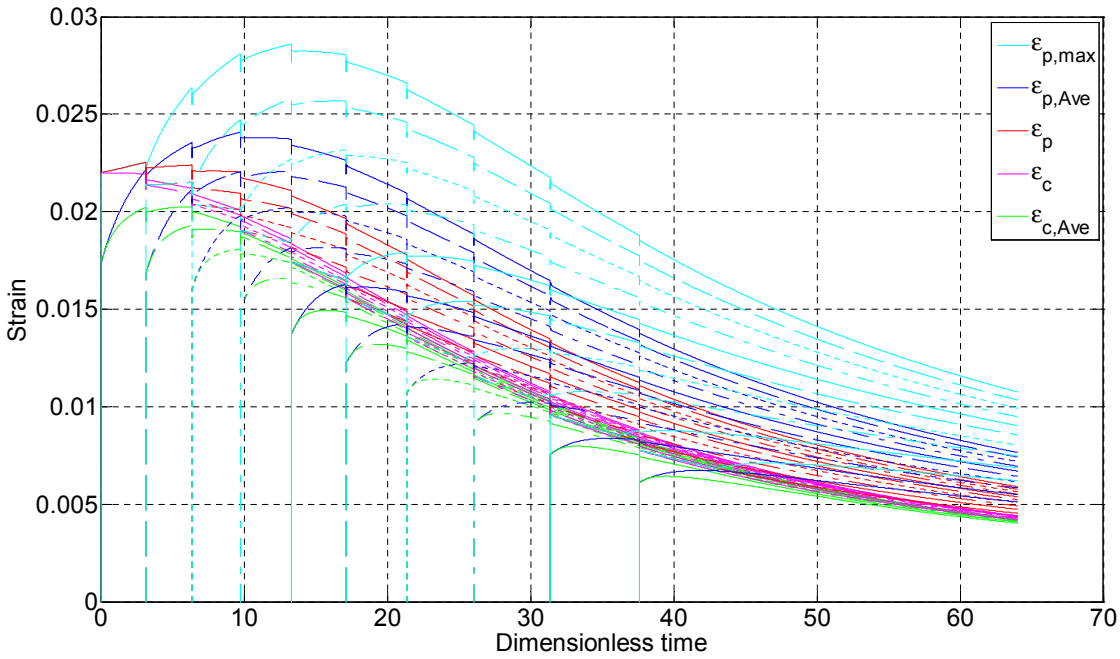

Figure 3.58: Strain plots versus time for a system of ten layers. Layer gap: 0.667 mm, vertical displacement: 8 mm, projectile type: FSP

Fig. 3.56 corresponding to a layer to layer gap of 0.444 mm, the strain in Layer 1 is higher while in Layer 10 is lower. Except for Layer 1, all the strains in subsequent layers start with lower values compared with their counterparts in the 0.444 mm case. Comparing the behavior in Fig. 3.58 with that in Fig. 3.48, all the results are similar, i.e. the strains in Layer 1 and Layer 10 are almost the same with those in Layer 1 and Layer 3.

Fig. 3.59 shows some important results obtained for the case of 0.667 mm layer to layer gaps. We have already discussed many cases showing variations among key quantities when changing both layer to layer gap size and number of layers. Fig. 3.59 does not provide any new information beyond what we have seen in previous comparisons. Results for important quantities obtained from study of three-layer and ten-layer FSP impact cases are listed in Table 3.5.

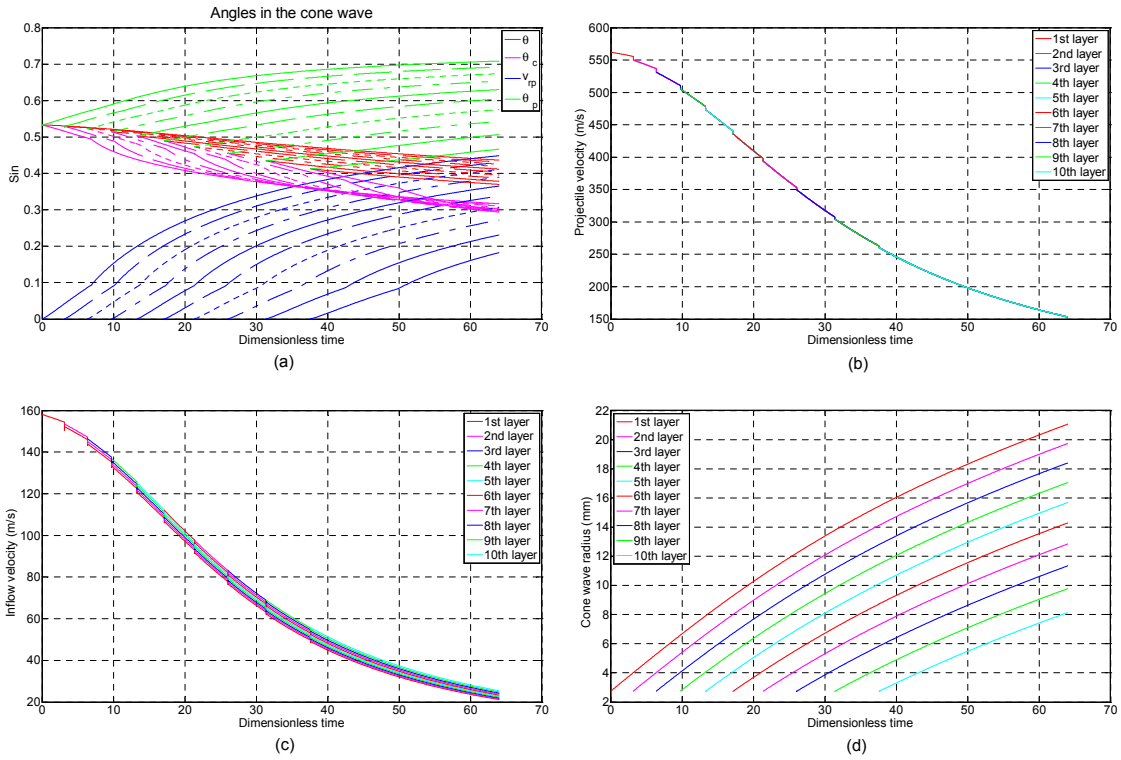

Figure 3.59: Behavior of various key quantities (0.667 mm layer to layer gaps) for the case of an FSP projectile impacting a 10-layer system: (a) Angles at the cone wave front, θ_c, and the projectile edge, θ_p, as well as the effective cone wave angle, θ, and the angle difference, $V_{rp} = |\theta_c - \theta_p|$; (b) projectile velocity; (c) inflow velocity and (d) cone wave radius R_c.

From Table 3.5, we can see that the results in the FSP cases are more affected by layer to layer gap size than by the number of layers. The results for 2 mm layer to layer gap size in the three-layer cases are close to those for 0.444 mm layer to layer gaps in the ten-layer cases, while the other groups of results, i.e. 3 mm layer gap in the three-layer cases and 0.667 mm layer gap in ten-layer cases are are also close. Variables such as effective angle $\sin\theta$, $\sin\theta_p$ in the first layer and $\sin\theta_c$ in the last layer are hardly affected by the number of layers or the layer to layer gap size, while quantities like the remaining projectile velocity and inflow velocity are strongly affected by the layer to layer gap size. Thus,

Table 3.5: Comparison of some important quantities obtained from study of single-layer, three-layer and ten-layer cases.

Parameters	Three layers		Ten layers	
Layer gap (mm)	2.0	3.0	0.444	0.667
Time consumed	73	68	72	64
$\max(\varepsilon_{p,max})$ in top layer	0.026	0.027	0.026	0.0285
Effective angle $\sin\theta$	0.39	0.40	0.39	0.40
Average $\sin\theta_p$	0.61	0.58	0.61	0.58
$\sin\theta_p$ in top layer	0.69	0.70	0.70	0.70
$\sin\theta_p$ in bottom layer	0.54	0.46	0.55	0.47
Average $\sin\theta_c$	0.28	0.30	0.285	0.305
$\sin\theta_c$ in top layer	0.27	0.30	0.27	0.295
$\sin\theta_c$ in bottom layer	0.29	0.31	0.30	0.31
Residual velocity (m/s)	120	146	120	150
Residual inflow velocity (m/s)	16	21	16	22

due to the difference in the projectile masses, there are many differences in the behavior of key quantities seen in the FSP projectile impact cases versus the 9 mm projectile impact cases.

Penetration cases: 9 mm

Results for cases of projectile penetration were obtained in a similar way to those in the three-layer penetration cases. The failure criterion is again is a strain limit of 0.02. The allowance for total vertical displacement is 12 mm, and the layer

to layer gap choices are are still 0.444 mm and 0.667 mm, respectively. All the other parameters remain as before.

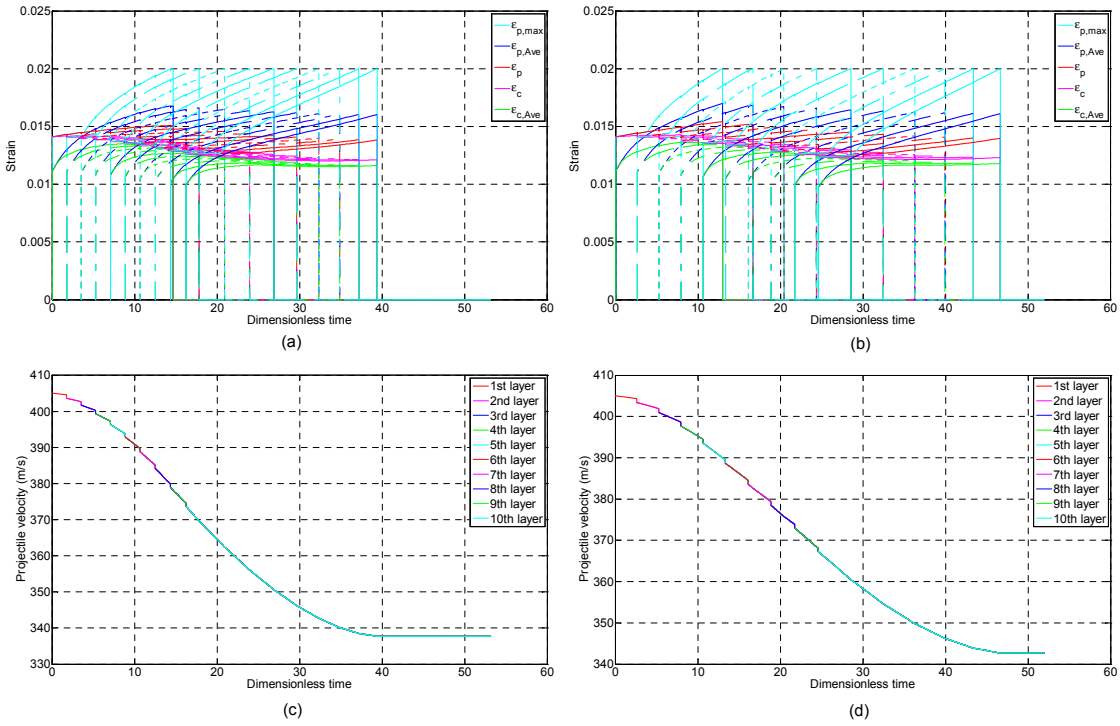

Figure 3.60: Various strains versus time for a ten layer system. Layer gaps: 0.444 mm and 0.667 mm, vertical displacement: 12 mm, projectile type: 9 mm

Fig. 3.60 shows the strain and velocity curves in a ten-layer system impacted by an 9 mm projectile and for cases where the layer to layer gaps are 0.444 mm and 0.667 mm, respectively. Comparing panels (a) and (b), we see that the initial velocity 406 m/s is large enough to penetrate all ten layers if the failure criterion is 0.02 strain. Panels (c) and (d) show that the residual velocity is larger when the layer to layer gap increases, which is consistent with what was seen in the three-layer case. This confirms our previous conclusion that it is better to combine the layers together into one (no gaps) in order to decelerate the projectile as much as possible within a certain distance.

Penetration cases: FSP

For the FSP cases we reduce the displacement allowance to 8 mm and increase the failure strain to 0.025. All the other parameter values remain the same.

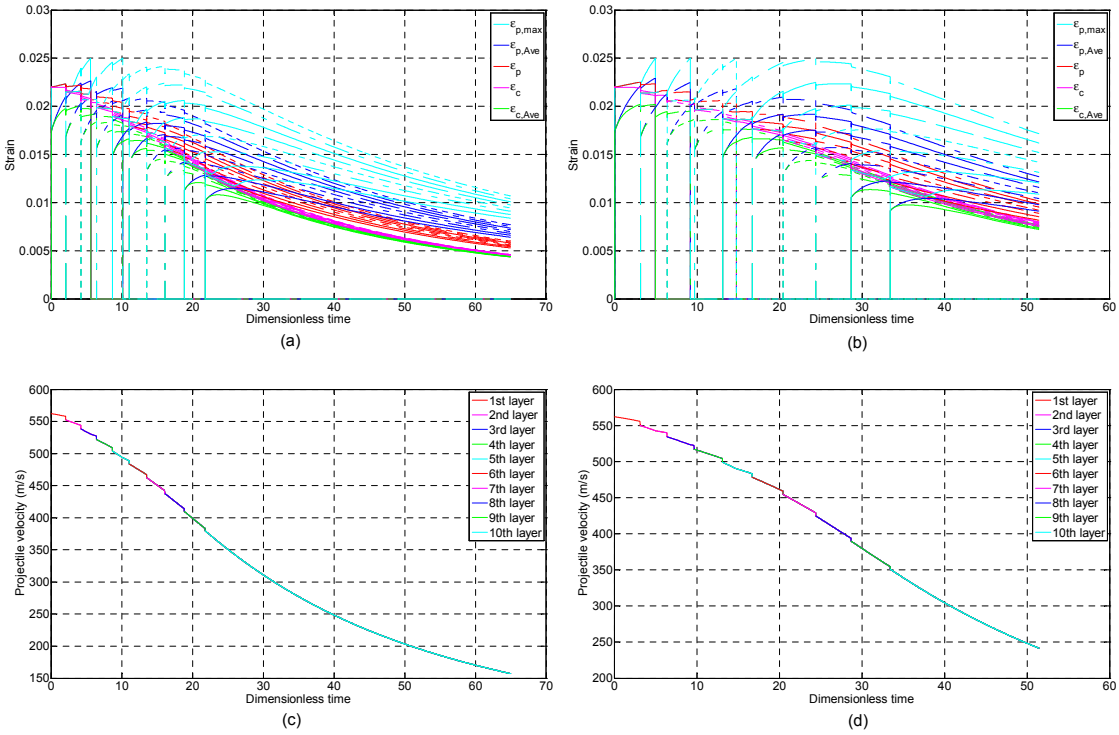

Figure 3.61: Strain versus lifetime curves for a system of ten ten layers impacted by an FSP. Layer gap: 0.444 mm and 0.667 mm, vertical displacement: 8 mm, projectile type: FSP

Fig. 3.61 shows the strain and velocity behavior vs. time for a 10 layer-system impacted by an FSP. Comparing panels (a) and (b), more layers are penetrated when the layer gap is increased, and the strain in the remaining layers becomes higher as well. The time consumed to reach an 8 mm displacement is $\tau = 52$ when the layer gap is 0.667 mm, while it is $\tau = 62$ when the layer gap is 0.444 mm. Correspondingly, the remaining velocity is 155 m/s compared to 193 m/s when the layer to layer gap is increased from 0.444 mm to 0.667 mm.

CHAPTER 4

CONCLUSIONS

4.1 Summary of the thesis

In this thesis, we have developed models for simulating the mechanical response of fibrous targets when impacted by rigid, high-velocity projectiles with the shape of a right circular cylinder. Both single layer and multiple-layer isotropic and biaxial membrane systems have been modeled.

First, a PC-based model was developed for projectile impact into a multi-layer system of axisymmetric membrane layers with non-zero spacings between them, which blended analysis and numerical simulation to characterize the interaction between the projectile and the various layers. In particular, we considered such performance measures as the critical strains in layers resulting in their failure, the strains in unfailed layers, critical layer gaps, the number of layers penetrated, and the residual velocity in cases where all layers have been penetrated. The model allowed variation of mechanical properties from layer to layer as well as variations in spacings between layers, in order to study their combined effects on the ballistic performance of the system. The ballistic impact response of fibrous material systems of particular interest in body armor was studied as well. In our simulations, the layers were assumed to fail immediately when the strain reached a critical value. In particular, we considered such performance measures as the critical strain in the layers, the strain in the top layers, the critical layer to layer gap, the number of layers penetrated, and the residual velocity when all layers have been penetrated. A few general conclusions can be drawn from our simulation results:

(1) In a single-layer system, as the cone wave induced by the projectile impact propagates, the strain first rises to a climax and eventually decreases, either suddenly when failure occurs (in which case the projectile is not stopped) or gradually as the projectile is brought to a halt.

(2) In multi-layer system with non-zero spacing, if no layers fail the strains versus time in the various layers are similar to that of a single-layer membrane except that time lags occur between layers as layers are engaged sequentially.

(3) Given the mass ratio of m_p/M_p and number of layers in the system, there is always a "critical projectile velocity" which is the minimal velocity required to penetrate all the layers. Accordingly, there is a "critical layer to layer gap" which is the minimum layer gap corresponding to penetration at the "critical projectile velocity". As the number of layers in the system increases, the "critical projectile velocity" decreases and the "critical layer layer gap" increases. When there are ten layers, the "critical velocity" drops to about about 80% of that of a single-layer, given all the other conditions remained unchanged. This lowering percentage is only dependent on $\Gamma_0 = m_p/M_p$ but not the material properties.

(4) When the total layer gap (sum of all gaps) G_n decreases, it becomes more difficult to penetrate layers, and the residual projectile velocity will be smaller if all are penetrated, but the system becomes more sensitive to a change in projectile velocity, i.e. a smaller velocity increase will lead to more layers failed (i.e., an 'all or nothing' type of behavior).

(5) As the projectile velocity decreases, it becomes more difficult to penetrate the layers, and the time to penetrate each layer becomes longer, and finally "current top layer strain" has no strain transition but is just the strain of the first

surviving layer.

Secondly, we also developed a semi-analytical model for a multi-layer, biaxial elastic membrane system impacted by a rigid, right circular cylinder (RCC). The model is a further evolution of a previous model for a single-layer membrane soon to be published. Some key assumptions and parameters were obtained from simulation results obtained from a Cornell modified DSM code which is based on the Finite Difference Method. In the numerical simulations, the main emphasis was on gaining a detailed understanding of the strain and displacement fields, as well as the velocity fields versus time. The panel was treated as a biaxial membrane with negligible shear stiffness compared to the tensile stiffness. Membranes made with Dyneema SK76 and Kevlar 29 were considered, which had yarns crossing in orthogonal directions. Numerical results were obtained through incremental integration using small time steps. Compared to the DSM-based simulation, there were several remarkable improvements: (1) The calculation time was accelerated by 500 times; (2) Results under different parameters could be obtained for much longer dimensionless times; and (3) Investigation of multiple-layered systems became feasible. Two types of projectiles, 9 mm and FSP, have been considered to simulate the strain and cone wave development in multiple-layered membranes made with Dyneema SK76.

In the case of the 9 mm projectile, several features were found.

(1) In a single-layer membrane, the strain pattern is like a four-branched star with each branch similar to a finger. With slip boundary conditions around the projectile, the tension in the yarns exists all the way from projectile center to tensile wave front.

(2) The form of the strain distribution from the projectile edge to the cone wave front is not dependent on the projectile mass, radius, and initial speed etc, but only on the material properties. Once the material is determined, the strain distribution along the yarn path can be obtained from an analytical function.

(3) In cases of slip, aside from the behavior immediately after impact, the peak strain in the x-direction yarns always appears at the intersection of the y-axis and the projectile edge. When the distance in the y-direction away from x-axis is greater than one projectile radius, the strain decreases sharply and there is large strain gradient from the yarns passing underneath the projectile to those passing outside the projectile.

(4) The peak strain is highly affected by the initial projectile velocity and the membrane thickness. The peak strain and initial projectile velocity have a near-linear relationship. For a given mass, the relationship between the membrane's thickness and the peak strain is much more complicated.

(5) In the case of multiple layers, and comparing three-layer and ten-layer results, we found the behavior is more affected by the layer to layer gap size than the number of layers. When the total layer gap sum is the same, the results are roughly the same, while changing the magnitude of the total layer gap will lead to a distinct change in behavior.

(6) The differences in strains and angles (effective angle, angles at cone wave front and projectile edge etc.) in different layers is higher when the layer to layer gap is increased. Increasing the number of layers but maintaining the total areal density has very little effect on the average values and nor the difference in values between the top and bottom layers.

(7) When increasing the layer to layer gap, some layers will not be involved in deceleration until a later time, and the projectile is decelerated less, and thus the residual velocity and inflow velocity are higher. Therefore in order to decelerate the projectile within a certain time or distance, it is better to combine the layers into a single layer, assuming the peak strain in the top layer is less than the imposed by the failure criterion.

The strain patterns and in the FSP impact cases are somewhat different from the 9 mm cases due to the differences in their masses and the target thickness. Besides the features (1), (3), (4), (5) and (7) introduced above, several unique features occur in the FSP cases as follows:

(1) In the single-layer case, the peak strain always appears right after of impact of the projectile. Therefore the membrane will either fail immediately after the impact, or not at all and the cone wave can grow until the projectile stops. The principal reason is that the FSP projectile mass is much smaller than that of the 9 mm projectile and the panel's thickness is larger than that in the 9 mm cases.

(2) Comparing FSP cases with 9 mm cases, we found that a projectile with high mass will induce a consistent and increasing strain in the membrane, while the lighter projectile can only induce a high strain initially. A lighter projectile with higher initial velocity can be decelerated more rapidly than a heavier projectile that has lower initial velocity.

(3) With the knowledge in (1), the peak strain after some time in the membrane is located at the tensile wave front along the x or y axis.

(4) In the multi-layer cases, the maximum strain appears at a later time after

the impact of projectile, due to the decrease of areal density ratio for the first layer engaged.

(5) If one or more layers fail, the strain in the remaining layers will become higher and thus there is a higher probability they fail as well, which is reverse of the 9 mm results.

4.2 Suggestions on future work

The current work is focused on the creation and implementation of semi-analytical models in isotropic and biaxial fibrous structures. The biaxial model is a further development of the isotropic model since it introduces properties mimicing "yarns" in two orthogonal directions, which is the fundamental property of fibrous materials, such as Dyneema® and Kevlar®, adopted in body armor systems.

In the biaxial model, the yarns are approximated as lying in plane and traveling in the two directions, where in reality, two yarns in the two perpendicular directions cross over each other in an alternating pattern of traversing above and below their crossing counterparts. In plain weave fabrics, for instance, each yarn alternates between crossing over and under the yarns in its path, whereas in other weaves, such as harness satins or basket weaves, yarns may pass above a group of several transverse yarns at a time before crossing to pass below a subsequent group. The result is that the yarn paths undulate out of plane and generate what is called a 'crimp angle' that can be several degrees depending on the tightness of the weave. The effect of the crimp is to allow for pseudo-strain when unequal loads occur in the two directions. For instance, pulling only in

one yarn direction straightens those yarns causing longitudinal fabric stretching (without causing true yarn strain), while at the same time inducing more crimp and higher crimp angles in the crossing yarns, thus causing transverse fabric shrinkage (without axially compressing the yarns). Preliminary numerical simulations, using a further modified version of the DSM code, suggest that the tensile wave velocity in both material and ground coordinates is slowed, the inflow velocity and displacement with respect to ground coordinates is increased and the overall true yarn strain distribution is affected and possibly lowered in magnitude as compared to cases where yarns are modeled in terms of a simple pin-jointed network. In future work these effects are candidates for study using a modified version of the DSM code, and the features seen are candidates for incorporation into the Cornell semi-analytical model.

We have assumed a right circular cylinder or RCC projectile shape, which has a flat nose, when in reality the nose of a projectile is shaped more as a half-sphere or half-ellipsoid or may have an 'ogive' shape. We also assume the projectile nose is rigid, where in reality, relatively soft materials are used (e.g., lead and copper), and we can expect deformation that will broaden the nose and increase the radius of the impact patch as well as reduce the tip velocity during the critical, first few microseconds after the impact of the first layer. This is likely to have a beneficial effect of magnitude of the local strains of the similar magnitude to the negative effects of layer-to-layer gaps (provided there is no hardened conical projectile encased within the softer material as in an APM2 armor piercing projectile). Another way to view the effect is that when the projectile deforms, a portion of its kinetic energy will convert into internal energy and heat, and the shape and the velocity decay will change, and layers otherwise penetrated may remain intact.

Another aspect to consider is the load-strain curve of the yarn, especially approaching failure. Most of our analysis has assumed a linear-brittle stress strain curve, whereas actual materials variously show stiffening effects with increasing strain and strain rate (particularly at ballistic loading rates), while others show strain softening behavior and possibly local yielding-like behavior, particularly yarns with distributed fiber strength. Furthermore there are rate effects where the fiber failure strength depends on the loading rate. These aspects are likely to be important in studying failure mechanisms, and in particular, explaining why some materials under-perform, whereas others over-perform, what the current models would predict.

The modeling of projectile impact in body armor systems is based mostly on theoretical analysis but there are also a few shaping functions with tuning parameters obtained from the Cornell-modified DSM code. These tuning parameters appear to be invariant to choices of other parameters like impact velocity, areal density ratio and yarn stiffness. The most important shape functions are those associated with near parabolic transverse roll-off of the tensile strain in the tensile wave beyond the transverse cone wave, as well as the opposite parabolic-like build-up of local strain concentration in yarns when traveling around the edge of the projectile from the yarn axis (at 0 degrees) to the crossing yarn axis (at 90 degrees). A better model would require deriving these effects more directly rather than empirically characterizing them, though qualitatively, the cause of these effects is easy to appreciate.

Future work will look deeper into all these aspects and would make the current model even more accurate, and possibly more efficient.

APPENDIX A

DIMENSIONLESS FRAMEWORK FOR NUMERICAL SOLUTIONS IN ISOTROPIC MATERIALS

A.1 Analysis and equations

In this section we reframe the problem in terms of various dimensionless quantities in order to make the calculations more transparent. We let τ be dimensionless time defined by

$$\tau = \frac{t}{t_p} \tag{A.1}$$

where

$$t_p = \frac{r_p}{a_0} \tag{A.2}$$

is time required for the tensile wave front to travel a distance equal to the projectile radius. For the cone wave-front, the normalized velocity and displacement are, respectively,

$$C(\tau) = \frac{c\left(\tau t_p\right)}{a_0} \tag{A.3}$$

$$R_c(\tau) = \frac{r_c\left(\tau t_p\right)}{r_p} = \frac{r_p}{r_p} + \int_0^{\tau t_p} \frac{c(s)}{a_0} ds = 1 + \int_0^{\tau} C(\zeta) d\zeta \tag{A.4}$$

Normalized quantities describing the various strains and strain rate are

$$\Xi_c(\tau) = \varepsilon_c\left(\tau t_p\right) \tag{A.5}$$

$$\Xi_p(\tau) = \varepsilon_p\left(\tau t_p\right) = \Xi_c(\tau) R_c(\tau) \tag{A.6}$$

$$\Xi_{p,0} = \varepsilon_{p,0} \tag{A.7}$$

and

$$\dot{\Xi}_p(\tau) = \frac{\partial \varepsilon_p\left(\tau t_p\right)}{\partial \tau} = \frac{\partial \varepsilon_p\left(\tau t_p\right)}{\partial t}\frac{\partial t}{\partial \tau} \tag{A.8}$$

Normalized quantities for the projectile velocity and displacement are

$$\Psi(\tau) = \frac{V\left(t_p\tau\right)}{a_0} \tag{A.9}$$

$$\Psi_0 = \frac{V_0}{a_0} \tag{A.10}$$

$$\Delta(\tau) = \frac{\delta\left(\tau t_p\right)}{r_p} = \int_0^\tau \Psi(\zeta)d\zeta \tag{A.11}$$

and

$$\frac{d\Delta(\tau)}{d\tau} = \frac{d\delta\left(\tau t_p\right)}{r_p dt}\frac{dt}{d\tau} = \frac{V(t)}{r_p}t_p = \frac{V(t)}{a_0} = \Psi(\tau) \tag{A.12}$$

Normalized quantities for the in-flow displacement and velocity are

$$U_c(\tau) = \frac{u_c\left(t_p\tau\right)}{\varepsilon_{p,0}r_p} \tag{A.13}$$

$$\dot{U}_c(\tau) = \frac{\partial U_c(\tau)}{\partial \tau} = \frac{1}{\varepsilon_{p,0}r_p}\frac{\partial u_c(t)}{\partial t}\frac{dt}{d\tau} = \frac{1}{\varepsilon_{p,0}r_p}\dot{u}_c(t)t_p = \frac{\dot{u}(t_p\tau)}{\varepsilon_{p,0}a_0} \tag{A.14}$$

and

$$\dot{U}_{c,0} = \frac{\dot{u}_{c,0}}{\varepsilon_{p,0}a_0} = -1 \tag{A.15}$$

Regarding key equations, Eq. (2.14) and (2.11) become

$$C(\tau) = \sqrt{\frac{\Xi_c(\tau)}{1+\Xi_c(\tau)}} = \sqrt{\frac{\Xi_p(\tau)}{R_c(\tau)+\Xi_p(\tau)}} \tag{A.16}$$

The dimensionless cone wave radius becomes

$$R_c(\tau) = \left(\left(1+\Xi_{p,0}\right)^{2/3} + \frac{3}{2}\int_0^\tau \sqrt{\Xi_p(\zeta)}d\zeta\right)^{2/3} - \Xi_{p,0} \tag{A.17}$$

We let the cone angle be re-parameterized as

$$\Gamma(\tau) = \gamma\left(\tau r_p/a_0\right) \tag{A.18}$$

so

$$\sin\Gamma(\tau) = \frac{\Delta(\tau)}{\sqrt{\left(R_c(\tau)+\Xi_{p,0}U_c(\tau)-1\right)^2+\Delta(\tau)^2}} \tag{A.19}$$

and similarly

$$\cos\Gamma(\tau) = \frac{R_c(\tau)+\Xi_{p,0}U_c(\tau)-1}{\sqrt{\left(R_c(\tau)+\Xi_{p,0}U_c(\tau)-1\right)^2+\Delta(\tau)^2}} \tag{A.20}$$

Also from Eq. (2.41), (2.42) and (2.43), we have

$$\Xi_p(\tau) = \frac{R_c(\tau)}{2}\left(\sqrt{1+4\kappa_c(\tau)^2}-1\right) \tag{A.21}$$

where

$$\kappa_c(\tau) = \frac{\cos\Gamma\Xi_{p,0}\dot{U}_c(\tau)+\sin\Gamma(\tau)\Psi(\tau)}{1-\cos\Gamma(\tau)} \tag{A.22}$$

Finally inflow displacement and inflow velocity become

$$U_c(\tau) = -\ln\left(\frac{1+\tau}{R_c(\tau)}\right) - \int_0^\tau \frac{\dot{\Xi}}{\Xi_{p,0}}\ln\left(\frac{1+\tau-\zeta}{R_c(\tau)}\right)d\zeta \tag{A.23}$$

and

$$\dot{U}_c(\tau) = -\frac{1}{1+\tau} - \frac{1}{\Xi_{p,0}} \int_0^\tau \frac{\dot{\Xi}_p(\zeta)}{1+\tau-\zeta} d\zeta \tag{A.24}$$

The deceleration and velocity are

$$\frac{d\Psi(\tau)}{d\tau} = -\Theta_p \Xi_p(\tau) \sin\Gamma(\tau) \tag{A.25}$$

and

$$\Psi(\tau) = \Psi_0 - \Theta_p \int_0^\tau \Xi_p(\zeta) \sin\Gamma(\zeta) d\zeta \tag{A.26}$$

A.2 Initial conditions

For the initial conditions we have

$$\Xi_{p,0} = \left(\frac{\Psi_0}{\sqrt{2}}\right)^{\frac{4}{3}} \left(\frac{1}{1+\Xi_{p,0}}\right)^{\frac{1}{3}} \left(1 + \left(\frac{\Xi_{p,0}}{\Psi_0}\right)^2\right)^{\frac{2}{3}} \tag{A.27}$$

where $\Psi_0 = V_0/a_0$. A first approximation is

$$\Xi^{(1)}_{p,0} = \left(\frac{\Psi_0}{\sqrt{2}}\right)^{\frac{4}{3}} \tag{A.28}$$

a second approximation is

$$\Xi^{(2)}_{p,0} = \left(\frac{\Psi_0}{\sqrt{2}}\right)^{\frac{4}{3}} \left(\frac{1}{1+\Xi^{(1)}_{p,0}}\right)^{\frac{1}{3}} \left(1 + \left(\frac{\Xi^{(1)}_{p,0}}{\Psi_0}\right)^2\right)^{\frac{2}{3}} \tag{A.29}$$

and a third approximation, which we use, is

$$\Xi_{p,0} \approx \left(\frac{\Psi_0}{\sqrt{2}}\right)^{\frac{4}{3}} \left(\frac{1}{1+\Xi^{(2)}_{p,0}}\right)^{\frac{1}{3}} \left(1 + \left(\frac{\Xi^{(2)}_{p,0}}{\Psi_0}\right)^2\right)^{\frac{2}{3}} \tag{A.30}$$

Also

$$\Psi_0 = V_0/a_0,\ \Delta(0) = \Delta_0 = 0,\ \dot{U}_c(0) = \dot{U}_{c,0} = -1,\ U_c(0) = U_{c,0} = 0 \tag{A.31}$$

and

$$\sin\Gamma(0) = \frac{\Psi_0}{\sqrt{\left(\sqrt{\frac{\Xi_{p,0}}{1+\Xi_{p,0}}} - \Xi_{p,0}\right)^2 + \Psi_0^2}} \tag{A.32}$$

and

$$\cos\Gamma(0) = \frac{\sqrt{\frac{\Xi_{p,0}}{1+\Xi_{p,0}}} - \Xi_{p,0}}{\sqrt{\left(\sqrt{\frac{\Xi_{p,0}}{1+\Xi_{p,0}}} - \Xi_{p,0}\right)^2 + \Psi_0^2}} \tag{A.33}$$

A.3 Summary of key equations to solve numerically

With the above initial conditions, the set of equations to solve is

$$R_c(\tau) = \left(\left(1+\Xi_{p,0}\right)^{\frac{2}{3}} + \frac{3}{2}\int_0^\tau \sqrt{\Xi_p(\zeta)}d\zeta\right)^{\frac{2}{3}} - \Xi_{p,0} \tag{A.34}$$

$$C(\tau) = \sqrt{\frac{\Xi_p(\tau)}{R_c(\tau)+\Xi_p(\tau)}} \tag{A.35}$$

Also we have

$$\Xi_p(\tau) = \frac{R_c(\tau)}{2}\left(\sqrt{1+4\kappa_c(\tau)^2} - 1\right) \tag{A.36}$$

where

$$\kappa_c(\tau) = \frac{\cos\Gamma\Xi_{p,0}\dot{U}_c(\tau) + \sin\Gamma(\tau)\Psi(\tau)}{1-\cos\Gamma(\tau)} \tag{A.37}$$

and

$$\sin\Gamma(0) = \frac{\Psi_0}{\sqrt{\left(\sqrt{\frac{\Xi_{p,0}}{1+\Xi_{p,0}}} - \Xi_{p,0}\right)^2 + \Psi_0^2}} \tag{A.38}$$

$$\cos\Gamma(0) = \frac{\sqrt{\frac{\Xi_{p,0}}{1+\Xi_{p,0}}} - \Xi_{p,0}}{\sqrt{\left(\sqrt{\frac{\Xi_{p,0}}{1+\Xi_{p,0}}} - \Xi_{p,0}\right)^2 + \Psi_0^2}} \tag{A.39}$$

Also we know

$$\frac{d\Psi(\tau)}{d\tau} = -\Theta_p \Xi_p(\tau)\sin\Gamma(\tau) \tag{A.40}$$

$$\Psi(\tau) = \Psi_0 - \Theta_p \int_0^\tau \Xi_p(\zeta)\sin\Gamma(\zeta)d\zeta \tag{A.41}$$

$$\Delta(\tau) = \frac{\delta(\tau t_p)}{r_p} = \int_0^\tau \Psi(\zeta)d\zeta \tag{A.42}$$

The convolutions are

$$U_c(\tau) = -\ln\left(\frac{1+\tau}{R_c(\tau)}\right) - \int_0^\tau \frac{\dot{\Xi}}{\Xi_{p,0}} \ln\left(\frac{1+\tau-\zeta}{R_c(\tau)}\right) d\zeta \tag{A.43}$$

and

$$\dot{U}_c(\tau) = -\frac{1}{1+\tau} - \frac{1}{\Xi_{p,0}} \int_0^\tau \frac{\dot{\Xi}_p(\zeta)}{1+\tau-\zeta} d\zeta \tag{A.44}$$

APPENDIX B

DIMENSIONLESS FRAMEWORK FOR NUMERICAL SOLUTIONS IN BI-AXIAL MEMBRANES

B.1 Analysis and equations

In this section we reframe the problem in terms of various dimensionless quantities in order to make the calculations more transparent. We let τ be dimensionless time defined by

$$\tau = \frac{t}{t_p} \tag{B.1}$$

where

$$t_p = \frac{r_p}{a_0} \tag{B.2}$$

is time required for the tensile wave front to travel a distance equal to the projectile radius. For the cone wave-front, the normalized velocity and displacement are, respectively,

$$C(\tau) = \frac{c(\tau t_p)}{a_0} \tag{B.3}$$

and

$$R_c(\tau) = \frac{r_c(\tau t_p)}{r_p} = \frac{r_p}{r_p} + \frac{a_0}{r_p}\int_0^{\tau t_p} \frac{c(s)}{a_0} ds = 1 + \int_0^{\tau} C(\zeta) d\zeta \tag{B.4}$$

In the dimensionless framework we have $\Omega_c(\tau) = \vartheta(r_c(t))$, so

$$\Omega_c(\tau) = \begin{cases} 1 - \frac{1}{6}\left(\frac{1}{R_c(\tau)}\right)^2 + \left(\frac{\pi}{4} - \frac{5}{6}\right)\left(\frac{1}{R_c(\tau)}\right)^{14} + \frac{1}{3}\left(1 - \frac{1}{2}\left(\frac{1}{R_c(\tau)}\right)^2\right)(R_c(\tau) - 1), \\ \qquad 1 < R_c(\tau) < 2 \\ \\ \frac{23}{24} + \frac{7}{16}\left[(R_c(\tau) - 1) - \frac{1}{3\,(R_c(\tau) - 1)}\right], \qquad R_c(\tau) > 2 \end{cases} \tag{B.5}$$

Normalized quantities describing the various strains and strain rate are

$$\Xi_c(\tau) = \varepsilon_c(\tau t_p) \tag{B.6}$$

$$\bar{\Xi}_c(\tau) = \bar{\varepsilon}_c(\tau t_p) \tag{B.7}$$

$$\Xi_p(\tau) = \varepsilon_p(\tau t_p) = \Xi_c(\tau) R_c(\tau) \tag{B.8}$$

$$\bar{\Xi}_p(\tau) = \bar{\varepsilon}_p(\tau t_p) = \Xi_c(\tau) R_c(\tau) \tag{B.9}$$

$$\Xi_{p,0} = \Xi_{c,0} = \varepsilon_{p,0} \tag{B.10}$$

and

$$\dot{\Xi}_p(\tau) = \frac{\partial \varepsilon_p(\tau t_p)}{\partial \tau} = \frac{\partial \varepsilon_p(\tau t_p)}{\partial t}\frac{\partial t}{\partial \tau} = \dot{\varepsilon}_p(t) t_p = \frac{\dot{\varepsilon}_p(t) r_p}{a_0} \tag{B.11}$$

$$\dot{\Xi}_c(\tau) = \frac{\partial \varepsilon_c(\tau t_p)}{\partial \tau} = \frac{\partial \varepsilon_c(\tau t_p)}{\partial t}\frac{\partial t}{\partial \tau} = \dot{\varepsilon}_c(t) t_p = \frac{\dot{\varepsilon}_c(t) r_p}{a_0} \tag{B.12}$$

Normalized quantities for the projectile velocity and displacement are

$$\Psi(\tau) = \frac{V(t_p\tau)}{a_0} \tag{B.13}$$

$$\Psi_0 = \frac{V_0}{a_0} \tag{B.14}$$

$$\Delta(\tau) = \frac{\delta(\tau t_p)}{r_p} = \int_0^\tau \Psi(\zeta)d\zeta \tag{B.15}$$

and

$$\frac{d\Delta(\tau)}{d\tau} = \frac{d\delta(\tau t_p)}{r_p dt}\frac{dt}{d\tau} = \frac{V(t)}{r_p}t_p = \frac{V(t)}{a_0} = \Psi(\tau) \tag{B.16}$$

Normalized quantities for the in-flow displacement and velocity are

$$U_c(\tau) = \frac{u_c(t_p\tau)}{\varepsilon_{p,0}r_p} \tag{B.17}$$

$$\dot{U}_c(\tau) = \frac{\partial U_c(\tau)}{\partial\tau} = \frac{1}{\varepsilon_{p,0}r_p}\frac{\partial u_c(t)}{\partial t}\frac{dt}{d\tau} = \frac{1}{\varepsilon_{p,0}r_p}\dot{u}_c(t)\frac{t_p d\tau}{d\tau} = \frac{\dot{u}_c(t_p\tau)}{\varepsilon_{p,0}a_0} \tag{B.18}$$

$$\dot{U}_{c,0} = \frac{\dot{u}_{c,0}}{\varepsilon_{p,0}a_0} = -1 \tag{B.19}$$

We let the cone wave speed be

$$C(\tau) = \sqrt{\frac{\Xi_c(\tau)}{1+\Xi_c(\tau)}} \tag{B.20}$$

Also we let the effective cone angle (calculated using a straight line from the tip of the cone wave-front to the projectile edge) be re-parameterized as

$$\hat{\Phi}_c(\tau) = \hat{\gamma}_c(\tau t_p) \tag{B.21}$$

so that

$$\sin\hat{\Phi}_c(\tau) = \frac{\Delta(\tau)}{R_c(\tau) - 1} \tag{B.22}$$

$$\cos\hat{\Phi}_c(\tau) = \sqrt{1 - \sin\hat{\Phi}_c(\tau)^2} \tag{B.23}$$

The cone angle at the cone wave front is re-parameterized as

$$\bar{\Phi}_c(\tau) = \bar{\gamma}_c(\tau t_p) \tag{B.24}$$

$$\sin\bar{\Phi}_c(\tau) = \begin{cases} \dfrac{\sin\hat{\Phi}_c(\tau)C(\bar{\gamma}_c)^2\cos^2\hat{\Phi}_c(\tau-1)}{2\sqrt{3}G(\tau)\left(\hat{J}_{11}(\tau) - \hat{J}_{12}(\tau)\right)}, & 1 < R_c(\tau) < 2 \\ \dfrac{\sin\hat{\Phi}_c(\tau)C(\bar{\gamma}_c)^2\cos^2\hat{\Phi}_c(\tau-1)}{2G(\tau)\left(\sqrt{3}\left(\hat{J}_{21}(\tau) - \hat{J}_{22}(\tau)\right) + J_{21}(\tau) - J_{22}(\tau)\right)}, & R_c(\tau) > 2 \end{cases} \tag{B.25}$$

where $C(\bar{\gamma}_c)$, $G(\tau)$, $\hat{J}_{21}(\tau)$, $\hat{J}_{22}(\tau)$, $J_{21}(\tau)$ and $J_{22}(\tau)$ were introduced in Section 3.2.6.

We also have

$$\Xi_c(\tau) = \frac{\sqrt{1 + 4K_c^2(\tau)} - 1}{2} \tag{B.26}$$

where

$$K_c(\tau) = \kappa_c(\tau t_p) = \frac{\cos\hat{\Phi}(\tau)\Xi_{p,0}\dot{U}_c(\tau) + \sin\hat{\Phi}(\tau)\Psi(\tau)}{1 - \cos\hat{\Phi}(\tau)} \tag{B.27}$$

Additionally,

$$\Xi_p(\tau) = \Xi_c \sqrt{\frac{\cos^2(\bar{\gamma}_c)}{2}\left[1 + 4\frac{\tan^2(\bar{\gamma}_c)}{\cos^2(\bar{\gamma}_c)}\left(\frac{A(r_c) + \Theta(r_c)}{A(r_c)}\right)^2\right]} \tag{B.28}$$

$$\dot{U}(\tau) = -\frac{\Xi_c(\zeta)}{\Xi_{c,0}}\frac{1 - \exp(-\tau/\tau_0)}{\tau/\tau_0} \tag{B.29}$$

$$U_c(\tau) = \int_0^\tau \dot{U}(s)ds \tag{B.30}$$

Also,

$$\frac{d\Psi(\tau)}{d\tau} = -\Theta_p \Upsilon_c(\tau)\Xi_c(\tau)\sin\bar{\Phi}_c(\tau)\Omega_c(\tau) \tag{B.31}$$

and

$$\Psi(\tau) = \Psi_0 - \Theta_p \int_0^\tau \Upsilon_c(\zeta)\Xi_c(\zeta)\sin\bar{\Phi}_c(\zeta))\Omega_c(\zeta)d\zeta \tag{B.32}$$

and the normalized deceleration force on the projectile is defined as

$$\begin{aligned} N(\tau) &= \frac{t_p}{a_0 M_p}F_p(t) = \frac{r_p}{a_0^2 M_p}F_p(t) = \frac{d\Psi(\tau)}{d\tau} \\ &= -\Theta_p \Upsilon_c(\tau)\Xi_c(\tau)\sin\bar{\Phi}_c(\tau)\Omega_c(\tau) \end{aligned} \tag{B.33}$$

where

$$\Theta_p = 4r_p^2\frac{2\rho h}{M_p + m_p},\ \Gamma_0 = \frac{m_p}{M_p} \tag{B.34}$$

and where we let

$$\Upsilon_c(\tau) = \bar{\omega}_c(\tau t_p) = \frac{1 + \Gamma_0}{1 + \Gamma_c(\tau)} \tag{B.35}$$

where

$$\Gamma_c(\tau) = \frac{m_c(\tau t_p)}{M_p},\ \Gamma_0 = \frac{m_p}{M_p} \tag{B.36}$$

Finally, we have the dimensionless versions of the average strains (averaged over the width of the projectile) at the projectile edge and cone wave-front and the peak strain around the projectile edge at about ±45° to the main axis. These are respectively

$$\bar{\Xi}_c(\tau) = \left[1 - \frac{1}{6}\left(\frac{1}{\min(2, R_c(\tau))}\right)^2 + \left(\frac{\pi}{4} - \frac{5}{6}\right)\left(\frac{1}{R_c(\tau)}\right)^{14}\right]^{\frac{1}{2}} \Xi_c(\tau) \tag{B.37}$$

$$\hat{\Xi}_p(\tau) = \Xi_p(\tau) \max\left(1, 1 + H_1(\tau)\right) \tag{B.38}$$

$$\bar{\Xi}_p(\tau) = \Xi_p(\tau)\left(1 + \frac{H_2(\tau)}{3}\right) \tag{B.39}$$

where

$$H_1(\tau) = \frac{1 + K_{m,1}(R_c(\tau) - 1)}{1 + K_a(R_c(\tau) - 1)} - 1 - \left(\frac{1}{R_c(\tau)}\right)^6 \tag{B.40}$$

$$H_2(\tau) = \frac{1 + K_{m,2}(R_c(\tau) - 1)}{1 + K_a(R_c(\tau) - 1)} - 1 - \frac{1}{2}\left(\frac{1}{R_c(\tau)}\right)^4 + 3\left(\frac{\pi}{4} - \frac{2}{3}\right)\left(\frac{1}{R_c(\tau)}\right)^5 \tag{B.41}$$

and where

$$K_{m,1} = 0.380,\ K_{m,2} = 0.400,\ K_a = 0.141 \tag{B.42}$$

B.2 Dimensionless initial conditions

For the virtual initial conditions we have

$$\Xi_{p,0} = \Xi_{c,0} \tag{B.43}$$

and

$$\Xi_{p,0} = \left(\frac{1}{4(1 + \Xi_{p,0})}\right)^{\frac{1}{3}} \left(\Xi_{p,0}^2 + \Psi_0^2\right)^{\frac{2}{3}} \tag{B.44}$$

where $\Psi_0 = V_0/a_0$. A first approximation is

$$\Xi_{p,0}^{(1)} = \left(\frac{\Psi_0}{\sqrt{2}}\right)^{\frac{4}{3}} \tag{B.45}$$

a second approximation is

$$\Xi_{p,0}^{(2)} = \left(\frac{1}{4\left(1 + \Xi_{p,0}^{(1)}\right)}\right)^{\frac{1}{3}} \left(\left(\Xi_{p,0}^{(1)}\right)^2 + \Psi_0^2\right)^{\frac{2}{3}} \tag{B.46}$$

and a third approximation is

$$\Xi_{p,0} = \Xi_{p,0}^{(3)} = \left(\frac{1}{4\left(1 + \Xi_{p,0}^{(2)}\right)}\right)^{\frac{1}{3}} \left(\left(\Xi_{p,0}^{(2)}\right)^2 + \Psi_0^2\right)^{\frac{2}{3}} \tag{B.47}$$

Also

$$\Psi_0 = V_0/a_0,\ \Delta(0) = \Delta_0 = 0,\ \dot{U}_c(0) = \dot{U}_{c,0} = -1,\ U_c(0) = U_{c,0} = 0 \tag{B.48}$$

and

$$\cos\hat{\Phi}(0) = \cos\bar{\Phi}(0) = \frac{\sqrt{\Xi_{p,0}/(1+\Xi_{p,0})} - \Xi_{p,0}}{\sqrt{\left(\left(\sqrt{\Xi_{p,0}/(1+\Xi_{p,0})} - \Xi_{p,0}\right)^2 + \Psi_0^2\right.}} \tag{B.49}$$

and

$$\sin\hat{\Phi}(0) = \sin\bar{\Phi}(0) = \frac{\Psi_0}{\sqrt{\left(\sqrt{\Xi_{p,0}/(1+\Xi_{p,0})} - \Xi_{p,0}\right)^2 + \Psi_0^2}} \tag{B.50}$$

BIBLIOGRAPHY

[1] S. L. Phoenix and P. K. Porwal. A new membrane model for the ballistic impact response and V_{50} performance of multi-ply fibrous systems. *International Journal of Solids and Structures*, 40 (2003) 6723-6765.

[2] P. K. Porwal and S. L. Phoenix. Modeling system effects in ballistic impact into multi-layered fibrous materials for soft body armor. *International Journal of Fracture*, 135 (2005) 217-249.

[3] S. L. Phoenix, A. K. Yavuz and P. K. Porwal. A new interference approach for ballistic impact into stacked flexible composite body armor, *AIAA Journal*, 48 (2010) 490-501.

[4] D. M. Grigoryan. Normal impact on a unbounded thin diaphragm. *PPM*, 13 (1949) 277-284.

[5] M. P. Galin. Impact on a flexible plate. *Sbornik Statei Instituta Mekhaniki*, 1949.

[6] Kh. A. Rakhmatulin and Yu. A. Dem'yanov. Strength under high transient loads. (1961) 94-152 (English translation, Israel Program for Scientific Translations, 1966).

[7] J. R. Vinson and J. A. Zukas. On the ballistic impact of textile armor. *ASME J. Appl. Mech.*, 42 (1975) 263-268.

[8] D. Roylance. Wave propagation in a viscoelastic fiber subjected to transverse impact. *ASME J. Appl. Mech.*, 40 (1973) 143-148.

[9] D. Roylance and S. S. Wang. Penetration mechanics of textile structures ballistic materials and penetration mechanics. Amsterdam: *Elsevier*, (1980) 273-292.

[10] J. R. Vinson and J. M. Walker. Ballistic impact of thin-walled composite structures. *Am. Inst. Aeornaut. Astronaut. J.*. 35 (1997) 875-878.

[11] S. W. R. Lee and C. T. Sun. Dynamic penetration of graphite/epoxy laminates impacted by a blunt-eneded projectile. *Compos. Sci. Technol.*, 49 (1993) 368-380.

[12] I. S. Chocron-Benloulo, J. Rodriguez and V. Sanchez-Galvez. A simple analytical model to simulate textile fabric ballistic impact behavior. *Text. Res. J.*, 67 (1997) 34-41.

[13] I. S. Chocron-Benloulo, J. Rodriguez and V. Sauchez-Galvez, A simple analytical model to simulate textile fabric ballistic behavior. *Text Res J*, 67 (1997) 520-528

[14] B. R. Scott. The penetration of compliant laminates by compact projectiles. In: *Proceedings of the 18th International Symposium of Ballistics*, San Antonio, Texas, (1999) 1181-1191.

[15] J. D. Walker. Constitutive model for fabrics with explicit static solution and ballistic limit. In: *Proceedings of the 18th International Symposium of Ballistics*, San Antonio, Texas, (1999) 1231-1239.

[16] J. D. Walker. Ballistic limits of fabrics with resin. In: *Proceedings of the 19th International Symposium of Ballistics*, Interlaken, Switzerland, (2001) 1409-1414.

[17] B. A. Cheeseman and T. A. Bogetti. Ballistic impact into fabric and compliant composite laminates. *Compos. Struct.*, 61 (2003) 161-173.

[18] C.-F. Yen, B. R. Scott, P. Dehmer and B. A. Cheeseman. A comparison between experiment and numerical simulation of fabric ballistic impact. In: *Proceedings of the 23rd International Symposium of Ballistics*, Tarragona, Spain, 2007, 853-864.

[19] C.-F. Yen and B. R. Scott. Analytic Design Trends of Fabric Armor. In: *Proceedings of the 22nd Int. Symp. on Ballistics*, Vancouver, Nov. 2005.

[20] B. R. Scott, P. Dehmer and T. Schmidt. Time Resolved Observation of the Deformation and Surface Strain of a Textile Fabric Subject to Ballistic Impact. In: *Proceedings of the 22nd Int. Symp. on Ballistics,* Vancouver, Nov. 2005.

[21] Y. Duan, M. Keefe, T. A. Bogetti and B. A. Cheeseman. Modeling friction effects on the ballistic impact behavior of a single-ply high-strength fabric. *Int J Impact Eng*, 31 (2005) 996-1012.

[22] Y. Duan, M. Keefe, T. A. Bogetti and B. A. Cheeseman. Modeling the role

of friction during ballistic impact of a high strength plain weave fabric. *Int Compos Struct*, 68 (2005) 331-337.

[23] Y. Duan, M. Keefe, T. A. Bogetti, B. A. Cheeseman and B. Powers. A numerical investigation of the influence of friction on energy absorption by a high strength fabric subjected to ballistic impact. *Int J Impact Eng*, 32 (2006) 1299-1312.

[24] Y. Duan, M. Keefe, T. A. Bogetti and B. Powers. Finite element modeling of transverse impact on a ballistic fabric. *Int J Mech Sci*, 2006 (48) 33-43.

[25] V. P. W. Shim, C. T. Lim and K. J. Foo. Dynamic mechanical properties of fabric armour. *Int J Impact Eng*, 25 (2001) 1-15.

[26] C. T. Lim, V. P. W. Shim and Y. H. Ng. Finite element modeling of the ballistic impact of fabric armor. *Int J Impact Eng*, 28 (2003) 13-31.

[27] G. R. Johnson, S. R. Beissel and P. M. Cunniff. A computational model for fabrics subjected to ballistic impact. In: *Proceedings of the 18th International Symposium on Ballistics*, Vol. 2 (1999) 962-969.

[28] D. A. Shockey, D. C. Erlich and J. W. Simons. Improved barriers to turbine engine fragments, US Department of Transportation. Menlo Park, CA: *SRI International*, 2000.

[29] G. M. Zhang, R. C. Batra and J. Zheng. Effect of frame size frame type and clamping pressure on the ballistic performance of soft body armor. *Composites: Part B*, 39 (2008), 476-489.

[30] S. Kawabata, M. Niwa and H. Kawai. The finite-deformation theory of plain-weave fabrics. Part I: The biaxial-deformation theory. *J. Text. Inst*, 64 (1973) 21-46.

[31] S. Kawabata, M. Niwa and H. Kawai. The finite deformation theory of plain-weave fabrics. Part I: The uniaxial-deformation theory. *J. Text. Inst.*, 64 (1973) 47-61.

[32] S. Kawabata, M. Niwa and H. Kawai. The finite-deformation theory of plain-weave fabrics. Part I: The shear-deformation theory. *J Text. Inst.*, 64 (1973) 62-85.

[33] I. Ivanov and A. Tabiei. Loosely woven fabric model with viscoelastic

crimped fibres for ballistic impact simulations. *Int J Numer Method Eng*, 61 (2004) 1565-1583.

[34] M. J. King, P. Jearanaisilawong and S. Socrate. A continuum constitutive model for the mechanical behavior of woven fabrics. *Int J Solid Struct*, 42 (2005) 3867-96.

[35] P. Boisse, B. Zouari and A. Gasser. A mesoscopic approach for the simulation of woven fibre composite forming. *Compos Sci Technol*, 65 (2005) 429-436.

[36] P. Boisse, A. Gasser and G. Hivet. Analyses of fabric tensile behavior: determination of the biaxial tension-strain surfaces and their use in forming simulations. *Compos Part A*, 32 (2001) 1395-1414.

[37] X. Peng and J. Cao. A dual homogenization and finite element approach for material characterization of textile composites. *Compos Pt B: Eng* 33 (2002) 45-56.

[38] M. Grujicic, W. C. Bell, G. Arakere, T. Hea and B. A. Cheeseman. A mesoscale unit-cell based material model for the single-ply flexible-fabric armor. *Materials and Design*, 30 (2009) 3690-3704.

[39] M. Grujicic, B. Pandurangan, U. Zecevici, K. L. Koudela and B. A. Cheeseman. Ballistic performance of Alumina/S-2 glassCreinforced polymer-matrix composite hybrid lightweight armor against armor piercing (AP) and non-AP projectiles, *Multidiscp Model Mater Struct.*, 3(3) (2007) 287-312.

[40] A. Shahkarami and R. Vaziri. A continuum shell finite element model for impact simulation of woven fabrics. *International Journal of Impact Engineering*, 34 (2007) 104-119.

[41] A. Shahkarami, R. Vaziri, A. Poursartip and K. Williams. A numerical investigation of the effect of projectile mass on the energy absorption of fabric panels subjected to ballistic impact. In: *Proceedings of the 20th international symposium on ballistics*, (2002) 802-809.

[42] E. M. Parsons, T. Weerasooriya, S. Sarva and S. Socrate. Impact of woven fabric: Experiments and mesostructure-based continuum-level simulations. *Journal of the Mechanics and Physics of Solids*, 58 (2010) 1995-2021.

[43] N. K. Naik, P. Shrirao and B.C.K. Reddy. Ballistic impact behaviour of wo-

ven fabric composites. *Formulation International Journal of Impact Engineering*, 32 (2006) 1521-1552.

[44] N. K. Naik and P. Shrirao. Composite structures under ballistic impact. *Int J Impact Eng*, 66 (2004) 579-590.

[45] M. Mamivand and G. H. Liaghat. A model for ballistic impact on multilayer fabric targets. *International Journal of Impact Engineering*. 37 (2010) 806-812.

[46] S. Feli, M. H. Yas and M. R. Asgari. An analytical model for perforation of ceramic/multi-layered planar woven fabric targets by blunt projectiles. *Composite Structures*, 93 (2011) 548-556.

[47] I. S. Chocron-Benloulo and V. Sanchez-Galvez. A new analytical model to simulate impact onto ceramic/composite armors. *Int J Impact Eng*. 21 (1998) 461-471.

[48] R. Zaera and V. Sanchez-Galvez, Analytical modeling of normal and oblique ballistic impact on ceramic/metal lightweight armours. *Int J Impact Eng*. 21 (1998) 133-148.

[49] R. Barauskas and A. Abraitiene. Computational analysis of impact of a bullet against the multilayer fabrics in LS-DYNA. *International Journal of Impact Engineering*, 34 (2007) 1286-1305.

[50] R. Barauskas and A. Abraitiene. Modelling of a Bullet Interaction Against the Multilayer Textile Package in LSDYNA. In: Tsahalis DT, editor. *Proceedings of the first international conference from scientific computing to computational engineering*, Athens, Greece, 2004.

[51] R. Barauskas and A. Vilkauskas. Modeling of bullet interaction against the life protection textile. In: *Proceedings of the Nordic LS-DYNA users- conference*, Gothenburg, Sweden, 2002, Engineering Research Nordic AB.

[52] B. Gu. Analytical modeling for the ballistic perforation of planar plain woven fabric target by projectile. *Composites (Part B)*, 34 (2003 361-371.

[53] M. M. Shokrieh and G. H. Javadpour. Penetration analysis of a projectile in ceramic composite armor. *Compos Struct*, 82 (2008) 269-276.

[54] H. D. Espinosa, N. S. Brar, G. Yuan, Y. Xu and V. Arrieta. Enhanced ballistic performance of confined multi-layered ceramic targets against long rod penetrators through interface defeat. *International Journal of Solids and Structures*, 37 (2000) 4893-4913.

[55] C.-C. Liang, M.-F. Yang, P.-W. Wu and T.-L. Teng. Resistant performance of perforation of multi-layered targets using an estimation procedure with marine application. *Ocean Engineering*, 32 (2005) 441-468.

[56] A. Tabiei and G. Nilakaltan. Ballistic impact of dry woven fabric composites. *Appl Mech Rev*, 61 (2008) 010801 pp.1-12.

[57] K. Krishnan, S. Sockalingam, S. Bansal and S. D. Rajan. Numerical simulation of ceramic composite armor subjected to ballistic impact. *Composites Part B: Engineering*, 41 (2010) 583-593.

[58] J. R. Vinson and J. M. Walker. Ballistic impact of thin-walled composite structures. *Am. Inst. Aeronaut. Astronaut. J.*, 35 (1997) 875-878.

[59] H. M. Wen. Predicting the penetration and performance of FRP laminates struck normally by projectiles with different nose shapes. *Compos. Struct.*, 49 (2000) 321-329.

[60] R. Clegg. Application of a coupled anisotropic material model to high velocity impact response of composite textile armor. In: *18th international symposium and exhibition on ballistics*, San Antonio, Texas, USA, November 15-19, 1999, Century Dynamics, Inc. TP052.

[61] M. Tarafaoui and S. Akesbi. A finite element model of mechanical properties of plain weave. *Colloids Surf A: Physicochemical Eng Aspects*, 187-188 (2001) 439-448.

[62] M. Park, J. Yoo and D. Chung. An optimization of a multi-layered plate under ballistic impact. *Int J Solids Struct*, 42 (2005) 123-137

[63] P. Elek, S. Jaramaz and D. Mickovic, Modeling of perforation of plates and multi-layered metallic targets, *Int J Solids Struct*, 42 (2005) 1209-1224.

[64] I. Marom and S. R. Bodner. Projectile perforation of multi-layered beams. *Int J Mech Sci*, 21 (1979) 489-504.

[65] P. M. Cunniff. An analysis of the system effects in woven fabrics under ballistic impact. *Textile Research Journal*, 62 (1992) 495-509.

[66] P. M. Cunniff. Decoupled response of textile body armor. *Proceedings of the 18th International Symposium of Ballistics*, San Antonio, TX, (1999a) 814-821.

[67] P. M. Cunniff. Vs-Vr relationships in textile system impact. *Proceedings of the 18th International Symposium of Ballistics*, San Antonio, TX, (1999b).

[68] P. M. Cunniff. Dimensional parameters for optimization of textile-based body armor systems. *Proceedings of the 18th International Symposium of Ballistics*, San Antonio, TX, (1999c) 1303-1310.

[69] G. Ben-Dor, A. Dubinsky and T. Elperin. Optimization of light weight body armor using experimental data. *International Journal of Fracture*, 100 (1999) 29-33

[70] G. Ben-Dor, A. Dubinsky, T. Elperin and N. Frage. Optimization of two component ceramic armor for a given impact velocity. *Theoretical and Applied Fracture Mechanics*, 33 (2000) pp. 185-190

[71] G. Ben-Dor, A. Dubinsky and T. Elperin. Optimization of two-component composite armor against ballistic impact. *Composite Structures*, 69 (2005) pp. 89-94

[72] M. Park, J. Yoo and D.-T. Chung. An optimization of a multi-layered plate under ballistic impact. *International Journal of Solids and Structures*, 42 (2005) 123-137.

[73] M. Cheng, W. Chen and T. Weerasooriya. Experimental investigation of the transverse mechanical properties of a single Kevlar KM2 fiber. *International Journal of Solids and Structures*, 41 (2004) 6215-6232.

[74] M. Cheng and W. Chen. Experimental investigation of the stress-stretch behavior of EPDM rubber with loading rate effects. *International Journal of Solids and Structures*, 40(18) 2003, 4749-4768.

[75] T. Borvik, M. Langseth, O. S. Hopperstad and K. A. Malo. Perforation of 12 mm thick steel plates by 20 mm diameter projectiles with flat, hemispherical and conical noses part I: experimental study. *International Journal of Impact Engineering*, 27 (2002) 19-35.

[76] T. Borvik, M. Langseth, O. S. Hopperstad and K. A. Malo. Perforation of 12 mm thick steel plates by 20 mm diameter projectiles with flat, hemispherical and conical noses part II: numerical simulations. *International Journal of Impact Engineering*, 27 (2002) 37-64.

[77] T. Borvik, J. R. Leinum, J. K. Solberg, O. S. Hopperstad and M. Langseth. Observations on shear plug formation in Weldox 460 E steel plates impacted by blunt-nosed projectiles. *Int J Impact Eng*, 25 (2001) 553-572.

[78] T. Borvik, K. Holen, M. Langseth and K. A. Malo. An experimental set-up used in Ballistic penetration. In: *Jones N, Talaslidis DG, Brebbia CA, Manolis GD (Editors) Proceedings of the fifth international symposium on structures under shock and impact*, Thessaloniki, Greece, (1998), June 24-26, 683-692.

[79] T. Borvik, M. Langseth, O. S. Hopperstad and K. A. Malo. Ballistic penetration of steel plates. *Int J Impact Eng*, 22 (1999) 855-887.

[80] N. K. Gupta and V. Madhu. Normal and oblique impact of a kinetic energy projectile on mild steel plates. *International Journal of Impact Engineering*, 12 (1992) 333-344.

[81] N. K. Gupta, M. A. Iqbal and G. S. Sekhon. Experimental and numerical studies on the behavior of thin aluminum plates subjected to impact by blunt- and hemispherical-nosed projectiles. *International Journal of Impact Engineering*, 32 (2006) 1921-1944.

[82] N. K. Gupta, M. A. Iqbal and G. S. Sekhon. Effect of projectile nose shape, impact velocity and target thickness on deformation behavior of aluminum plates. *International Journal of Solids and Structures*, 44 (2007) 3411-3439

[83] N. K. Gupta, M. A. Iqbal and G. S. Sekhon. Effect of projectile nose shape, impact velocity and target thickness on the deformation behavior of layered plates. *Int J Impact Eng*, 35 (2008) 37-60.

[84] R. R. Franzen, D. L. Orphal and C. E. Anderson Jr. The influence of experimental design on depth of penetration (DOP) test results and derived ballistic efficiencies. *International Journal of Impact Engineering*, 19 (1997) 727-737.

[85] T. Saburi, S. Kubota, M. Yoshida, Y. Wada and Y. Ogata. Projectile accelerator and numerical simulation. *International Journal of Impact Engineering*, 35 (2008) 1764-1769.

[86] V. Madhua, K. Ramanjaneyulua, T. B. Bhata and N. K. Gupta. An experimental study of penetration resistance of ceramic armour subjected to projectile impact. *International Journal of Impact Engineering*, 32 (2005) 337-350.

[87] T. Brvik, A. H. Clausen, O. S. Hopperstad and M. Langseth. Perforation of AA5083-H116 aluminium plates with conical-nose steel projectiles-experimental study. *International Journal of Impact Engineering*, 30 (2004) 367-384.

[88] Z. Rosenberg, Y. Yeshurun and J. Tsaliah. More on the thick backing technique for ceramic tile against AP projectiles. *12th International symposium on ballistics*, ADPA, San Antonio, Texas, USA, (1990) 197-201.

[89] Z. Rosenberg and Y. Yeshurun. The relation between ballistic efficiency and compressive strength of ceramic tiles, *International Journal of Impact Engineering*, 7 (1988) 357-362.

[90] R. L. Woodward and B. J. Baxter. Ballistic evaluation of ceramics: influence of test conditions. *International Journal of Impact Engineering*, 15 (1994) 119-124.

[91] W. A. Gooch and M. S. Burkins. Ballistic development of US high density tungsten carbide ceramics. *Pac Rim IV international conference on advanced ceramics and glass*, Hawaii (2001) 53-61.

[92] V. Murat, E. Zeki, B. A. Konduk and A. H. Ucisik. Ballistic performance of alumina ceramic armors. *Pac Rim IV international conference on advanced ceramics and glass*, Hawaii (2001) 103-110.

[93] D. Sherman and D. G. Brandon. The ballistic failure mechanisms and sequence in semi-infinite supported alumina tiles, *Journal of Materials Research*, 12 (1997) 1335-1343.

[94] A. Alavi-Nia and G. R. Hoseinia. Experimental study of perforation of multi-layered targets by hemispherical-nosed projectiles. *Materials and Design*, 32 (2011) 1057-1065

[95] G. N. Nurick and C. E. Walters. The ballistic penetration of multiple thin plates separated by an air gap. In: *Proceedings of SEM conference on experimental mechanics*. The Society of Experimental Mechanics, Inc., (1990) 631-637.

[96] S. Dey, T. Borvik, X. Teng, T. Wierzbicki and O. S. Hopperstad. On the ballistic resistance of double-layered steel plates: an experimental and numerical investigation. *Int J Solids Struct*, 44 (2007) 6701-6723.

[97] S. Dey, T. Borvik, O. S. Hopperstad, J. R. Leinum and M. Langseth. The effect of target strength on the perforation of steel plates using three different projectile nose shapes. *Int J Impact Eng*, 30 (2004) 1005-1038.

[98] J. Radin and W. Goldsmith. Normal projectile penetration and perforation of layered targets. *Int J Impact Eng*, 7 (1988) 229-259.

[99] X. Teng, T. Wierzbicki and M. Huang, Ballistic resistance of double-layered armor plates, *Int J Impact Eng*, 35 (2008) 870-884.

[100] B. Parga-Landa and F. Hernandez-Oliveres, An analytical model to predict impact behaviour of soft body armors. *International Journal of Impact Engineering*, 16 (1995) 455-466.

[101] G. Ben-Dor, A. Dubinsky and T. Elperin. Effect of air gaps on ballistic resistance of targets for conical impactors. *Theoretical and Applied Fracture Mechanics*, 30 (1998) 243-249.

[102] G. Ben-Dor, A. Dunbinsky and T. Elperin. On the ballistic resistance of multi-layered targets with air gaps. *Int. J. Solids Structures*, 35 (1998) 3097-3103.

[103] G. Ben-Dor, A. Dubinsky and T. Elperin, Ballistic properties of multilayered concrete shields, *Nucl Eng Des*, 239 (2009) 1789-1794.

[104] H. H. Billon and D. J. Robinson. Model for the ballistic impact of fabric armour. *International Journal of Impact Engineering*, 25 (2001) 411-422.

[105] W. R. Novotny, E. Cepus, A. Shahkarami, R. Vaziri and A. Poursartip. Numerical investigation of the ballistic efficiency of multi-ply fabric armours during the early stages of impact. *International Journal of Impact Engineering*, 34 (2007) 71-88.

[106] N. V. David, X.-L. Gao and J. Q. Zheng, Ballistic resistant body armor: contemporary and prospective materials and related protection mechanisms. *Applied Mechanics Reviews*, 62 (2009) 050802 1-19.